NON-EQUILIBRIUM THERMOMECHANICS OF MULTIFUNCTIONAL ENERGETIC STRUCTURAL MATERIALS

A Dissertation
Presented to
The Academic Faculty

By

Vindhya Narayanan

In Partial Fulfillment
Of the Requirements for the Degree
Doctor of Philosophy in Aerospace Engineering

Georgia Institute of Technology

December, 2005

NON-EQUILIBRIUM THERMOMECHANICS OF MULTIFUNCTIONAL ENERGETIC STRUCTURAL MATERIALS

Aprroved by:

Dr. Sathyanaraya Hanagud
School of Aerospace Engineering
Georgia Institute of Technology

Dr. Massimo Ruzzene
School of Aerospace Engineering
Georgia Institute of Technology

Dr. George Kardomateas
School of Aerospace Engineering
Georgia Institute of Technology

Dr. Jennifer Jordan
Air Force Research Laboratory
Eglin Air Force Base

Dr. David L. McDowell
The George W. Woodruff School of Mechanical Engineering
G*eorgia Institute of Technology*

Dr. Naresh N. Thadhani
School of Materials Science and Engineering
Georgia Institute of Technology

Dr. Suhithi M. Peiris
Research and Technology Department
Naval Surface Warfare Center

Date Approved: November 27, 2005

ACKNOWLEDGEMENTS

I would like to thank my advisor Dr. S. Hanagud for providing me with the opportunity to conduct this research and for his constant guidance in my endeavors and for sharing with me his knowledge and expertise.

I would like to acknowledge my dissertation committee members Dr. David. L. McDowell, Dr. Naresh N. Thadhani, Dr. Suhithi M. Peiris and Dr. Jennifer Jordan for their advice and suggestions. I would also like to thank Dr. Massimo Ruzzene and Dr. George Kardomateas for serving on my dissertation committee.

I would like to express my gratitude and appreciation to Dr. Lu for her constant help and support during my stay at Georgia Tech. I would like to thank all my colleagues and friends for their support and encouragement.

I would especially like to thank my parents, V. Narayanan and Shoba Narayanan, and my sister, Divya Narayanan, for their unwavering support and constant encouragement and for their infinite faith and belief in me. I wish to acknowledge my sister for all the indispensable help she has rendered me during her stay at Georgia Tech. I would like to thank her and my parents for constantly being there for me.

Contents

List of Tables

List of Figures

SUMMARY

Shock waves create a unique environment of high pressure, high temperature, large strains and high strain-rates. It has been observed that chemical reactions, of certain mixtures of metal and metal oxide or intermetallics, are exothermic and can lead to the synthesis of new materials that are not possible under other conditions. This observation resulted in the development of materials that could be used as binary energetic materials. The binary energetic materials are of significant interest to the energetic materials community because of their capability of releasing high heat content during chemical reactions and the relative insensitivity of these types of energetic materials. These binary mixtures of energetic materials provide an opportunity to develop a dual functional material with both strength and energetic characteristics. When mixtures like aluminum and iron-oxide or nickel and aluminum are synthesized at nanoscales, their mechanical strength can be increased because of the nanostructure, while their energetic characteristics are also improved significantly. Additional incorporation of structural reinforcements and binders, at the nano level, can further increase the strength of these materials. These dual functional materials provide both strength and energetic characteristics when desired. They can be used in applications where usually combinations of different monofunctional materials are currently used for structural strength or energetic characteristics. These dual functional materials also have dual branches of failure criteria. One is the strength based failure criteria. The second is the reaction based failure criteria that implies that chemical reactions should not initiate when only strength is desired. However, a complete chemical reaction should take place when needed. It is thus, essential that mechanisms of chemical reactions are understood.

Shock-induced chemical reactions pose many challenges in experiment and instrumentation. Thus, this thesis, is addressed to the theoretical development of constitutive models of shock-induced chemical reactions in energetic composites, formulated in the framework of non-equilibrium thermodynamics and mixture theories, in a continuum scale. A hybrid non-equilibrium thermodynamic framework that combines the concepts of internal variables and thermodynamic fluxes (extended irreversible thermodynamics) is used. The analytical modeling procedure includes the selection of internal state variables and thermodynamic fluxes (or extended state variables) from underlying chemical reaction processes. Previously, Lu and Hanagud have introduced the use of hybrid non-equilibrium thermodynamic variables and internal variables to study high strain-rate phase transition, with a mixture theory based on simply connected boundaries between the species. In this thesis, the use of hybrid variables in the framework of non-equilibrium thermodynamics is expanded to study shock-induced or assisted chemical reactions in binary energetic composites. The governing system of partial differential equations is formulated in the framework of extended irreversible thermodynamics. A mixture theory in which the N components of the mixture are homogenously distributed throughout the mixture is used. This represents the intimate mixing of the reactants which is important in the reaction initiation process. Lu also suggested the use of simply connected boundary mixture theory to study chemical reactions that are based on the original Arrhenius equation and Onsager's classical irreversible thermodynamics. However, the mechanism to reach the transition state, time delays in chemical reactions, shock-induced or assisted chemical reactions or uniformly blended mixture theories were not considered. No partial differential equations (PDE's) were integrated. These are developed in this thesis and are included as follows. Transition state based chemical reaction models are introduced and incorporated with the conservation equations that can be used to

calculate and simulate the shock-induced reaction process. The energy that should be supplied to reach the transition state has been theoretically modeled by considering both the pore collapse mechanism and the plastic flow with increasing yield stress behind the shock wave. A non-equilibrium thermodynamics framework and the associated evolution equations are introduced to account for time delays that are observed in the experiments of shock-induced or assisted chemical reactions. An appropriate representation of the particle size effects is introduced by modifying the initial energy state of the reactants. The constraints on the resulting constitutive equations from the second law of thermodynamics are discussed. The system of conservation equations, constitutive equations and chemical reaction equations are integrated numerically in one-dimensional strain conditions, by using a numerical method known as the MUSCL scheme. The MUSCL scheme reduces significantly the computationally induced oscillations. This scheme has not been used for the calculation of shock-induced chemical reactions. Numerical results are presented for shock-induced reactions of mixtures of Al, Fe_2O_3 and Ni, Al with epoxy as the binder. The results indicate that as the porosity and the plastic flow increase, the temperature in the mixture also increases leading to increased concentration of the product. The relaxation times associated with the pore collapse and the chemical reaction are modeled as functions of the state of the system.

The theoretical model, in the continuum scale, requires parameters that should be experimentally determined. The experimental characterization has many challenges in measurement and development of nano instrumentation. An alternate approach to determine these parameters is through ab-initio calculations. Thus, this thesis has initiated ab-initio molecular dynamics approach to calculate and simulate chemical reactions of binary energetic materials. Specifically, the case of aluminum and nickel is considered. In this first level of ab-initio calculations, only thermal effects in the

initiation of chemical reactions is discussed.

Chapter I

INTRODUCTION

In the past, shock-induced physics and chemistry have been used to synthesize new materials [44][48][102][113] with unique microstructures. This area of research was initiated in 1960's and the progress over the years has been reviewed in several review papers [12][15][17][113]. Chemical reactions that occur during the shock process in mixtures like Ni-Al [13][14][49][130][133][140], are exothermic. These exothermic reactions were used to develop binary energetic materials. In addition to Ni-Al, there are many other intermetallic-energetic materials like Ti-Si [94][113], Mo-Si [81][118] and Nb-Si [25].

Intermetallics form one class of binary energetic materials where the two components of the mixture are both metals. There is another class of binary energetic materials that consist of mixtures of metals and metal oxides. In this class, metals like aluminum constitute the fuel and metal-oxides like iron-oxide (Fe_2O_3) form the oxidizer [111][112][122]. Such a mixture of aluminum and iron-oxide can release a significant amount of energy through an exothermic reaction when the mixture is subjected to a shock or thermal loading. In addition to $Al - Fe_2O_3$ mixture, there are other metal/metal-oxide mixtures that can be used as the binary energetic material [44].

The word 'thermite' was first used to describe the reduction of a metal-oxide by

aluminum through an exothermic reaction [122]. These reactions can achieve significantly high temperatures. For example, the reaction between Al and Fe_2O_3 can reach temperatures of 3000°C [122]. But now, the term 'thermite' refers to a much broader category of compounds as compared to its initial use. Thermite reactions are oxidation-reduction reactions that occur between a metal and a metallic or a non-metallic oxide to form a stable oxide and the corresponding metal or non-metal of the initial reactant oxide. This reaction is generally exothermic in nature. These mixtures have a variety of uses. Their exothermic nature makes them ideal candidates for energetic materials. Since very often their products are in the molten state and these can be separated using gravity (heavier metal vs. a lighter oxide), they have metallurgical applications. They have a number of pyrotechnic and combustion uses (propellants) since their self-sustaining reactions can be adjusted by the addition of an inert diluent. They also have uses in the synthesis of ceramics and composite materials and are used in the preparation of ceramic linings in metal pipes. There is a comprehensive review article on thermite mixtures and their reactions by Wang et. al. [122].

The binary energetic materials, consisting of intermetallics or metals and metal-oxides, are of significant interest to the energetic materials community because of their capability of releasing high heat content during a chemical reaction and the relative insensitivity of these types of energetic materials. Even though binary energetic materials have the potential to release a significant amount of heat, the rate of release of the heat energy is much lower than the mono-molecular energetic materials [39]. Similarly, a complete reaction is not always realized. To increase the rate of reaction and obtain complete release of heat energy, there is a considerable amount of research being conducted to synthesize these materials at nano scales [39][112]. Aumann et. al. [8] developed a gas condensation method to produce 20-40 nm particles

of MnO_3 and aluminum, with an energy density greater than 16 kJ/cm^3. Tillotson et. al. [111][112] developed a sol-gel technique to synthesize iron oxide and aluminum mixtures at nanometer scales. Tannenbaum et. al. [121] have studied modifying the sol-gel process to be able to control the sizes of the pores in the iron-oxide xerogels and thus control the energetics of these mixtures. A significant number of studies are being conducted to analyze and understand the behavior of these mixtures that are synthesized at a nanometer level [123][131][132].

Nano synthesis of these binary mixtures of energetic materials provides an opportunity to develop a dual functional material with both strength and energetic characteristics. When mixtures like aluminum and iron-oxide or nickel and aluminum are synthesized at nanoscales, their mechanical strength can be increased because of the nanostructure. Additional incorporation of structural reinforcements and binders, at the nano level, can further increase the strength of these materials. Such a dual functional material has been synthesized with nano-sized nickel, nano-sized aluminum, epoxy, carbon nanotubes and teflon by mixing and pressing these materials [134]. These dual functional materials can provide both strength and energetic characteristics when each function is desired. These materials can be used in applications where usually combinations of different monofunctional materials are used for either structural strength or energetic characteristics.

Among many possible applications, an example is that of a kinetic energy projectile that usually consists of a structural casing (usually made of steel)[37][38], that houses monomolecular energetic material (figure 1). If we focus on the structural casing, a systems designer has the choice of many inert metallic materials like steel that can be used for the casing. Similarly, many organic monomolecular energetic materials can be used as energetic materials. In many applications, the purpose of

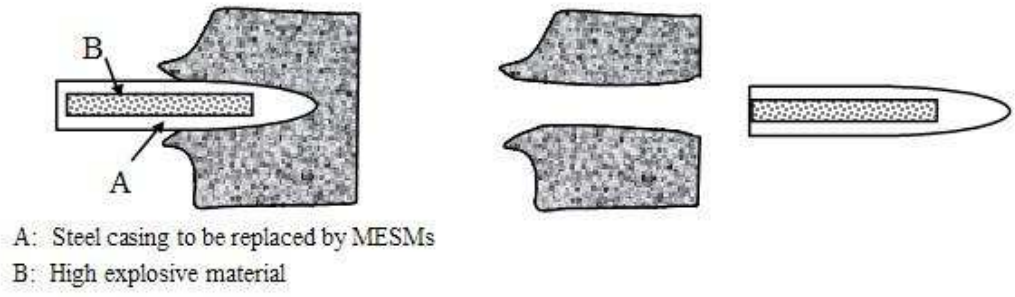

Figure 1: Kinetic-energy projectile

the structural casing and the associated nose shape of the projectile are mainly to provide the strength that is needed to penetrate through selected targets. Following the penetration, as needed, the reaction of the monomolecular energetic material is initiated. However, if we can have one material that can provide both the functions of structural strength and energetic characteristics, the entire projectile can have the energetic characteristics while providing penetration capabilities when needed and thus, reducing the weight and increasing the efficiency of the system. Such materials are denoted by the term "multi-functional energetic structural materials (MESM)".

A second possible application of the dual functional energetic structural materials is to design structural components of a rocket that eventually leaves minimum amount of space debris.

To design projectiles and other similar structural systems, it is necessary to characterize these materials and study the performance of the structure during practical applications. A binary energetic structural material should be characterized for its strength characteristics and energetic characteristics. Because of the dual functions of these materials, there are dual branches of failure criteria. One is the strength based failure criteria. The second is the reaction based failure criteria. The second criteria

is used to ensure that a structure, like a projectile, designed by using these materials will not chemically react during phases of operation such as penetration through a target. (However, the material should also react completely when needed.) Thus, it is necessary to characterize the constitutive relations of these dual functional materials and understand the initiation and sustained chemical reactions, during shock loading, which can result from an impact and penetration through selected targets. These targets can include metallic, concrete or soil targets.

The chemical reactions of these multifunctional energetic materials is a multiscale phenomena. However, most designs rely on numerical methods that can simulate impact and penetration at a continuum level. Thus initially, the objective of the thesis is to study the behavior at a continuum scale. Later reactions at an ab-initio level will be discussed.

The sections of this thesis are divided as follows. Chapter 2 provides a literature review of the work that has been done by researchers in their respective areas in the past. Chapter 3 provides the main objectives of this work and the approach that is utilized in meeting those objectives. Chapter 4 details the derivation of the set of partial differential hyperbolic equations that governs the problem. It provides the foundation for the numerical analysis of specific problems. Chapter 5 provides the results obtained in the numerical study of the thermite mixture of aluminum (Al) and iron-oxide (Fe_2O_3) using the framework developed in chapter 4. Chapter 6 includes the study of the intermetallic mixture of nickel (Ni) and aluminum (Al). Chapter 7 provides the ab-initio molecular dynamics simulations of the thermally induced chemical reaction in the nickel-aluminum intermetallic mixture. A detailed discussion of the results obtained in this work is included in chapter 8. Chapter 9 contains the conclusions and recommendations for future work.

Chapter II

BACKGROUND

The analysis of multi-functional materials at the continuum level is multidisciplinary. Different disciplines include physics, chemistry, materials science, solid mechanics and mathematics related to the numerical integration of partial differential equations. The main focus in this thesis is the shock induced/assisted chemical reactions in multi-functional materials and the prediction of the initiation of chemical reaction and the extent of reactions. This chapter provides the background related to this area. A review of the other subject areas that include Thermodynamics, Ab-initio molecular dynamics and numerical integration of nonlinear partial differential equations is provided in the appendix.

2.1 CHEMICAL REACTIONS IN BINARY ENERGETIC MATERIALS

2.1.1 Thermochemical vs. Mechanochemical Model

Many different explanations have been proposed for the initiation of chemical reaction in binary metal/metal-oxide energetic materials. They are described as models. Two such proposed mechanisms are the thermo-chemical model and the mechano-chemical model. In the thermochemical model, the additional pressure-volume energy in the

system is assumed to result in an elevated temperature that will drive the chemical reaction with associated high stresses. Boslough [17] experimentally measured the shock temperature in a thermite mixture with 50% porosity using radiation pyrometry. Based on the results, he observed an initial spike in the temperature when the mixture is shock-impacted. This spike is attributed to the collapse of pores in the mixture. This increased temperature then leads to a chemical reaction initiation. Reaction initiation described, based on such a mechanism, is called a thermochemical model. Furthermore, Boslough attributed that the dynamic mixing that occurs at the shock front controls the rate of the chemical reaction. Thermochemical models suggest that reactions take place in a very thin region while in reality, it has been found that the reactions occur over a wide region and covers a time duration of up to 100 ns [12][13][15][130][133]. A thermodynamic equilibrium is assumed in this model.

The second model that explains the initiation of chemical reactions is the mechanochemical model. According to this model, inter-particle contacts result in high stresses and enhanced plastic deformations leading to a "more intimately" mixed condition, and the resulting reactions. Plastic deformation is assumed to enhance the solid-state reactivity. Thadhani et al [113] experimentally studied the particle size effects on shock-induced chemical reactions. From their observations, they attributed the initiation of chemical reactions in shock compression of powders of mixtures of Ti and Si to the solid-state mechanochemical processes and explained the initiation of chemical reaction based on plastic flow and mechanical deformations around the voids. They also studied [94] a number of mixtures such as Ti-Si, Ti-Al and Ti-B and subsequently showed that the chemical reaction initiation and the reaction rate significantly vary with the mechanical properties of the reactants.

2.1.2 Shock-initiated vs. Shock-assisted chemical reactions

Researchers associate two different mechanisms to describe the chemical reactions in energetic materials due to shock waves. The two different reaction mechanisms are defined as the shock-induced or shock-initiated chemical reactions and the shock-assisted chemical reactions. Shock-assisted chemical reactions are thermally initiated reactions that occur through an increase in the bulk temperature due to the passage of a shock wave. The reactions are also assumed to occur in time-scales of "thermal equilibrium" while shock-induced chemical reactions are initiated by mechanisms resulting from the increase of pressure or stress and are assumed to occur in time scales associated with "pressure equilibrium" [118]. In other words, the shock-assisted chemical reactions are assumed to occur via the thermochemical model and the shock-induced chemical reactions via the mechanochemical model.

Vandersall et. al [118] studied the chemical reactions in a mixture of molybdenum and silicon using shock-recovery experiments. By calculating the peak shock pressure and mean bulk temperature, they found that the loading conditions affected the mechanism of the chemical reaction. The cylindrical implosion geometry experiments led to shock-assisted chemical reactions while the planar pressure geometry experiments underwent shock-induced chemical reactions. In the former case, the mean bulk temperature exceeded the melting temperature of either one or both components and thus, led to partial or complete reaction, respectively. In the latter case, it was the high peak shock pressure that was reached (22-40GPa) that led to the initiation of chemical reaction. In this case, the mean bulk temperature was lower than the melting point of Si (which has the lower melting point of the two components). The microstructures of the products obtained in those experiments were also observed to

be different, with the thermally-initiated microstructure being governed by the melting and solidification process and the pressure-initiated microstructure being defined by the deformation, plastic flow and enhanced mixing between the components. Meyers et al [81] experimentally studied shock-assisted and shock-induced reactions for Nb-Si and Mo-Si mixtures. They modified the Krueger-Vreeland threshold energy by including a term that denoted the plastic deformation and showed that plastic deformation or intense shear localization plays an important role and can trigger chemical reactions. Their results seemed to indicate that the reactions in this case were more shock-induced rather than shock-assisted.

When a binary energetic mixture is shock loaded, the components of the mixture can undergo deformation and plastic flow leading to enhanced mixing. There could be several factors which hinder this process such as excessive quantity of one reactant, lack of sufficient space for mixing between the reactants, namely insufficient void volume and mechanical properties of the reactants such as brittleness. Under these conditions, the binary mixture may not undergo shock-induced chemical reactions but at the same time the bulk temperature of the mixture would have increased due to the shock process by other mechanisms,to a temperature greater than the reaction initiation temperature in the mixture and thus, a chemical reaction might occur due to this high temperature [94].

Post-shock analysis of the microstructure of the mixture will not reveal if the mixture underwent a shock-induced or a shock-assisted chemical reaction. It is not possible to judge from the postmortem microstructural analysis if the reactants of the energetic mixture reacted due to the deformation, plastic flow and enhanced contact and mixing between reactants (in time scales of pressure equilibrium) or as a result

of an increase in mean bulk temperature that occurs in time scales of thermal equilibrium. However, the postmortem analysis can be used to gain understanding about the mechanism of reaction initiation, if this microstructure were analyzed just prior to the onset of reaction in the mixture. Researchers conduct time-resolved measurements during the impact loading and use the pressure or stress profiles to decide if the reaction was shock-initiated or shock-assisted [10][11][12][113][128].

2.1.3 Various factors that affect reactions in energetic materials

Batsanov [12] reviewed the shock and particle velocity measurements of reactions in the condensed state. He proposed that particles of various constituents diffuse with each other once the shock front passes through the mixture and that the fragmentation of the shock wave leads to the formation of domains of 10nm in size and it is at the interface of these domains where the chemical reaction initiates. Iyer at al [54] studied the effects of impact velocity on the chemical reaction initiation and found an inverse relation between the particle size and impact velocity threshold for reaction initiation [40]. Shock wave velocities and stress profiles were measured using piezoelectric gages. Horie et. al. have modeled shock-induced chemical reactions [49][133] and the burn rate of conventional explosives [43][47]. They have also formulated a hydrodynamic model, with equations of conservation, for the analysis and interpretation of shock-induced chemical reactions in inorganic powder mixtures of binary energetic materials [15]. They assumed the process to be in thermodynamic equilibrium and thus made use of equilibrium thermodynamic state variables for their study. Studies [27][101][114] of the effects of morphology (particle size) on the chemical reaction between Ni and Al showed that the reaction initiation and the extent of reaction depends on the morphology of the initial mixture. Do et. al. [25]

studied the shock-induced chemical reactions for a silicon-niobium system by performing numerical simulations at the mesoscopic level. Thadhani et al. studied the effects of morphology on shock-induced chemical reactions in an intermetallic mixture of titanium and silicon, experimentally[113]. The post-shock material analysis and nanosecond time-resolved pressure measurements showed medium morphology particles of Si underwent chemical reactions but not the fine or coarse powders of Si. The reason attributed to these observations were that the fine particles formed agglomerates that made it harder to achieve good mixing between Ti and Si and the coarse particles of Si fractured and deformed and were entrapped within the Ti particles, making it harder for the initiation of chemical reactions.

Royal et. al. [94] experimentally studied mixtures of Ti-Si, Ti-Al and Ti-B and observed that mechanical properties such as Young's modulus and yield stress affects the initiation of chemical reactions under shock loading. A low yield stress leads to greater plastic flow which causes one material to flow and surround the other material. This could obstruct the mixing process between reactants and inhibit the reaction process. Brittle materials like Boron tend to deform and fracture and the particles get mixed with the second reactant, thus, providing a favorable mixture for initiation of chemical reactions. Such mixtures, therefore, tend to undergo reactions during the shock compression phase (shock-induced) whereas mixtures containing Al tend to undergo reaction in the post-shock phase due to an increased temperature (shock-assisted) as a result of the loading conditions.

2.2 DETONATION MODELS FOR MONOMOLECULAR ENERGETIC MATERIALS

The stimulus for the investigation of flame propagation was provided by catastrophic explosions that occurred in coal mines in the nineteenth century. [26] This led to the discovery of gaseous detonations with supersonic velocity. This velocity could not be described in terms of thermal conductivity and diffusion process and it was Mallard and Le Chatelier who explained the phenomenon of combustion propagation based on a compression mechanism [26]. The Russian physicist Michelson described the detonation theory of mono-molecular energetic materials on the basis of shock wave theory with the energy being released at the shock front [26]. This was later independently deduced by Chapman and Jouget and the theory widely came to be known as the Chapman-Jouget (CJ) theory. They proposed a rule, which states that the detonation velocity is defined by the tangent from the initial state to the pressure-volume curve. More explicitly, combining the mass and linear momentum conservation equations leads to a line in the pressure-volume plane, called the Rayleigh line. This line contains the detonation velocity as a parameter. When the energy conservation equation is also included in the analysis, a curve in the pressure-volume plane is obtained, known as the hugoniot curve. The conservation conditions would then require that the final solution lie on both the Rayleigh line as well as the Hugoniot curve. There are three possibilities for the intersection between the Rayleigh line and the Hugoniot. This is depicted in fig. 2. Rayleigh line 2 is a tangent to the Hugoniot and thus, there is exactly one solution. The point of tangency define the detonation velocity D, which is a unique variable. Line 1 does not intersect the Hugoniot and thus, there are no solutions for velocities lesser than the detonation velocity D. Line 3 intersects the Hugoniot leading to two possible solutions. Point S and W denote a strong and weak solution respectively. The flow at the strong point (S) is subsonic with respect

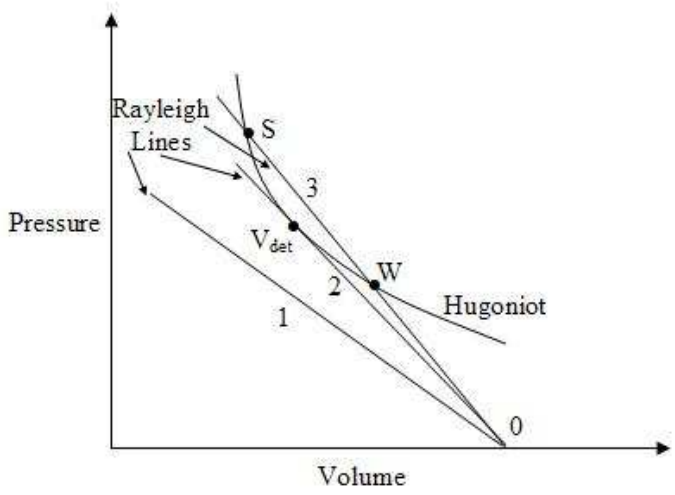

Figure 2: Chapman Jouget detonation theory

to the front and thus, a disturbance behind the front can overtake it. Thus, a rarefaction wave will overtake the detonation at this point reducing its strength. On the other hand, the weak point (W) is supersonic with respect to the front and thus, the rarefaction wave will always fall behind this region.

This effectively states that each mixture has a unique detonation velocity independent of the specimen dimensions and geometry. Since the Chapman-Jouget (CJ) theory considers shock detonation to be instantaneous, one has to conclude that shock compression and chemical reaction transformation to detonation products occur at the shock front itself. Thus, the Chapman-Jouget (CJ) detonation model was sometimes called the "Zero-reaction zone" model [26]. This model therefore does not give us any information about shock-initiation and reaction propagation.

The idea of a finite chemical reaction zone was proposed many years after the CJ theory was proposed. Zeldovich developed a detonation model with a finite chemical reaction zone. At the same time, Von Neumann and Doring independently proposed

a similar model [26][35]. Hence the new theory came to be known as the Zeldovich-von-Neumann-Doring (ZND) theory. The ZND model was developed to account for observations that the Chapman-Jouget (CJ) theory did not consider. This theory considers a finite chemical reaction zone. It considers the material behind the shock to be only compressed by the shock wave with no chemical changes in this region. Behind this compressed region is where the chemical reaction initiates because of the high temperature induced by the compression or other related processes.

However, both the CJ theory and the ZND model are one-dimensional. It could not account for multidimensional detonation and phenomenon such as the spinning detonation. This phenomenon was observed in 1926 by Campbell and Woodhead when they investigated detonation in mixtures of carbon monoxide and oxygen. They observed that the wave front consists of waves with each wave having a corresponding band in the cross-sectional region of the reaction products. This kind of detonation was termed spin detonation and it has been found to occur very frequently in the detonation process [135]. There are two reasons attributed to the occurrence of this phenomenon. The first of these is that the reaction occurs periodically and the second reason states that the ignition zone moves along a helical path near the outer surface of the specimen, near the wall enclosing the specimen. Some researchers did attempt to explain the phenomena of spinning detonation based on the ZND model. For example, Shchelkin and Troshin [95] attempted to explain the spinning detonation based on oblique shocks in the ZND model and the unstable mechanism based on the hot spot mechanism. Hot spots are small regions where the conditions are favorable for the local initiation of chemical reactions. In the Shchelkin and Troshin model [95], the detonation front is unstable and detonation occurs only in a few places (hot spots or triple shock configuration locations) and then proceeds to other locations through repeated collisions. If these collisions do not occur, hot spots do not spread

and detonation may not take place. Instead a reaction-quenching wave is produced. But the existence of reaction quenching waves in stable detonations led to the development of a new concept to explain the chemical reaction breakdown phenomenon.

For liquid explosives, the intensity of the shock wave and thus, the initiation of detonation and completion of the chemical reaction depends on the heat or energy release of the liquid explosive. This energy release lends support to the shock wave and helps the detonation to grow. If this energy is greater than the cooling due to the rarefaction waves, then the shock intensity increases and thus detonation will occur. On the other hand, if the rarefaction waves are more powerful than the energy release of the shock wave, then a breakdown of detonation will occur. For a solid explosive, detonation and breakdown phenomenon are characterized by a similar struggle between the maximum rate of energy release and the rate of loss of energy due to the cooling caused by the adiabatic waves. In porous solids, it is thought that hot spots (areas where the conditions are conducive for a chemical reaction to initiate) are formed that aids in the transition of the shock to detonation [26]. There have been numerous studies conducted over the years on the characteristics and behavior of hot spots such as interaction among hot spots, growth condition and reaction criteria in hot spots [7][47][123][131][132]. Mechanistic burn models that account for the microstructure of the mixture have been developed [50]. This model describes the hot-spot formation based on three different energy localization mechanisms, those of void collapse, shear banding and friction.

Tarver [110] proposed a detonation model with four principal zones: "a very thin leading shock front in which the unreacted explosive mixture is compressed and accelerated in the direction of shock propagation, a much thicker relaxation zone in which

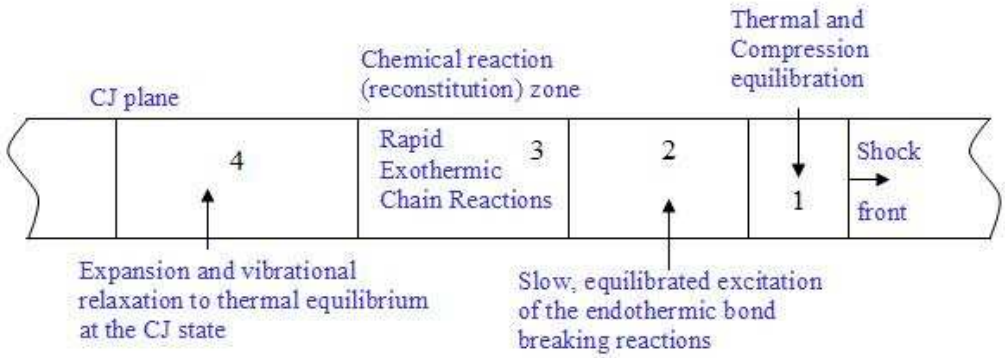

Figure 3: Tarver's Detonation Model

the rotational and vibrational modes of the unreacted explosive gases approach thermal equilibrium, a relatively thin zone in which the chemical energy is released by rapid chain propagation and branching reactions into highly vibrationally excited reaction product gases and another very thick relaxation zone in which the product gases expand and vibrationally relax toward thermodynamic equilibrium at the CJ state". This has been pictorially represented in fig. 3. In the first region, viscous effects play a significant role and cannot be neglected. Chemical induction takes place in the second zone through the relaxation of rotational and vibrational degrees of freedom. In this process, some molecules are in a high vibration state and begin to dissociate forming an intermediate high energy compound. This comprises the third zone or the chemical reaction zone. And following this, is the relaxation of the reaction products to the CJ state as vibrational de-excitation is achieved.

2.3 CHEMICAL KINETICS

A chemical reaction is said to have taken place when the chemical composition of the reactants undergo changes. It results in the formation and breaking of chemical bonds

between atoms. It could be the formation of a compound, (for example- formation of water from hydrogen and oxygen, eqn. 1) or the dissociation of a compound (for example- dissociation of a hydrogen molecule into hydrogen atoms, eqn. 2)

$$H_2 + O_2 \rightarrow H_2O \tag{1}$$

$$H_2 \rightarrow 2H \tag{2}$$

In the late 1890's, the Scottish chemist Sir William Ramsay discovered the elements helium, neon, argon, krypton and xenon. These elements, along with radon, were placed in group VIIIA of the periodic table and nicknamed inert (or noble) gases because they did not to react with other elements. This is because of their electronic configurations. They have a complete valence shell - their outermost orbital holds the full capacity of electrons and hence these elements display no tendency to react with other elements. Thus, the reason atoms react with each other is to reach a state in which their valence shell is filled. This is a stable configuration and all reactions take place with an aim to reach this configuration. There are two methods by which this is achieved.

- Ionic bonds - In this case, atoms exchange electrons with one another. Thus, one element/molecule loses electrons and another gains the same such that each one completes its valence shell. For example, if we consider the reaction between sodium (Na) and chlorine (Cl) to form sodium chloride (NaCl), Na has one electron in its outermost shell and it gives this to the chlorine which has seven in its outermost shell. Thus, by this reaction, chlorine completes its required eight electrons in its ultimate shell and sodium which has a complete penultimate shell also gets a complete valence shell as the penultimate shell now becomes the ultimate shell.

- Covalent bonds - In this case, atoms share electrons to complete their respective valence shells. This type of bonds is very often seen in carbon which has a half-filled valence shell of four electrons. This can be seen in the reaction between carbon (C) and oxygen (O) to form carbon-di-oxide (CO_2), where the carbon shares two electrons with each of the oxygen to get the four electrons it needs to get a complete valence shell and similarly, oxygen obtains its required two electrons.

Chemical reactions are accompanied by a change in the energy of the system. In some cases, energy is given out to the surroundings, usually in the form of heat and such reactions are called exothermic reactions. In other instances, the system absorbs energy from the surroundings and this type of reactions are called endothermic reactions. Reactions can either take place spontaneously or require some kind of a trigger in order to get the atoms to react. Sodium and chlorine react spontaneously whereas hydrogen and oxygen do not spontaneously to form water. Some energy has to be added to the system to start or initiate the reaction. This energy is called the activation energy (E_a). The amount of activation energy that is required differs from reaction to reaction and depends on the state of the system.

The rate at which a chemical reaction proceeds is measured by a quantity θ, which is called the chemical reaction rate. If we think of the reaction rate as a finite probability of a given reaction occurring, then it is just the collision frequency times the number of successful collisions between the molecules of the reactants with an activation energy greater than E_a. The Swedish scientist Svante Arrhenius in 1889, gave the well-known and much-used expression for the chemical reaction rate constant as

$$k = A \exp\left(-\frac{E_a}{RT}\right) \tag{3}$$

where R is the universal gas constant, T is the absolute temperature and A is the pre-exponential factor.

The chemical reaction rate Θ is then defined to be a product of the rate constant and concentration of the reactants as shown below :

$$\Theta = k \prod_{s} \left[\frac{\bar{\rho}^{s} c}{{}^{s}M} \right]^{{}^{s}\varsigma} \tag{4}$$

where ${}^{s}\varsigma$ is the stoichiometric coefficient for species s, ${}^{s}M$ is the molar mass for species s and ${}^{s}c$ is the mass concentration for species s. For example, if we consider the thermite reaction, $2Al + Fe_2O_3 \rightarrow Al_2O_3 + 2Fe$,

$$\Theta = {}^{+}k \left[\frac{\bar{\rho}^{Al} c}{{}^{Al}M} \right]^{2} \left[\frac{\bar{\rho}^{Fe_2O_3} c}{{}^{Fe_2O_3}M} \right] \tag{5}$$

The rate of the reaction has dimensions of moles per liter per second. It was Arrhenius who first proposed the concept of an "activated complex". An activated complex is an intermediate stage of the reaction path when the complex is neither completely made of reactants nor completely made of products. It has both reactant-like and product-like bonds. When Arrhenius proposed this concept, it was thought to be a state that the reactants have to reach in order to form the products. Thus, the reaction proceeds only if the energy is sufficient to reach the activated complex i.e., if it can cross the energy barrier of the activated complex (see fig. 4). This concept plays a key role in the analysis of chemical reactions.

A major breakthrough in reaction dynamics is attributed to the work of Eyring and Polanyi in 1931, when they proposed a semi-empirical calculation of the potential energy surface from the reactants to the products passing through a transition state.

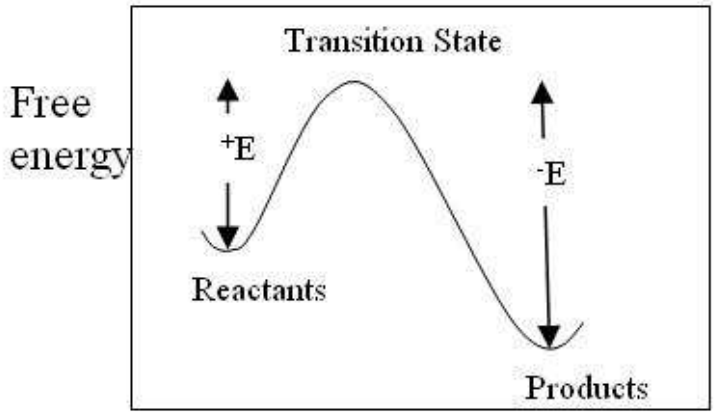

Figure 4: Reaction Path

In 1935, Eyring, Evans and Polanyi formulated the transition state theory where they provided an expression for the Arrhenius pre-exponential factor A [137].

$$k = \frac{\kappa T}{h} K^{\ddagger} = \frac{\kappa T}{h} \frac{Q^{\ddagger}}{\prod_{s}^{s+} Q} \exp\left(\frac{-E_0}{\kappa T}\right) \tag{6}$$

where κ is the Boltzmann's constant, h is Planck's constant and Q is the partition energy. The symbol ‡ refers to the transition state. If the reaction mechanism consists of more than one elementary step, then each stage of the reaction will have a transition state and thus the reaction might pass through multiple transition states.

Zewail, the Nobel Prize laureate for Chemistry in 1999 described transition state to encompass all the intermediate stages between the reactants and products. He defined it to consist of any and all stages that have potential energies significantly different from the reactants and products. He then defined the point of highest energy as the saddle point. This configuration in the reaction path is what is called the activated complex and is very commonly referred to as the transition state. This particular point of the reaction path is chosen as the transition state from the point of view of chemical kinetics as it defines the rate of a chemical reaction and also the

probability of the occurrence of a reaction. The transition state was thought to be a hypothetical state of the reaction long after it was proposed by Arrhenius but Zewail's group succeeded experimentally to isolate and observe the transition structure $I...CN^{\ddagger}$ in the dissociation of ICN to give I and CN [137].

One of the reactions criteria that has been used for solid explosives is the Merzhanov reaction criteria [79]. This criteria is based on the thermal explosion of hot spots. The analytical equation that describes this phenomenon is given by [79].

$$\begin{aligned}
&\tfrac{\partial\theta}{\partial\tau} = \exp\,\theta \,+\, \tfrac{1}{\delta}\left(\tfrac{\partial^2\theta}{\partial\xi^2} + \tfrac{n}{\xi}\tfrac{\partial\theta}{\partial\xi}\right) \\
&\tau = 0 \begin{cases} \theta = 0 & \xi < 1 \\ \theta = -\theta_0 & \xi > 1 \end{cases} \qquad \theta_0 > 0 \\
&\tau \geq 0 \;\; \xi = 0 \;\; \tfrac{\partial\theta}{\partial\xi} \,=\, 0 \\
&\qquad\quad \xi = \infty \;\; \tfrac{\partial\theta}{\partial\xi} \,=\, 0
\end{aligned} \tag{7}$$

where the variables are

$$\begin{aligned}
\theta \;&=\; \tfrac{E}{RT_0^2}\,(T - T_0) \\
\xi \;&=\; \tfrac{x}{r} \\
\tau \;&=\; t\tfrac{Q}{c\rho}\tfrac{E}{RT_0^2}k_0 \exp\,\left(-\tfrac{E}{RT_0}\right) \\
\delta \;&=\; \tfrac{Q}{\lambda}\tfrac{E}{RT_0^2}r^2 k_0 \exp\,\left(-\tfrac{E}{RT_0}\right) \\
\theta_0 \;&=\; \tfrac{E}{RT_0^2}\,(T_0 - T_1) \\
\beta \;&=\; \tfrac{RT_0}{E}
\end{aligned} \tag{8}$$

In the above expressions, T is the absolute temperature, t is the time, T_0 is the initial hot spot temperature, T_1 is the temperature of the medium, r is the hot spot

radius, Q is the heat of reaction, E is the activation energy, k_0 is the pre-exponential factor, c is the specific heat, λ is the thermal conductivity coefficient, ρ is the density and n is the hot spot symmetry factor (n=0 for planar hot spot, n=1 for cylindrical hot spot and n=2 for spherical hot spot).

Thus, using the above analytical expression that defines the environment in and around a hot spot, a reaction criteria based on the conditions in the hot spot is formulated. This criteria is useful for modeling at the mesoscopic level where the sizes of the individual species along with the pores and hot spots are considered.

A significant amount of the work and conclusions in shock-induced chemical reactions are based on experiments [13][102][113][118][140]. The theoretical works [14][15] made use of the Arrhenius equation to study chemical reactions in the reactive systems. In this proposed thesis work, the Arrhenius equation is used to model chemical reactions but it is modified to take care of the sun of the effects that are observed in this application. More details are presented in later sections of this thesis. One important point that needs to be emphasized is the importance of the transition state in chemical reactions. The energy required to initiate a chemical reaction depends on the energy required to reach the transition state and thus it is very important to be able to identify the transition state. Experiments and calculations at the atomistic and quantum level provide a good source of information on the reaction dynamics [137]. At the continuum level, the transition state can be identified from energy considerations.

Chapter III

OBJECTIVES/OUTLINE OF THE THESIS

The objectives of the thesis are as follows

1. The primary objective is to formulate constitutive models and chemical reaction models for energetic structural materials that contain intermetallics and binders or mixtures of metal, metal-oxides and binders. Specifically, the objective is to develop these constitutive models in the framework of non-equilibrium thermodynamics (extended irreversible thermodynamics) and uniformly blended mixture theory, in a continuum scale and to use a hybrid framework of combination of internal variables and non-equilibrium thermodynamics state variables. Such a system of variables has been used, in the past, to study high strain-rate phase transitions. In Lu's work, the simply connected boundary mixture theory was used to describe the polycrystalline materials subject to high strain-rate operations. According to this mixture theory, the different components of the mixture occupy a different volume fraction and have a different fraction of boundary surface. In this work, the mixture theory that is used is the homogenously blended mixture theory, which better fits the mixture that is modeled in this research. The present objective is to modify the theory to accommodate the uniformly blended mixture theory; include additional non-equilibrium fluxes of porosity and plastic flow; and formulate evolution equations for reaction rate. To assist the formulation of constitutive relations, Tarver's model for monomolecular energetic materials is modified for binary energetic materials.

2. The objective is to include both thermomechanical models and mechanochemical models in the constitutive equations, by including quantitative models for pore collapse flux and high strain-rate plastic flow flux. This objective also includes formulation of all the mechanisms that can take the unreacted energetic structural materials to the transition state when the given energetic material is subjected to a shock loading.

3. Determine constraints imposed by the second law of thermodynamics and obtain expressions for the change in entropy and temperature as a function of all the processes involved in the shock-induced chemical reaction of energetic materials.

4. The next objective is to integrate the system of equations, under conditions of one-dimensional strain (by using MUSCL scheme to numerically integrate the PDE's), to study chemical reactions and the effects of plastic flow, pore collapse, effect of the binder and particle sizes.

5. The fifth objective is to model the chemical reactions in ab-initio scales. Specifically, the objective is to study initiation of chemical reactions in energetic materials by thermal loading using ab-initio molecular dynamics and to discuss the study of shock-induced chemical reactions. The objective includes numerical solution to specific cases of energetic structural materials.

Chapter IV

NON-EQUILIBRIUM THERMODYNAMIC CONTINUUM MODEL OF AN ENERGETIC STRUCTURAL MATERIAL

Experimental study of shock-induced chemical reactions in energetic materials show that chemical reactions occur with a delay of the order of 100 ns following the passage of the shock front [12][13][130][133]. The reactions, therefore, do not take place at the shock front. Thus, we cannot explain the time delay in reaction assuming that we have thermodynamic equilibrium conditions behind and ahead of the shock front and that all non-equilibrium processes are restricted to the shock front. It is necessary to model the initiation and completion of chemical reactions behind the shock front by using appropriate non-equilibrium thermodynamic models. Thus, a modification of the Zeldovich-Von Neumann- Doring (ZND) theory of detonation is proposed for binary energetic materials and structural energetic materials in the framework of a non-equilibrium thermodynamic ZND (NEZND). The ZND theory was developed to explain the processes observed behind the shock wave front of a monomolecular energetic material [109]. In the proposed NEZND model for binary energetic materials, the process is divided into four main regions behind the shock front. This is pictographically represented in fig. 5. Immediately behind the shock front is a narrow region where the heat conduction and viscosity effects are significant and hence cannot be neglected. Behind this is a void collapse region. In this region or zone, the voids collapse due to increased pressure and thus compress the mixture. In the compressed material behind this region, reaction initiation occurs as a result of the

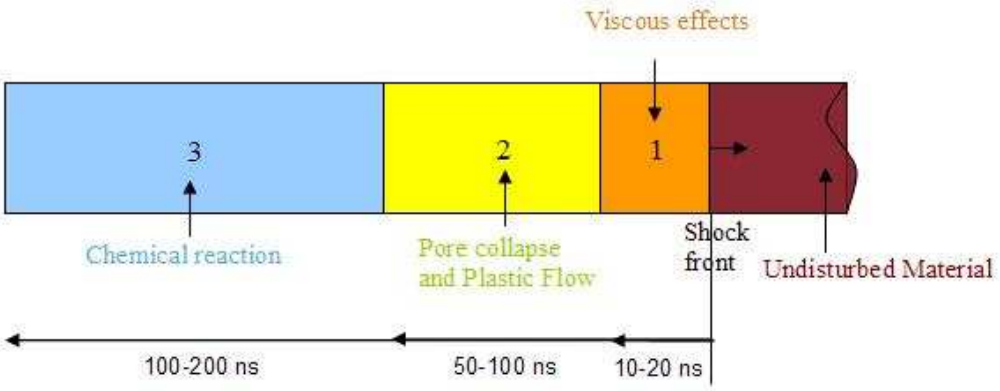

Figure 5: Processes behind the shock front

increased pressure and temperature which results from the shock compression, pore collapse and plasticity. The ZND model assumed the reaction initiation to occur as a result of shock compression only [26]. The fourth region is the place where the reaction is completed in the mixture. This chemical reaction model is similar to the model that Tarver used in his paper for $H_2 - Cl_2$,O_3 and $H_2 - O_2$ systems [110].

4.1 Mixture Theory

In this thesis, the system that is analyzed is not made of a single component. It is a composite of energetic materials, more specifically, a binary energetic material which may have additional materials such as a binder and/or a structural reinforcements. In addition, a chemical reaction can lead to products which will add to the number of components in the mixture. Thus, it is necessary to use a mixture theory that links the individual species property to the characteristics of the composite or the mixture.

A mixture theory similar to the one that is defined, in references [26][59][91], is used to describe the porous mixture of binary energetic materials. According to this mixture theory, the N components of the mixture are homogeneously distributed throughout the volume (fig. 6). Any infinitesimal volume of the specimen would therefore consist of all the N species of the mixture. In the limit, this infinitesimal volume tends to a point x in the continuum. Each species carries a partial stress while the voids carry no stress. Partial stress of species s is the stress that acts on that particular species s. The species state variables are: temperature ${}^sT$, density ${}^s\rho$, species mass fraction ${}^sc$, velocity ${}^sv_i$, stresses ${}^s\sigma_{ij}$, heat flux ${}^sq$, mass transportation flux ${}^sg_i$ and chemical reaction rate Θ. The superscript s refers to the species of the mixture: for example in the case of the thermite reaction between Al and Fe_2O_3,

$$2Al \ + \ Fe_2O_3 \ \rightarrow \ 2Fe \ + \ Al_2O_3 \tag{9}$$

s = 1 indicates Al, s = 2 represents Fe_2O_3, s = 3 is Al_2O_3 and s = 4 refers to Fe, the latter two being the products obtained in a chemical reaction between Al and Fe_2O_3. Al_2O_3 and Fe are the products following the chemical reaction. The associated average quantities of density, stress, heat flux etc are denoted by the corresponding symbols without the pre-super index s but with a bar instead on top of

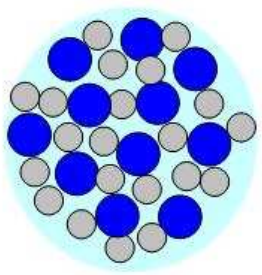

Figure 6: Components of the mixture

the symbols. All components of the mixture are taken to be at the same temperature T at a point in the continuum.

A list of the variables involved in the equations along with the relationship between the species quantities and the mixture quantities are listed below. The species quantities are represented by a superscript 's' on the left side of the variable and the mixture quantity is denoted by a bar over the variable.

1. Density

$$\bar{\rho} = \sum_s {}^s\rho \tag{10}$$

2. Concentration

$${}^sc = \frac{{}^s\rho}{\bar{\rho}} \tag{11}$$

3. Velocity

$$\bar{v}_i = \frac{1}{\bar{\rho}} \sum_s {}^s\rho {}^sv_i = \sum_s {}^sc {}^sv_i \tag{12}$$

4. Stress

$$\bar{\sigma}_{ij} = \sum_s {}^s\sigma_{ij} \tag{13}$$

5. Specific Internal Energy

$$\bar{e} = \sum_s {}^sc {}^se \tag{14}$$

6. Heat Flux

$$\bar{q}_i \;=\; \sum_s {}^sq_i + {}^sg_i {}^se \tag{15}$$

The equations representing conservation of mass, momentum and energy and constitutive equations are formulated for each species of the mixture. The corresponding equations for the mixture as a whole are obtained by applying the mixture theory on the species equations. The species equations are summed

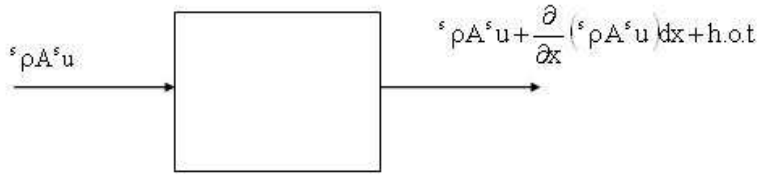

Figure 7: A control volume depicting the contributions to the mass balance equation for a one-dimensional problem

over all the species to obtain the mixture equation. Thus, the individual species properties define the properties of the mixture. The equations are formulated in the Eulerian framework.

4.2 Conservation equations

4.2.1 Mass balance Equation

A composite energetic structural material is considered as a mixture of components. The mass of each species is conserved. The time rate of change of any quantity in the Eulerian framework has two contribution-

$$\begin{aligned} Rate\ of\ change\ of\ mass\ &= Change\ of\ mass\ due\ to\ convection \\ &+ Change\ of\ mass\ due\ to\ source\ term \end{aligned} \tag{16}$$

In an Eulerian co-ordinate system, the volume of each control volume $\Delta x, \Delta y, \Delta z$ remains a constant with time and space. So the time rate of change of mass within the control volume can be expressed as -

$$\text{Rate of change of mass } = \frac{\partial^s m}{\partial t} = dx\ dy\ dz \frac{\partial^s \rho}{\partial t} \tag{17}$$

There is a flow of mass into and out of the control volume, as depicted in fig. 7. The difference in the mass flow into and out of the control volume is the convection of mass that affects the mass balance in the control volume.

$$\text{Convection of mass } = \frac{\partial}{\partial x_i}\left({}^{s}\rho^{s}v_i\right) dx\ dy\ dz \tag{18}$$

Chemical reactions can occur between the species in the mixture. These reactions cause a change in the quantity of each species and thus affects the mass of each species in the mixture. Thus, the source for the change in mass of the species is written in terms of the chemical reaction. Chemical reaction rate is defined as follows:

$$\theta = \frac{1}{{}^{s}\zeta}\frac{\partial\left[\chi\right]}{\partial t} \tag{19}$$

where ${}^{s}\varsigma$ is the stoichiometric coefficient and $[\chi]$ is the concentration of species s in moles per liter =

$$[\chi] = \frac{{}^{\mathrm{s}}m/{}^{s}M}{\mathrm{dx\ dy\ dz}} \tag{20}$$

where ${}^{s}M$ is the mass of each species and ${}^{s}M$ is the molecular mass of species s. Thus, we get,

$$\text{source term due to a reaction } = {}^{\mathrm{s}}\varsigma{}^{\mathrm{s}}\mathrm{M}\ \theta\mathrm{dx\ dy\ dz} \tag{21}$$

Substituting equations (17),(18) and (21) into equation (16), the mass balance equation for species s is as obtained as

$$\frac{\partial^s \rho}{\partial t} + \frac{\partial}{\partial x_i}\left({}^s\rho^s v_i\right) = {}^s\varsigma^s \mathrm{M}\theta \tag{22}$$

In addition to the mass of each species being conserved, the mass of the system as a whole is conserved and thus, the mass balance equation for the mixture is obtained. To obtain the mass balance equation for the mixture, the mass balance equation for each species is obtained by adding all the species equations. To obtain the mass balance equation for the mixture from the species mass balance equations, the mixture density and the average velocity of the mixture are defined based on the species properties.

$$\bar{\rho} = \sum_s {}^s\rho \tag{23}$$

$$\bar{v}_i = \frac{1}{\bar{\rho}} \sum_s {}^s\rho^s v_i = \sum_s {}^s c^s v_i \tag{24}$$

Another relation that is required to obtain eqn. (26) from eqn. (22) is conservation of mass during a chemical reaction, the total of all mass changes must add to zero, i.e,

$$\sum_s \left({}^s M^s \zeta\right) = 0 \tag{25}$$

Thus, making use of equations (23, 24 and 25), we obtain the conservation equation of mass for the mixture.

$$\frac{\partial \bar{\rho}}{\partial t} + \frac{\partial\left(\bar{\rho}\bar{v}_i\right)}{\partial x_i} = 0 \tag{26}$$

4.2.2 Concentration Balance Equation

The fraction of mass of species s per unit volume as the volume tends to zero at a point is defined as-

$$ {}^{s}c = \frac{{}^{s}\rho}{\bar{\rho}} \tag{27} $$

Based on this definition, it can be seen that the concentration of all species must always add to 1.

$$ \sum_{s} {}^{s}c \; = \; 1 \tag{28} $$

Substituting eqn. (27) into the mass balance equation for each species (eqn. 22), we can obtain the mass balance equation for each species in terms of the non-dimensional variable concentration and can be used in place of species mass balance equation.

$$ \bar{\rho}\frac{d^{s}c}{dt} + \frac{\partial^{s} g_i}{\partial x_i} = \Theta^{s} M^{s} \varsigma \tag{29} $$

where the mass diffusion flux ${}^{s}g_i$ is defined as follows -

$$ {}^{s}g_i = {}^{s}\rho({}^{s}v_i - \bar{v}_i) \tag{30} $$

The concentration balance equation is calculated for (N-1) of the N species in the mixture. The concentration of the fourth species is obtained by applying

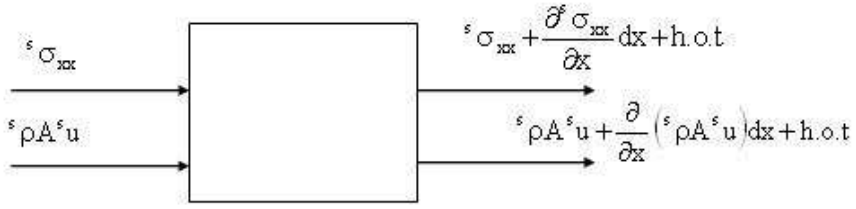

Figure 8: A control volume depicting the contributions to the linear momentum equation for a one-dimensional problem

the condition that the concentrations of all the species must add to 1 (eqn. 28. The N-th equation that is used is the mass balance equation of the mixture which gives the density of the mixture. These N equations will then completely define the mass or concentration of each of the N species in the mixture.

4.2.3 Linear momentum balance equation

The next property for which the conservation equation is obtained is the linear momentum. Linear momentum is defined as the product of mass times the velocity of the component. Each species in the mixture has to satisfy the linear momentum conservation equation -

$$\begin{aligned} Rate\ of\ change\ of\ momentum\ &= Change\ of\ momentum\ due\ to\ convection \\ &+ Change\ of\ momentum\ due\ to\ source\ term \end{aligned} \tag{31}$$

Equation (32) gives the rate of change of linear momentum where the mass of species s has been written as a product of density times the volume of the control volume.

$$\text{Rate of change of linear momentum } = \frac{\partial\left({}^{s}m{}^{s}v_i\right)}{\partial t} = dxdydz\frac{\partial\left({}^{s}\rho{}^{s}v_i\right)}{\partial t} \tag{32}$$

Equation (33) shows the convection of momentum into and out of the control volume.

$$\begin{aligned}
&-\left[{}^{s\rho}A_{jk}{}^{s}v_i.{}^{s}v_i + \tfrac{\partial}{\partial x_i}\left({}^{s\rho}A_{jk}{}^{s}v_i.{}^{s}v_i\right)dx_i + h.o.t\right] \\
\text{Convection term} = \; &+{}^{s}\rho A_{jk}{}^{s}v_i.{}^{s}v_i + {}^{\mathrm{s}}\zeta^{\mathrm{s}}M\theta dx_i A_{jk}{}^{s}v_i \\
&= \tfrac{\partial}{\partial x_i}\left({}^{s}\rho{}^{ss}v_i.{}^{s}v_i\right)dx_i A_{jk} + {}^{\mathrm{s}}\zeta^{\mathrm{s}}M\theta dx_i A_{jk}{}^{s}v_i
\end{aligned} \tag{33}$$

The source term for the linear momentum is contributed by the stresses acting on the volume element. The gradient of stress times the velocity is the driving force for the change in linear momentum.

$$\text{Source} = \left({}^{s}\sigma_{ji} + \frac{\partial^{s}\sigma_{ji}}{\partial x_j}dx_j\right)A_{kl} - {}^{s}\sigma_{ji}A_{kl} = \frac{\partial^{s}\sigma_{ji}}{\partial x_j}dx_j A_{kl} \tag{34}$$

Substituting equations (32), (33) and (34) into equation (31) and simplifying, the linear momentum equation for species s is obtained as the control volume tends to zero.

$${}^{s}\rho\frac{D^{s}v_i}{Dt} = \frac{\partial^{s}\sigma_{ji}}{\partial x_j} \tag{35}$$

where the Eulerian time derivative $\frac{D}{Dt}$ has been used in the above equation and is defined as shown -

$$\frac{D}{Dt} = \frac{\partial}{\partial t} + {}^{s}v_i \frac{\partial}{\partial x_i} \tag{36}$$

The linear momentum equation is summed over all the species to obtain the average mixture behavior.

$$\bar{\rho}\frac{D\bar{v}_i}{Dt} + \sum_s \frac{\partial}{\partial x_i}\left({}^{s}g_i {}^{s}v_i\right) = \frac{\partial \bar{\sigma}_{ji}}{\partial x_j} \tag{37}$$

In obtaining the average linear momentum equation from the species equation, the definition of the average stress from the species stress is obtained as -

$$\bar{\sigma}_{ij} = \sum_s {}^{s}\sigma_{ij} \tag{38}$$

The net momentum supply to the mixture due to chemical reaction from all the species or constituents is taken to be zero [91].

$$\sum_s \left({}^{s}\zeta {}^{s}M\theta^{s}v_i\right) = 0 \tag{39}$$

Thus, we make use of equations (23), (24), (38), (30), (22), (26) and (39) to obtain the mixture linear momentum equation (37) from the species equation (35). This equation is a vector equation and has three components indicated by the subscript i. It gives the velocity components along the three co-ordinate directions.

4.2.4 Energy Balance Equation

The first law of thermodynamics represents the conservation of energy. The rate of change of energy two contributions - one from the convection term and the second from the source term.

$$\begin{aligned} Rate\ of\ change\ of\ energy\ &= Change\ of\ energy\ due\ to\ convection \\ &+ Change\ of\ energy\ due\ to\ source\ term \end{aligned} \tag{40}$$

The total energy is made of two parts - the internal energy and the kinetic energy. This total energy needs to be conserved. The energy can be written in terms of the specific energy, namely, specific internal energy ${}^{s}e$ and the specific kinetic energy $\frac{1}{2}{}^{s}v_i.{}^{s}v_i$. Specific quantities are the quantities per unit mass. Equations (41) and (42) represent the rate of change of energy and the convection term respectively.

$$\text{Rate of change of energy} = \frac{\partial \left[{}^{s}m \left({}^{s}e + \frac{1}{2}{}^{s}v_i.{}^{s}v_i\right)\right]}{\partial t} = dxdydz \frac{\partial \left[{}^{s}\rho \left({}^{s}e + \frac{1}{2}{}^{s}v_i.{}^{s}v_i\right)\right]}{\partial t} \tag{41}$$

$$\text{Convection of energy} = - dxdydz \frac{\partial \left[{}^{s}\rho {}^{s}v_i \left({}^{s}e + \frac{1}{2}{}^{s}v_i.{}^{s}v_i\right)\right]}{\partial x_i} \tag{42}$$

There are many different kinds of energy and all of these contribute to the source term for the energy balance equation. The ones that are the most prominent in this work is listed in the following expression.

$$\text{Source term in a control volume } = \text{ heat energy } + \text{ mechanical work} + \text{ chemical potential energy } + \text{ energy due to chemical reaction} \tag{43}$$

Equation (44) provides the source term in the energy balance equation due to the heat energy.

$$\text{Heat energy} = -\frac{\partial^s q_i}{\partial x_i} dxdydz \tag{44}$$

where q_i is the heat transferred per unit time through a unit area in the i-th direction, known as the heat flux.

The next term is that due to mechanical work. Work and energy are inter-convertible and thus, work contributes to the energy balance in the system. The mechanical work occurs as a result of the stresses that act in the system and is given by -

$$\text{Rate of mechanical work} = -\frac{\partial \left({}^s\sigma_{ji}{}^s v_i\right)}{\partial x_j} dxdydz \tag{45}$$

Chemical potential energy is a measure of how much the energy of a system would change if the number of particles in the system were to change. For a multicomponent mixture with chemical reaction, it is necessary to include this term in the energy balance equation. Equation (46) describes the change in energy due to the chemical potential.

$$\text{Rate of change of chemical potential energy} = {}^s\mu \frac{\partial^s N}{\partial t} = {}^{ss}\zeta \theta^s \mu dxdydz \tag{46}$$

A chemical reaction causes a change in the energy of the system. Energy can be absorbed (endothermic reaction) or released (exothermic reaction) depending on the type of reaction. In the case of binary energetic materials, a chemical reaction between the components leads to an exothermic reaction. The standard enthalpy change of reaction is the enthalpy change that occurs in a system when one mole of matter is transformed by a chemical reaction under standard conditions. One of the common enthalpy changes that has been determined for a variety of materials in nature is the enthalpy of formation. It is the change in enthalpy that occurs when 1 mole of a substance is formed from its elements in the standard state. The enthalpy change associated with a reaction under any conditions can be computed from the standard enthalpy change of formation of the reactants and the products. Thus, the exothermic energy release can be expressed in terms of the enthalpy of formation ${}^{s}\Delta H_f^{\circ}$ of the components of the mixture as expressed below -

$$\begin{aligned} \textit{Rate of change of energy due to chemical reaction} &= {}^{s}\Delta H_f^0 \tfrac{\partial\, {}^{s}N}{\partial t} \\ &= {}^{s}\Delta H_f^0\, {}^{s}\varsigma\, \Theta dxdydz \end{aligned} \tag{47}$$

Substituting equations (41), (43), (44), (45), (46) and (47) into equation (40) and as the control volume goes to zero in the limit

$${}^{s}\rho \frac{D^s e}{Dt} = -\frac{\partial^s q_i}{\partial x_i} + {}^{s}\sigma_{ji} \frac{\partial^s v_i}{\partial x_j} + \theta^s \varsigma \left({}^{s}\mu + {}^{s}\Delta H_f^{\circ} \right) \tag{48}$$

To obtain the energy balance equation for the mixture, the energy equation (eqn. 48) for each species is summed over all the species. The following relations are made use of in stating the energy conservation principle for the mixture. The net energy supply to the mixture during a chemical reaction is zero [91].

$$\sum_s {}^s\varsigma\, {}^sM\theta\, {}^se = 0 \tag{49}$$

The heat flux variable for the mixture is defined to include the heat flow due to thermal diffusion as well as mass diffusion [72][91] -

$$\bar{q}_i \;=\; \sum_s {}^sq_i + {}^sg_i\, {}^se \tag{50}$$

The energy balance equation for the mixture is

$$\bar{\rho}\frac{D\bar{e}}{Dt} = -\frac{\partial \bar{q}_i}{\partial x_i} + \bar{\sigma}_{ji}\frac{\partial \bar{v}_i}{\partial x_j} + \theta \sum_s {}^s\varsigma \left({}^s\mu + {}^s\Delta H_f^\circ + \frac{1}{2}{}^sv.{}^sv\, {}^sM \right) \tag{51}$$

4.3 Constitutive Equations

The next set of equations that have to be formulated is the constitutive equations that govern the behavior of the composite energetic structural material. The constitutive relations describe the relationship between the thermodynamic variables.

4.3.1 Mechanical Relations

4.3.1.1 Decomposition of Stress Tensor

To describe the constitutive relations of an isotropic composite material, the stress tensor is decomposed into two parts - the hydrostatic component and the deviatoric stress component (the stress tensor is assumed to be symmetric).

$$ {}^{s}\sigma_{ij} = -{}^{s}P\delta_{ij} + {}^{s}\sigma'_{ij} \tag{52} $$

where

$$ {}^{s}P = -\frac{1}{3}{}^{s}\sigma_{ii} \tag{53} $$

is the hydrostatic component and

$$ {}^{s}\sigma'_{ij} = {}^{s}\sigma_{ij} + {}^{s}P\delta_{ij} \tag{54} $$

is the deviatoric stress component. It is further assumed that the deviatoric stress component can be divided into an equilibrium and a non-equilibrium part.

$$ {}^{s}\sigma'_{ij} = {}^{s}\sigma^{e'}_{ij} + {}^{s}\sigma^{ne'}_{ij} \tag{55} $$

The following equations are then obtained by decomposing the stress tensor -

$$ \bar{\sigma}_{ij} = -\bar{P}\delta_{ij} + \bar{\sigma}'_{ij} \tag{56} $$

$$\bar{P} = -\frac{1}{3}\bar{\sigma}_{ii} \tag{57}$$

$$\bar{\sigma}^{'}_{ij} = \bar{\sigma}_{ij} + \bar{P}\delta_{ij} \tag{58}$$

$$\bar{\sigma}^{'}_{ij} \; = \; \bar{\sigma}^{e'}_{ij} \; + \; \bar{\sigma}^{ne'}_{ij} \tag{59}$$

4.3.1.2 Linear Elastic Constitutive Relationship

The equilibrium deviatoric stress is related to the deformation rate in the system through an elastic relation. The deformation rate is defined as follows -

$${}^{s}V_{ij} = \frac{1}{2}\left(\frac{\partial {}^{s}v_i}{\partial x_j} + \frac{\partial {}^{s}v_j}{\partial x_i}\right) \tag{60}$$

The elastic relation between the equilibrium deviatoric stress and the deformation rate tensor is written in the rate form as shown below -

$${}^{s}\dot{\sigma}^{e\,\prime}_{ij} \;\; = \;\; {}^{s}C_{ijkl}\,{}^{s}V_{kl} \tag{61}$$

where ${}^{s}C_{ijkl}$ is a fourth order tensor or the linear elastic constant that relates the stress to the strain. In an isotropic solid, C_{ijkl} is equal to 2G.

The linear elastic relation for the mixture property is obtained from the species equation (eqn. 61) as -

$$\dot{\bar{\sigma}}_{ij}^{e\,\prime} = \bar{C}_{ijkl}\,\bar{V}_{kl} \tag{62}$$

where the the elastic constants are defined by the following relation -

$$\bar{C}_{ijkl} = \sum_{s} {}^{s}C_{ijkl}\,{}^{s}V_{kl}\left(\bar{V}_{kl}\right)^{-1} \tag{63}$$

4.3.1.3 Plasticity

A solid is assumed to yield when

$$f\left(\sigma_{ij}^{'}\right) = Y \tag{64}$$

In ideal plasticity,

$$f\left(\sigma_{ij}^{'}\right) \leq Y \tag{65}$$

There are two specific yield conditions that are commonly used in the literature.

- Von-Mises Yield Condition

$$\frac{1}{2}\left\{\left(\sigma_{xx}-\sigma_{yy}\right)^2+\left(\sigma_{yy}-\sigma_{zz}\right)^2+\left(\sigma_{zz}-\sigma_{xx}\right)^2\right\}+3\sigma_{xy}^2+3\sigma_{xz}^2+3\sigma_{yz}^2 = Y \tag{66}$$

- Tresca Yield Condition

$$\tau_{\max} = \frac{\sigma_{\max}-\sigma_{\min}}{2} = \frac{Y}{2} \tag{67}$$

However, when a solid is subjected to a shock loading, it has been observed that the yield stress significantly increases behind the shock front and returns to the value of Y in a short interval [80][6]. The plastic flow leads to a significant increase in the temperature [4][5]. One of the mechanisms of taking the reactants to the transition state is through this heating and the resulting temperature increase due to plastic work. Armstrong et al [6][136] have explained this increase in the temperature based on dislocation dynamics. The dislocation pile-up avalanche model of Armstrong is one of the only plasticity models to date, that can explain the experimentally observed increase in temperature due to plastic flow. All the other models underpredict the temperature increase [4]. According to the theory of dislocation based-plasticity, the dislocations pile-up and then undergo sudden relaxation. The pile-up of the dislocations increases the yield stress in a short region behind the shock front and the relaxation of the dislocations brings the yield stress back to its original value. This increase has been experimentally observed to be in the range 3-4 [80]. These experiments conducted a post-shock measurement of the increase in the yield stress. It is possible that a transient measurement of the yield stress increase might show the factor of increase to be greater than 3 or 4. So a factor of increase (α_Y) from 1 to 10 is considered in this work. Thus, the objective is to modify the usual continuum based yield condition to account for the increase in yield stress behind the shock front. The model should also reflect the fact that the yield stress returns to its original value (Y_0) after a short interval. Thus, the following model is proposed.

If $\frac{P}{Y_0} > 1$, at $t = t_0$

$$Y^{ne} = Y_0 \left(-\frac{P}{Y_0} \right) \alpha_Y \tag{68}$$

and at $t > t_0$, we have an evolution equation for the yield stress.

$$\dot{Y}^{ne} + \hat{\beta} Y^{ne} = \hat{\beta} Y_0 \tag{69}$$

where $\hat{\beta}$ is a material constant. For a special case of one-dimensional strain in the x direction of the x-y-z co-ordinate system, the yield condition at $t = t_0$ is

$$\left| \frac{\sigma_{xx} + 2\sigma_{yy}}{3} \right| > Y_0 \;\; at \; t = t_0 \tag{70}$$

At $t > t_0$, eqn. (69) is solved to obtain

$$Y = \left[Y_0 \left(-\frac{P}{Y_0} \right) \alpha_Y - Y_0 \right] e^{-\hat{\beta}(t-t_0)} + Y_0 \tag{71}$$

In this formulation, strain hardening is not considered but it can be included by modifying the derived relationship.

4.3.1.4 Viscosity

The non-equilibrium deviatoric stresses are one of the extended irreversible state variables that describes an irreversible process immediately behind the shock front. They are related to the viscosity in the system. Viscosity is a measure of the resistance that an object imparts to deformation by shear stress. Isaac Newton postulated that the shear stress induced in the material due to the viscous forces is proportional to the velocity gradient in the same. The

coefficient of proportionality that relates the stress to the velocity gradient is the coefficient of viscosity.

$$\sigma_{ij} \;=\; \eta_{ijkl}\, V_{kl} \tag{72}$$

There is another quantity called the bulk viscosity. This is the coefficient of proportionality that relates the deviatoric stress to the velocity gradient. Thus, the non-equilibrium deviatoric stresses are described in terms of this bulk viscosity. Since the analysis is in the framework of extended irreversible thermodynamics, an evolution equation with a relaxation time is introduced to describe these non-equilibrium deviatoric stresses. In addition, a cross flux term is also introduced in this equation. The mass diffusion of species in the mixture will have an effect on the viscosity of the mixture and at the same time, the viscosity will affect the extent to which the species can diffuse into one another. Thus, the non-equilibrium deviatoric stress is also related to the density gradient of the species.

$${}^{s}\tau_{\sigma}\,{}^{s}\dot{\sigma}_{ij}^{ne\prime} = -{}^{s}\sigma_{ij}^{ne\prime} + {}^{s}\eta_{ijkl}\,{}^{s}V_{kl} + {}^{s}\eta_{ijk}^{\eta g}\frac{\partial\left({}^{s}c\bar{\rho}\right)}{\partial x_k} \tag{73}$$

where ${}^{s}\tau_{\sigma}$ is the relaxation time for the viscous phenomenon, ${}^{s}\eta_{ijkl}$ is the coefficient of viscosity that relates the non-equilibrium deviatoric stresses to the deformation gradient and ${}^{s}\eta_{ijk}^{\eta g}$ is the cross-flux coefficient that relates the viscosity to the mass diffusion.

By summing the species equation, the mixture evolution equation for the non-equilibrium stresses is written as -

$$\bar{\tau}_\sigma \dot{\bar{\sigma}}_{ij}^{ne\prime} = -\bar{\sigma}_{ij}^{ne\prime} + \bar{\eta}_{ijkl}\bar{V}_{kl} + \sum_s {}^s\eta_{ijk}^{\eta g}\frac{\partial\left({}^sc\bar{\rho}\right)}{\partial x_k} \tag{74}$$

where the average relaxation time $\bar{\tau}_\sigma$ is equal to the species relation time ${}^s\tau_\sigma$, i.e

$$\bar{\tau}_\sigma \;=\; {}^s\tau_\sigma \tag{75}$$

and the mixture viscosity coefficient is defined as -

$$\bar{\eta}_{ijkl} = \sum_s {}^s\eta_{ijkl}{}^sV_{kl}\left(\bar{V}_{kl}\right)^{-1} \tag{76}$$

4.3.2 Equation of State (EOS)

The equation of state is an expression that describes the relationship between the hydrostatic pressure, density and temperature in the system. It is usually an equation that relates the pressure to the density and temperature in the system, i.e

$$P \;=\; P(\rho, T) \tag{77}$$

In this case, we are modeling energetic materials. They are not made of a single species but are actually binary energetic materials which could have additional components such as binders and structural reinforcements. In addition, a reaction between the binary mixture would lead to additional components in the

form of products. Each of these species needs to be defined by an equation of state. There are many different forms for the equation of state - empirical, phenomenological as well as experimental relations. In this work, the reactants and products are described by the Birch-Murnaghan equation of state [15] while the steel and epoxy are described by the Gruneisen equation of state. The Birch-Murnaghan equation of state is based on the finite strain formalism in the Eulerian framework. It has been used to fit curves to experimental results very successfully. On the other hand, the $U_s - u_p$ relation between the shock velocity (U_s) and the particle velocity (u_p) is an empirical relation that has had remarkable success in describing the Hugoniot of many materials over the decades. It is a tried and trusted equation of state. The $U_s - u_p$ equation is as follows -

$$U_s = C + Su_p \tag{78}$$

where C is the bulk sound velocity at zero pressure and S is the slope of the linear equation between U_s and u_p. It has been found that the $U_s - u_p$ equation and the Birch-Murnaghan equation converge even at large compression ratios, provided the higher order terms are made small [55]. This would imply that the Birch-Murnaghan equation can be justifiably used to describe the Hugoniot of the reactants and products as the experimental results that satisfy the $U_s - u_p$ relation will also satisfy the Birch-Murnaghan equation. The derivation of the Mie-Gruneisen equation of state incorporates the $U_s - u_p$ relation and is one of the most popular equations of state used in the literature. Thus, it is used to describe the Hugoniot curves in steel and epoxy. More details about these equations is presented below.

4.3.2.1 Mie-Gruneisen equation of state

The basis of the Mie-Gruneisen equation lies in combining the Rankine-Hugoniot relations with the empirical relation between the shock velocity and the particle velocity. This relation is -

$$U_s = C + Su_p + S'u_p^2 + ... \tag{79}$$

Usually, a linear relation more than adequately fits the experimental results. Using C to non-dimensionalize the relation we obtain -

$$\frac{U_s}{C} = 1 + S\frac{u_p}{C} + S'C\left(\frac{u_p}{C}\right)^2 + ... \tag{80}$$

The Rankine-Hugoniot relations are the mass, momentum and energy conservation equations across a shock. It is named after physicists William John Macquorn Rankine and Pierre Henri Hugoniot [124]. These equations are listed below -

$$\rho\left(U_s - u_p\right) = \rho_0 U_s \tag{81}$$

$$P - P_0 = \rho_0 U_s u_p \tag{82}$$

$$e - e_0 = \frac{1}{2}\left(P + P_0\right)\left(\nu_0 - \nu\right) \tag{83}$$

The compression of the material is defined in terms of the specific volume and using the mass conservation equation can be rewritten in terms of the velocities.

$$\mu = 1 - \frac{\rho_0}{\rho} = \frac{u_p}{U_s} \tag{84}$$

Assuming the initial pressure P_0 to be 0, the momentum balance equation can be rewritten as shown -

$$\frac{P}{K_0} = \frac{u_p}{C}\left[1 + S\frac{u_p}{C} + S'C\left(\frac{u_p}{C}\right)^2 + ...\right] \tag{85}$$

where $K_0 = \rho_0 C^2$ is the isentropic bulk modulus. Assuming a linear relation between U_s and u_p, the momentum balance equation can be simplified to the following-

$$P = \frac{K_0\mu}{(1 - S\mu^2)} \tag{86}$$

The thermal contribution to the equation of state is accounted for by introducing the Gruneisen parameter Γ which is defined as

$$\Gamma = \frac{1}{\rho}\left(\frac{\partial P}{\partial e}\right)_\nu \tag{87}$$

Substituting the compression expression in the energy balance equation and then using the definition of the Gruneisen parameter, the expression for pressure (Mie-Gruneisen equation of state) is obtained as -

$$P = \frac{K_0\mu\left[1 + \Gamma/2\left(\mu/(1-\mu)\right)\right]}{\left[1 - S\mu\right]^2} + \Gamma\rho e \tag{88}$$

4.3.2.2 Birch-Murnaghan equation of state

The Birch-Murnaghan equation of state is derived from the Eulerian finite-strain formalism which is expressed as -

$$f = \frac{1}{2}\left[\left(\frac{\rho}{\rho_0}\right)^{2/3} - 1\right] \tag{89}$$

The isentropic bulk modulus K is defined as -

$$K = -\nu\left(\frac{\partial P}{\partial \nu}\right)_T \tag{90}$$

The bulk modulus at the reference pressure ($P_0 = 0$) and its derivative with respect to pressure can be related to the parameters C and S of the $U_s - u_p$ relation. Then the isentropic bulk modulus can be defined as -

$$K_0 \;=\; \rho_0 C^2 \tag{91}$$

$$K_0^{'} \;=\; 4S \,-\, 1 \tag{92}$$

The second derivative of K_0 is related to the Gruneisen parameter Γ_0 and the parameters C, S of the $U_s - u_p$ relation.

$$K_0 K_0^{''} = 2S^2 - 4S\left(1 + \frac{\Gamma_0}{2}\right) + 12S^{'}C \tag{93}$$

The pressure is then related to the finite strain as follows -

$$\frac{P}{3f\left(1+2f\right)^{5/2}} = K_0\left(1 + a_1 f + a_2 f^2 + ...\right) \tag{94}$$

where

$$a_1 = \frac{3}{2}\left(K_0^{'} - 4\right) \tag{95}$$

and

$$a_2 = \frac{3}{2}\left[K_0 K_0^{''} + K_0^{'}\left(K_0^{'} - 7\right) + \frac{143}{9}\right] \tag{96}$$

The Birch-Murnaghan equation is then defined as the first-order expansion of the pressure in the finite strain f, which would imply that all higher order terms such as a_2 equals zero. The equation is -

$$P \;=\; \frac{K_0}{K_0^{'}}\;\left[\left(\frac{\rho}{\rho_0}\right)^{K_0^{'}} \;-\; 1\right] \tag{97}$$

This is the basic form of the equation. To account for the temperature effects, this equation is modified.

$$P \;=\; \frac{K_0}{K_0^{'}}\;\left[\left(\frac{\rho}{\rho_0}\right)^{K_0^{'}} \;-\; 1\right] \;+\; C_v\,\Gamma\rho_0\;\left(T \;-\; T_0\right) \tag{98}$$

where Γ is the Gruneisen parameter and C_v is the heat capacity at constant volume. This equation is used to describe the hydrostatic pressure of the reactants and products, namely $Al, Fe_2O_3, Fe\,and\,Al_2O_3$.

4.3.2.3 Mixture EOS

The Birch-Murnaghan equation can be used to describe each species in the mixture. But we are interested in describing the state of the mixture as a whole, in this continuum model. An appropriate mixture theory has been used to describe the mixture properties as a function of the species properties. The same has to be done for the pressure. The total pressure in the mixture has to have contributions from each species present in the system. However each species will not contribute equally to the total pressure as they are not present in the same quantity in the mixture. Thus, the contribution of the pressure from each species is proportional to the concentration of the species in the mixture. An approximate expression for the mixture equation of state for the reactants and products can then be given by -

$$\bar{P} = \sum_{s} {}^{s}c \left\{ \frac{{}^{s}\beta_{T_0}}{{}^{s}n} \left[\left(\frac{\bar{\rho}}{\bar{\rho}_0} \right)^{{}^{s}n} - 1 \right] + {}^{s}C_v {}^{s}\Gamma_0 {}^{s}\rho_0 \left(T - T_0 \right) \right\} \tag{99}$$

$\bar{\rho}_0$ is the reference density of the system. Normally in a one component system or in a mixture where no reaction occurs, the concentration of the components or species is a constant. It does not change with time. In this case, the reference density can be calculated at the beginning of the analysis depending on what the components are and what their standard densities are. However, in the case of systems with chemical reactions, the concentration of the species is not a constant. It changes with time, which implies that a specific concentration has a different reference density as a function of time and the progress of chemical reaction. For example, a system before reaction with only aluminum and iron-oxide would have a reference density that depends only on the densities of these two species. However, after reaction, we have additional species,

namely the components, alumina and iron. It is not correct to still retain the same reference density as the former case as that reference density does not account for the presence of the products at all. This would mean that a new reference density will have to be used for the latter case that includes the standard densities of the products. Thus, this change in the reference density with the change in the concentration of the species needs to be accounted for in the model, which is the case in this work. Numerical results that validate this concept as well as the mixture equation of state is presented in the next chapter.

4.3.2.4 Porous equation of state

The equations derived in the previous subsections have usually been used to describe solid species. The materials being studied have normally been fully dense specimens. In this work, porous materials are considered, which implies a less than 100% dense material. The porosity is important to initiate chemical reactions when needed. Porosity affects the state of the system. It causes a change in the temperature and pressure of the material. Thus, the porosity is a variable that needs to be included in the description of the equation of state. The porosity is defined as the ratio of a solid mixture to that of the porous mixture. It is denoted by the variable α -

$$\alpha = \frac{\rho_{solid}}{\rho_{porous}} \tag{100}$$

Based on this definition, when the porous mixture becomes completely dense, the porosity attains a value of 1.

To take into account the porosity of the mixture and a time dependent pore

collapse flux that is important during a shock loading, a P-α model [18][46][78] is used as the basis, to describe the equation of state of the mixture. Fig. 9 depicts the equation of state for a porous mixture. There are two parts to the curve, one when the mixture is porous and the second is when the mixture becomes completely solid and attains a porosity of 1. Now the equation of state for the porous part of the curve can be represented functionally as

$$P = f\left(\frac{\rho_p}{\rho_{p0}} - 1\right) \tag{101}$$

The subscript 'p' indicates that it is the porous density. This equation can then be rewritten as follows-

$$\begin{aligned} P &= f\left(\frac{\rho_p}{\rho_{s0}}.\frac{\rho_{s0}}{\rho_{p0}} - 1\right) = f\left(\frac{\rho_p}{\rho_{s0}}\alpha_0 - 1\right) \\ &= f\left(\frac{\rho_s/\alpha}{\rho_{s0}/\alpha_0} - 1\right) \end{aligned} \tag{102}$$

where the ratio $\frac{\rho_s}{\rho_{s0}}.\frac{\alpha_0}{\alpha}$ is always greater than one for a porous mixture. For a solid mixture, the ratio $\frac{\alpha_0}{\alpha}$ is equal to one and thus, the equation reduces to the solid equation of state.

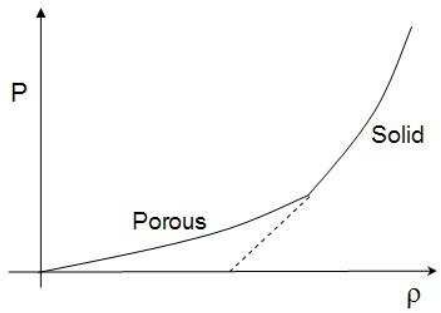

Figure 9: A schematic representation of the Hugoniots of a porous mixture and a dense solid mixture

4.3.3 Porosity Evolution Equation

The void content in a porous mixture is described in terms of the porosity, which has been defined in eqn. (100). The porosity or void fraction does not remain constant in the mixture. As the shock wave passes through the mixture, it can collapse the pores and thus reduce the fraction of voids. This implies a reduction in the value of porosity in the mixture occurs. It is then necessary to have a model that describes the change in the porosity of the mixture with time. It has also been observed that all the pores do not instantaneously collapse at the shock front. One of the rate of change contributions is from the flux or convection term of the variable and the second is the source term for the variable. In the case of porosity, we introduce the porosity flux $\bar{J}^{\alpha}$, the spatial gradient of which is the convection term for the rate of change of porosity. The relation between the porosity and the pressure works both ways. Change in one causes a change in the other. Since the pressure [15] plays a significant role in the evolution of porosity, the source term for the porosity evolution equation is the rate of change of pressure in the mixture. The evolution equation for the porosity α is then described by -

$$\dot{\alpha} = -\frac{\partial J_i^{\alpha}}{\partial x_i} + l_{\alpha}\dot{\bar{P}} \tag{103}$$

where l_{α} is the coefficient that accounts for the effects of pressure on porosity. A quadratic dependence of porosity on pressure is assumed [15] When all the voids in the mixture have collapsed, the porosity α will have a value of 1. Since the porosity is defined as the ratio of the density of the mixture without voids

to the density of the mixture with voids (eqn.100), it has a lower limit of one when the mixture is 100% dense and there are no voids present in it.

4.3.4 Void Collapse Flux

The evolution of the porosity includes the void collapse flux. This flux is similar in concept to the more commonly encountered flux in thermodynamics, namely, the heat flux. It describes the flow of porosity from one end of the mixture to the other. The void collapse process is an irreversible process that does not occur instantaneously behind the shock front. Instead, there is a time delay before the process occurs. This time delay is accounted for in the expression for the void collapse flux, by introducing a relaxation time. The relaxation time has units of time and is a variable that defines how much the void collapse flux is delayed. It defines how long it takes after the passage of the shock front before the voids actually collapse.

The void collapse flux is introduced in eqn. (103). The state of the system affects the void collapse flux. So the void collapse flux is taken to be a function of temperature and total stress, or in other words, temperature, pressure and deviatoric stress.

$$\tau_\alpha \dot{J}_i^\alpha = -J_i^\alpha + k_{ij}^{\alpha p}\frac{\partial \bar{P}}{\partial x_j} + k_{ij}^{\alpha T}\frac{\partial \bar{T}}{\partial x_j} + k_j^{\alpha\sigma}\frac{\partial \bar{\sigma}'_{ji}}{\partial x_j} \tag{104}$$

where $k_{ij}^{\alpha P}$, $k_{ij}^{\alpha T}$ and $k_{jk}^{\alpha\sigma}$ are material constants for void collapse flux. They define the dependence of the void collapse flux on the pressure, temperature and deviatoric stress, respectively. The extent of impact each of these spatial

gradients has on the void collapse flux is included by these material constants. τ_α is the relaxation time associated with the void collapse, to incorporate the fact that irreversible processes such as void collapse do not take place right at the shock wave but occur only after a certain time lag.

The relaxation time τ_α is not a constant in the system. It accounts for the time lag in the void collapse process behind the shock front. This time-lag depends on the state of the mixture. For different loading conditions, the mixture will respond with different time delays, depending on how fast the particles are moving to collapse the voids in the mixture. Thus, the void collapse relaxation time is modeled as a function of the velocity of the mixture, in an exponential form.

$$\tau_\alpha = \tau_{\alpha 0} \exp\left(-\lambda_\alpha \frac{\bar{u}t}{L}\right) \tag{105}$$

where L is the characteristic length of the specimen, t is the time after impact and $\tau_{\alpha 0}$ and λ_α are constant.

4.3.5 Chemical Reaction

The problem of concern is the shock-induced chemical reactions in energetic materials. It is thus necessary to have a constitutive relation that describes the evolution of the reaction rate. Mixtures like *Al and* Fe_2O_3 or *Ni and Al* do not react at the room temperature. The composite can react if it is supplied with energy to take the system to its transition state. This energy that should be supplied can be in the form of heat.

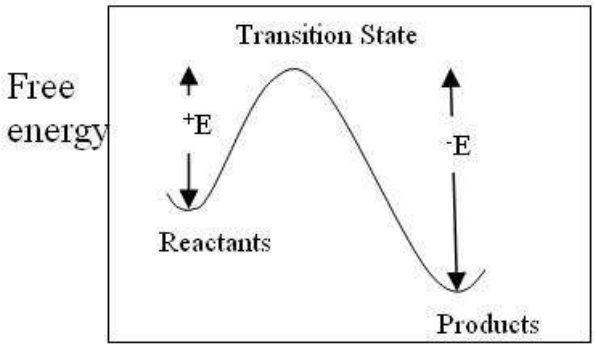

Figure 10: The reaction path from reactants to products

In the case of shock-induced chemical reactions, the same energy is supplied by the shock wave acting on the composite. Two different mechanisms can supply the energy as a result of the shock propagation in the composite. One of the mechanisms is the irreversible pore collapse that can result in heat and energy supply to the composite from the shock loading [135]. The second mechanism is through the plastic work resulting from the shock propagation through the composite. In either case or a combination of the two cases, it is necessary that additional energy E_α is supplied to the composite before a reaction can start. From fig. 10, one can note that

$$E_\alpha \; > \; E_{reactants} \; > \; E_{products} \tag{106}$$

According to the theory of transition states, there could be multiple states that the reaction passes through as it proceeds from the reactants to the products. The one-dimensional projection of this path is depicted in fig.(11). This figure also shows the projection of the multiple transition states to a single transition state, which is what we use in this work. At the continuum level, the transition state can be identified from energy considerations. There are two points that

needs to be remembered. Firstly, the energy of the transition state is higher than the energy of both the reactants as well as the products. Given multiple options for the transition state, the reactants will first reach the state that has the lowest energy among the various possibilities. Thus, the probability that the transition state is the one, among all the options, with the lowest energy is very high. This state is then chosen as the transition state for the reaction. The specific calculations identifying the transition state for the thermite mixture of aluminum and iron-oxide is presented in the next chapter.

The chemical reaction is usually described in terms of the reaction rate which describes how fast the reaction proceeds. The most well-known expression to describe the reaction process, once the transition state is reached, is the Arrhenius equation. According to this famous model, the chemical reaction rate constant k is given by -

$$k \;=\; A \exp\left(-\frac{E_a}{RT}\right) \tag{107}$$

where E_a is the activation energy necessary for the reaction to occur, A is the pre-exponential factor, R is the universal gas constant and T is the temperature in the system. The reaction rate Θ is the product of the reaction rate constant and the concentration of the reactants in moles per liter, as defined in eqn. (108).

$$\Theta = k \prod_{s} \left[\frac{\bar{\rho}^{s} c}{{}^{s}m}\right]^{{}^{s}\varsigma} \tag{108}$$

There is a time delay associated with both pore collapse and the plastic work. Both these take place behind the shock front. Similarly, it is assumed that the

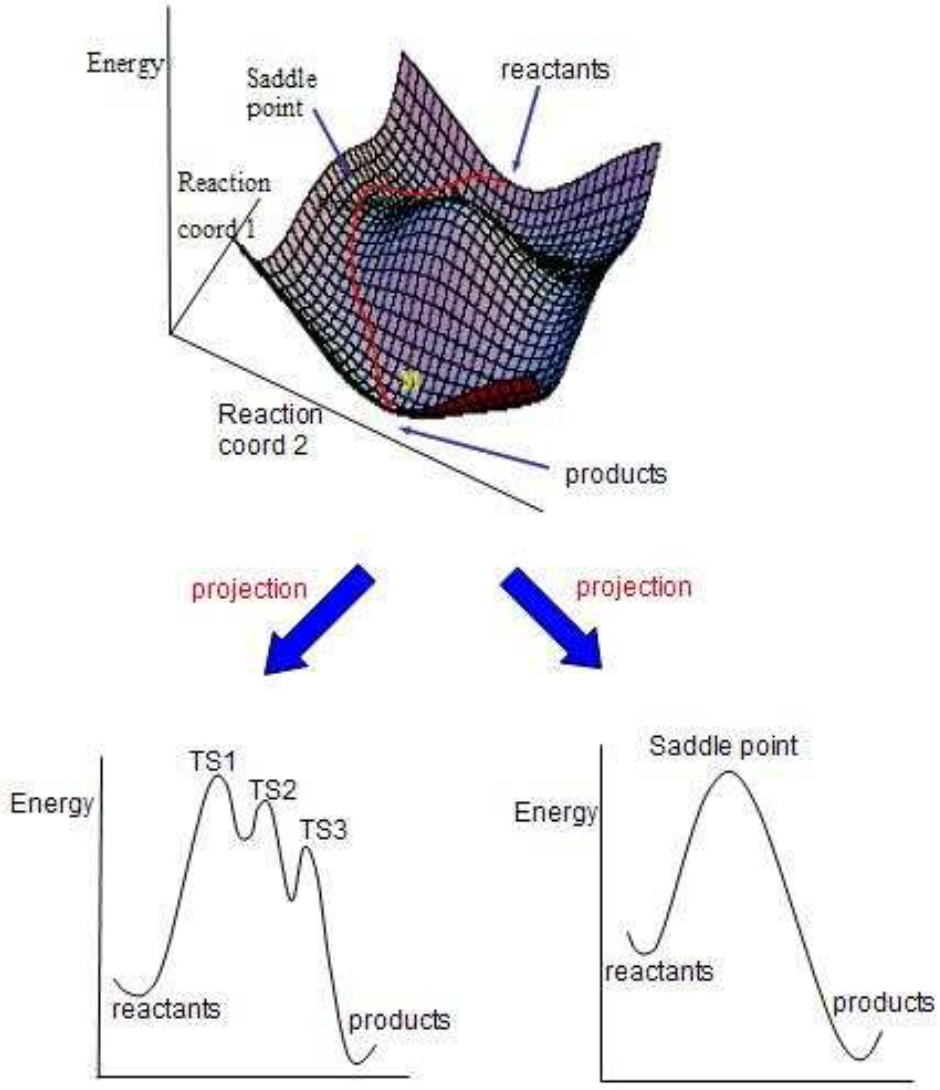

Figure 11: Trajectory of the reaction from the reactants to the products, through the transition state

chemical reaction rate does not equal the Arrhenius rate immediately behind the shock front or at the instant E_α is supplied. It is assumed that there is a time delay associated with the reaction initiation. This means that at $E = E_\alpha$, the reaction can start but the reaction rate increases as the energy supply increases and a time delay is associated with the increasing reaction rate. In summary, this can be larger than the time lag needed to take the system to the transition state. The time lag can be modelled by introducing a relaxation time τ_Θ in the evolution equation for the reaction rate Θ. Thus, in our chemical reaction model, the Arrhenius equation is modified to account for the time-lag between the shock front and chemical reaction. This is done by introducing the time rate of change of the reaction rate along with an associated relaxation time, as depicted in eqn. (109) .

$$\tau_\Theta \dot{\Theta} + \Theta = {}^{+}A \exp\left(-\frac{{}^{+}E}{R\bar{T}}\right) \prod_{s+} \left[{}^{s+}\chi\right]^{{}^{s+}\varsigma} \tag{109}$$

For $\tau_\Theta = 0$, the reaction rate attains its value when $E = E_\alpha$ of the transition state.

In this equation, τ_Θ is the relaxation time for the chemical reaction, + represent the reactants, A is the pre-exponential factor, E is the energy barrier that needs to be crossed for the reaction to take place and χ is the concentration of the species s in moles per liter.

For a chemical reaction to initiate, it is necessary for the reactants to be in contact with one another. More intimate the contact, better are the chances for the initiation of a chemical reaction. As the shock wave passes through the mixture, the temperature in the mixture increases due to the shock processes.

The temperature could increase beyond the melting temperature of one or both the reactants, leading to melting of the reactants. This causes reactants to come in better contact with one another since one of the reactants is now in the liquid state, leading to a possibility of a chemical reaction. So in this thesis, for the aluminum-based mixtures that are analyzed, the initiation of chemical reaction is based on the melting temperature of the reactants. The reactant with the lower of the two melting temperatures is selected as the criterion for chemical reaction initiation. The effect of pressure on the melting temperature is not included in this analysis.

In the chemical reaction model (eqn. 109), a relaxation time τ_Θ is introduced to account for the time lag between the shock front and the chemical reaction process. This relaxation time is not a constant in the system. It varies with the state of the system, depending on the loading conditions. If a mixture is impacted with a very large velocity of impact, then the pressure and temperature in the system will rise to a much larger value than if the velocity of impact is small. Thus, the initiation of chemical reaction will also be faster in the former case as compared to the latter case. The relaxation time needs to account for such a scenario. Since the chemical reaction is modeled based on the temperature in the system, the relaxation time is also modeled based on the temperature in the system. An exponential expression is assumed for the relaxation time to account for the decay in the time delay behind the shock front. Equation (110) gives the expression for the chemical reaction relaxation time -

$$\tau_\Theta = \tau_{\Theta 0} \exp\left(-\lambda_\Theta \frac{T}{T_m}\right) \tag{110}$$

where T_m is the melting temperature used for the chemical reaction initiation, T is the temperature in the mixture and $\tau_{\Theta 0}$ and λ_Θ are constants.

4.3.6 Heat Flux

Due to the various processes that occur in this problem, different spatial locations of the mixture will be at different temperatures. Heat transfer by conduction occurs when there is such a temperature gradient within the material. Heat energy flows from a region of higher temperature to a region of lower temperature. This is described by Fourier's law of heat conduction as follows-

$$\vec{q} = -k\vec{\nabla}T \tag{111}$$

where $\vec{q}$ is the heat flux vector and k is the thermal conductivity of the material. It relates the heat flux to the temperature gradient and basically defines just how much transfer of heat energy occurs for different materials.

The heat flux is one of the processes that occurs after a time delay and not at the shock front. It is one of the first regions of our four region model, depicted in fig. 5. Thus, the Fourier law of heat conduction has to be modified to bring in the effect of the relaxation time that takes care of the time lag behind the shock front. The heat flux for each species ${}^s\hat{q}$ has contributions from the thermal diffusion process as well as the mass diffusion process, as expressed in eqn. (50). A single heat flux equation is used to describe both components with a common relaxation time and heat conduction co-efficient. The total species heat transport flux ${}^s\hat{q}$ is, thus, governed by the following evolution equation,

where it is governed by the temperature gradient that exits in the mixture.

$$ {}^{s}\tau_q {}^{s}\dot{\hat{q}}_i = -{}^{s}\hat{q}_i - {}^{s}k_{q_{ij}} \frac{\partial T}{\partial x_j} \tag{112} $$

The mixture heat flux equation is then obtained by summing the species equation to obtain -

$$ \bar{\tau}_q \dot{\bar{q}}_i = -\bar{q}_i - \bar{k}_{q_{ij}} \frac{\partial \bar{T}}{\partial x_j} \tag{113} $$

where the mixture heat conduction coefficient is described by the following relation

$$ \bar{k}_{q_{ij}} = \sum_s {}^{s}k_{q_{ij}} \tag{114} $$

The species relaxation time for the heat flux is assumed to be the same for each of the components in the mixture. The mixture relaxation time is then equal to this species relaxation time constant.

$$ \bar{\tau}_q = {}^{s}\tau_q \tag{115} $$

4.3.7 Mass Diffusion Flux

Each species in the mixture has a different velocity. This individual velocity of each species is different from the mixture velocity. This brings in the concept of diffusion velocity, which is defined as the difference of the velocity of the species s from the average velocity of the mixture.

$$^{s}\hat{v}_i \ = {}^{s}v_i - \bar{v}_i \tag{116}$$

where $^{s}\hat{v}_i$ is the diffusion velocity of species s.

Using eqn. (116), mass diffusion is then defined as the product of density and the diffusion velocity of the species.

$$^{s}g_i = {}^{s}\rho^{s}\hat{v}_i \tag{117}$$

This quantity describes the relative motion of the species s of the mixture due to its diffusion velocity. In particular, this velocity can take into account the higher acceleration of a lighter element like aluminum and the resulting collision of Al with Fe_2O_3 or Ni. Fick [116] proposed a mathematical description for the mass diffusion based on an anology with the heat conduction equation, namely, for a binary mixture at uniform total density

$$\vec{g} = -\kappa_g \vec{\nabla}^{s}\rho \tag{118}$$

where κ_g is a phenomenological coefficient which may depend upon the densities and temperature of the mixture. The mass diffusion is another one the fluxes that occurs after a time delay behind the shock front and not instantaneously at the shock front. For our model, we, thus, formulate the mass diffusion equation in the framework of extended irreversible thermodynamics, by introducing the relaxation time in the mass diffusion equation. The mass diffusion, as depicted in eqn. (118), depends on the density gradient of each species. The flow of mass from one region to another is governed by the amount of mass present in the two locations. In addition, a cross-flux term that accounts for the effect

of viscosity on the mass diffusion is also incorporated. Viscosity plays a role in determining how much each species can diffuse into one another. Similar to the cross-flux term that was included in the viscosity equation (eqn. 73), its counterpart is included in the description of the mass diffusion flux. Thus, the mass diffusion flux ${}^{s}g_i$ for each species s is described by the following evolution equation -

$$ {}^{s}\tau_g \, {}^{s}\dot{g}_i + {}^{s}g_i = -{}^{s}\kappa^{g}_{ij} \frac{\partial(\bar{\rho}^{s} c)}{\partial x_j} + {}^{s}\kappa^{\eta g}_{ijk} \frac{\partial(\bar{v}_j)}{\partial x_k} \tag{119} $$

where ${}^{s}\tau_g$ is the associated relaxation time for each species, ${}^{s}\kappa^{g}_{ij}$ is the diffusion constant that shows the dependence of mass diffusion on the density gradient of the species and ${}^{s}\kappa^{\eta g}_{ijk}$ is the cross-flux coefficient that relates the viscosity effects and the mass diffusion flux. This equation has to be described for each species. It cannot be summed to form a mixture equation of state. On summing over all the species, the mass diffusion flux becomes zero. This is because the diffusion of mass of one species is negated by the diffusion of the other species. Thus, we have -

$$ \sum_{s} {}^{s}g_i \; = \; 0 \tag{120} $$

4.4 Entropy and Second law of thermodynamics

The complete set of equations that governs the current problem has been presented in the previous sections. These constitutive equations should satisfy the

second law of thermodynamics which states that the rate of entropy production in any process is always non-decreasing. In this section, we therefore, provide details about the entropy and the entropy flux. In the next section, using these definitions, the constraints imposed by the second law of thermodynamics is investigated.

4.4.1 Entropy

The function entropy can be split into two different parts [90]

$$dS = dS_i + dS_e \tag{121}$$

where the subscript i refers to the change in entropy due to internal processes and e refers to changes in entropy dues to interactions with the external environment. The entropy increase dS_i is never negative. It is equal to zero for a reversible process and greater than zero for an irreversible process. It is equal to the rate of entropy production ${}^s\eta$ [59].

$$\frac{ds_i}{dt} = {}^s\eta \tag{122}$$

Thus, the specific entropy s for each species is governed by the following equation

$${}^s\rho\frac{d^s s}{dt} + \frac{\partial^s J_i^s}{\partial x_i} = {}^s\eta \tag{123}$$

To obtain the mixture equation for the entropy, all equations for the species are added. Using equations (23, 24 and 30) and the following equations,

$$\bar{J}_i^s = \sum_s [{}^s J_i^s + {}^s s^s g_i] \tag{124}$$

$$\bar{\eta} = \sum_s [{}^s \eta + {}^s s^s \varsigma^s M \Theta] \tag{125}$$

the mixture evolution equation for entropy obtained.

$$\bar{\rho} \frac{d\bar{s}}{dt} + \frac{\partial \bar{J}_i^s}{\partial x_i} = \bar{\eta} \tag{126}$$

The entropy flux of the mixture includes, in addition to the species flux, the contribution to the entropy by the mass diffusion flux. Similarly, the rate of entropy production in the mixture also includes the effect of chemical reaction on the entropy s. Equation (123) goes beyond the usual description of the second law of thermodynamics. Here the assumption is made that the second law holds at every spatial point and at any instant of time [59].

In the framework of extended irreversible thermodynamics, the entropy flux of the mixture $\bar{J}_i^s$ is a function of all the other fluxes in the system as opposed to just the heat flux like in equilibrium thermodynamics [59]. All the terms involved in the description of the entropy flux is indicated in the following equation -

$$\vec{\bar{J}}^s = \vec{\bar{J}}^s(\vec{J}^\alpha, \Theta, \vec{\bar{q}}, {}^s\vec{g}, \bar{T}, \vec{\bar{\sigma}}^{ne'}, \vec{v}) \tag{127}$$

or in gradient form, it is expressed as -

$$\frac{\partial \bar{J}_j^s}{\partial x_j} = \frac{\partial \bar{J}_j^s}{\partial \bar{J}_i^\alpha}\frac{\partial \bar{J}_i^\alpha}{\partial x_j} + \frac{\partial \bar{J}_j^s}{\partial \Theta}\frac{\partial \Theta}{\partial x_j} + \frac{\partial \bar{J}_j^s}{\partial \bar{q}_i}\frac{\partial \bar{q}_i}{\partial x_j} + \sum_s \frac{\partial \bar{J}_j^s}{\partial^s g_i}\frac{\partial^s g_i}{\partial x_j} + \frac{\partial \bar{J}_j^s}{\partial \bar{T}}\frac{\partial \bar{T}}{\partial x_j} + \frac{\partial \bar{J}_j^s}{\partial \bar{\sigma}_{ik}^{ne'}}\frac{\partial \bar{\sigma}_{ik}^{ne'}}{\partial x_j} + \varpi\frac{\partial \bar{v}_j}{\partial x_j} \tag{128}$$

The last term in this equation accounts for the effect of porosity on the entropy flux. A change in the porosity of the mixture affects the entropy in the system. The porosity can be viewed as a quantity that flows from one spatial location to another and so its effect on the entropy flux is considered by including the velocity gradient. $\varpi(\alpha)$ is the coefficient that relates the effect of porosity on the entropy flux and hence assumed to be a function of the porosity in the mixture.

For brevity, the following notations are used in equation (128).

$$\Lambda_{ji}^1 = \frac{\partial \bar{J}_j^s}{\partial \bar{J}_i^\alpha} \tag{129}$$

$$\Lambda_j^2 = \frac{\partial \bar{J}_j^s}{\partial \Theta} \tag{130}$$

$$\Lambda_{ji}^3 = \frac{\partial \bar{J}_j^s}{\partial \bar{q}_i} \tag{131}$$

$${}^s\Lambda_{ji}^4 = \frac{\partial \bar{J}_j^s}{\partial^s g_i} \tag{132}$$

$$\Lambda_j^5 = \frac{\partial \bar{J}_j^s}{\partial \bar{T}} \tag{133}$$

$$\Lambda^6_{jik} = \frac{\partial \bar{J}^s_j}{\partial \bar{\sigma}^{ne'}_{ik}} \tag{134}$$

4.4.2 Second Law of Thermodynamics

To derive the expression for the rate of entropy production, the Helmholtz free energy $\bar{f}$ of the composite is defined as

$$\bar{f} = \bar{e} - \bar{T}\bar{s} \tag{135}$$

where $\bar{e}$ is the internal energy, $\bar{T}$ is the temperature and $\bar{s}$ is the entropy.

$\bar{f}$ is function of all the state variables as shown below -

$$\bar{f} = \bar{f}\left(\bar{T}, \alpha, \vec{J}^{\alpha}, \Theta, {}^{s}c, {}^{s}\vec{g}, \vec{\bar{q}}, \vec{\bar{\bar{\sigma}}}^{e'}, \vec{\bar{\bar{\sigma}}}^{ne'}, \bar{P}\right) \tag{136}$$

Then,

$$\begin{aligned} \dot{\bar{f}} \;=\; & \tfrac{\partial \bar{f}}{\partial \bar{T}}\dot{\bar{T}} \;+\; \tfrac{\partial \bar{f}}{\partial \alpha}\dot{\alpha} \;+\; \tfrac{\partial \bar{f}}{\partial J^{\alpha}_i}\dot{J}^{\alpha}_i \;+\; \tfrac{\partial \bar{f}}{\partial \Theta}\dot{\Theta} \;+\; \sum_s \tfrac{\partial \bar{f}}{\partial {}^{s}c}\,{}^{s}\dot{c} \\ & +\; \sum_s \tfrac{\partial \bar{f}}{\partial {}^{s}g_i}\,{}^{s}\dot{g}_i \;+\; \tfrac{\partial \bar{f}}{\partial \bar{q}_i}\dot{\bar{q}}_i \;+\; \tfrac{\partial \bar{f}}{\partial \bar{\sigma}^{e'}_{ij}}\dot{\bar{\sigma}}^{e'}_{ij} \;+\; \tfrac{\partial \bar{f}}{\partial \bar{\sigma}^{ne'}_{ij}}\dot{\bar{\sigma}}^{ne'}_{ij} \;+\; \tfrac{\partial \bar{f}}{\partial \bar{P}}\dot{\bar{P}} \end{aligned} \tag{137}$$

Multiplying by density $\bar{\rho}$

$$\bar{\rho}\dot{\bar{f}} \;=\; \bar{\rho}\dot{\bar{e}} \;-\; \bar{\rho}T\,\dot{\bar{s}} - \bar{\rho}\dot{T}s \tag{138}$$

Substituting eqn. (126)

$$\bar{\rho}\dot{\bar{f}} = \bar{\rho}\dot{\bar{e}} - T\bar{\eta} + T\bar{J}^s_{i,i} - \bar{\rho}\dot{T}s \tag{139}$$

The second law of thermodynamics states that rate of entropy production is always greater than or equal to zero and thus, we have -

$$T\bar{\eta} = \bar{\rho}\dot{\bar{e}} - \bar{\rho}\dot{\bar{f}} - \bar{\rho}\bar{s}\dot{\bar{T}} + \dot{\bar{T}}\nabla\cdot\bar{J}^s_{i,i} \geq 0 \tag{140}$$

Equations (137), (51) and (128) are substituted into equation (140),

$$\begin{aligned}
\bar{T}\bar{\eta} = &-\tfrac{\partial\bar{q}_i}{\partial x_i} + \bar{\sigma}_{ji}\tfrac{\partial\bar{v}_i}{\partial x_j} - \Theta\sum_s {}^s\varsigma\left({}^s\mu + {}^s\Delta H^\circ_f + \tfrac{1}{2}{}^s v_i.{}^s v_i{}^s M\right)\\
&+\bar{T}\Lambda^1_{ji}\tfrac{\partial J^\alpha_i}{\partial x_i} + \bar{T}\Lambda^2_j\tfrac{\partial\Theta}{\partial x_j} + \bar{T}\Lambda^3_{ji}\tfrac{\partial\bar{q}_i}{\partial x_j} + \sum_s \bar{T}^s\Lambda^4_{ji}\tfrac{\partial^s g_i}{\partial x_j}\\
&+\bar{T}\Lambda^5_j\tfrac{\partial\bar{T}}{\partial x_j} + \bar{T}\Lambda^6_{jik}\tfrac{\partial\bar{\sigma}^{ne'}_{ik}}{\partial x_j} + \bar{T}\varpi\tfrac{\partial\bar{v}_j}{\partial x_j} - \bar{\rho}\bar{s}\dot{\bar{T}}\\
&-\bar{\rho}\tfrac{\partial\bar{f}}{\partial\bar{T}}\dot{\bar{T}} - \bar{\rho}\tfrac{\partial\bar{f}}{\partial\alpha}\dot{\alpha} - \bar{\rho}\tfrac{\partial\bar{f}}{\partial J^\alpha_i}\dot{J}^\alpha_i - \bar{\rho}\tfrac{\partial\bar{f}}{\partial\Theta}\dot{\Theta} - \sum_s\bar{\rho}\tfrac{\partial\bar{f}}{\partial{}^s c}{}^s\dot{c}\\
&-\sum_s\bar{\rho}\tfrac{\partial\bar{f}}{\partial{}^s g_i}{}^s\dot{g}_i - \bar{\rho}\tfrac{\partial\bar{f}}{\partial\bar{q}_i}\dot{\bar{q}}_i - \bar{\rho}\tfrac{\partial\bar{f}}{\partial\bar{\sigma}^e_{ij}}\dot{\bar{\sigma}}^{e'}_{ij} - \bar{\rho}\tfrac{\partial\bar{f}}{\partial\bar{\sigma}^{ne'}_{ij}}\dot{\bar{\sigma}}^{ne'}_{ij} - \bar{\rho}\tfrac{\partial\bar{f}}{\partial\bar{P}}\dot{\bar{P}}
\end{aligned} \tag{141}$$

The mixture constitutive relations (eqns. 29, 62, 73, 103, 104, 109, 112, 119) are substituted in the above equation and the terms are rearranged.

$$
\begin{aligned}
\bar{T}\eta^s &= \left(\overline{T}\Lambda^3_{ji} - \delta_{ij}\right)\frac{\partial \bar{q}_i}{\partial x_j} + \left\{\begin{array}{l} \overline{T}\Lambda^1_{ji} + \overline{\rho}\frac{\partial \overline{f}}{\partial \alpha}\left[1 + \ell_\alpha\left(1 - \ell_\alpha\frac{\partial \overline{P}}{\partial \alpha}\right)^{-1}\frac{\partial \overline{P}}{\partial \alpha}\right] \\ -\bar{\rho}\frac{\partial \overline{f}}{\partial \overline{P}}\left(1 - \ell_\alpha\frac{\partial \overline{P}}{\partial \alpha}\right)^{-1}\frac{\partial \overline{P}}{\partial \alpha} \end{array}\right\}\frac{\partial J^\alpha_i}{\partial x_i} \\
&+ \left\{\begin{array}{l} \bar{\sigma}_{ji} + \delta_{ij}\ell_\alpha\left(1 - \ell_\alpha\frac{\partial \overline{P}}{\partial \alpha}\right)^{-1}\bar{\rho}^2\frac{\partial \overline{P}}{\partial \bar{\rho}}\frac{\partial \overline{f}}{\partial \alpha} + \bar{\rho}^2\frac{\partial \overline{P}}{\partial \bar{\rho}}\frac{\partial \overline{f}}{\partial \overline{P}}\left(1 - \ell_\alpha\frac{\partial \overline{P}}{\partial \alpha}\right)^{-1}\delta_{ij} \\ +\overline{T}\varpi\left(\alpha\right)\delta_{ij} - \frac{\bar{\rho}}{\tau_g}\sum_s \frac{\partial \overline{f}}{\partial {}^s g_i}{}^s k^{\eta g}_{ij} - \bar{\rho}\frac{\partial \overline{f}}{\partial \overline{\sigma}^{e'}_{kl}}\overline{C}_{klij} - \frac{\bar{\rho}}{\tau_\sigma}\frac{\partial \overline{f}}{\partial \bar{\sigma}^{ne'}_{kl}}\bar{\eta}_{klij} \end{array}\right\}\frac{\partial \bar{v}_i}{\partial x_j} \\
&+ \frac{\partial g^s_i}{\partial x_j}\left\{\sum_s \overline{T}^s\Lambda^4_{ji} + \bar{\rho}\frac{\partial \overline{f}}{\partial \alpha}\ell_\alpha\left(1 - \ell_\alpha\frac{\partial \overline{P}}{\partial \alpha}\right)^{-1}\frac{1}{\bar{\rho}}\frac{\partial \overline{P}}{\partial {}^s C}\delta_{ij} + \frac{\partial \bar{f}}{\partial {}^s C}\delta_{ij} + \bar{\rho}\frac{\partial \overline{f}}{\partial \overline{P}}\left(1 - \ell_\alpha\frac{\partial \overline{P}}{\partial \alpha}\right)^{-1}\frac{\partial \overline{P}}{\partial {}^s C}\frac{1}{\bar{\rho}}\delta_{ij}\right\} \\
&+ \left\{\bar{T}\Lambda^5_i + \frac{\bar{\rho}}{\tau_\alpha}\frac{\partial \bar{f}}{\partial J_i}k^{\alpha T}_{ij}\delta_{ij} + \frac{\bar{\rho}}{\tau_q}\frac{\partial \bar{f}}{\partial \bar{q}_i}k^q_{ij}\delta_{ij}\right\}\frac{\partial \bar{T}}{\partial x_i} + \left\{\begin{array}{l} -\bar{\rho}\bar{s} - \bar{\rho}\frac{\partial \overline{f}}{\partial \overline{T}} - \bar{\rho}\frac{\partial \overline{f}}{\partial \alpha}\ell_\alpha\left(1 - \ell_\alpha\frac{\partial \overline{P}}{\partial \alpha}\right)^{-1}\frac{\partial \bar{P}}{\partial \overline{T}} \\ -\bar{\rho}\frac{\partial \overline{f}}{\partial \overline{P}}\left(1 - \ell_\alpha\frac{\partial \overline{P}}{\partial \alpha}\right)^{-1}\frac{\partial \overline{P}}{\partial \overline{T}} \end{array}\right\}\dot{T} \\
&- \sum_s {}^s\varsigma\Theta\left\{\begin{array}{l} {}^s\mu + {}^s\Delta H^0_f + \frac{1}{2}\left({}^s V_i \cdot {}^s V_i\right){}^s M - \frac{\partial \overline{f}}{\partial \alpha}\ell_\alpha\left(1 - \ell_\alpha\frac{\partial \overline{P}}{\partial \alpha}\right)^{-1}\frac{\partial \overline{P}}{\partial {}^s C}{}^s M \\ -\frac{\partial \overline{f}}{\partial \overline{P}}\left(1 - \ell_\alpha\frac{\partial \overline{P}}{\partial \alpha}\right)^{-1}\frac{\partial \overline{P}}{\partial {}^s C}{}^s M - \frac{\partial \bar{f}}{\partial {}^s C}{}^s M \end{array}\right\} \\
&+ \left\{\frac{\bar{\rho}}{\tau_g}\sum_s \frac{\partial \bar{f}}{\partial {}^s g_i}k^g_{ij}\delta_{ij} - \frac{\bar{\rho}}{\tau_g}\frac{\partial \bar{f}}{\partial \sigma^{ne'}_{ij}}\sum_s {}^s\eta^{ng}_{ijk}\delta_{jk}\right\}\frac{\partial ({}^s c\bar{\rho})}{\partial x_i} + \bar{T}\Lambda^2_j\frac{\partial \Theta}{\partial x^2_j} - \frac{\bar{\rho}}{\tau_\Theta}\frac{\partial \bar{f}}{\partial \Theta}A_{\exp}\left(\frac{-\Delta G}{RT}\right)\prod_{s+}\left[\mathrm{X}\right]^{\mathrm{s}+} \\
&+ \bar{\mathrm{T}}\Lambda^6_{ijk}\frac{\partial \bar{J}^{ne'}_{ik}}{\partial x_j} + \frac{\bar{\rho}}{\tau_\alpha}\frac{\partial \bar{f}}{\partial J^\alpha_i}k^{\alpha\sigma}_i\frac{\partial \bar{\sigma}^{e'}_{ij}}{\partial x_j} + \frac{\bar{\rho}}{\tau_\alpha}\frac{\partial \bar{f}}{\partial J^\alpha_i}k^{\alpha\sigma}_i\frac{\partial \bar{\sigma}^{ne'}_{ij}}{\partial x_j} + \frac{\bar{\rho}}{\tau_\alpha}\frac{\partial \bar{f}}{\partial J^\alpha_i}k^{\alpha P}_{ij}\delta_{ij}\frac{\partial \bar{P}}{\partial x_i} \\
&+ \frac{\bar{\rho}}{\tau_\alpha}\frac{\partial \bar{f}}{\partial J^\alpha_i}J^\alpha_i + \frac{\bar{\rho}}{\tau_\Theta}\frac{\partial \bar{f}}{\partial \Theta}\Theta + \frac{\bar{\rho}}{\tau_q}\frac{\partial \bar{f}}{\partial \bar{q}_i}\bar{q}_i + \frac{\bar{\rho}}{\tau_\sigma}\frac{\partial \bar{f}}{\partial \bar{\sigma}^{ne'}_{ij}}\bar{\sigma}^{ne'}_{ij} + \frac{\bar{\rho}}{\tau_g}\sum_s \frac{\partial \bar{f}}{\partial {}^s g_i}{}^s g_i
\end{aligned}
\tag{142}
$$

The rate of entropy production $\bar{\eta}^s$ is always greater than or equal to zero. A linear relation is assumed between the fluxes and their respective forces. The fluxes will therefore, contribute quadratically to the entropy production in the mixture.

$$
\frac{\partial \bar{f}}{\partial J^\alpha_i} = \frac{\tau_\alpha}{\bar{\rho}}\left(k^T_{ij}\right)^{-1}J^\alpha_i \tag{143}
$$

$$
\frac{\partial \bar{f}}{\partial \bar{q}_i} = \frac{\bar{\tau}_q}{\bar{\rho}}\frac{\left(k^T_{ij}\right)^{-1}}{\bar{T}}\bar{q}_i \tag{144}
$$

$$
\frac{\partial \bar{f}}{\partial \Theta} = \frac{\tau_\Theta}{\bar{\rho}}\frac{M\left(\bar{v}_i.\bar{v}_i\right)}{A\exp\left(-\frac{\Delta G}{RT}\right)}\Theta \tag{145}
$$

$$\frac{\partial \bar{f}}{\partial^s g_i} = \frac{\tau_g}{\bar{\rho}} \frac{{}^s k_{g_{ij}}}{{}^s k_{g_{ijk}} C_j} {}^s g_i \tag{146}$$

The coefficients of all the gradients of the variables must equal zero. This gives rise to the following expressions.

$$\overline{T}\Lambda^3_{ji} - \delta_{ij} = 0 \tag{147}$$

$$\bar{\sigma}^{ne'}_{ij} - \frac{\bar{\rho}}{\tau_g} \sum_s \frac{\partial \overline{f}}{\partial^s g_i} {}^s k^{\eta g}_{ij} - \frac{\bar{\rho}}{\tau_\sigma} \frac{\partial \overline{f}}{\partial \bar{\sigma}^{ne'}_{kl}} \bar{\eta}_{klij} = 0 \tag{148}$$

$$\bar{\sigma}^{e'}_{ji} - \bar{\rho} \frac{\partial \overline{f}}{\partial \overline{\sigma}^{e'}_{kl}} \overline{C}_{klij} = 0 \tag{149}$$

$$\bar{\rho}^2 \frac{\partial \overline{P}}{\partial \bar{\rho}} \frac{\partial \overline{f}}{\partial \overline{P}} \left(1 - \ell_\alpha \frac{\partial \overline{P}}{\partial \alpha}\right)^{-1} \delta_{ij} - \bar{P}\delta_{ij} = 0 \tag{150}$$

$$\delta_{ij} \ell_\alpha \left(1 - \ell_\alpha \frac{\partial \overline{P}}{\partial \alpha}\right)^{-1} \bar{\rho}^2 \frac{\partial \overline{P}}{\partial \bar{\rho}} \frac{\partial \overline{f}}{\partial \alpha} + \overline{T} \varpi(\alpha) \delta_{ij} = 0 \tag{151}$$

$$\overline{T}\Lambda^1_{ji} + \bar{\rho} \frac{\partial \overline{f}}{\partial \alpha} \left[1 + \ell_\alpha \left(1 - \ell_\alpha \frac{\partial \overline{P}}{\partial \alpha}\right)^{-1} \frac{\partial \overline{P}}{\partial \alpha}\right] - \bar{\rho} \frac{\partial \overline{f}}{\partial \overline{P}} \left(1 - \ell_\alpha \frac{\partial \overline{P}}{\partial \alpha}\right)^{-1} \frac{\partial \overline{P}}{\partial \alpha} = 0 \tag{152}$$

$$\bar{T}\Lambda^5_i + \frac{\bar{\rho}}{\tau_\alpha} \frac{\partial \bar{f}}{\partial J_i} k^{\alpha T}_{ij} \delta_{ij} + \frac{\bar{\rho}}{\tau_q} \frac{\partial \bar{f}}{\partial \bar{q}_i} k^q_{ij} \delta_{ij} = 0 \tag{153}$$

$$-\bar{\rho}\bar{s} - \bar{\rho} \frac{\partial \overline{f}}{\partial \bar{T}} - \bar{\rho} \frac{\partial \overline{f}}{\partial \alpha} \ell_\alpha \left(1 - \ell_\alpha \frac{\partial \overline{P}}{\partial \alpha}\right)^{-1} \frac{\partial \bar{P}}{\partial \bar{T}} - \bar{\rho} \frac{\partial \overline{f}}{\partial \overline{P}} \left(1 - \ell_\alpha \frac{\partial \overline{P}}{\partial \alpha}\right)^{-1} \frac{\partial \overline{P}}{\partial \bar{T}} = 0 \tag{154}$$

$$
\begin{array}{l}
{}^{s}\mu + {}^{s}\Delta H_f^0 + \frac{1}{2}\left({}^{s}v_i \cdot {}^{s}v_i\right){}^{s}M - \frac{\partial \bar{f}}{\partial \alpha}\ell_\alpha \left(1 - \ell_\alpha \frac{\partial \overline{P}}{\partial \alpha}\right)^{-1} \frac{\partial \overline{P}}{\partial {}^{s}c}{}^{s}M \\
-\frac{\partial \bar{f}}{\partial \overline{P}} \left(1 - \ell_\alpha \frac{\partial \overline{P}}{\partial \alpha}\right)^{-1} \frac{\partial \overline{P}}{\partial {}^{s}c}{}^{s}M - \frac{\partial \bar{f}}{\partial {}^{s}c}{}^{s}M \;\; = \;\; 0
\end{array}
\tag{155}
$$

$$
\begin{array}{l}
\sum\limits_{s} \overline{T}{}^{s}\Lambda_{ji}^{4} + \bar{\rho}\frac{\partial \bar{f}}{\partial \alpha}\ell_\alpha \left(1 - \ell_\alpha \frac{\partial \overline{P}}{\partial \alpha}\right)^{-1} \frac{1}{\bar{\rho}} \frac{\partial \overline{P}}{\partial {}^{s}C}\delta_{ij} \\
+\frac{\partial \bar{f}}{\partial {}^{s}C}\delta_{ij} + \bar{\rho}\frac{\partial \bar{f}}{\partial \overline{P}} \left(1 - \ell_\alpha \frac{\partial \overline{P}}{\partial \alpha}\right)^{-1} \frac{\partial \overline{P}}{\partial {}^{s}C} \frac{1}{\bar{\rho}}\delta_{ij} \;\; = \;\; 0
\end{array}
\tag{156}
$$

$$
\frac{\bar{\rho}}{\tau_g} \sum_{s} \frac{\partial \bar{f}}{\partial {}^{s}g_i} k_{ij}^{g} \delta_{ij} - \frac{\bar{\rho}}{\tau_g} \frac{\partial \bar{f}}{\partial \sigma_{ij}^{ne'}} \sum_{s} {}^{s}\eta_{ijk}^{ng} \delta_{jk} \;\; = \;\; 0 \tag{157}
$$

$$
\bar{T}\Lambda_j^2 \frac{\partial \Theta}{\partial x_j^2} - \frac{\bar{\rho}}{\tau_\Theta} \frac{\partial \bar{f}}{\partial \Theta} A_{\exp} \left(\frac{-\Delta G}{RT}\right) \prod_{5+} [\mathrm{X}]^{\mathrm{T}} \;\; = \;\; 0 \tag{158}
$$

$$
\bar{\mathrm{T}}\Lambda_{ijk}^{6} \frac{\partial \bar{J}_{ik}^{ne'}}{\partial x_j} + \frac{\bar{\rho}}{\tau_\alpha} \frac{\partial \bar{f}}{\partial J_i^\alpha} k_i^{\alpha\sigma} \frac{\partial \bar{\sigma}_{ij}^{e'}}{\partial x_j} \;\; = \;\; 0 \tag{159}
$$

$$
\frac{\bar{\rho}}{\tau_\alpha} \frac{\partial \bar{f}}{\partial J_i^\alpha} k_i^{\alpha\sigma} \frac{\partial \bar{\sigma}_{ij}^{ne'}}{\partial x_j} + \frac{\bar{\rho}}{\tau_\alpha} \frac{\partial \bar{f}}{\partial J_i^\alpha} k_{ij}^{\alpha P} \delta_{ij} \frac{\partial \bar{P}}{\partial x_i} \;\; = \;\; 0 \tag{160}
$$

From these expressions, the derivative of f with respect to all the variables are obtained.

$$
\frac{\partial \bar{f}}{\partial \bar{T}} = -\bar{s} + \frac{\partial \bar{P}/\partial \bar{T}}{\partial \bar{P}/\partial \bar{\rho}} \frac{\left[\bar{T}\varpi\left(\alpha\right) - \bar{P}\right]}{\bar{\rho}^2} \tag{161}
$$

$$
\frac{\partial \bar{f}}{\partial \bar{\sigma}_{kl}^{e'}} = \frac{\bar{C}_{klij}^{-1}}{\bar{\rho}} \bar{\sigma}_{ji}^{e'} \tag{162}
$$

$$
\frac{\partial \bar{f}}{\partial \bar{\sigma}_{ij}^{ne'}} = \frac{\bar{\tau}_\sigma}{\bar{\rho}} \bar{\eta}_{ijkl}^{-1} \bar{\sigma}_{kl}^{ne'} \tag{163}
$$

$$
\frac{\partial \bar{f}}{\partial \bar{P}} = \left(1 - l_\alpha \frac{\partial \bar{P}}{\partial \alpha}\right) \left(\frac{\partial \bar{P}}{\partial \bar{\rho}}\right)^{-1} \frac{\bar{P}}{\bar{\rho}^2} \tag{164}
$$

$$\frac{\partial \bar{f}}{\partial J_i^{\alpha}} = \frac{\tau_{\alpha}}{\bar{\rho}} \left(k_{ij}^{T}\right)^{-1} J_i^{\alpha} \tag{165}$$

$$\frac{\partial \bar{f}}{\partial \bar{q}_i} = \frac{\bar{\tau}_q}{\bar{\rho}} \frac{\left(k_{ij}^{T}\right)^{-1}}{\bar{T}} \bar{q}_i \tag{166}$$

$$\frac{\partial \bar{f}}{\partial \Theta} = \frac{\tau_{\Theta}}{\bar{\rho}} \frac{M\left(\bar{v}_i.\bar{v}_i\right)}{A \exp\left(-\frac{\Delta G}{R\bar{T}}\right)} \Theta \tag{167}$$

$$\frac{\partial \bar{f}}{\partial \alpha} = -\frac{\bar{T}\varpi\left(\alpha\right)}{l_{\alpha}\bar{\rho}^2} \left(\frac{\partial \bar{P}}{\partial \bar{\rho}}\right)^{-1} \left(1 - l_{\alpha} \frac{\partial \bar{P}}{\partial \alpha}\right) \tag{168}$$

$$\frac{\partial \bar{f}}{\partial {}^{s}c} = \frac{{}^{s}\mu + {}^{s}\Delta H_f^0}{{}^{s}M} + \frac{1}{2}\left({}^{s}v_i.{}^{s}v_i\right) + \frac{\partial \bar{P}/\partial {}^{s}c}{\partial \bar{P}/\partial \bar{\rho}} \left(\frac{\bar{T}\varpi\left(\alpha\right) - \bar{P}}{\bar{\rho}^2}\right) \tag{169}$$

$$\frac{\partial \bar{f}}{\partial {}^{s}g_i} = \frac{\tau_g}{\bar{\rho}} \frac{{}^{s}k_{g_{ij}}}{{}^{s}k_{g_{ijk}} C_j} {}^{s}g_i \tag{170}$$

$$\Lambda_{ji}^{1} = \frac{1}{\bar{\rho}\bar{T}} \frac{\partial \bar{P}/\partial \alpha}{\partial \bar{P}/\partial \bar{\rho}} \left(\bar{T}\varpi\left(\alpha\right) + \bar{P}\right) + \frac{\varpi\left(\alpha\right)}{l_{\alpha}\bar{\rho}} \left(\frac{\partial \bar{P}}{\partial \bar{\rho}}\right)^{-1} \left(1 - l_{\alpha} \frac{\partial \bar{P}}{\partial \alpha}\right) \tag{171}$$

$$\Lambda_j^2 = \frac{M\left(v_i.v_i\right)}{\bar{\rho}\bar{T}} \prod_{s+} \left[{}^{s+}\chi\right]^{s+\varsigma} \Theta \left(\frac{\partial \Theta}{\partial x_j}\right)^{-1} \tag{172}$$

$$\Lambda_{ji}^{3} = \frac{\delta_{ij}}{\bar{T}} \tag{173}$$

$${}^{s}\Lambda_{ji}^{4} = -\frac{\left({}^{s}\mu + {}^{s}\Delta H_f^0\right)\delta_{ij}}{{}^{s}M} - \frac{1}{2}\left({}^{s}v_i.{}^{s}v_i\right)\delta_{ij} \tag{174}$$

$$\Lambda_i^5 = -\frac{k_{ij}^{\alpha T}}{k_{ij}^{\alpha P}} \frac{J_i^{\alpha}}{\bar{\rho}\bar{T}} - \frac{\bar{q}_i}{k_T \bar{T}^2} \tag{175}$$

$$\delta_{jk}\Lambda^{6}_{jik} = -\frac{k_{\alpha\sigma}}{k_{\alpha P}}\frac{J^{\alpha}_{i}}{\bar{T}} \tag{176}$$

Using these expressions, the final expression for the rate of entropy production is obtained as-

$$\begin{aligned}\bar{T}\bar{\eta} = &\underbrace{\left(k^{\alpha p}_{ij}\right)^{-1} J^{\alpha}_{i} J^{\alpha}_{j}}_{PoreCollapseFlux} + \underbrace{\frac{M\bar{v}_{i}.\bar{v}_{i}}{A\exp\left(-E/R\bar{T}\right)}}_{ChemicalReaction}\Theta\Theta + \underbrace{\frac{\left(k^{q}_{ij}\right)^{-1}}{\bar{T}}\bar{q}_{i}\bar{q}_{j}}_{HeatFlux} \\ &+ \underbrace{\bar{\eta}_{ijkl}\bar{\sigma}^{ne'}_{kl}\bar{\sigma}^{ne'}_{ij}}_{Viscosity} + \underbrace{\sum_{s}\left({}^{s}\kappa^{\eta g}_{ijk}C_{k}\right)^{-1}{}^{s}\kappa^{g}_{ij}\,{}^{s}g_{i}\,{}^{s}g_{j}}_{MassDiffusionFlux} \geq 0\end{aligned} \tag{177}$$

This equation is always positive provided

$$\left(k^{\alpha p}_{ij}\right)^{-1} \geq 0 \tag{178}$$

$$A\exp\left(-E/R\bar{T}\right) \geq 0 \tag{179}$$

$$\bar{\eta}_{ijkl} \geq 0 \tag{180}$$

$$\left(k^{q}_{ij}\right)^{-1} \geq 0 \tag{181}$$

$$\left(k^{q}_{ij}\right)^{-1} \geq 0 \tag{182}$$

$$\left({}^{s}\kappa^{\eta g}_{ijk}C_{k}\right)^{-1}{}^{s}\kappa^{g}_{ij} \geq 0 \tag{183}$$

To get the expression for temperature, we go back to the following equation $\bar{\mathrm{f}} = \bar{\mathrm{e}} - \mathrm{T}\bar{\mathrm{s}}$ from which we get the following equation

$$\mathrm{T}\frac{\mathrm{d}\bar{\mathrm{s}}}{\mathrm{d}\bar{\mathrm{e}}} = 1 - \frac{\mathrm{dT}}{\mathrm{d}\bar{\mathrm{e}}}\bar{\mathrm{s}} - \frac{\mathrm{d}\bar{\mathrm{f}}}{\mathrm{d}\bar{\mathrm{e}}} \tag{184}$$

Using the binomial expansion, this can be approximated to

$$\frac{1}{\mathrm{T}} = \frac{\mathrm{d}\bar{\mathrm{s}}}{\mathrm{d}\bar{\mathrm{e}}}\left[1 + \left(\frac{\mathrm{dT}}{\mathrm{d}\bar{\mathrm{e}}}\bar{\mathrm{s}} + \frac{\mathrm{d}\bar{\mathrm{f}}}{\mathrm{d}\bar{\mathrm{e}}}\right)\right] \tag{185}$$

Substituting the above obtained expressions for Helmholtz free energy as a function of all the state variables, we obtain the following expression for temperature:

$$\frac{1}{\mathrm{T}} = \frac{\mathrm{d}\bar{\mathrm{s}}}{\mathrm{d}\bar{\mathrm{e}}} + \frac{\mathrm{d}\bar{\mathrm{s}}}{\mathrm{d}\bar{\mathrm{e}}}\left[\begin{array}{l} \frac{\bar{C}^{-1}_{klij}}{\bar{\rho}}\bar{\sigma}^{e'}_{ji}\frac{d\bar{\sigma}^{e'}_{kl}}{d\bar{\mathrm{e}}} + \frac{\bar{\tau}_\sigma}{\bar{\rho}}\bar{\eta}^{-1}_{ijkl}\bar{\sigma}^{ne'}_{kl}\frac{\bar{\eta}^{-1}_{ijkl}\bar{\sigma}^{ne'}_{kl}}{\bar{\rho}}\frac{d\bar{\sigma}^{ne'}_{ij}}{d\bar{\mathrm{e}}} + \frac{\tau_\alpha}{\bar{\rho}}\left(k^T_{ij}\right)^{-1}J^\alpha_i\frac{dJ^\alpha_j}{d\bar{\mathrm{e}}} \\ + \left(1 - l_\alpha\frac{\partial\bar{P}}{\partial\alpha}\right)\left(\frac{\partial\bar{P}}{\partial\bar{\rho}}\right)^{-1}\frac{\bar{P}}{\bar{\rho}^2}\frac{d\bar{P}}{d\bar{\mathrm{e}}} + \frac{\bar{\tau}_q}{\bar{\rho}}\frac{\left(k^T_{ij}\right)^{-1}}{\bar{T}}\bar{q}_i\frac{d\bar{q}_j}{d\bar{\mathrm{e}}} \\ + \frac{\tau_\Theta}{\bar{\rho}}\frac{M(\bar{v}_i.\bar{v}_i)}{A\exp\left(-\frac{\Delta G}{RT}\right)}\Theta\frac{d\Theta}{d\bar{\mathrm{e}}} - \frac{\bar{T}\varpi(\alpha)}{l_\alpha\bar{\rho}^2}\left(\frac{\partial\bar{P}}{\partial\bar{\rho}}\right)^{-1}\left(1 - l_\alpha\frac{\partial\bar{P}}{\partial\alpha}\right)\frac{d\alpha}{d\bar{\mathrm{e}}} \\ + \left\{\frac{{}^s\mu + {}^s\Delta H^0_f}{{}^sM} + \frac{1}{2}\left({}^sv_i.{}^sv_i\right) + \frac{\partial\bar{P}/\partial^s c}{\partial\bar{P}/\partial\bar{\rho}}\left(\frac{\bar{T}\varpi(\alpha) - \bar{P}}{\bar{\rho}^2}\right)\right\}\frac{d^s c}{d\bar{\mathrm{e}}} \\ + \frac{\tau_g}{\bar{\rho}}\frac{{}^sk_{g_{ij}}}{{}^sk_{g_{ijk}}C_k}{}^sg_i\frac{d^sg_i}{d\bar{\mathrm{e}}} \end{array}\right] \tag{186}$$

Thus, the governing set of equations to analyze the shock-related chemical reactions in binary energetic materials has been formulated. It has been developed in the framework of extended irreversible thermodynamics and internal variable theory. The concept of extended irreversible thermodynamics is not being introduced for the first time in this work. It has been used by researchers in the past [72]. However, it has not been used by researchers in their analysis of

shock-related chemical reactions in energetic materials. Most of the work in this field has been by making the assumption of thermal equilibrium. As has been explained in this work, this assumption is not entirely valid for the problems we wish to study. Thus, processes such as chemical reaction, porosity and void collapse flux are studied in the framework of extended irreversible thermodynamics. Extended irreversible thermodynamics is a tool, similar to concepts of continuum mechanics or finite difference numerical schemes, that aid in the analysis of new problems of interest.

4.5 Particle Size Effects

The initiation of chemical reaction and its subsequent propagation is affected by the morphology of the particles. The particles could range anywhere from being a micro-sized particle to being nano-sized. They could be fine or coarse grained in nature. These properties of the particles play a role in the shock process and its subsequent effects such as the initiation of chemical reaction [31][115].

As the particle size decreases, the reaction initiates faster in the mixture and propagates faster, i.e., a nano-sized mixture can react faster than a mixture made of micro-sized particles [51]. This phenomenon is usually explained based on the basis of the surface energy of the particles. As the particle size decreases, the number of atoms on the surface of the particle increases and hence, the surface energy increases [65]. An increase in the surface energy implies that the reactants are now in a higher energy state than they would have been in otherwise. This implies that the activation energy required by the reactants to reach

the transition state is now reduced. This process is schematically depicted in figure 12. It shows how the surface energy raises the energy of the reactants and consequently decreases the activation energy necessary for the reaction.

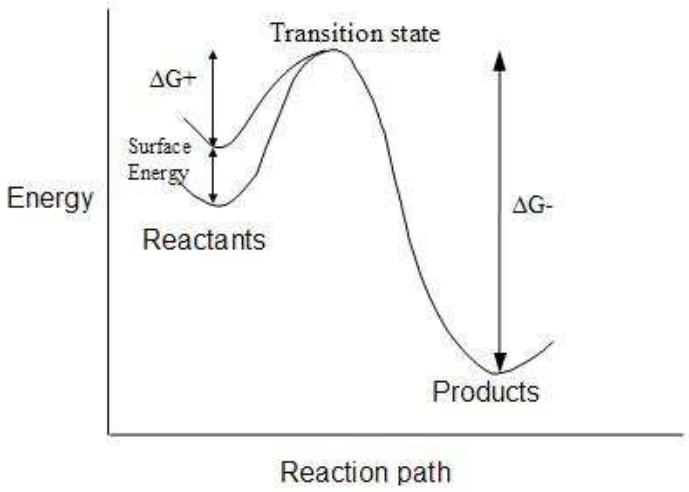

Figure 12: Effect of surface energy on the activation energy of the chemical reaction

The fact that a change in the surface energy due to varying particle sizes leads to faster initiation and propagation of the reaction can be explained based on its relation to the melting temperature of the species [66][138][139]. The increase in surface energy causes a reduction in the melting temperature of the particle [62]. Consequently, as the particle size decreases, the melting temperature decreases [51]. Hunt et. al [51] presented a figure in their paper which shows how the melting temperature of aluminum varies as the particle size decreases from approximately 200nm to 10nm. This is shown in fig. 13. When one of the species in a mixture melts, it leads to better mixing between the reactants. This enhances the mixing between the reactants leads to faster initiation of chemical reaction and its subsequent propagation.

Thus, the particle size effects can be included in the continuum model by considering the melting temperature of the reactants as a function of the particle size and the surface energy of the particles. In a binary energetic mixture, one reactant has a lower melting temperature than the other and will consequently undergo melting first. The effect of particle sizes will then be affected by this reactant. Thus, the surface energy and melting temperature of this single reactant is related to the particle size. The derivation of the surface energy expression is presented next.

During the melting process, the solid and liquid particles are assumed to be in thermal and chemical equilibrium.

$$\begin{aligned} T_s &= T_l \\ \mu_s &= \mu_l \end{aligned} \tag{187}$$

where T is the temperature which is a function of the particle radius r, μ is

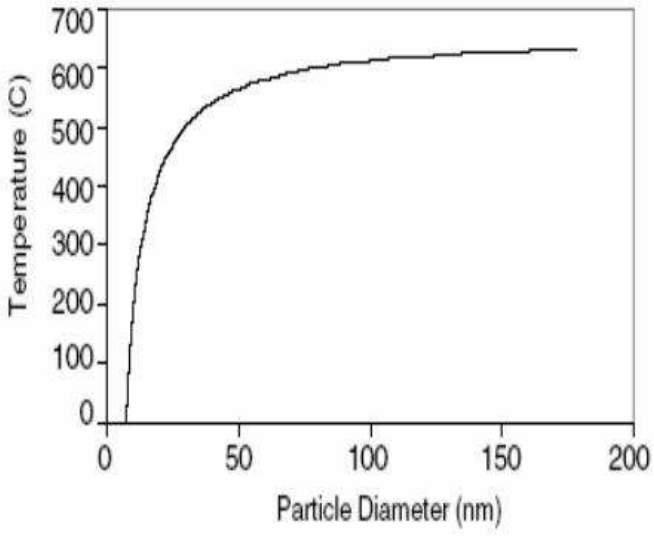

Figure 13: Variation of melting temperature of Aluminum with particle size [51]

the chemical potential and the subscripts s and l refer to the solid and liquid physical states respectively.

In thermodynamics, there are four quantities that are measured in units of energy. These four quantities are functions of temperature, pressure, volume and entropy and are also called thermodynamic potentials. The first of these quantities is the internal energy e.

The second thermodynamic potential is the Helmoholtz free energy (f) defined in eqn. (188). It is obtained from the first and second laws of thermodynamics. It can be related to the work performed by the system under either constant volume or constant temperature conditions. Hence the term 'free' energy as it denotes the energy that is free or available to do work.

$$f \;=\; e \;-\; Ts \tag{188}$$

The third thermodynamic potential is the enthalpy (H) of a system. It is defined in terms of the internal energy, pressure and volume of the system (eqn. 189). In a constant pressure process with only P-V mechanical work, the change in enthalpy gives the heat flow in or out of the system. Thus, it is sometimes also called the heat content of a system.

$$H \;=\; e \;+\; PV \tag{189}$$

The fourth and final thermodynamic potential is the Gibbs free energy (G), named after the American physicist Willard Gibbs. It is defined in eqn. (190)

as a function of the enthalpy, temperature and entropy of the system. It is one of the most important of the thermodynamic potentials. It provides a criterion for the reversibility of a process and under conditions of constant temperature and constant pressure, it tells us how much work is available in the system.

$$G \;=\; H \;-\; Ts \tag{190}$$

A function F(x,y) can be expressed in the differential form as -

$$dF = \left(\frac{\partial F}{\partial x}\right)_y dx + \left(\frac{\partial F}{\partial y}\right)_x dy \tag{191}$$

A perfect differential has the property that the order of its differentiation is immaterial. If F(x,y) is a perfect differential, then it can be expressed mathematically as -

$$\frac{\partial^2 F}{\partial x \partial y} = \frac{\partial^2 F}{\partial y \partial x} \tag{192}$$

The four thermodynamic potentials are perfect differentials. Using the definitions given above (eqns. 188, 189, 190), the following relations, known as Maxwell's relations can be obtained. In these equations, μ_i is the chemical potential of species i and N_i is the number of moles of species i.

$$\left(\frac{\partial T}{\partial V}\right)_{s,N_i} = -\left(\frac{\partial P}{\partial s}\right)_{V,N_i} \tag{193}$$

$$\left(\frac{\partial \mu_i}{\partial V}\right)_{s,N_i} = -\left(\frac{\partial P}{\partial N_i}\right)_{V,s,N_j \neq N_i} \tag{194}$$

$$\left(\frac{\partial T}{\partial P}\right)_{s,N_i} = \left(\frac{\partial V}{\partial s}\right)_{P,N_i} \tag{195}$$

$$\left(\frac{\partial \mu_i}{\partial P}\right)_{s,N_i} = \left(\frac{\partial V}{\partial N_i}\right)_{P,s,N_j \neq N_i} \tag{196}$$

$$\left(\frac{\partial \mu_i}{\partial s}\right)_{P,N_i} = \left(\frac{\partial T}{\partial N_i}\right)_{P,s,N_j \neq N_i} \tag{197}$$

$$\left(\frac{\partial s}{\partial V}\right)_{T,N_i} = \left(\frac{\partial P}{\partial T}\right)_{V,N_i} \tag{198}$$

$$\left(\frac{\partial \mu_i}{\partial V}\right)_{T,N_i} = -\left(\frac{\partial P}{\partial N_i}\right)_{V,T,N_j \neq N_i} \tag{199}$$

$$\left(\frac{\partial \mu_i}{\partial T}\right)_{V,N_i} = -\left(\frac{\partial s}{\partial N_i}\right)_{V,T,N_j \neq N_i} \tag{200}$$

$$\left(\frac{\partial s}{\partial P}\right)_{T,N_i} = -\left(\frac{\partial V}{\partial T}\right)_{P,N_i} \tag{201}$$

$$\left(\frac{\partial \mu_i}{\partial T}\right)_{P,N_i} = -\left(\frac{\partial s}{\partial N_i}\right)_{P,T,N_j \neq N_i} \tag{202}$$

$$\left(\frac{\partial \mu_i}{\partial P}\right)_{T,N_i} = \left(\frac{\partial V}{\partial N_i}\right)_{P,T,N_j \neq N_i} \tag{203}$$

Now substituting the expression for the chemical potential and applying the equilibrium condition, eqn. (187) can be restated as -

$$-\underline{S}_l dT + \underline{V}_l dP_l = -\underline{S}_s dT + \underline{V}_s dP_s \tag{204}$$

where $\underline{S}$ is the molar entropy and $\underline{V}$ is the molar volume. We have the following relation that relates the molar entropy of melting to the molar enthalpy of melting -

$$\Delta \underline{S}_m = \frac{\Delta \underline{H}_m}{T_\infty} \tag{205}$$

where T_∞ is the melting temperature of the bulk material (macro particle).

When a solid reactant is melting, there is an interface that separates the two physical states. The pressure across the interface is not the same. The difference in the solid and liquid pressure is related to the surface tension at the interface. The pressure differential across the melting interface can be given as [74] :

$$P_s - P_l = 2\frac{\gamma^{sl}}{r} \tag{206}$$

where γ^{sl} is the surface tension at the interface. It is assumed that the pressure of the liquid does not change much during the melting process [74]. This implies that $dP_l = 0$. Using eqn. (205) and integrating eqn. (206) across the radius of the particle from r = 0 to r = ∞, we obtain the expression for the surface tension in the material to be -

$$\gamma^{sl} = \frac{\Delta \underline{H}_m \left(T_\infty - T_r\right) r}{2\underline{V}_s T_\infty} \tag{207}$$

This equation gives the surface tension in the material as a function of the particle size. This can be converted to an expression of surface energy, specific to

each material. This energy is then incorporated in the expression for the activation energy, which governs the chemical reaction. Thus, the chemical reaction in the mixture becomes particle-size dependent, through the surface energy term. This expression for the specific case of aluminum and iron-oxide is derived in the next chapter which provides a description of the shock-induced chemical reactions of this thermite mixture under one-dimensional strain conditions.

The complete set of equations necessary to analyze the shock-related chemical reactions in a binary energetic material has been formulated in this chapter. These equations are generic equations and are independent of the mixture being analyzed. They can easily be applied to study any combination of energetic mixtures. Thus, a highly useful framework that can be applied universally to study energetic mixtures has been developed in this work. An example case-study is presented in the next chapter. An energetic mixture of aluminum and iron-oxide in an epoxy binder is analyzed. A detailed description of the analysis along with the results obtained has been presented.

Chapter V

ANALYSIS OF A THERMITE MIXTURE OF ALUMINUM AND IRON-OXIDE

First, a composite mixture of energetic materials that is studied is the thermite mixture of aluminum (Al) and iron-oxide (Fe_2O_3). This mixture is selected due to the highly exothermic nature of the chemical reaction between the reactants. In addition to the metal and metal-oxide, a binder is also included in the mixture. The binder analyzed in this work is epoxy. Thus, a mixture consisting of $Al-Fe_2O_3-epoxy$ is studied under one-dimensional strain conditions.

5.1 Hugoniot Calculation

In this problem, we have 5 species in the mixture - two reactants (Al *and* Fe_2O_3), two products (Fe *and* Al_2O_3) and the binder epoxy. Structural reinforcements are not considered in the numerical calculations. When the impact of a projectile on the energetic material is considered, the projectile is modeled separately. In this work, the projectile is made of steel. The two equations of state used to describe the hydrostatic components of these species are the Birch-Murnaghan equation for Al, Fe_2O_3, Fe and Al_2O_3 and the Mie-Gruneisen equation for steel and epoxy.

The hydrostatic component of the reactants and the products is described by the Birch-Murnaghan equation of state -

$$P(\rho, T) = \frac{\beta_{T_0}}{n}\left[\left(\frac{\rho}{\rho_0}\right)^n - 1\right] + C_v\Gamma_0\rho_0\left(T - T_o\right) \tag{208}$$

where the Gruneisen parameter Γ is given by -

$$\Gamma = \nu\left(\frac{\partial P}{\partial e}\right)_\nu \tag{209}$$

$$\beta_T = -\nu\left(\frac{\partial P}{\partial \nu}\right)_\theta = \beta_{T_0}\left(\frac{\nu}{\nu_0}\right)^{-n} \tag{210}$$

β_{T_0} and $n = \beta'_{T_0}$ are constants specific to each species. Table 1 lists the values of these parameters for all the species in the thermite reaction [15].

Table 1: The material properties for the Birch-Murnaghan equation of state for the thermite exothermic reaction between Al and Fe_2O_3[15]

Property	Al (s)	Fe_2O_3 (s)	Al_2O_3 (l)	Fe (l)
$\rho_0\,(kg/m^3)$	2700	5274	2960	6590
β_{T_0} (GPa)	7.64	20.27	25.20	13.60
n	3.56	4.35	5.00	3.97
Γ	2.35	1.99	1.32	2.10
$C_v\,(kJ/kgK)$	0.931	0.607	0.714	0.450

The Mie-Gruneisen equation of state is used to describe the hydrostatic pressure of steel and epoxy [9][16][75].

$$P = \frac{K_0\mu\left[1 + \Gamma/2\left(\mu/(1-\mu)\right)\right]}{\left[1 - S\mu\right]^2} + \Gamma\rho e \tag{211}$$

The parameters for these two materials is expressed in table 2.

Table 2: The material properties for the Mie-Gruneisen equation of state for epoxy and steel [9][16][75]

Property	Epoxy (s)	Steel (s)
$\rho_0\,(kg/m^3)$	1185	7770
$C\,(km/s)$	2.6	4.57
S	1.59	1.49
Γ	2.18	1.93

5.2 Validation of the numerical scheme

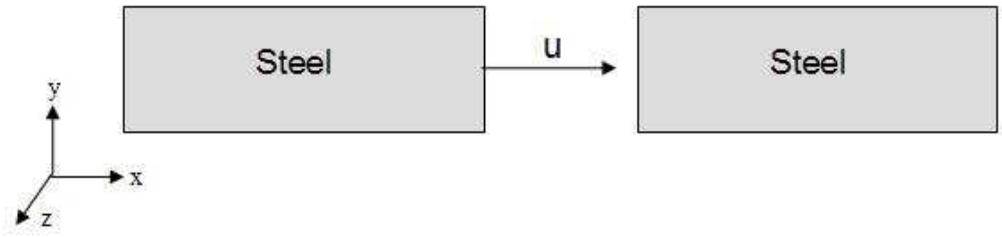

Figure 14: Impact of a steel projectile on a steel target under one-dimensional strain conditions

The problem that is the main focus of study is the impact of a steel projectile on the energetic structural material. The steel projectile travels at a specified initial velocity and impacts the energetic structural material which is at rest. This problem is analyzed using the MUSCL scheme for spatial finite difference with a TVD Runge-Kutta scheme for the time integration. A first step is to

validate the finite difference scheme and the program. A test case was first studied. Impact of a steel projectile on a steel target under one-dimensional strain conditions is studied. This is schematically depicted in fig. 14. The differential equations under one-dimensional strain were used in the analysis. These include the mass balance equation, the momentum balance equation and the stress-strain relation. The hydrostatic component was modeled using the Mie-Gruneisen equation of state and the deviatoric stress is modeled assuming linear elastic relations. These equations are listed below -

$$\frac{\partial \rho}{\partial t} + \frac{\partial \left(\rho v_x\right)}{\partial x} = 0 \tag{212}$$

$$\rho \frac{D v_x}{D t} = \frac{\partial \sigma_{xx}}{\partial x} \tag{213}$$

$$\sigma_{ii} = -P + \sigma_{ii}^{'} \tag{214}$$

where the deviatoric stress is given by

$$\begin{aligned} \dot{\sigma}_{xx}^{'} &= \tfrac{4}{3} G_{st} \tfrac{\partial v_x}{\partial x} \\ \dot{\sigma}_{yy}^{'} &= \dot{\sigma}_{zz}^{'} = -\tfrac{2}{3} G_{st} \tfrac{\partial v_x}{\partial x} \end{aligned} \tag{215}$$

and the hydrostatic pressure is given by [16]

$$P = \frac{\rho_0 C^2 \mu \left[1 + \left(1 - \Gamma/2\right) \mu\right]}{\left[1 - \left(S - 1\right) \mu\right]^2} + \Gamma e \tag{216}$$

Since the projectile and the target are of the same material, the wave should project equally in both these materials. The velocity, pressure and density

should remain the same at the interface. Figure 15 depicts the results that were obtained. Figure 16 shows the values that are obtained for two different velocities of impact. When the velocity of impact is increases, the pressure reached in the projectile and the target also increases. Simultaneously, greater compression of the material is also achieved, as is observed from the density ratio. Sections of the projectile that were not affected by the shock wave earlier are now influenced by it. The magnitude of the variables do not change as the wave moves further into the projectile and the target. Figure 17 shows this for two time intervals of 0.19 μs and 0.46 μs.

The next case that was studied is the impact of a projectile on a target made of a dissimilar material. An aluminum target was selected (See fig. 18). The equations considered in this case include the mass balance equation, the momentum balance equation, the energy balance equation and the stress-strain relation. The mass and momentum balance equations and the stress-strain relations are the same as those used in the previous case study (eqns. 212, 213, 215 and 214). In addition, the energy balance equation is -

$$\rho \frac{D\bar{e}}{Dt} = -\frac{\partial q_i}{\partial x_i} + \sigma_{xx} \frac{\partial \bar{v}_x}{\partial x} \tag{217}$$

The stress in the aluminum is once again divided into the hydrostatic component and the deviatoric stress component. The deviatoric stress component is described using the linear elastic relation as in the steel case and the hydrostatic component is described using the Birch-Murnaghan equation.

$$\begin{aligned} \dot{\sigma}_{xx} &= \tfrac{4}{3} G_{Al} \tfrac{\partial v_x}{\partial x} \\ \dot{\sigma}_{yy} &= \dot{\sigma}_{zz} = -\tfrac{2}{3} G_{Al} \tfrac{\partial v_x}{\partial x} \end{aligned} \tag{218}$$

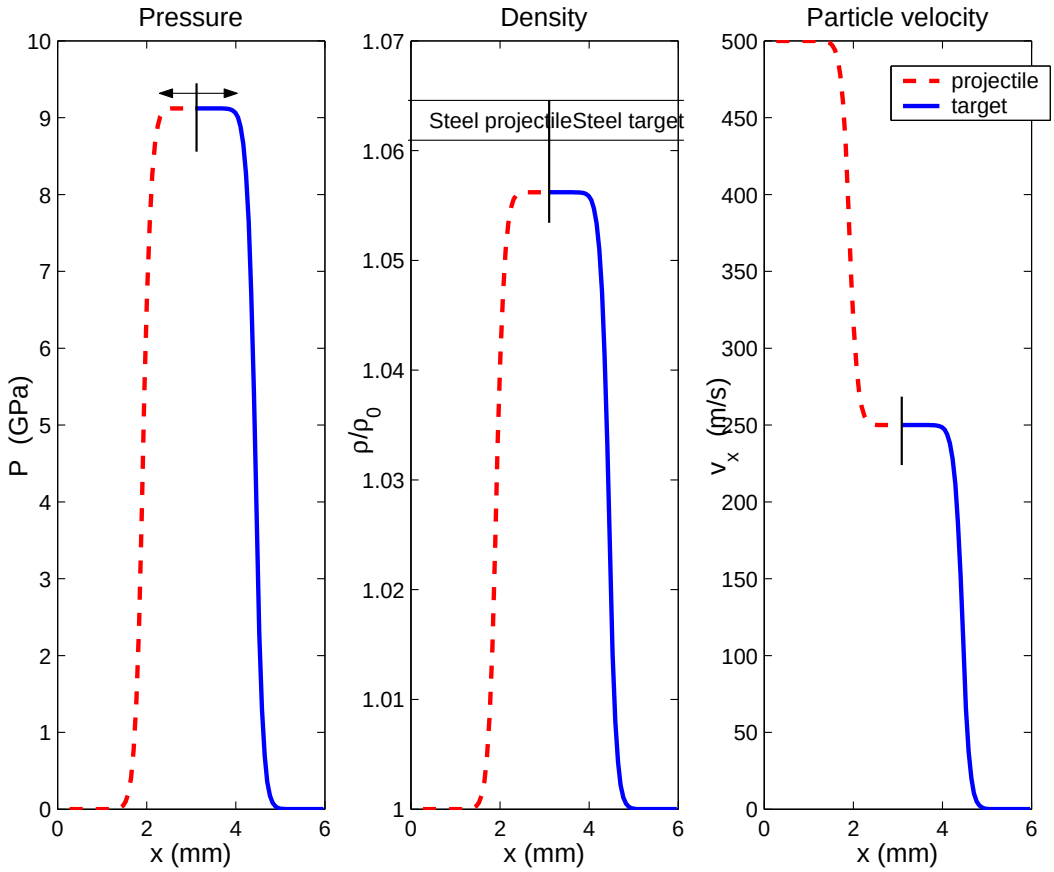

Figure 15: Pressure, density and velocity curves for the impact of a steel projectile at 500m/s on a stationary steel target. The dotted red line indicates the projectile and the solid blue line indicates the target

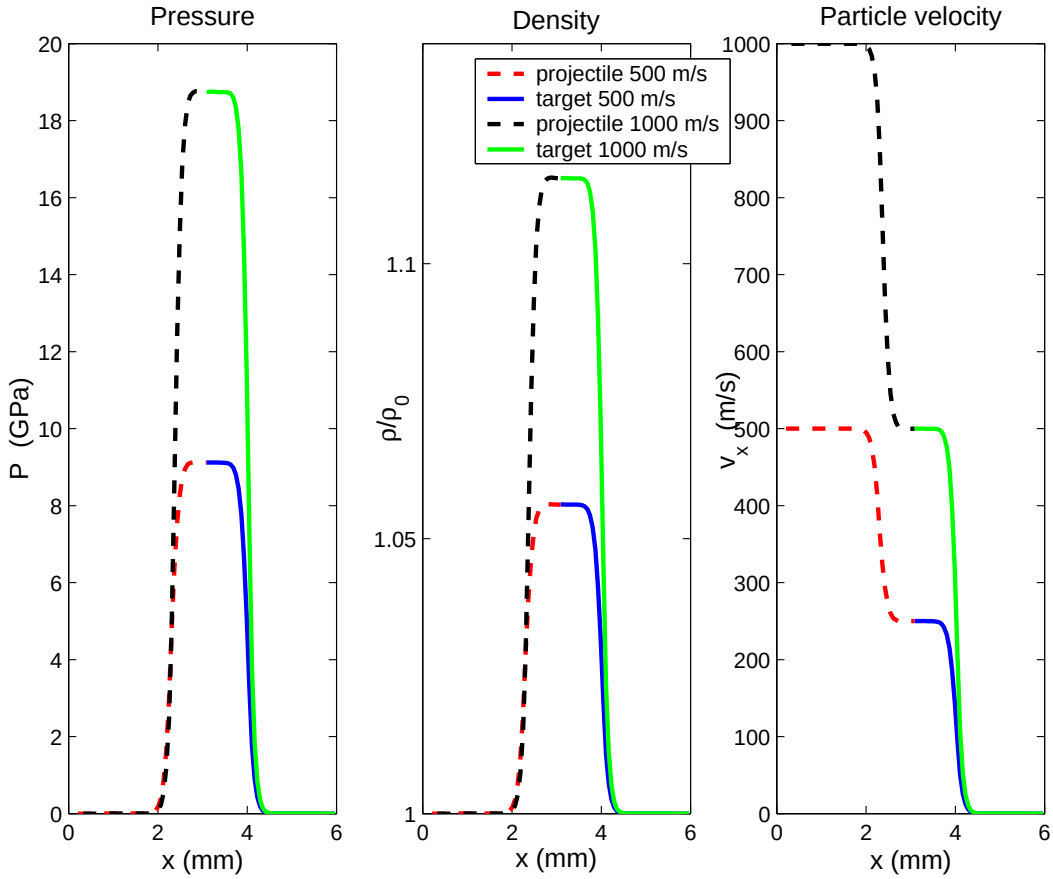

Figure 16: Pressure, density and velocity curves for the impact of a steel projectile at 500m/s and 1000m/s on a stationary steel target. The dotted (red = 500m/s, black = 1000m/s) line indicates the projectile and the solid (blue = 500m/s, green = 500m/s) line indicates the target

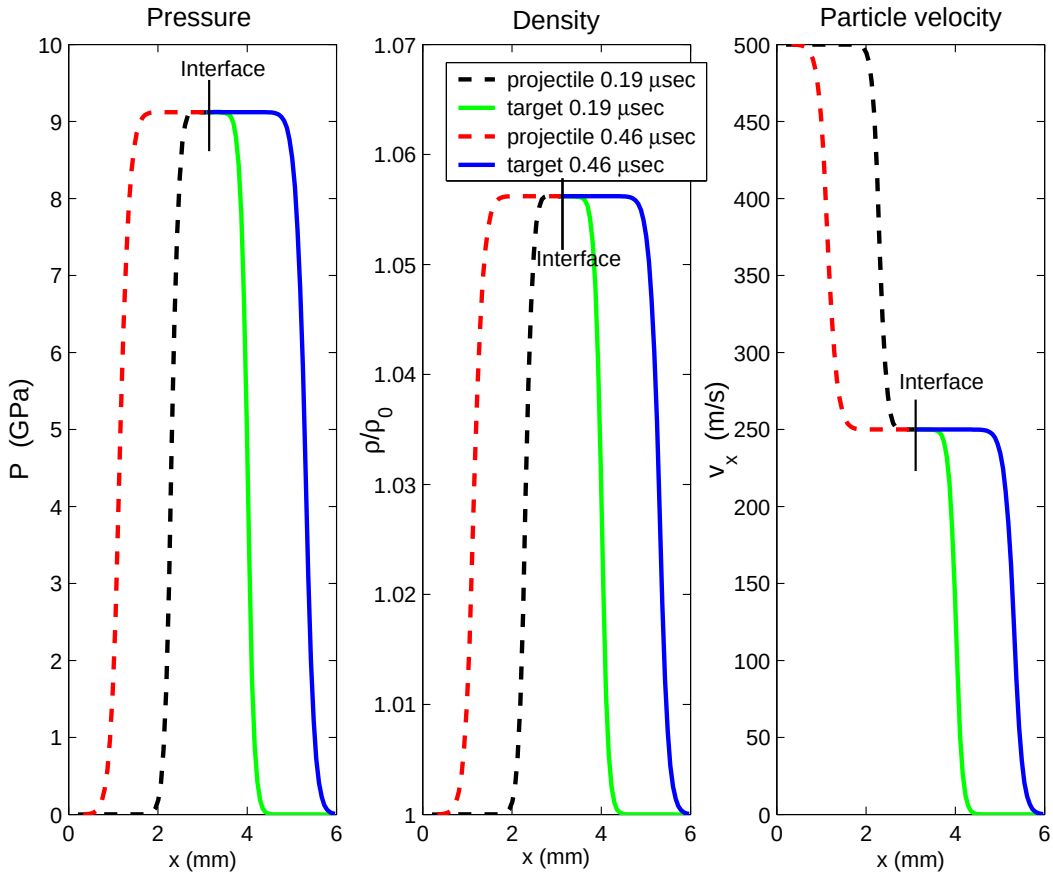

Figure 17: Pressure, density and velocity curves for the impact of a steel projectile at 500m/s on a stationary steel target at 0.19 μs and 0.46 μs. The dotted (black = $0.19\mu s$, red = $0.46\mu s$) line indicates the projectile and the solid (green = $0.19\mu s$, blue = $0.46\mu s$) line indicates the target

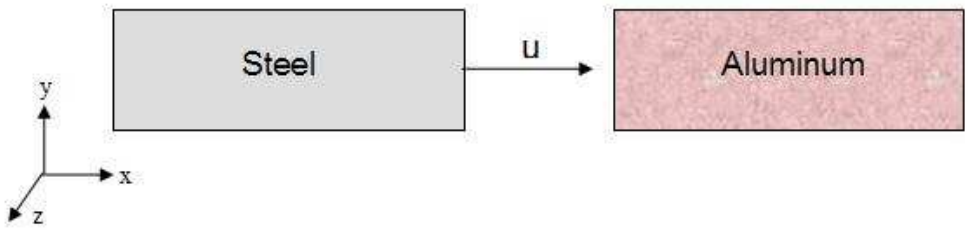

Figure 18: Impact of a steel projectile on an aluminum target under one-dimensional strain conditions

$$P(\rho, T) = \frac{\beta_{T_0}}{n}\left[\left(\frac{\rho}{\rho_0}\right)^n - 1\right] + C_v\Gamma_0\rho_0\left(T - T_o\right) \tag{219}$$

Figure 19 shows the pressure, density, velocity and temperature obtained for the impact of a steel projectile on an aluminum target at 500m/s impact velocity. Figure 19a shows the pressure wave generated after impact in both the projectile and the target. Since these two materials are not the same, the pressure profile in the two materials is not the same. Aluminum is a softer material than steel. On impact, aluminum would undergo greater compression as compared to steel. The compression is measured by the ratio of the current density to the reference density, i.e., ρ/ρ_0 where ρ is the density of the material at time t and ρ_0 is the reference density. Figure 19b shows that the aluminum compresses to about 1.17 whereas steel compresses only by about 1.02. These numbers indicate that the two materials are physically behaving in a manner that they should. The temperature in the aluminum particles increases more than in the steel projectile, by about 300K. At the interface due to this mismatch in temperatures, a large amount of thermal diffusion occurs. The heat flux flows from the aluminum to the steel at the interface, bringing the temperature of the aluminum down to the steel temperature. This is observed from the decrease in temperature from the peak temperature in the aluminum.

The analytical solution to the problem is given below. For the projectile,

$$\sigma_x \;=\; \rho c\left(v \;-\; v_0\right) \tag{220}$$

and for the target,

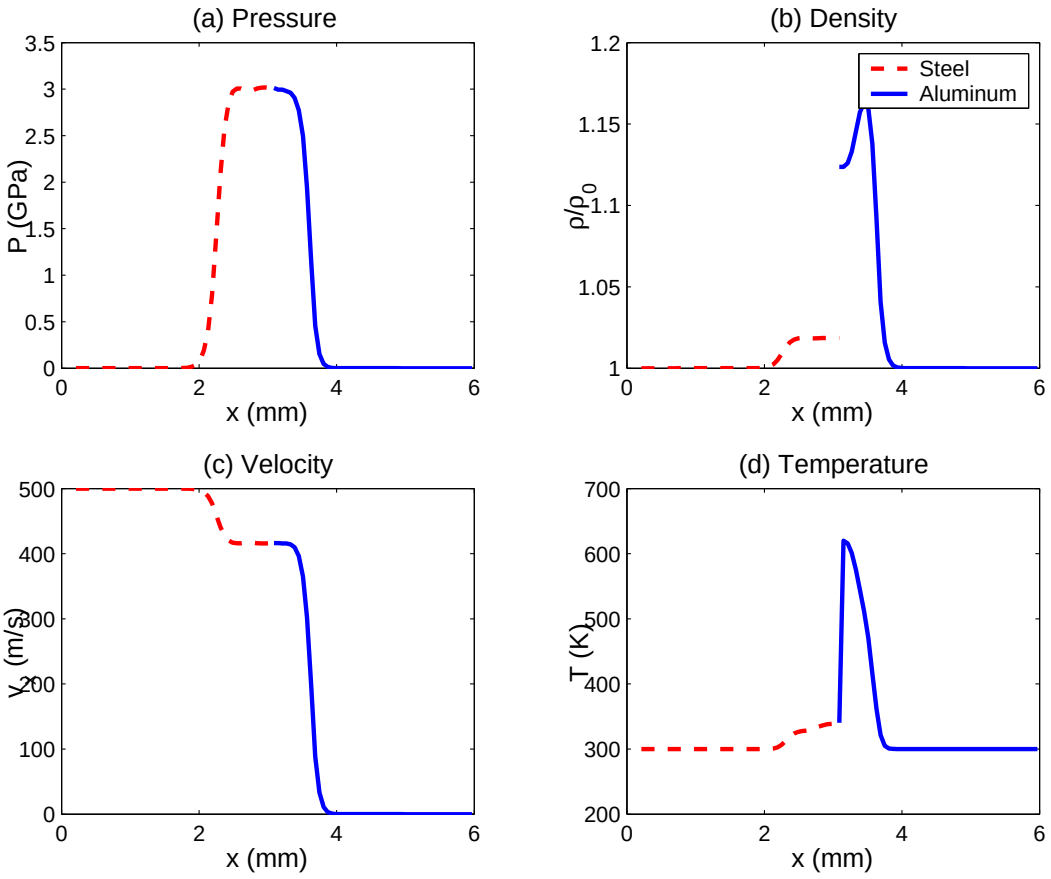

Figure 19: (a) Pressure, (b) density, (c) velocity and (d) temperature curves for the impact of a steel projectile at 500m/s on a stationary aluminum target. The dotted red line indicates the steel projectile and the solid blue line indicates the aluminum target

$$\sigma_x \;=\; -\,\rho c\,(v\,-\,0) \tag{221}$$

The above two examples were used as preliminary case studies to test the model. It was primarily used to test the stability and non-oscillatory nature of the MUSCL numerical scheme. The plots show hardly any oscillations at all, thus, proving the properties of this numerical scheme. Since the results obtained appear reasonable as compared to the analytical solution of the problem (eqns. 220) and 221, we now move onto analyzing the binary energetic thermite mixture.

5.3 Equation of state of the mixture

The target is made of a number of components. There are two reactants, two products and the binder. In some cases, the binder may participate in the reaction. Even without a reaction, the target is made of more than one component. Each component can be described by an equation of state. These equations have to be combined in such a way that they accurately describe the equation of state of the mixture. The total pressure in the mixture has to have contributions from each component. One of the ways this can be done is by using the concentration of each component. Each component's contribution to the total pressure is thus, considered to be proportional to its concentration in the mixture. The equation of state of the mixture can then be calculated by the following equation -

$$\bar{P} = \sum_s {}^s c \left\{ \frac{{}^s\beta_{T_0}}{{}^s n} \left[\left(\frac{\bar{\rho}}{\bar{\rho}_0} \right)^{{}^s n} - 1 \right] + {}^s C_v {}^s\Gamma_0 {}^s\rho_0 \left(T - T_o \right) \right\} \tag{222}$$

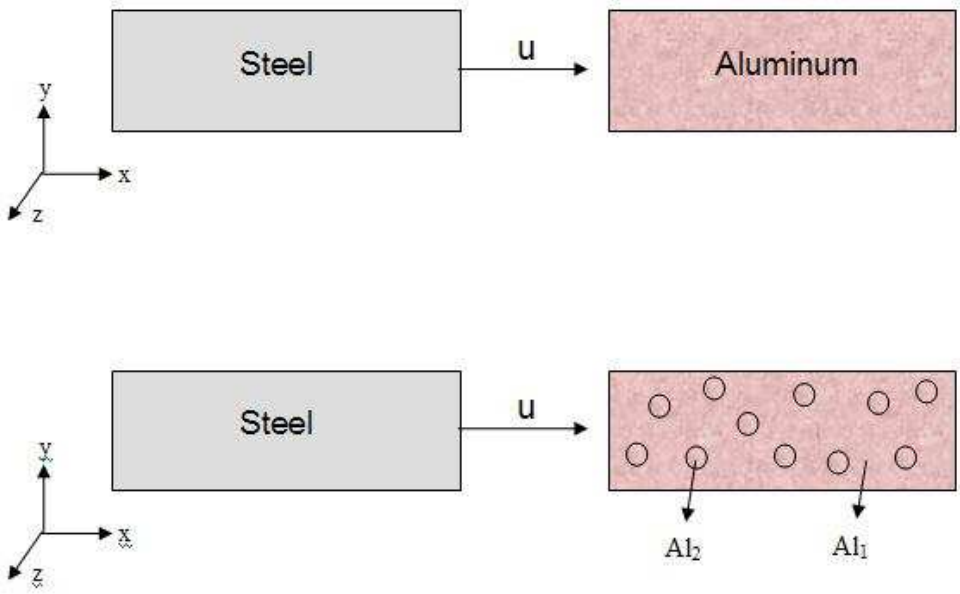

Figure 20: Impact of a steel projectile on an aluminum target under one-dimensional strain conditions. The top figure shows the impact on a pure aluminum target, considered as one component. The bottom figure shows the aluminum target split into two components, both made of aluminum, and modeled as a binary mixture

The next question that arises is if this mixture equation of state will accurately predict the equation of state of the mixture. This is answered by studying a test case. First, the impact of a steel projectile on a pure aluminum target is studied. Then the aluminum target is divided into two parts, both made of aluminum with concentration ${}^{Al}c$ and $1 - {}^{Al}c$. This target material is then modeled using the mixture equation of state. Fig. 20 depicts the two cases. Since the target in both the cases is pure aluminum, the results obtained by the mixture equation of state should be the same as that obtained when the target is modeled as being made of just one material. In the numerical simulation, the steel projectile strikes the aluminum target at a speed of 500 m/s. The results

obtained in these two cases are compared and presented in figures 21 and 22. Figure 21 shows the Hugoniot of the steel and the aluminum in the two cases. As can be seen from this figure, the Hugoniots of both the projectile and the target match exactly in both the scenarios. In fact, the results match so well that there is only one curve that is visible to the eye. This proves that the pressure calculated using the mixture equation of state, described by eqn. (222) is accurate. Similarly, fig. 22 shows the spatial distribution of the pressure, density and velocity in the aluminum in the target in the two cases of impact. Again there is an excellent match in the two cases. This validates the accuracy of the mixture equation of state, described by eqn. (222) .

5.4 Identification of the Transition State and Activation Energy

In order to study the shock-related chemical reactions in an energetic mixture, it is necessary to know the activation energy required for the reaction. The activation energy is the difference in energy between the reactants and the transition state. In order to obtain the activation energy, it is therefore, necessary to identify the transition state. In the last chapter, the procedure to identify the transition state at the continuum level, for any chemical reaction was described. It is identified based on energy considerations. The transition state for the reaction between aluminum and iron-oxide is now identified in this section, using the procedure outlined earlier.

The reaction between aluminum and iron-oxide gives iron and aluminum-oxide as the products.

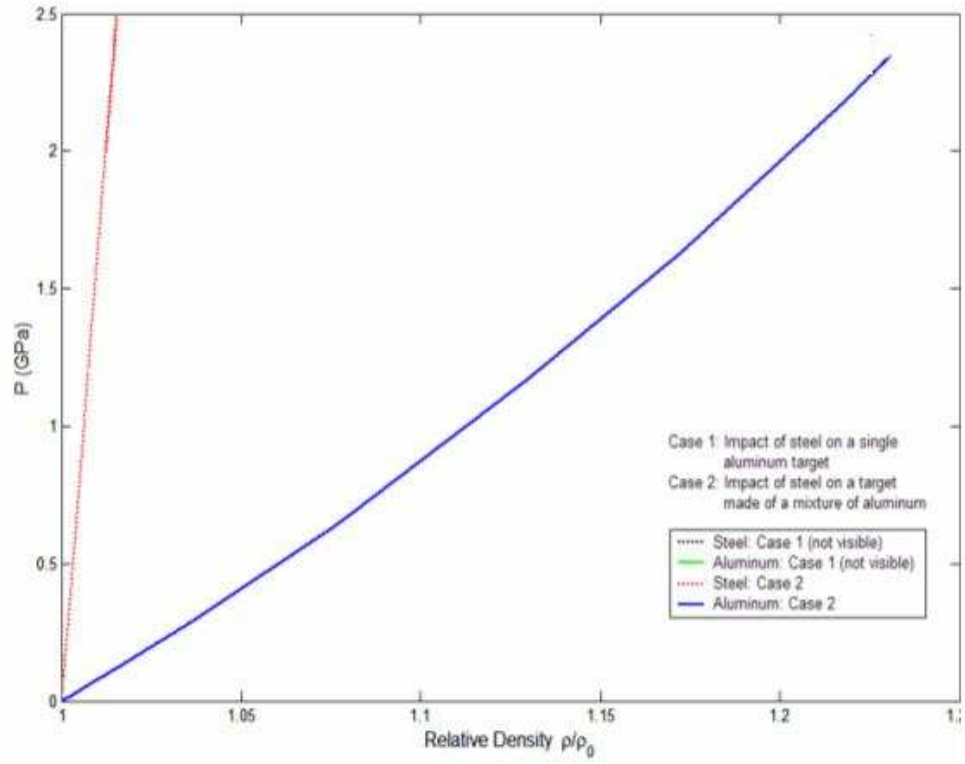

Figure 21: Hugoniots of the steel projectile and the Aluminum target. The red dotted line is the Hugoniot of the steel and the blue solid is the Hugoniot of the Aluminum for both the cases of impact 1) impact of a single aluminum target 2) impact of a mixture of aluminum

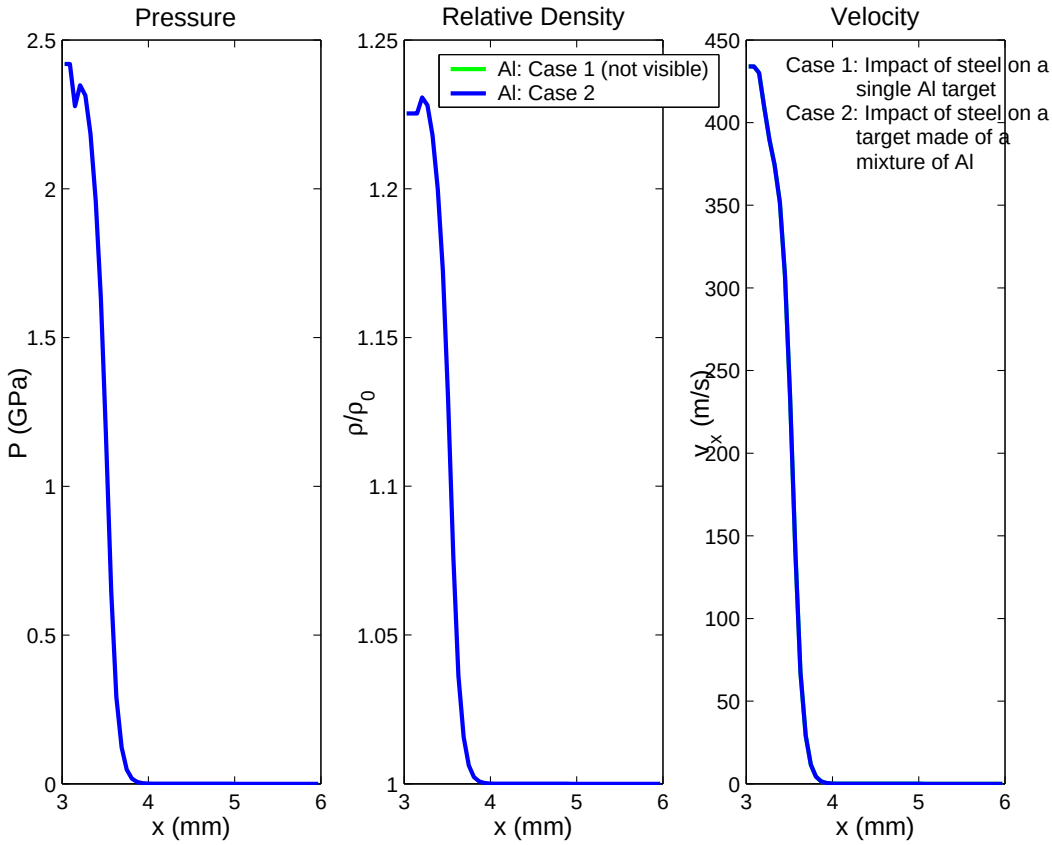

Figure 22: Spatial profiles of (a) pressure, (b) density and (c) velocity of the projectile and the target for both the cases of impact 1) impact of a single aluminum target 2) impact of a mixture of aluminum

$$2Al + Fe_2O_3 \rightarrow Al_2O_3 + 2Fe \tag{223}$$

The reaction is assumed to go to completion with no additional products formed other than iron and aluminum-oxide and solid state intermediate species. Different combinations of Al, O and Fe that can exist in the solid state, in nature, and that which can be formed by a stoichiometric reaction between Al and Fe_2O_3 were considered by looking at the database of chemical analysis [32]. The possible transition species are : (AlO,Al_2O) and (FeO, Fe). Considering combinations of these transition species, four reaction paths are possible. They are:

(a) $2Al + Fe_2O_3 \rightarrow AlO + 2FeO + Al \rightarrow Al_2O_3 + 2Fe$

(b) $2Al + Fe_2O_3 \rightarrow 2AlO + 1.3Fe + 0.3Fe_2O_3 \rightarrow Al_2O_3 + 2Fe$

(c) $2Al + Fe_2O_3 \rightarrow Al_2O + 0.6Fe + 0.7Fe_2O_3 \rightarrow Al_2O_3 + 2Fe$

(d) $2Al + Fe_2O_3 \rightarrow Al_2O + 2FeO \rightarrow Al_2O_3 + 2Fe$

The transition state has a higher energy than both the reactants and the products. It is the saddle point in the reaction path and has the highest energy. At the same time, the products that are formed are a more energetically favorable state than the reactants and thus have a lower energy state than the reactants. The Gibbs free energy for the reactants, products and the four transition states were plotted (fig.23). Two of the transition states have energies that fall between the energies of the reactants and those of the products. Hence, these two states cannot be the transition of the thermite reaction between aluminum and iron-oxide. The other two transition states $AlO + 2FeO + Al$ and $Al_2O + 0.6Fe + 0.7Fe_2O_3$ were found to satisfy the energy considerations. In

addition, it was found that $Al_2O + 0.6Fe + 0.7Fe_2O_3$ has a higher energy state than $AlO + 2FeO + Al$. Thus, in a chemical reaction, a greater input of energy would be required to reach the former transition state as opposed to the latter. Hence, the probability of the reaction proceeding through $AlO + 2FeO + Al$ is higher as the energy that is need to be supplied to attain this state is lower of the two possibilities. We are considering a single transition state and have a one-step reaction mechanism. The reaction mechanism was identified to be

$$2Al + Fe_2O_3 \rightarrow AlO + 2FeO + Al \rightarrow Al_2O_3 + 2Fe \tag{224}$$

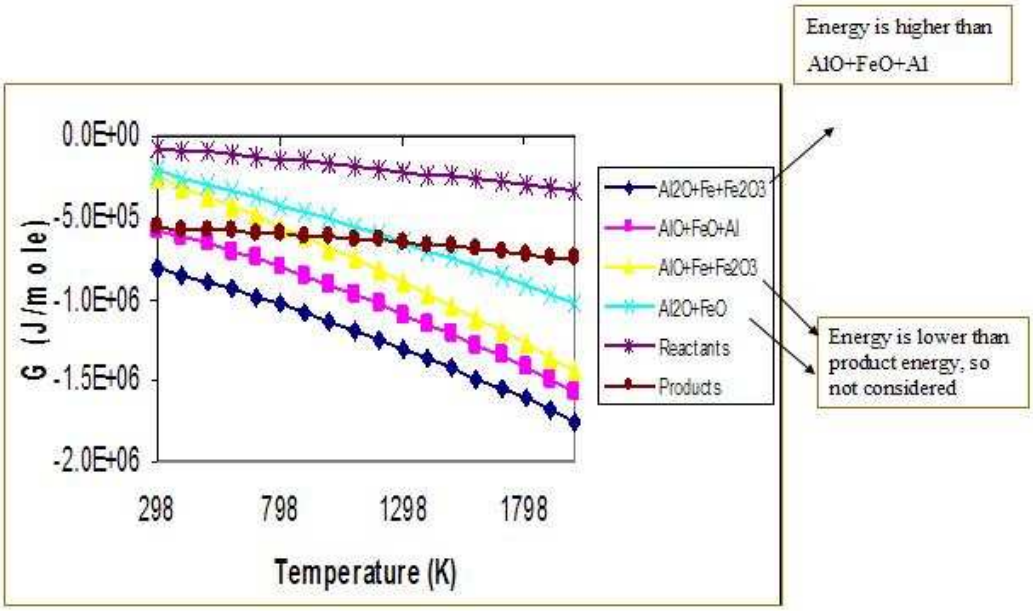

Figure 23: Plot of Gibbs Free Energy as a function of temperature for the reactants, products and each of the four possible transition states

This transition state has been experimentally verified by Peiris and Gump [42]. They studied the laser-initiated reactions in a number of thermite mixtures. In their analysis of the thermite mixture, they found evidence of the compound Al0. Fig. 24 shows the results they obtained at various intervals of time. It

also shows the time intervals when AlO was observed.

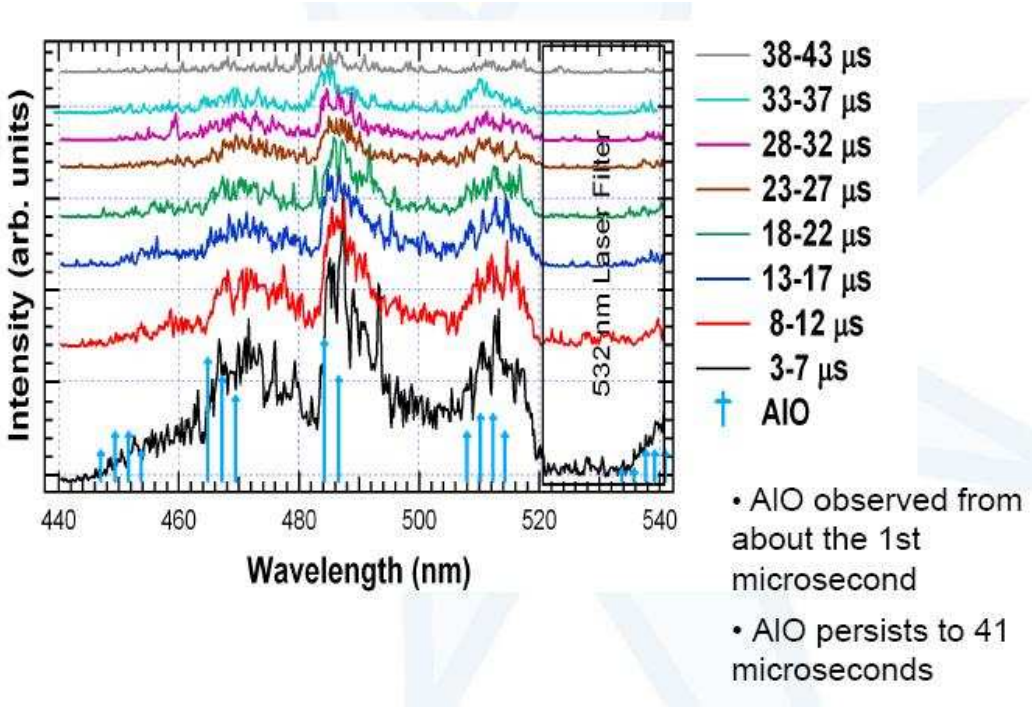

Figure 24: Emission spectrum of the laser-initiated chemical reaction between Al and Fe_2O_3 [42]

Now that the transition state has been identified, the next step is to calculate the energy difference between the transition state and the reactants. This would give us the activation energy necessary for the reaction. The activation energy for the reaction is calculated from the Gibbs free energy to reach the transition state AlO + 2FeO + Al. The energy of the reactants and the transition state change with the temperature and pressure conditions in the system and thus, the Gibbs free energy is calculated as a function of both the pressure and temperature., as shown in eqn. (225).

$$\Delta G(P',T') = \Delta H(P=P^o,298K) - T'\Delta S(P=P^o,298K) + \int_{T=298K}^{T'} \Delta C_p dT$$
$$-T' \int_{T=298K}^{T'} \frac{\Delta C_p}{T} dT + \int_{P=P^o}^{P'} (\Delta V)_{T'}\, dP \tag{225}$$

where G is the Gibbs free energy, H is the enthalpy, S is the entropy, V is the volume and C_p is the heat capacity at constant pressure and $\triangle$ indicates the difference between the transition state and the reactants. Expression for the enthalpy, entropy, volume and heat capacity at constant pressure are obtained from the database of the Facility for the Analysis of Chemical Thermodynamics [32].

5.5 One-dimensional strain problem of the thermite mixture

The transition state and the activation energy for the chemical reaction between aluminum and iron-oxide has been identified. The mixture equation of state obtained from the species equation of state has been derived. This equation has also been validated for accuracy. The next step is to analyze the shock-related chemical reactions in a mixture of *Al and* Fe_2O_3. The problem considered for the numerical simulation is that of the binary energetic material under one-dimensional strain conditions. This is shown in figure 25. The loading, condition of velocity of impact by the impact of a steel projectile or a prescribed pressure boundary condition, is applied in the x-direction. The pressure boundary condition is based on the fact that the impact of a projectile

provides a constant pressure on the target under one-dimensional strain conditions. The velocity is denoted by the symbol u. All quantities vary only in the x direction. There are no spatial gradients in the other two directions, namely, y and z directions. The stress tensor has three components (σ_{xx}, σ_{yy} *and* σ_{zz}). The one-dimensional strain is applied in the x-direction and hence, the stresses in the y and z direction are the same, i.e., $\sigma_{yy} = \sigma_{zz}$.

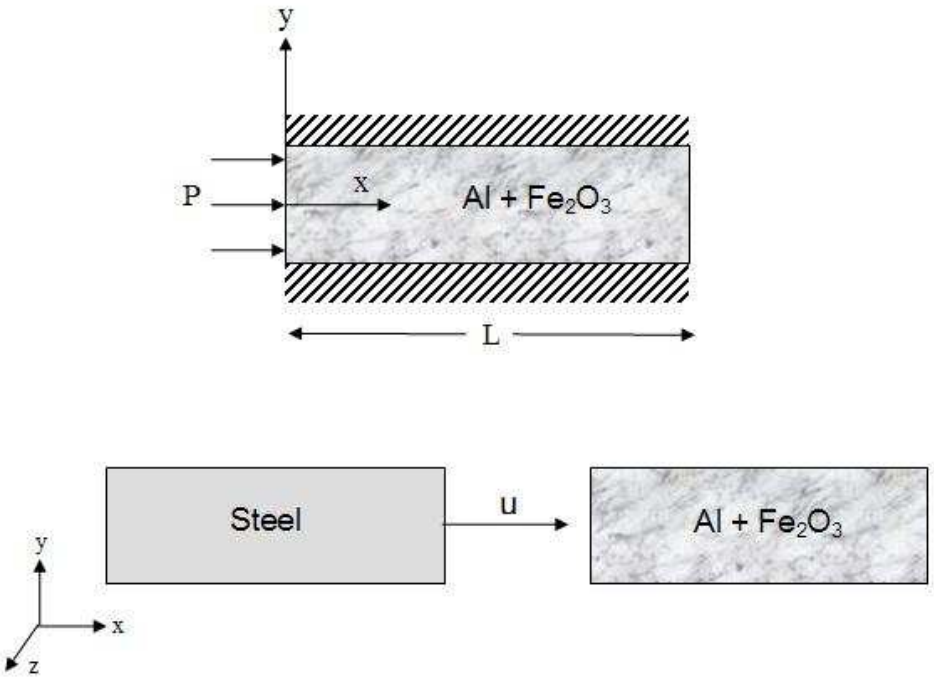

Figure 25: Impact of a steel projectile on the target made of Al and Fe_2O_3 under one-dimensional strain conditions. The top figure shows the energetic material under a pressure loading. The bottom figure shows the energetic material being impacted by a steel projectile at a particular impact velocity u.

The governing system of equations for the analysis of a one-dimensional strain problem are listed below-

$$\frac{\partial \bar{\rho}}{\partial t} + \frac{\partial \left(\bar{\rho}\bar{u}\right)}{\partial x} = 0 \tag{226}$$

$$\bar{\rho}\frac{D\bar{u}}{Dt} + \sum_s \frac{\partial}{\partial x}\left({}^s g_x {}^s u\right) = \frac{\partial \bar{\sigma}_{xx}}{\partial x} \tag{227}$$

$$\bar{\rho}\frac{D\bar{e}}{Dt} = -\frac{\partial \bar{q}_i}{\partial x_i} + \bar{\sigma}_{ji}\frac{\partial \bar{v}_i}{\partial x_j} + \theta \sum_s {}^s\varsigma \left({}^s\mu + {}^s\Delta H_f^\circ + \frac{1}{2}{}^s v.{}^s v {}^s M\right) \tag{228}$$

$$\bar{\rho}\frac{d^s c}{dt} = \Theta^s M {}^s\varsigma \tag{229}$$

$$\bar{P} = \sum_s {}^s c \left\{ \frac{{}^s\beta_{T_0}}{{}^s n}\left[\left(\frac{\bar{\rho}}{\bar{\rho}_0}\right)^{{}^s n} - 1\right] + {}^s C_v {}^s\Gamma_0 {}^s\rho_0 \left(T - T_o\right)\right\} \tag{230}$$

$$\begin{aligned} \dot{\bar{\sigma}}_{xx}^{e'} &= \tfrac{4}{3} G \tfrac{\partial v_x}{\partial x} \\ \dot{\bar{\sigma}}_{yy}^{e'} &= \dot{\bar{\sigma}}_{zz}^{e'} = -\tfrac{2}{3} G \tfrac{\partial v_x}{\partial x} \end{aligned} \tag{231}$$

$$Y = \left[Y_0\left(-\frac{P}{Y}\right)\alpha - Y_0\right] e^{-\beta(t-t_0)} + Y_0 \;\; at \; t > t_0 \tag{232}$$

$$\bar{\tau}_\sigma \dot{\bar{\sigma}}_{ii}^{ne\prime} = -\bar{\sigma}_{ii}^{ne\prime} + \bar{\eta}_i \frac{\partial \bar{u}}{\partial x} + \sum_s {}^s\eta_i^{\eta g} \frac{\partial\left({}^s c \bar{\rho}\right)}{\partial x} \tag{233}$$

$$\dot{\alpha} = -\frac{\partial J_i^\alpha}{\partial x_i} + l_\alpha \dot{\bar{P}} \tag{234}$$

$$\bar{\tau}_\alpha \dot{\bar{J}}^\alpha = -\bar{J}^\alpha + k_{\alpha p}\frac{\partial \bar{P}}{\partial x} + k_{\alpha T}\frac{\partial \bar{T}}{\partial x} + k_{\alpha\sigma}\frac{\partial\left(\bar{\sigma}_{xx} - \bar{\sigma}_{yy}\right)}{\partial x} \tag{235}$$

$$\bar{\tau}_q \dot{\bar{q}}_i = -\bar{q}_i - \bar{k}_{q_{ij}}\frac{\partial \bar{T}}{\partial x_j} \tag{236}$$

$$\bar{\tau}_\Theta \dot{\Theta} + \Theta = {}^+A \exp\left(-\frac{{}^+E}{R\bar{T}}\right) \prod_{s+} \left[{}^{s+}\chi\right]^{s+\varsigma} \tag{237}$$

There are 16 equations in 16 unknowns. The unknowns are $\rho, v_x, e_x, {}^{Al}c$, ${}^{Fe_2O_3}c$, ${}^{Fe}c$, $\bar{P}$, $\bar{\sigma}^{e'}_{xx}, \bar{\sigma}^{e'}_{yy}, \bar{\sigma}^{ne'}_{xx}, \bar{\sigma}^{ne'}_{yy}, \bar{Y}, \alpha, J^{\alpha}, \bar{q}$ *and* Θ. The individual species are taken into account in the mass conservation and energy conservation equations. The momentum equation considers only average mixture quantities. This is a first step to account for mixture constituents. Future work can include the modification of the momentum equation to include the individual species in place of the mixture. Equations (233, 235, 236 and 237) are the irreversible fluxes in this analysis. They have a relaxation time associated with the fluxes, namely the relaxation time for the porosity flux τ_{α}, relaxation time for the chemical reaction τ_{Θ}, relaxation time for the viscosity $\bar{\tau}_{\sigma}$ and relaxation time for the heat flux $\bar{\tau}_{q}$. When the relaxation times go to zero, the above extended irreversible thermodynamics equations reduce to the following equations -

$$\bar{J}^{\alpha} = k_{\alpha p}\frac{\partial \bar{P}}{\partial x} + k_{\alpha T}\frac{\partial \bar{T}}{\partial x} + k_{\alpha\sigma}\frac{\partial\left(\bar{\sigma}_{xx} - \bar{\sigma}_{yy}\right)}{\partial x} \tag{238}$$

$$\bar{\bar{q}} = -\bar{k}_{q}\frac{\partial \bar{T}}{\partial x} \tag{239}$$

$$\begin{aligned} \sigma^{ne'}_{xx} &= \eta_{x}\frac{\partial v}{\partial x} \\ \sigma^{ne'}_{yy} &= \eta_{y}\frac{\partial v}{\partial x} \end{aligned} \tag{240}$$

$$\Theta = {}^{+}A\exp\left(-\frac{{}^{+}E}{R\bar{T}}\right)\prod_{s+}\left[{}^{s+}\chi\right]^{{}^{s+}\varsigma} \tag{241}$$

One property these equations need to satisfy is that when they are reduced from their extended irreversible thermodynamics form, they have to go back

their original classical thermodynamics description. For each of the fluxes, this is described below-

- The pore collapse flux equation reduces to the following equation:

$$\bar{J}^{\alpha} = k_{\alpha p}\frac{\partial \bar{P}}{\partial x} + k_{\alpha T}\frac{\partial \bar{T}}{\partial x} + k_{\alpha \sigma}\frac{\partial\left(\bar{\sigma}_{xx} - \bar{\sigma}_{yy}\right)}{\partial x} \tag{242}$$

  where the pore collapse flux just depends on the temperature, pressure and deviatoric stress gradients. The pore collapse flux variable, in the context introduced in this thesis work, has not been used by other researchers and so the form of its equation is not compared with any previously published results.

- Without the relaxation time, the heat flux equation reduces to Fourier's law of heat conduction.

$$\bar{\bar{q}} = -\bar{k}_q\frac{\partial \bar{T}}{\partial x} \tag{243}$$

  This is the basic equation from which the extended irreversible thermodynamics form was built and thus, when reduced, it correctly reduces back to this thermodynamic form.

- The trace of a stress tensor is divided into parts. One is the hydrostatic pressure and the second is the deviatoric stress. This deviatoric stress is related to the velocity gradient through a coefficient known as the bulk viscosity in classical thermodynamics. When the equation that describes the non-equilibrium stresses is reduced from the framework of extended irreversible thermodynamics to classical thermodynamics, it should reduce to this form. On reducing eqn. (233), after neglecting the cross-flux terms, it reduces to-

$$\bar{\sigma}_{ii}^{ne'} \;=\; \bar{\eta}_i \, \frac{\partial \bar{u}}{\partial x} \tag{244}$$

which is the classical form.

- The foundation for the chemical reaction equation is the Arrhenius equation. The relaxation time was added to account for the time lag between the shock front and the occurence of a chemical reaction. Thus, when the relaxation time tends to zero, the evolution equation should revert to the original Arrhenius equation, which is what happens.

$$\Theta = {}^{+}A \exp\left(-\frac{{}^{+}E}{R\bar{T}}\right) \prod_{s+} \left[{}^{s+}\chi\right]^{{}^{s+}\varsigma} \tag{245}$$

5.6 Application of Pressure Boundary Condition on Al, Fe_2O_3 and epoxy

The composite of aluminum, iron-oxide and epoxy is analyzed using a pressure boundary condition. Aluminum and iron-oxide are in the ratio 40-60% by volume and the epoxy content is 10% by volume. The mixture is impact loaded with a compressive stress on the left end of the specimen. The pressure applied ranges from 3GPa to 24GPa. The pressure, temperature and velocity in the system due to the loading is presented in fig. 26. It is observed that as the loading increases, the pressure, temperature and velocity in the composite also consequently increases. The increase in velocity will lead to a smaller void collapse relaxation time which means the void collapse process occurs faster.

Thus, the chemical reaction initiates earlier and is sustained for a longer period of time when the pressure loading on the specimen increases.

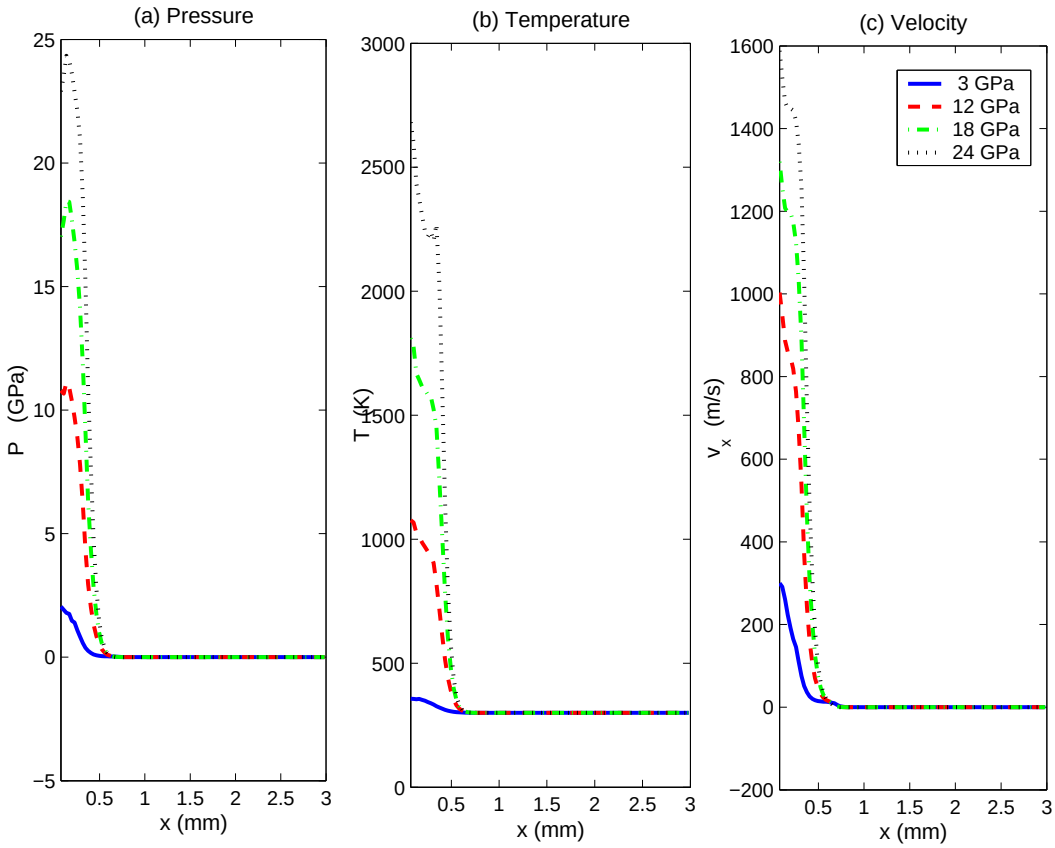

Figure 26: Effect of pressure boundary condition on the state of the composite

5.7 Impact of a steel projectile on Al, Fe_2O_3 and epoxy

Numerical analysis of the impact of the energetic material by a projectile is conducted. Aluminum and iron-oxide are in the ratio 40-60% by volume. The epoxy content and porosity are 10% and 20% by volume in all the calculations except where specified. The projectile is made of steel and strikes the material

at an impact velocity. The subsequent processes that take place in the composite due to the shock waves are studied. A complete reaction between Al and Fe_2O_3 gives a product concentration of iron of 0.4887.

5.7.1 Effect of Porosity

One of the mechanisms that leads to an increase in the temperature in the composite, taking the reactants to the transition state, is porosity. Fig. 27 is a plot of the temperature obtained in a mixture with no porosity and in mixtures with void fractions of 10%, 20% and 30%. The impact velocity is 1 km/s. The temperature is calculated at each spatial location as a function of the state of the system at each instant of time. As the shock wave passes through the mixtures, it collapses the pores. The pore collapse generates heat and leads to an increase in temperature. The plot shows that as the porosity increases, the temperature reached in the composite also increases. This increase in the temperature increases the rate of the reaction leading to a greater concentration of the product iron as seen plot (b) of the figure. As the porosity increases from 0% to 30%, temperature increases by 450K and the extent of reaction increases from 2.6% to 21%. This shows that void collapse is one of the mechanisms that adds energy to the system, taking the reactants to the transition state and that porosity enhances the reactive capabilities of the energetic materials.

Fig. 28 also shows has the same initial conditions. It compares the pressure and density in mixtures with void contents of 10%, 20% and 30%. A steel projectile impacts these materials at 1 km/s. In a porous material, work is done in collapsing the pores. Hence, as the porosity increases, more work is done in

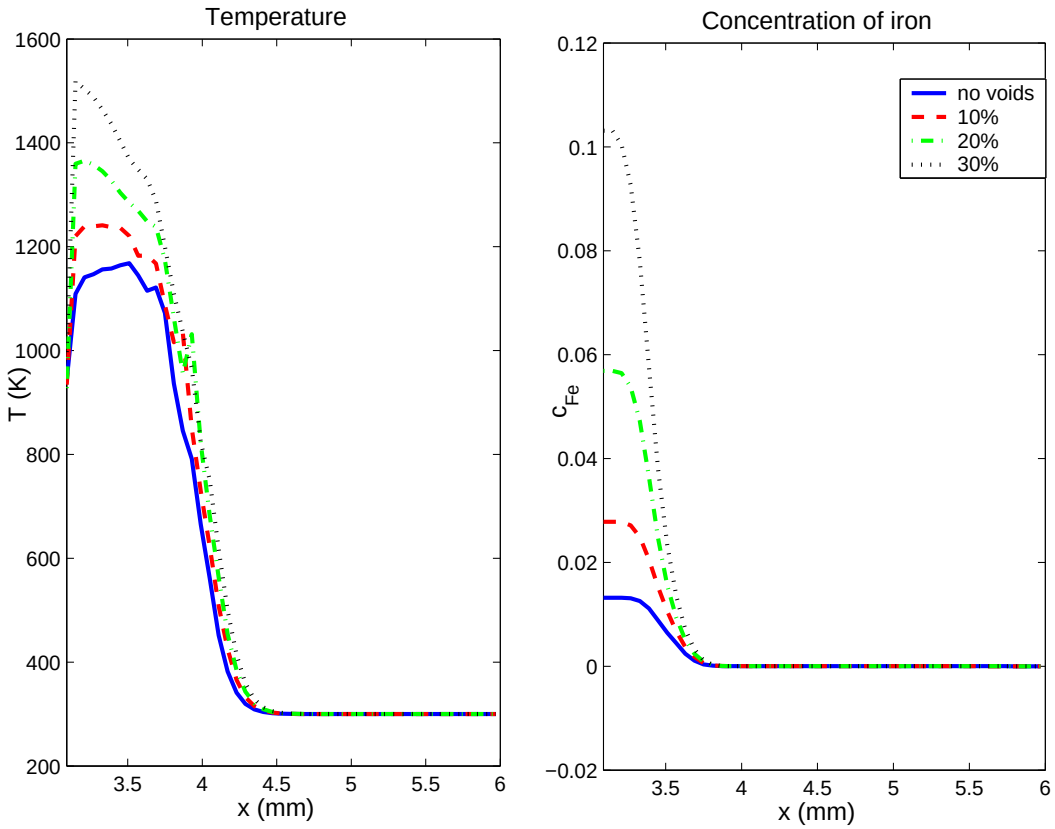

Figure 27: Effect of porosity on the temperature and extent of chemical reaction in the composite

collapsing the pores and hence the pressure generated in the mixture decreases. This can be observed from the figure.

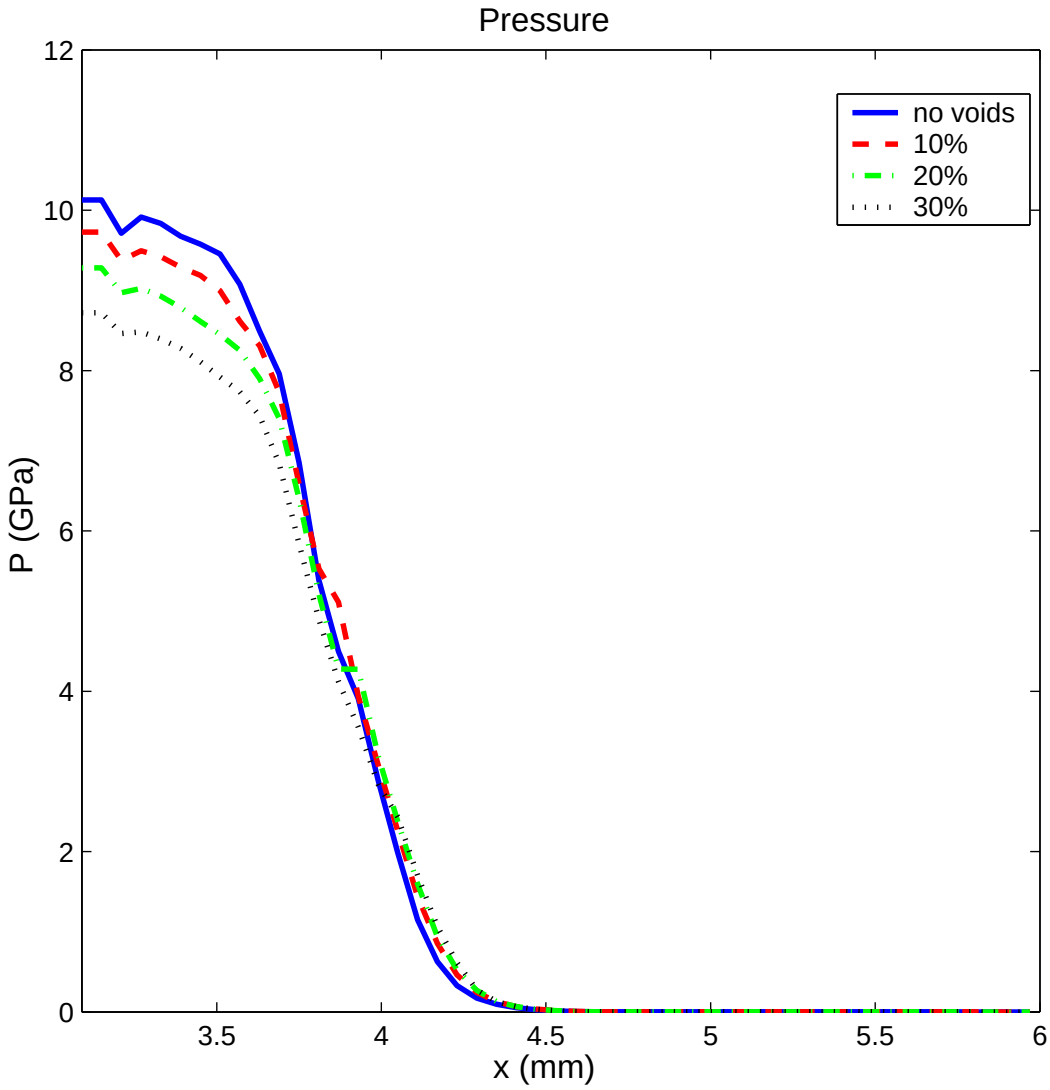

Figure 28: Effect of porosity on pressure and density of the composite

Fig. 29 gives the time profiles of pressure and temperature for the the solid mixture and the the mixture with three void contents of 10%, 20% and 30% at a constant void collapse relaxation time. Due to the different porosities, as time progresses, mixtures with greater porosities attain higher temperature. At the

same time, the pressure attained is lower since some of the mechanical work is done in collapsing the voids.

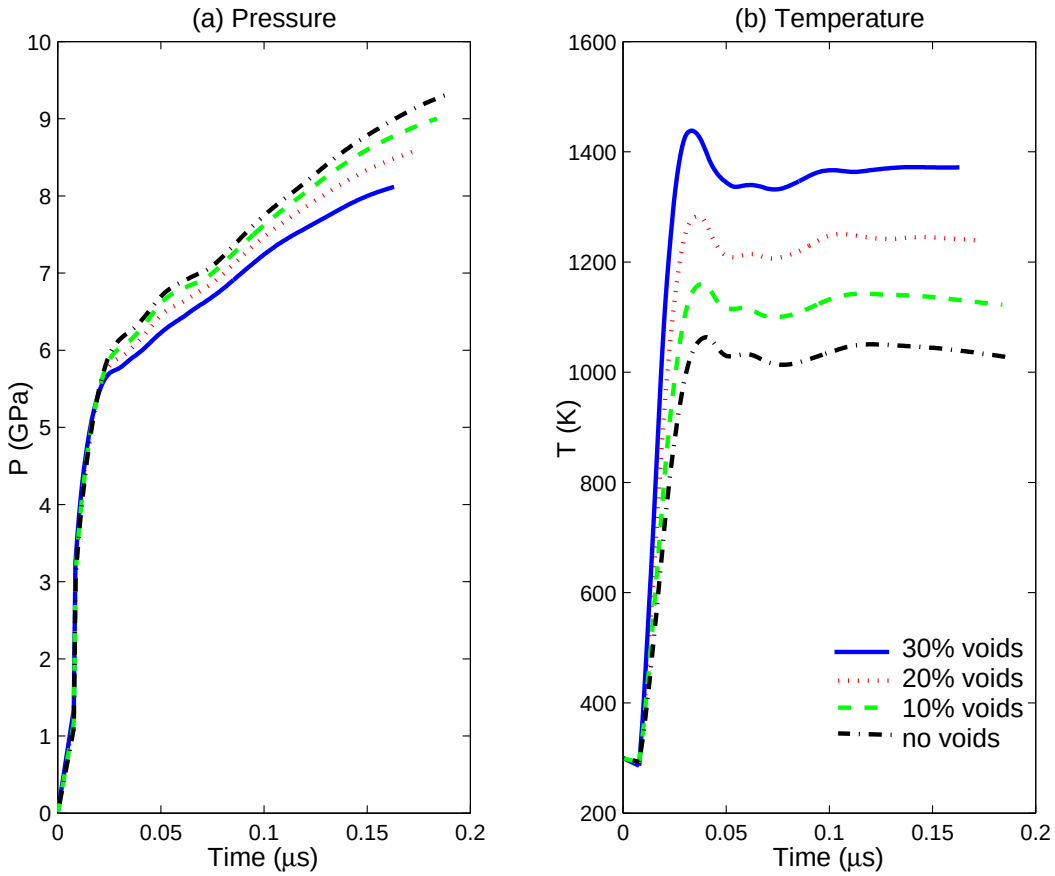

Figure 29: Time profiles of pressure and temperature for porous mixtures and a solid mixture

As time progresses and the shock wave moves into the composite specimen, more regions behind the shock wave undergo void collapse. The temperature and pressure in the system change as a result of this process. From fig. 30, the progression of the wave through the composite can be observed. It shows the pressure, temperature and porosity in the mixture at two different intervals of time - $0.08\mu s$ and $0.16\mu s$. In this numerical simulation, a steel projectile struck the composite at 500m/s. The porosity in the composite was 1.5 which

translates into a void fraction of 33%.

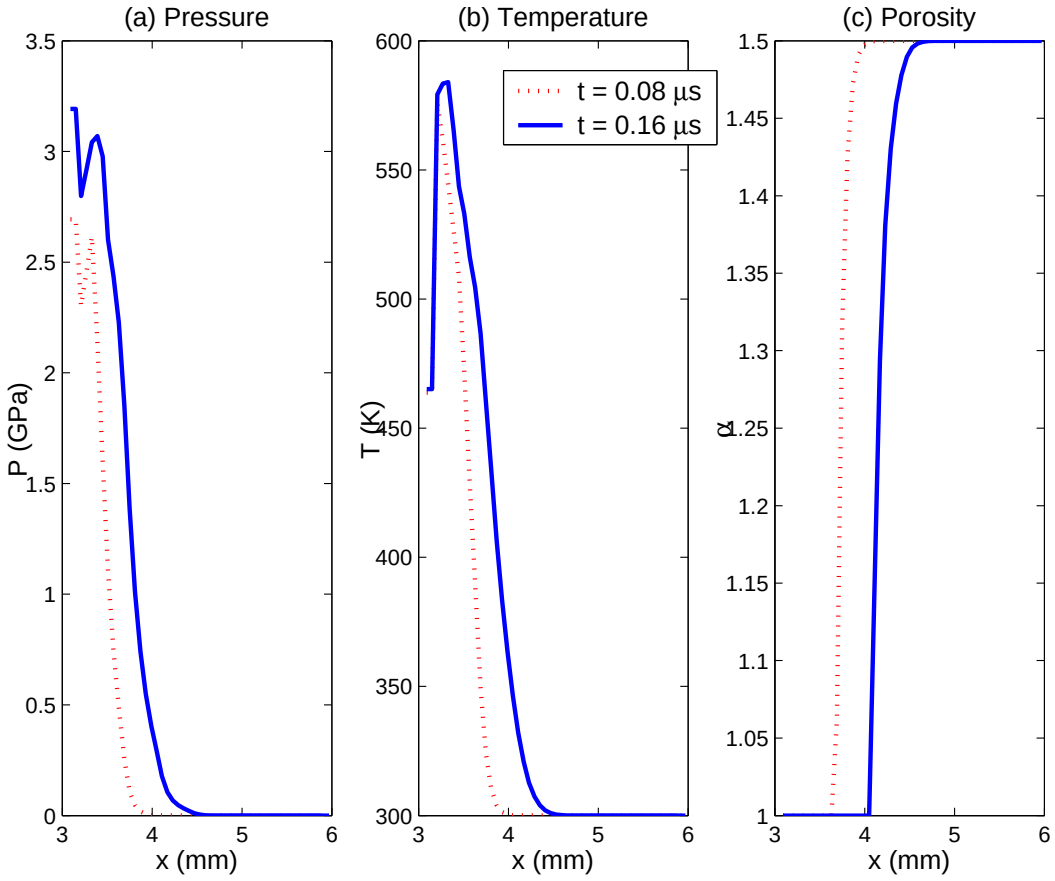

Figure 30: Pressure, temperature and porosity of the mixture at two different time intervals

5.7.2 Effect of Void Collapse Relaxation Time

The void collapse flux has a relaxation time τ_α associated with the void collapse process. This factor accounts for the delay in the pore collapse behind the shock front. If the relaxation time is longer, the time taken for the pore collapse process also becomes longer. In order to study the effect of the void collapse relaxation time, constant values of the relaxation time are selected in

this numerical simulation. Fig. 31 shows the porosity along the composite for two different values of the void collapse relaxation time - 60ns and 120ns. The initial porosity of the material was 1.25 which is a void fraction of 20%. It can be observed from the figure that as the void collapse relaxation time increases, the pore collapse region behind the shock front decreases, i.e., less of the material undergoes pore collapse. There is a delay in the pore collapse process behind the shock front.

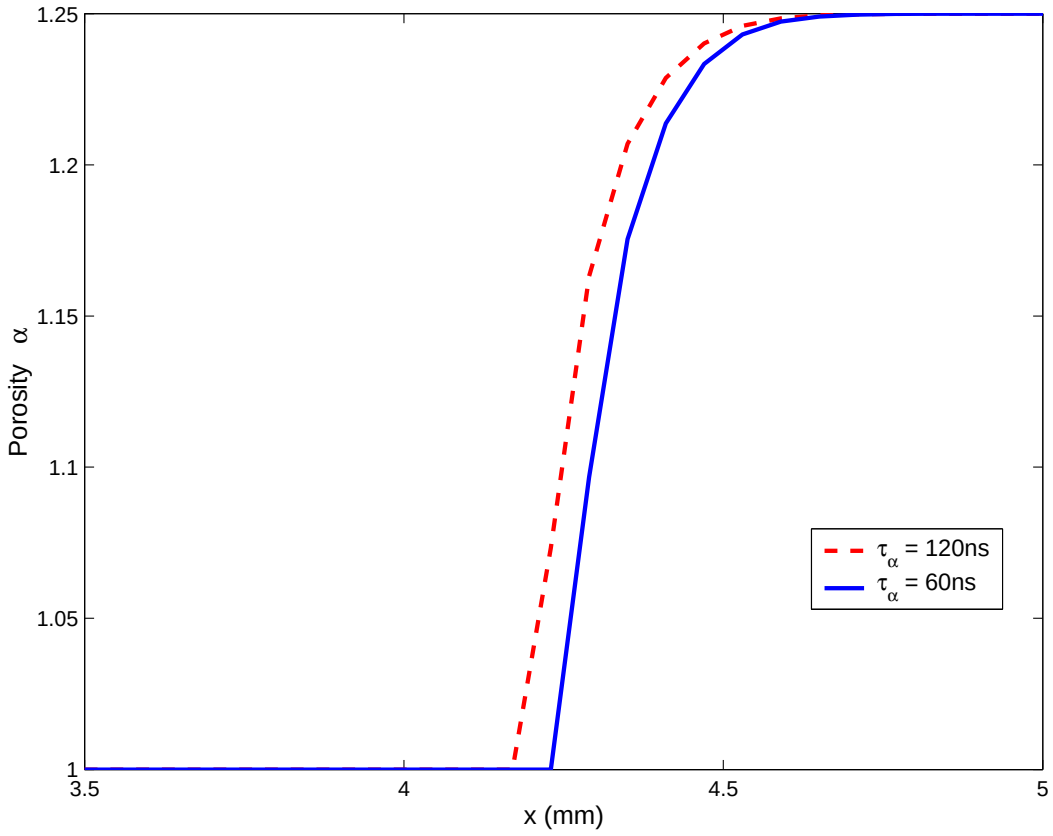

Figure 31: Effect of pore collapse relaxation time on the porosity in the composite

The relaxation time changes with the state of the system. The void collapse relaxation time is modeled as a function of the velocity. The effect of impact velocity on the void collapse relaxation time is depicted in fig. 32 for two cases -

impact velocity of 500m/s and 1000 m/s. As the velocity increases, the impact loading on the composite increases. Due to the greater loading, it takes lesser time for the voids to collapse in the composite. From plot (a), it can be observed that, along the length of the composite, the relaxation time decreases as the impact loading increases. This results in a faster collapse of voids and thus, a greater decrease in the porosity. Plot (b) gives the time profile of the relaxation time for the two impact loading cases. As time progresses, the relaxation time decreases and thus, voids begin to collapse faster. This decrease in the relaxation time is dependent on the loading, with the relaxation time decreasing at a slower rate for the lower impact velocity.

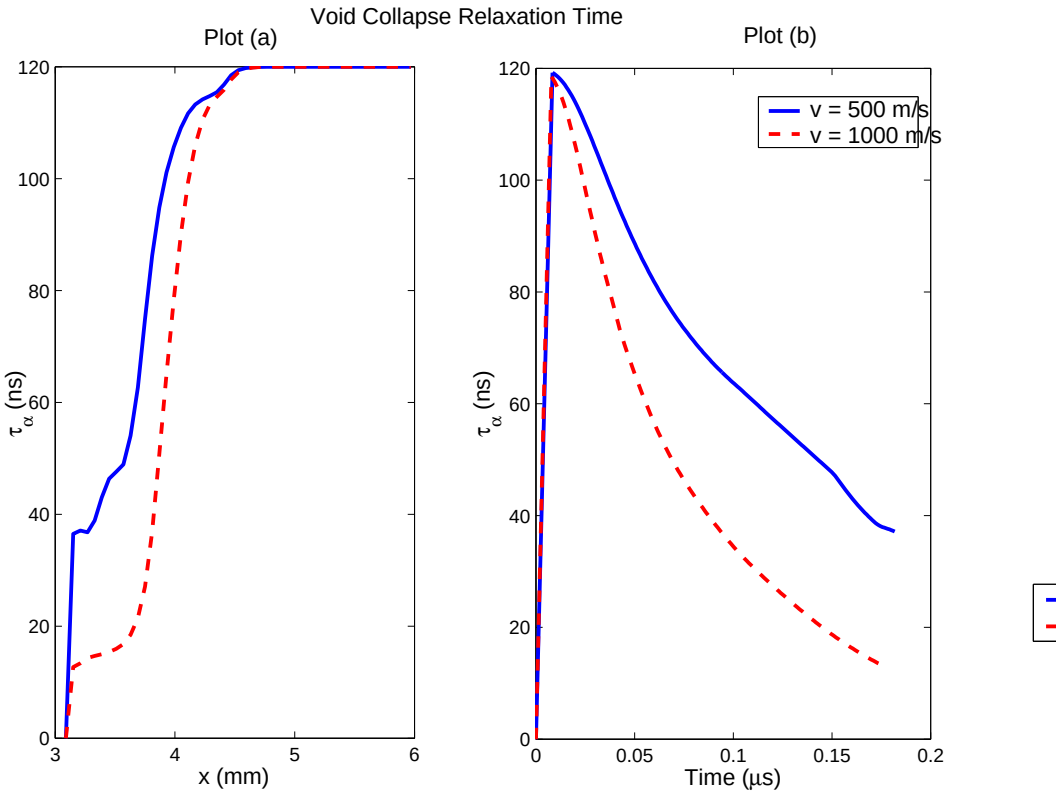

Figure 32: Effect of impact loading on the void collapse relaxation time in the composite

5.7.3 Effect of Chemical Reaction Relaxation Time

There is a time delay in the initiation of chemical reaction behind the shock front. This is described by the chemical reaction relaxation time τ_Θ. Fig. 33 depicts the concentration of the product iron for three different relaxation times - 100ns, 150ns and 200ns. As the relaxation time increases, it takes longer for the chemical reaction to initiate. So there will be lesser amount of the product concentration at any given time interval. Thus, we see that as the relaxation time goes from 100 to 150 to 200ns, the product concentration drops from 0.375 to 0.325 to 0.285.

5.7.4 Effect of loading condition on the composite

The processes that occur in the composite are a function of the loading that is applied on it. If the impact velocity on the composite is increased, the pressure, temperature and velocity reached in the system increases. These parameters affect the void collapse process and the initiation of chemical reaction. They have an influence on the relaxation times. Thus, the extent of reaction and the propagation of reaction is affected by the impact loading on the composite. This can be observed from fig. 34. This is a plot of the velocity, temperature and concentration of the product iron in the composite for three cases of impact velocity - 500m/s, 1000m/s and 1500m/s. As the impact velocity increases, the temperature in the system increases. Consequently, the reaction initiation occurs faster and thus, the product concentration at a given time is larger. The product concentration increases from 0 to 0.45 with an increase in the impact velocity. For an impact velocity of 500m/s, the temperature reached in the

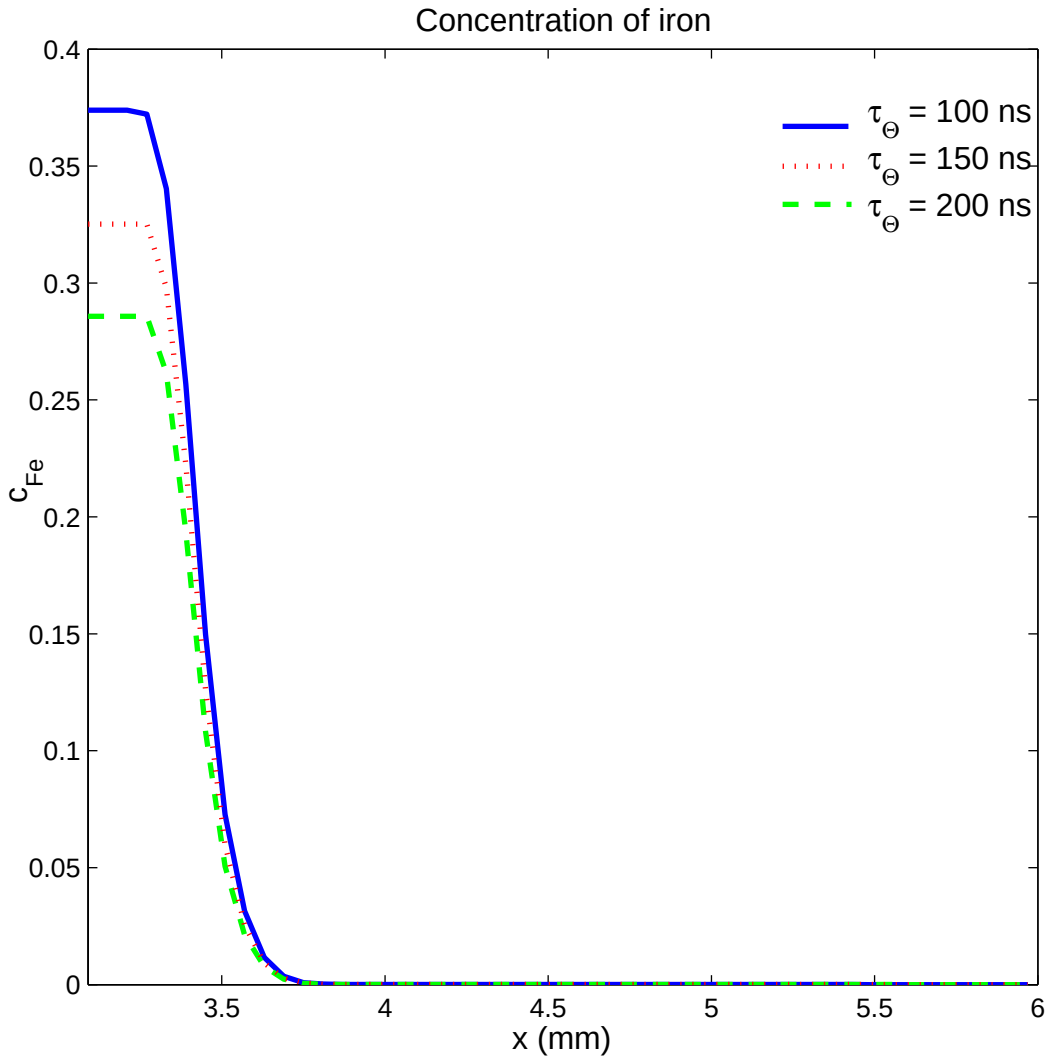

Figure 33: Effect of chemical reaction relaxation time on the reaction process

system is about 500K. This is below the reaction initiation temperature, which is 660°C or 933K. Hence, no reaction occurs in the system and the product concentration is 0.

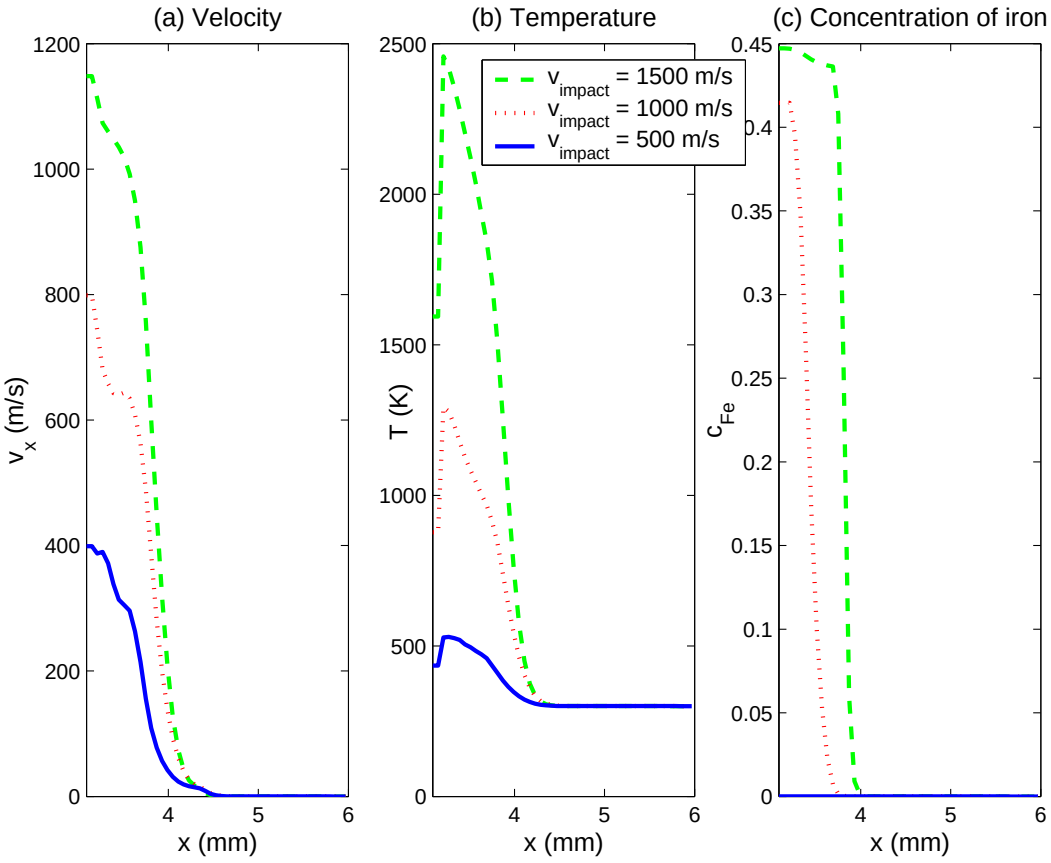

Figure 34: Effect of impact loading on the reaction process

5.7.5 Effect of Plastic Work

In addition to void collapse, the second mechanism that takes the reactants to the transition state is plastic work. Behind the shock front, there is an increase in the yield stress of the material due to the shock waves. This leads to a significant increase in the plastic work behind the shock front. This plastic

work causes an increase in the temperature. Fig. 35 depicts the temperature and concentration for various factors of yield increase, ranging from 1 to 10. It can be observed from the figure that the temperature increases in the composite due to the plastic work. And this increase in temperature causes an increase in the reaction process which is observed from the increased concentration of the product.

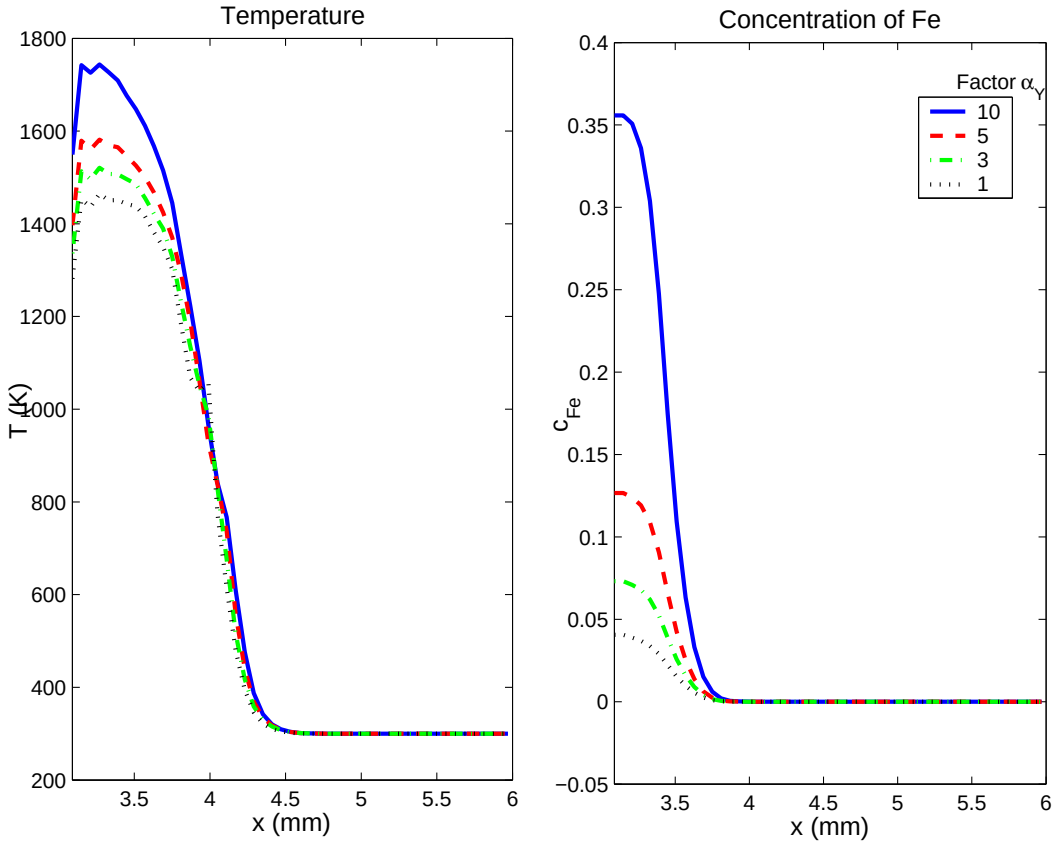

Figure 35: Effect of plastic work on the reaction process

5.7.6 Effect of Epoxy

In addition to the reactants, the reactive mixture also contains a binder - epoxy. The concentration of epoxy is varied and its effect on the concentration of the

product is studied. In this analysis, the epoxy is modeled as an inert material that does not participate in the reaction process. The epoxy content is varied from 10% to 30% and the concentration of the product iron is plotted in fig. 36. The figure shows that as the epoxy fraction in the mixture increases, it plays a inhibiting role on the reaction rate and thus, the concentration of the product decreases.

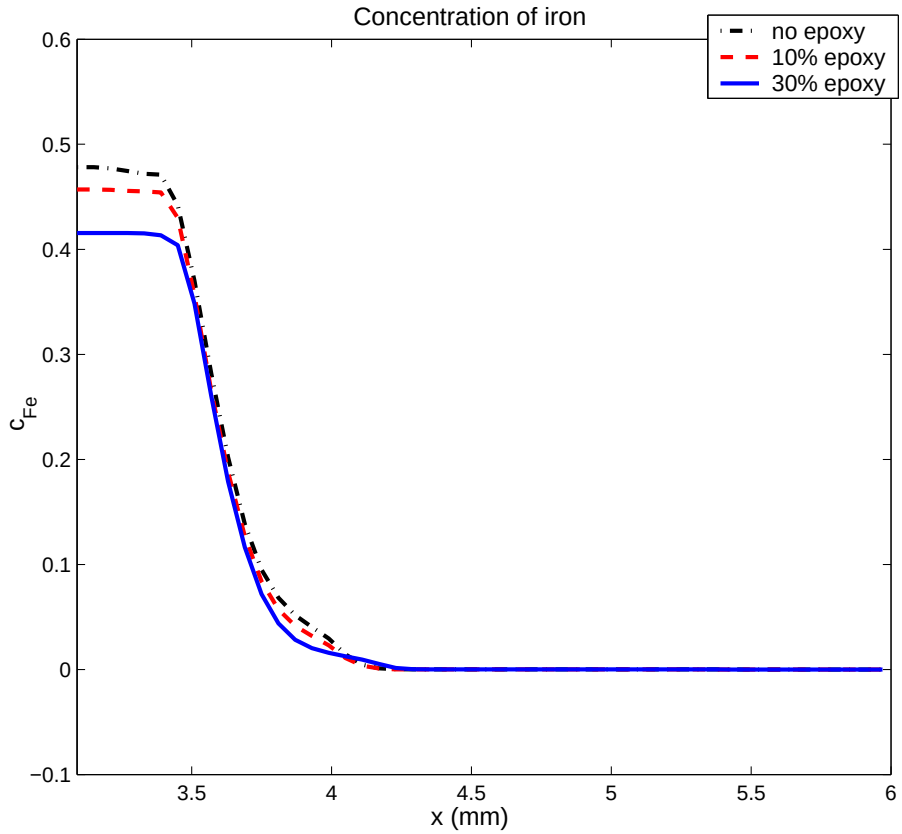

Figure 36: Effect of epoxy on the concentration of the product iron

5.7.7 Comparison with experimental results

The model that has been formulated in this work is compared with experimental results [58]. The gas-gun experiments are modeled by the impact of the steel projectile on the energetic composite. The explosive loading experiments are modeled by the application of a pressure boundary condition. Fig.

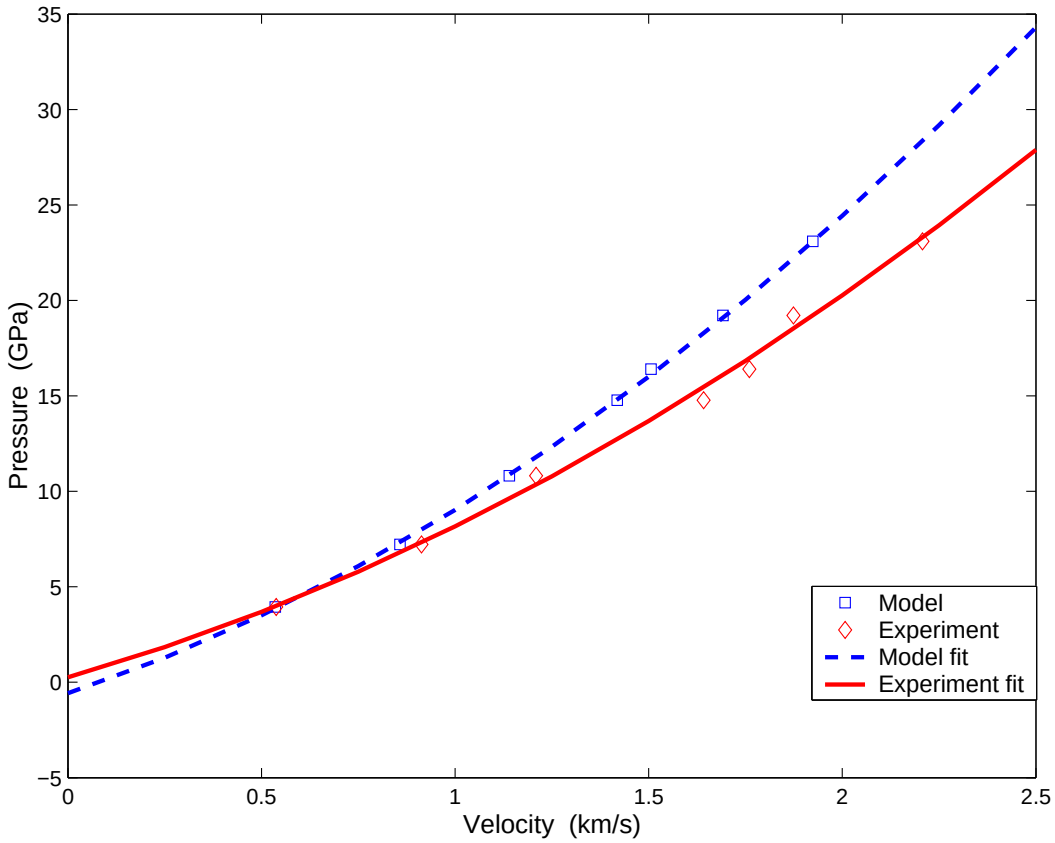

Figure 37: Comparison of experimental results with the numerical model for the explosive loading experiment

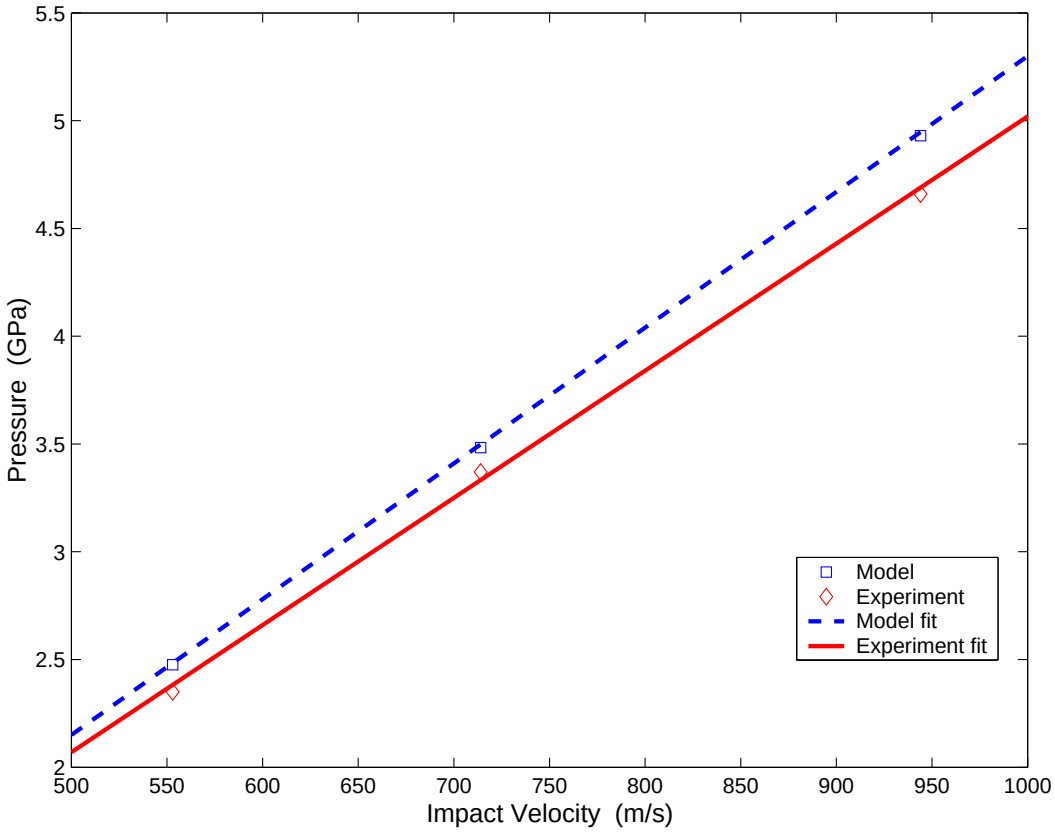

Figure 38: Comparison of experimental results with the numerical model for the Gas gun experiment

37 depicts the experimental results as well as the results obtained using the non-equilibrium thermodynamics model for the explosive loading experiments. Table 3 contains the data points used to plot the figure. The velocity obtained from the model is on the lower side of the experimental results, with the error being 0.4% at the lower end of the pressure boundary condition and 12% at the upper end of the pressure boundary condition. Fig. 38 depicts results obtained for the gas-gun tests. It is found that the pressure predicted by the model is on the higher side of the experimental results with the error being about 5%. It is observed that the model fits the data of the gas-gun experiments better than those of the explosive loading condition. This is because the explosive loading tests have been approximated by a constant pressure boundary condition. Whereas the gas-gun tests have been accurately modeled by an impact velocity condition. Table 4 provides the data used to obtain the figure.

Table 3: Experimental and model results obtained for the explosive loading of a mixture of $Al - Fe_2O_3 - epoxy$

Pressure (GPa)	Expt. particle velocity (km/s)	Model particle velocity (km/s)
3.94	0.538	0.535
7.22	0.913	0.857
10.82	1.209	1.14
14.77	1.642	1.4188
16.4	1.76	1.506
19.21	1.874	1.6919
23.09	2.207	1.924

5.7.8 Particle Size Effects

Morphology plays an important role in the initiation of chemical reactions in energetic mixtures. Fig. 39 shows optical micrographs of aluminum and iron-oxide particles taken by Ferranti and Thadhani [34]. Fig. 40 displays the SEM image of a mixture of aluminum and iron-oxide with an epoxy binder.

The particle size effects on chemical reactions is accounted in the model by including the surface energy term in the activation energy of the reaction. The particle size affects the melting temperature of the particle which in turn will affect the initiation of chemical reaction in the composite. The expression for the surface tension was derived in the last chapter (eqn. 207).

$$\gamma^{sl} = \frac{\Delta \underline{H}_m \left(T_\infty - T_r\right) r}{2 \underline{V}_s T_\infty} \tag{246}$$

In the thermite mixture of aluminum and iron-oxide, aluminum has a lower melting temperature than iron-oxide. So the surface energy term and hence the particle size effects, is calculated in terms of the melting temperature of aluminum. Figure 13 shows the variation of the melting temperature of aluminum as a function of its particle size.

Table 4: Experimental and model results obtained for the gas gun tests of a mixture of $Al - Fe_2O_3 - epoxy$

Impact Velocity (m/s)	Expt. Pressure (GPa)	Model Pressure (GPa)
553	2.35	2.4761
714	3.37	3.4829
944	4.66	4.9308

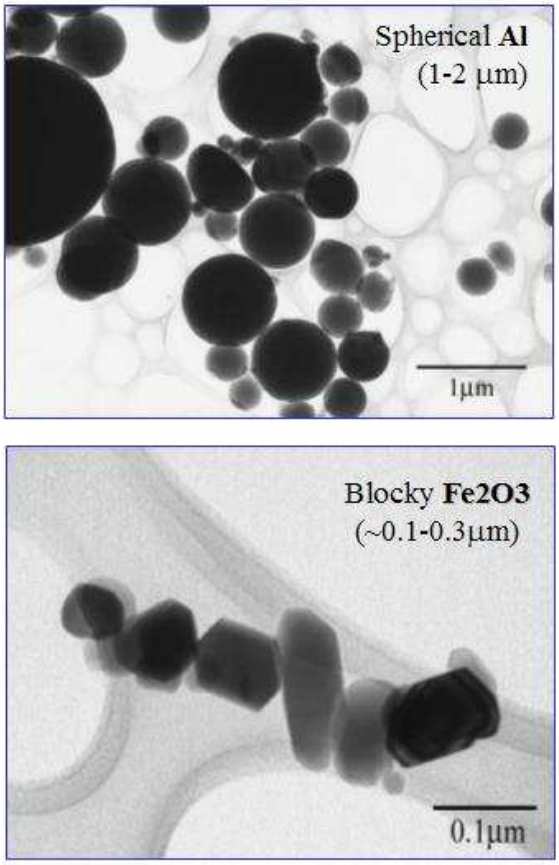

Figure 39: Optical micrographs of aluminum and iron-oxide particles. The top figure shows the Al particles and the bottom figure shows Fe_2O_3. These images are taken from Thadhani and Ferranti [34]

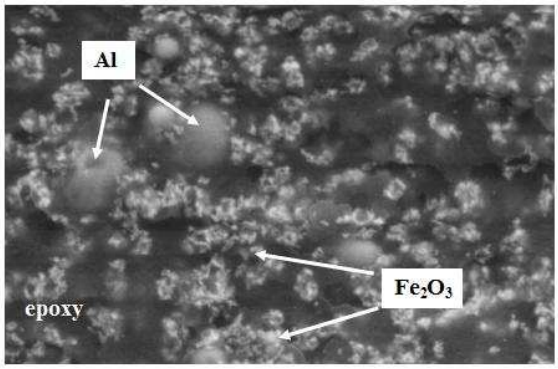

Figure 40: SEM images of a mixture of aluminum, iron-oxide and 50 % epoxy. These images are taken from Thadhani and Ferranti [34]

The surface energy is the product of the surface tension and the surface area per mole. To calculate the surface area per mole of aluminum, we need to know how many clusters of aluminum particles there are in one mole of aluminum. Assume one mole of aluminum has 'n' clusters. The clusters are assumed to be spherical in shape, with radius 'r' in SI units (meter), as depicted in fig. 41. The volume of each cluster is then equal to the volume of a sphere.

$$\text{Volume of cluster} = \frac{4}{3}\pi r^3 \times 10^{27}\, nm^3 \tag{247}$$

A volume of $1nm^3$ contains 62 atoms and one mole has Avogadro's number of atoms where Avogadro's number is equal to 6.023×10^{23} atoms. Thus, the number of clusters in one mole of aluminum is then obtained as -

$$Number\ of\ clusters = \frac{6.023 \times 10^{23}}{\frac{4}{3}\pi r^3 \times 10^{27} \times 62} \tag{248}$$

The surface area of a sphere is

$$\text{Surface area} = 4\pi r^2 (m^2) \tag{249}$$

From eqns. (248) and (249), the surface area per mole is

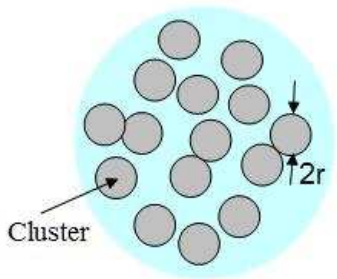

Figure 41: A mole of aluminum with clusters of radius r

$$\text{surface area per mole} = \frac{3 \times 6.023 \times 10^{-4}}{62r} \tag{250}$$

Multiplying this with eqn. (246) gives the surface energy.

$$\text{Surface energy} = \frac{1.5 \times 6.023 \times 10^{-4}}{62} \rho_{Al} \Delta H \left(1 - \frac{T_r}{T_\infty}\right) \tag{251}$$

This expression is then included in the activation energy expression. The melting temperature of bulk aluminum (T_∞) is 660°C. By varying T_r, the effect of particle sizes can be studied. Two mixtures of different particle sizes are compared. Mixture A consists of smaller particles (of the order of 30nm) and mixture B contains larger particles (approximately 170nm). Fig. 42 is a plot of the concentration of the product iron along the length of the mixture for the two cases. As the particle size decreases, the melting temperature decreases. This implies that mixture A will reach the reaction initiation temperature earlier than mixture B. Thus, at any given time, mixture A with the smaller particle sizes will have undergone reaction for a larger duration of time than mixture B. So mixture A will show more product concentration that mixture B. This can be observed from fig. 42 where mixture A is the red dotted curve and mixture B is depicted by the solid blue curve. The curve shows that the concentration of the product is greater in the case of mixture A as compared to mixture B.

Fig. 43 displays the time profiles of the product concentration for the two mixtures. Since the melting temperature is lower for mixture A as compared to mixture B, the time profile shows that the reaction initiates earlier in mixture A as compared to mixture B.

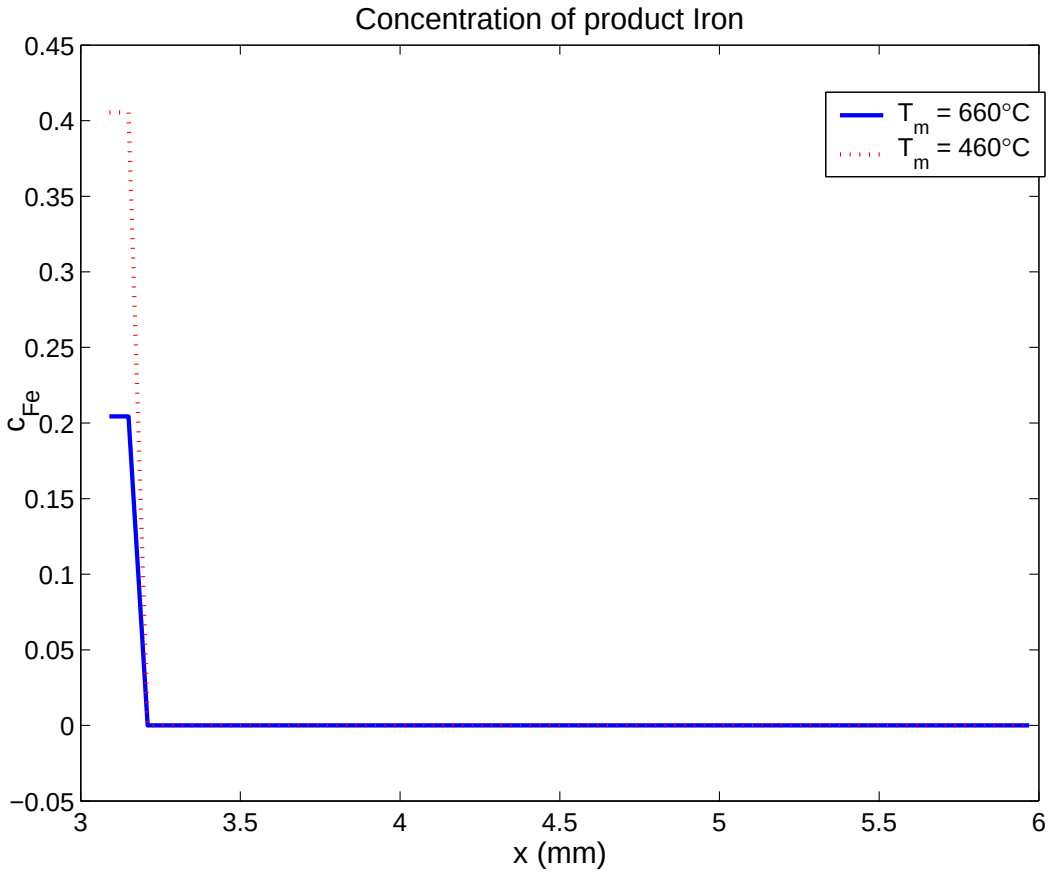

Figure 42: Effect of particle size on the reaction between the thermite mixture in terms of the concentration of the product iron (Fe)

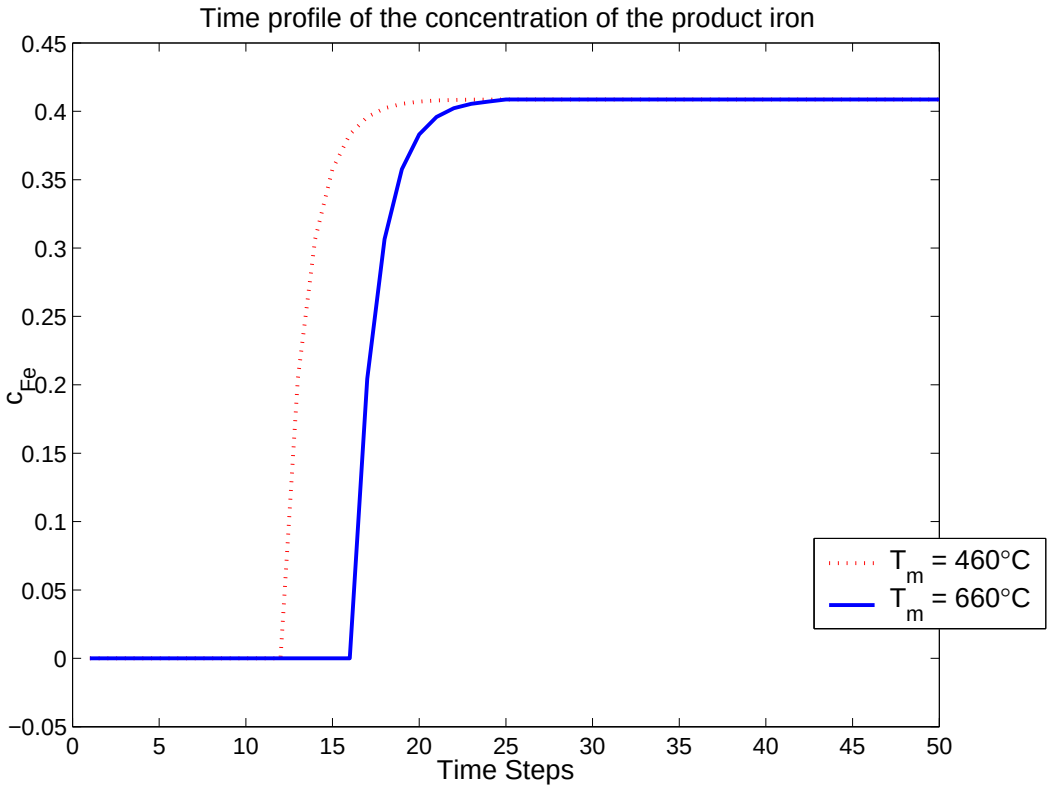

Figure 43: Time profile of the concentration of the product iron (Fe) as a function of particle size

The two mechanisms of porosity and plastic work that take the reactants to the transition state have been studied. The effect of plastic work on the increase in temperature has found to be more than the effect of porosity on the increase in temperature. While both definitely do play a role, plastic work is observed to have a more dominant effect on the initiation of chemical reaction. The loading on the composite has a definite effect on the processes that take place in the composite. The void collapse relaxation time and the chemical reaction relaxation time has been related to the state of the system and are seen to affect the void collapse process and the chemical reaction process respectively. The effect of particle size has been studied using the melting temperature of aluminum and it is observed that as the particle size decreases, the reaction initiates earlier,

leading to a greater concentration of the products of the reaction.

Chapter VI

ANALYSIS OF AN INTERMETALLIC MIXTURE OF ALUMINUM AND NICKEL

Energetic materials are classified into two broad categories. The first category includes mixtures of metals (that acts as the fuel) and metal-oxides (that acts as oxidiser). The thermite mixture of aluminum and iron-oxide analyzed using non-equilibrium thermodynamics in the previous chapter falls under this group. The second category are mixtures of two metals or intermetallic mixtures. Examples include Ni-Al, Ti-Si, Mo-Si etc. The mixtures also undergo exothermic reactions and release large amounts of energy.

The model that has been developed in this research can be applied to any combination of energetic materials. It is not limited to the thermite mixture of aluminum and iron-oxide. In this chapter, the model is applied to an intermetallic mixture of nickel and aluminum under one-dimensional strain conditions. Of the two components of the mixture, aluminum has the lower melting temperature and hence the chemical reaction initiation criteria is based on the melting temperature of aluminum.

6.1 Identification of Transition State

The reaction between nickel and aluminum can give rise to different reaction products depending on the starting composition and structure of the mixture [13][14][27][76][101][114] [140]. We consider two possibilities

$$Ni + 3Al \rightarrow NiAl_3 \tag{252}$$

$$3Ni + Al \rightarrow Ni_3Al \tag{253}$$

The transition state of both these reactions needs to be identified. The procedure followed is similar to that applied for the thermite mixture. Various compounds that are formed from a stoichiometric composition of nickel and aluminum are identified from the chemical database [32]. The Gibbs free energy of these compounds is then compared. The energy of the transition state must be greater than the energy of both the reactants and products. At the same time, given two possibilities, the one with the lower energy is selected as the transition state. This is because this state would require lesser supply of energy for the reaction to occur and hence has a higher probability of being the transition state of the reaction. Using these guidelines, the possible transition species for eqn. (252) were identified as Ni(s), Ni(l), Al(s), Al(l), NiAl(s), NiAl(l), $Ni_3Al(s)$ and $Ni_3Al(l)$ where 's' refers to the solid state and 'l' the liquid state. The possible reaction path using these transition species are -

(a) $Ni + 3Al \rightarrow Ni(l) + 3Al(l) \rightarrow NiAl_3$

(b) $Ni + 3Al \rightarrow Ni(l) + 3Al(s) \rightarrow NiAl_3$

(c) $Ni + 3Al \rightarrow Ni(s) + 3Al(l) \rightarrow NiAl_3$

(d) $Ni + 3Al \rightarrow NiAl(s) + 2Al(s) \rightarrow NiAl_3$

(e) $Ni + 3Al \rightarrow NiAl(s) + 2Al(l) \rightarrow NiAl_3$

(f) $Ni + 3Al \rightarrow NiAl(l) + 2Al(s) \rightarrow NiAl_3$

(g) $Ni + 3Al \rightarrow NiAl(l) + 2Al(l) \rightarrow NiAl_3$

(h) $Ni + 3Al \rightarrow 0.33Ni_3Al(s) + 2.67Al(l) \rightarrow NiAl_3$

(i) $Ni + 3Al \rightarrow 0.33Ni_3Al(s) + 2.67Al(s) \rightarrow NiAl_3$

(j) $Ni + 3Al \rightarrow 0.33Ni_3Al(l) + 2.67Al(s) \rightarrow NiAl_3$

(k) $Ni + 3Al \rightarrow 0.33Ni_3Al(l) + 2.67Al(l) \rightarrow NiAl_3$

The Gibbs free energy for each of these transition states is plotted in fig. 44. Based on the energy considerations mentioned above, the transition state was identified to be Ni(s)+Al(l), as it had energy greater than both the reactants and products and had the lowest energy among all the viable possibilities.

Similarly, the transition species for eqn. (253) were identified to be Ni(s), Ni(l), Al(s), Al(l), NiAl(s), NiAl(l), NiAl3(s) and NiAl3(l) [32]. The reaction path for these transition species are -

(a) $3Ni + Al \rightarrow 3Ni(l) + Al(l) \rightarrow Ni_3Al$

(b) $3Ni + Al \rightarrow 3Ni(l) + Al(s) \rightarrow Ni_3Al$

(c) $3Ni + Al \rightarrow 3Ni(s) + Al(l) \rightarrow Ni_3Al$

(d) $3Ni + Al \rightarrow NiAl(s) + 2Ni(s) \rightarrow Ni_3Al$

(e) $3Ni + Al \rightarrow NiAl(s) + 2Ni(l) \rightarrow Ni_3Al$

(f) $3Ni + Al \rightarrow NiAl(l) + 2Ni(s) \rightarrow Ni_3Al$

(g) $3Ni + Al \rightarrow NiAl(l) + 2Ni(l) \rightarrow Ni_3Al$

(h) $3Ni + Al \rightarrow 0.33NiAl_3(s) + 2.67Al(l) \rightarrow Ni_3Al$

(i) $3Ni + Al \rightarrow 0.33NiAl_3(s) + 2.67Al(s) \rightarrow Ni_3Al$

(j) $3Ni + Al \rightarrow 0.33NiAl_3(l) + 2.67Al(s) \rightarrow Ni_3Al$

(k) $3Ni + Al \rightarrow 0.33NiAl_3(l) + 2.67Al(l) \rightarrow Ni_3Al$

Fig. 45 depicts the Gibbs free energy of the transition states along with the reactants and product. Comparison of the energies determines the transition state for the reaction to be be Ni(l)+Al(l).

For the purposes of illustrating the application of the non-equilibrium thermodynamics continuum model on a mixture other than the thermite mixture of aluminum and iron-oxide, the reaction $Ni + 3Al \rightarrow NiAl_3$ is considered. Nickel

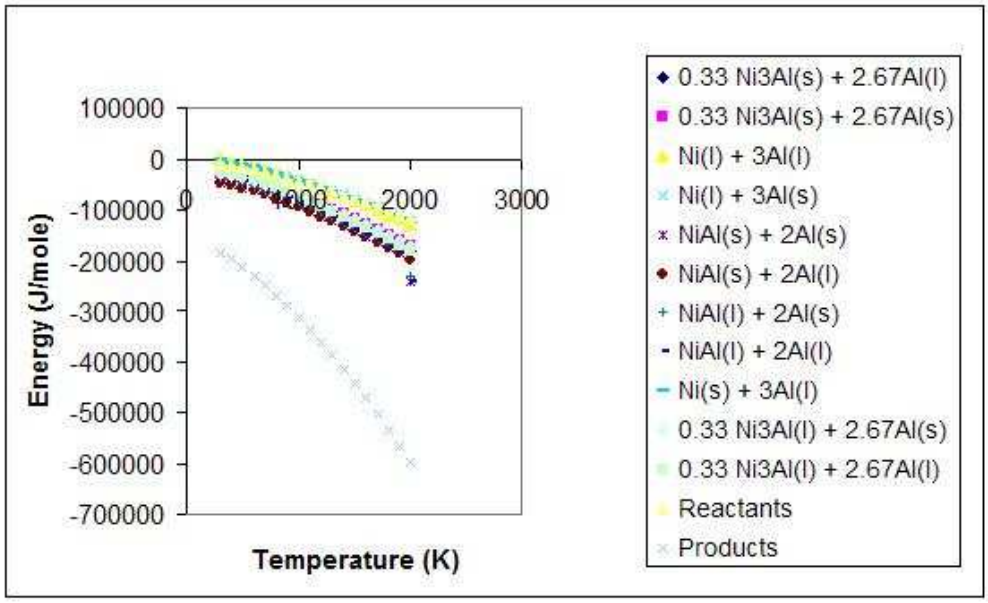

Figure 44: Plot of Gibbs Free Energy as a function of temperature for the reactants, products and the possible transition states for the reaction $Ni + 3Al \rightarrow NiAl_3$

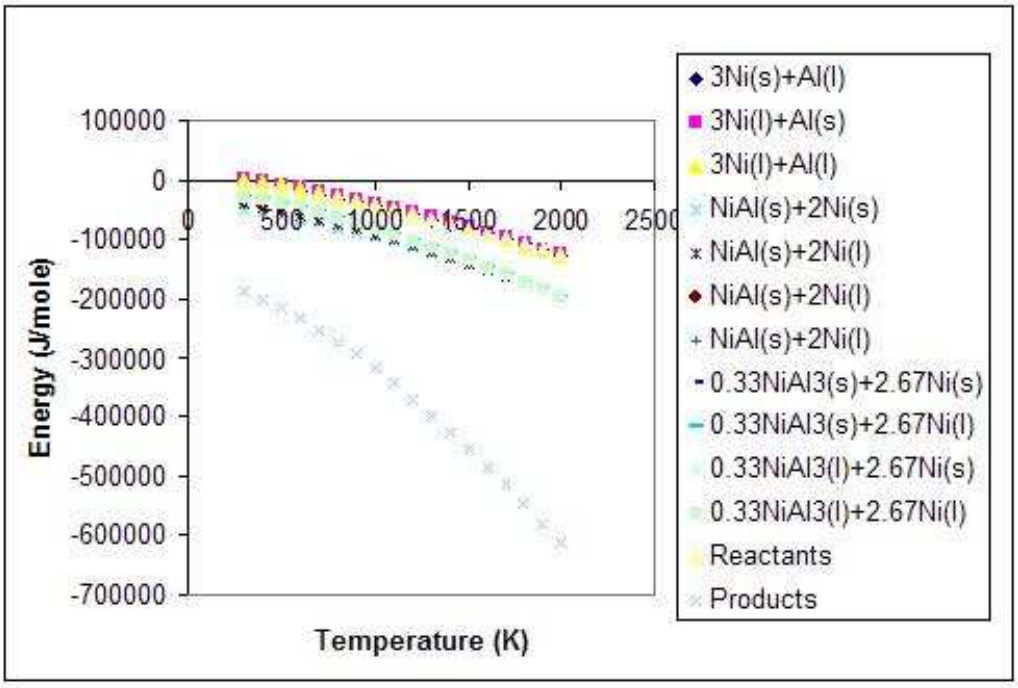

Figure 45: Plot of Gibbs Free Energy as a function of temperature for the reactants, products and the possible transition states for the reaction $3Ni + Al \rightarrow Ni_3Al$

and aluminum are in the ratio 30-70% by volume. Epoxy occupies 10% of the volume. Some results obtained by the impact of a steel projectile on the energetic composite is presented.

6.2 Effect of Impact Loading Condition

Fig. 46 depicts the temperature and concentration of $NiAl_3$ for different impact velocities. As the impact velocity increases from 500m/s to 1500m/s, the temperature in the system increases. Consequently, the reaction rate increases and the product concentration increases. It can also be observed from the figure that once the reaction goes to completion at a particular region, a further increase in temperature does not have any more effect on the reaction process. As the impact velocity increases, more regions of the specimen has a temperature beyond the reaction initiation temperature and hence the reaction process is seen to move spatially into the specimen.

6.3 Effect of Porosity

Fig. 47 shows the effect that porosity has on the reaction process. The void collapse process is one of the mechanisms by which the temperature in the system is increased to take the reactants to the transition state. As the porosity in the system increases from 0 to 30%, the temperature in the system increases and consequently, the reaction rate increases and thus, the product concentration increases.

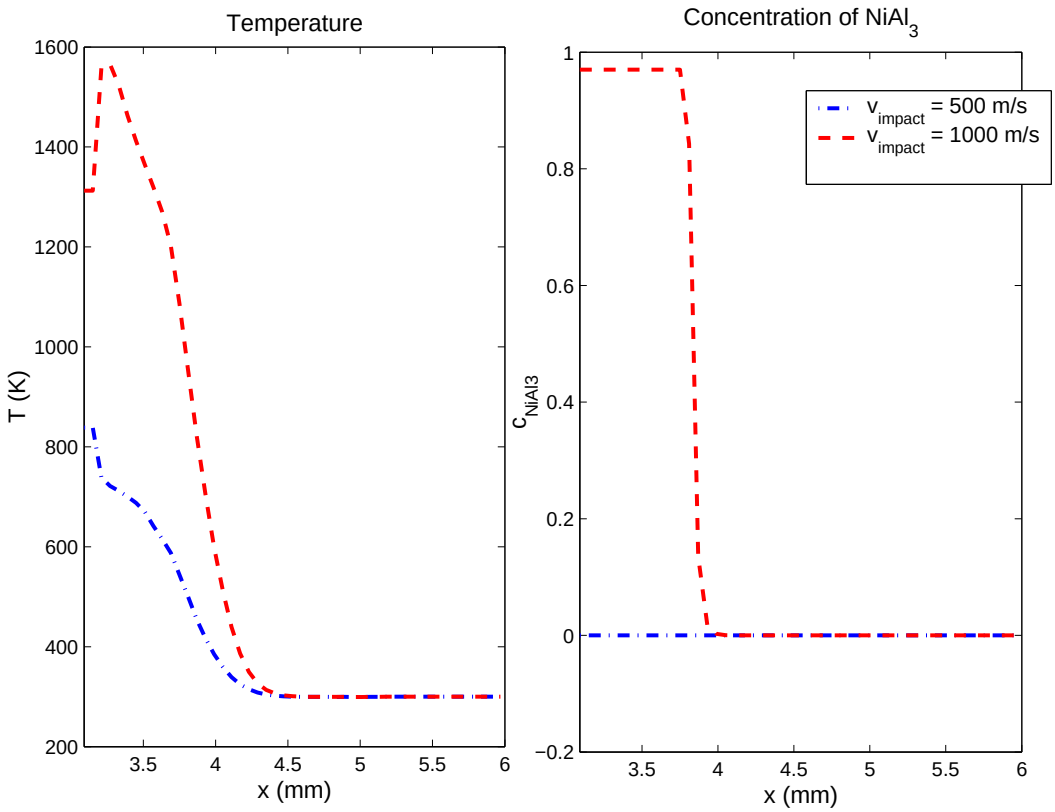

Figure 46: Effect of impact velocity on the reaction process between nickel and aluminum

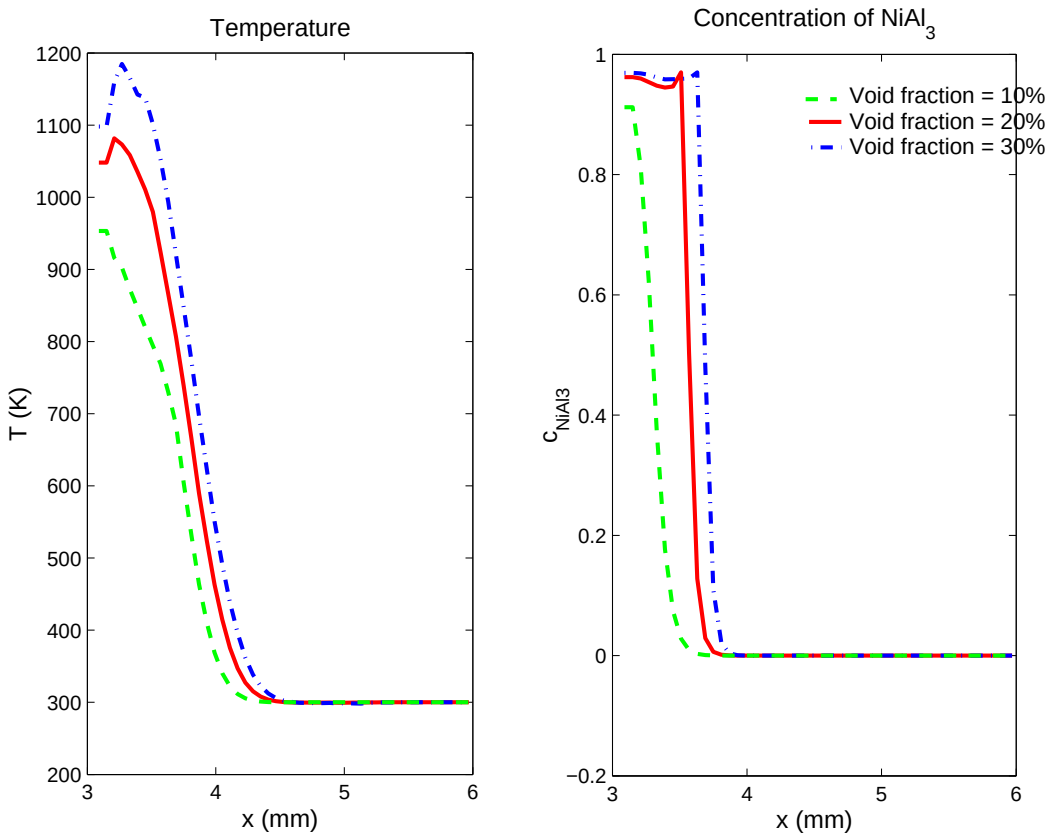

Figure 47: Effect of porosity on the reaction process between nickel and aluminum

This chapter provides a brief analysis of the intermetallic mixture of nickel and aluminum. The transition state for two possible reaction products ($NiAl_3$ and Ni_3Al) has been identified. For the purposes of numerical calculations, the reaction $Ni + 3Al \rightarrow NiAl_3$ has been considered. A steel projectile impacts the nickel-aluminum-epoxy composite. The effect of impact velocity and porosity on the reaction process has been modeled. In the next chapter, the intermetallic mixture is analyzed using molecular dynamics.

Chapter VII

ANALYSIS OF AN INTERMETALLIC MIXTURE USING MOLECULAR DYNAMICS

The intermetallic mixture of nickel (Ni) and aluminum (Al) is also studied using molecular dynamics. Experimental results indicate various possibilities for the products between these two materials depending on the material composition and structure and the initial loading conditions [13][14][27][76][101][114] [140]. Martin and Thadhani studied the Ni-Al intermetallic mixture with a polymer binder [76]. They performed differential thermal analysis of the samples of nickel and aluminum and observed thermally initiated reactions in the intermetallic mixture. A DTA analysis of such a mixture shows a reaction exotherm at the melting temperature of aluminum. This is depicted in fig. 48. This seems to indicate that Ni and Al react on heating when the melting temperature of aluminum is reached.

In this work, the chemical reaction between nickel and aluminum is modeled using ab-initio molecular dynamics. The basic idea is to observe the experimental results obtained in ref. [76] from first principles. Modeling a system at this level can also give us more information about the reaction mechanism. A detailed study of the chemical reaction can reveal the path taken during the

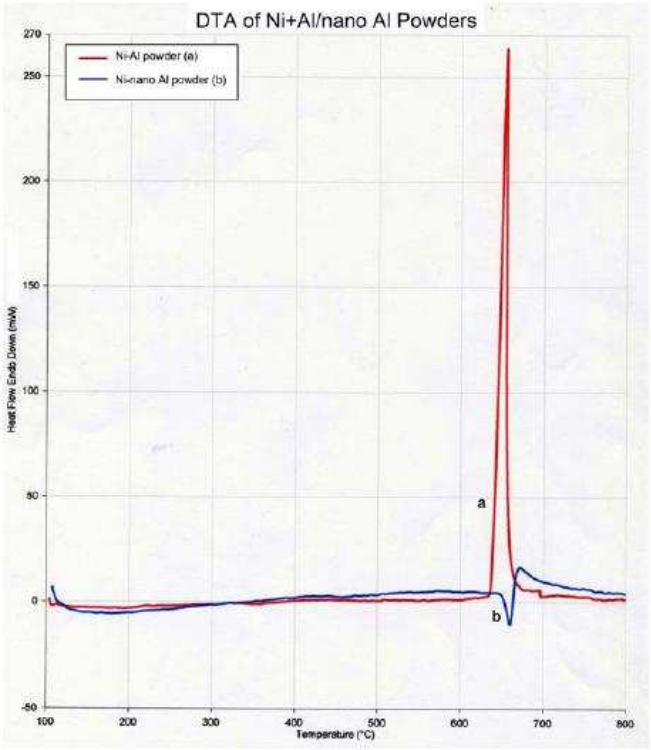

Figure 48: Differential thermial analysis of a mixture of nickel and aluminum showing a reaction exotherm at the melting temperature of aluminum. This plot is taken from the work of Martin and Thadhani [76]

reaction process. It can give us information about the intermediate states as well as the final products that are formed for different cases. Analysis of the conditions at which bonding begins to take place between the reactants to form the products can give us information about the reaction initiation criteria. It is thus, highly useful to model chemical reactions at the quantum level.

The molecular dynamics simulations are run at constant temperature conditions. The temperature is fixed at the melting temperature of aluminum at 660°C. This would enable us to see if nickel and aluminum show any propensity to reaction on thermal initiation. The procedure to control the temperature and fix its value using a dynamic friction mechanism was formulated by Nosé and Hoover [52]. A modification of this method is the Nosé-Hoover-chain thermostat where the temperature is controlled repetitively. The original thermostat temperature is again controlled, this new thermostat is then controlled and so on. This method is much more efficient in controlling and fixing the temperature [52]. The equations of motion for this process are -

$$M_i \ddot{R}_i = -\nabla_i E^{KS} - M_i \dot{\xi}_i \dot{R}_i \tag{254}$$

$$Q_1^n \ddot{\xi}_1 = \sum_i M_i \dot{R}_i^2 - g k_B T - Q_1^n \dot{\xi}_1 \dot{\xi}_2 \tag{255}$$

$$Q_k^n \ddot{\xi}_k = Q_{k-1}^n \dot{\xi}_{k-1}^2 - k_B T - Q_k^n \dot{\xi}_k \dot{\xi}_{k+1} (1 - \delta_{kK}) \;\; where \; k = 2, 3, ..., K \tag{256}$$

T is the temperature that is being controlled, $\dot{\xi}_1$ is the dynamic friction coefficient and g is the number of degrees of freedom to which the thermostat chain is coupled. These equations of motion require a very accurate integration scheme.

One such scheme used in molecular dynamics packages is a high order Suzuki Yoshida integrator.

In 1848, Auguste Bravais was the first scientist to correctly identify all the possible arrangements of a crystal lattice. A crystal lattice has an ordered periodic arrangement of the atoms as opposed to an amorphous solid. There are seven crystal systems-

- Triclinic
- Monoclinic
- Orthorhombic
- Tetragonal
- Rhombohedral
- Hexagonal
- Cubic

And these seven crystal systems give rise to 14 possible arrangements of atoms as depicted in fig. 49. Aluminum and nickel are in the face-centered cubic (fcc) arrangement. A lattice is defined by three translation vectors a, b and c such that the atomic arrangement looks the same from any point r as when viewed by another point $\acute{r}$ defined as

$$\vec{r'} = \vec{r} + u\vec{a} + v\vec{b} + w\vec{c} \tag{257}$$

where u, v and w are arbitrary integers. If a suitable choice of u,v and w can be made such that the above equation is always satisfied for any two points, then the lattice and the translation vectors are said to be primitive. This implies

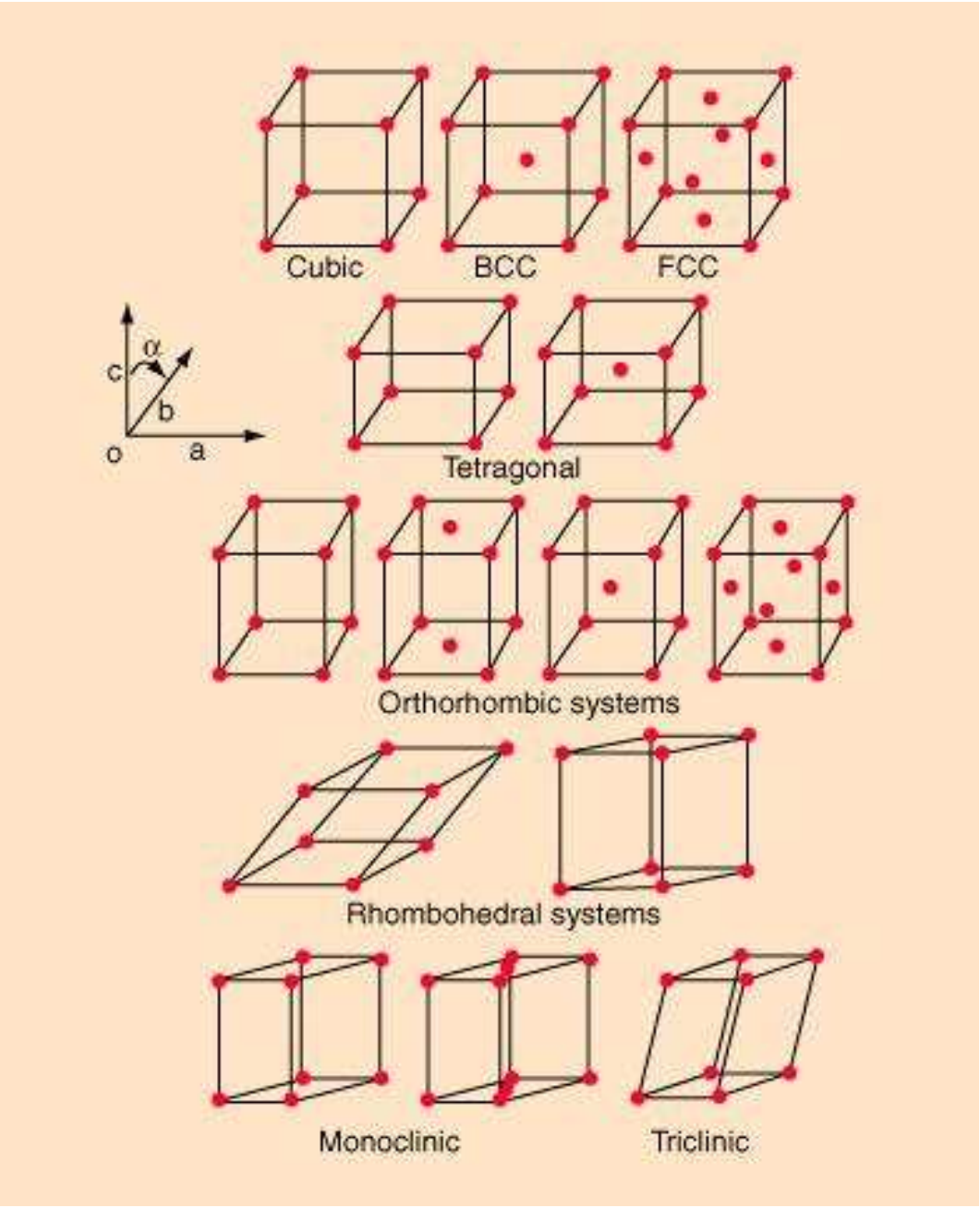

Figure 49: The 14 Bravais Lattices

there is no building block smaller than this structure that can completely define the lattice. The face-centered cubic structure of nickel and aluminum is not a primitive cell. The primitive cell for the fcc structure is a rhombohedral arrangement defined by one corner atom and three face-centered atoms [60]. These four atoms also define the primitive cell vectors of the system. This is depicted in fig. 50. The primitive cell vectors $\acute{a}, \acute{b}$ and $\acute{c}$ are defined as -

$$\begin{aligned} a' &= \tfrac{a}{2}\hat{i} + \tfrac{a}{2}\hat{j} \\ b' &= \tfrac{a}{2}\hat{j} + \tfrac{a}{2}\hat{k} \\ c' &= \tfrac{a}{2}\hat{i} + \tfrac{a}{2}\hat{k} \end{aligned} \tag{258}$$

where a is the size of the cubic cell. The angles between the primitive cell vectors are 60°.

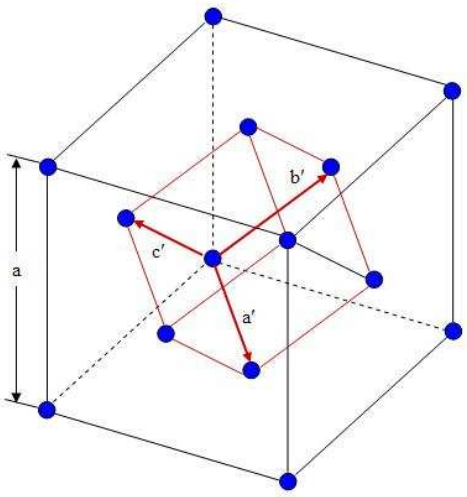

Figure 50: The rhombohedral primitive cell of the face-centered cubic crystal

The molecular dynamics calculation of the nickel and aluminum system are run in the commercially available package CPMD, which is an acronym for Car-Parrinello Molecular Dynamics. The system consists of 5 layers of nickel followed by 5 layers of aluminum. The nickel and aluminum layers are separated

by a gap of 6 A°. Each layer consists of 4 atoms. The atoms are arranged in a rhombohedral framework as it is the primitive cell of the face-centered cubic crystal lattice. For each layer in an fcc crystal, the position of one atom in the layer, along with the lattice constants can be used to obtain the co-ordinates of the other atoms. The position of one atom on each layer was obtained from the hands-on sessions of the VASP package [119]. This information was as input in the PHONON package. This package generates the co-ordinates in a supercell given the position of one atom and the lattice vector. Using this package, the co-ordinates of all the atoms in the system were obtained - 4 atoms for each layer.

Since we are running Car-Parrinello molecular dynamics, the first step before running any MD simulations is the optimization of the wave functions in order to obtain the minimum energy of the system. The default convergence criteria in CPMD is 1e-5. But it was observed after several trial runs that this convergence criteria was too restrictive for the wave function optimization problem of our system. Thus, this criteria was relaxed by two orders of magnitude and set at 1e-3. In addition, while optimizing the system for the wave functions, the atoms were not allowed to relax. The preconditioned conjugate gradient method was used for the minimization procedure. Once the simulation ends, a file is created in which the optimized wave functions of the system are stored. And these values are used in the subsequent MD run.

The next step in the simulation process is the molecular dynamics calculation. As has been mentioned earlier, the Car-Parrinello molecular dynamics is used. Since we are interested in seeing the behavior of the material at the melting temperature of aluminum, the temperature in the system is kept fixed at 933K (or 660°C, which is the melting temperature of aluminum), using the keyword

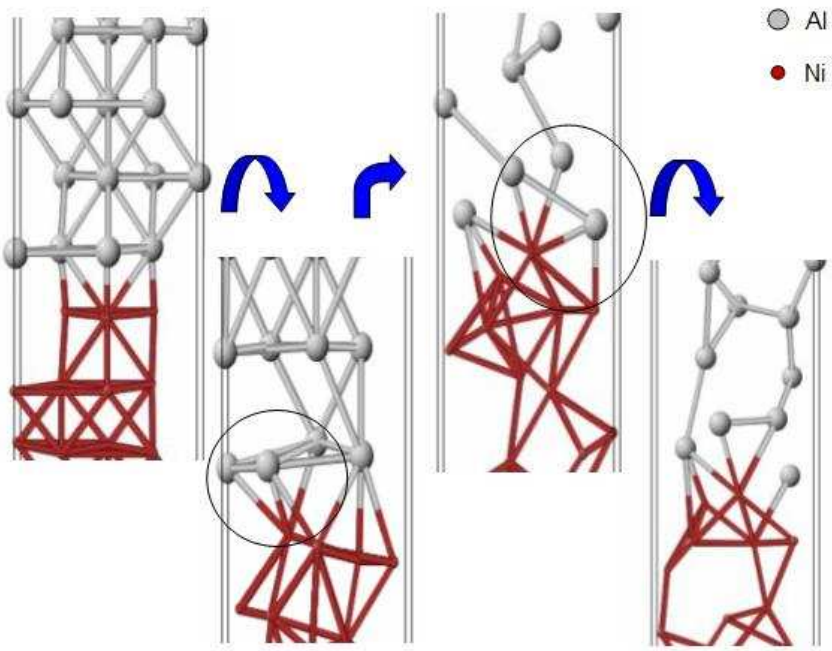

Figure 51: Molecular dynamics simulation of a Ni-Al system of 40 atoms at a temperature of 660°C at various intermediate time steps. The grey atoms are aluminum and the red are nickel atoms. The circled sections mark two possible intermediate or transition structures - $NiAl_3$ and Ni_2Al_3

TEMPERATURE. The CPMD package is equipped with a command TEMPCONTROL that allows the temperature in the system to remain constant, within a specific range defined by the user. In this MD run, the temperature is kept at 660±5°C, using the TEMPCONTROL keyword. The MD run uses the optimized wave functions of the system that was obtained in the first step of the calculations. The MD simulation runs for a total of 7500 steps where the time interval between each step is 5 a.u. Each atomic unit of time is equivalent to 0.0241888428 fs. The positions of the atoms are recorded every 10 steps. By studying these positions, it is possible to see how the system behaves as it evolves. Fig. 51 depicts the results obtained at various intermediate points. From these plots, possible intermediate states or transition structures can be identified to be $NiAl_3$ and Ni_2Al_3. Experiments conducted on the thermal initiation/explosion of Ni and Al have obtained these compounds intermediate structures [114][140]. Fig. 52 is a close-up shot of the positions of the atoms from the MD run, in which this behavior of the nickel and aluminum atoms to form a tetragonal structure can be observed. Fig. 53 is a schematic representation of the same structure.

In addition to studying the Ni-Al system at the melting temperature of Al, additional molecular dynamic simulations were also carried out at other temperatures of 0K, 100°C, 400°C, 500°C and 600°C. The results obtained are shown in figs. 54, 55, 56, 57 and 58 respectively. From these figures, it can be observed that there is no interaction between Ni and Al atoms at 0K and 100°C, whereas at all other temperatures, it can be observed that the there is an interaction between the Ni and Al atoms at these temperature, indicating the possibility of a chemical reaction. Experimental observations indicate that

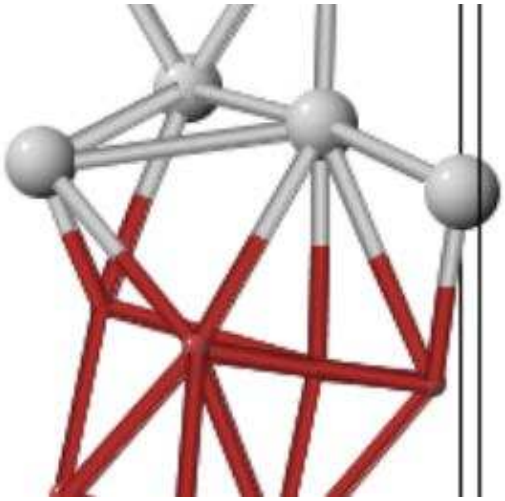

Figure 52: The tetragonal structure observed from the interaction between the nickel and aluminum atoms during a molecular dynamics simulation in CPMD at a temperature of 660°C. The grey atoms are aluminum and the red are nickel atoms.

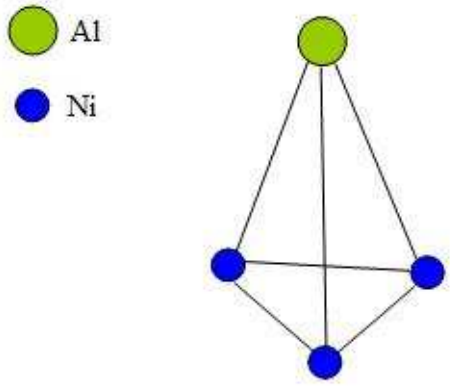

Figure 53: A schematic representation of the tetragonal structure formed from the interaction between the nickel and aluminum atoms during a molecular dynamics simulation in CPMD at a temperature of 660°C

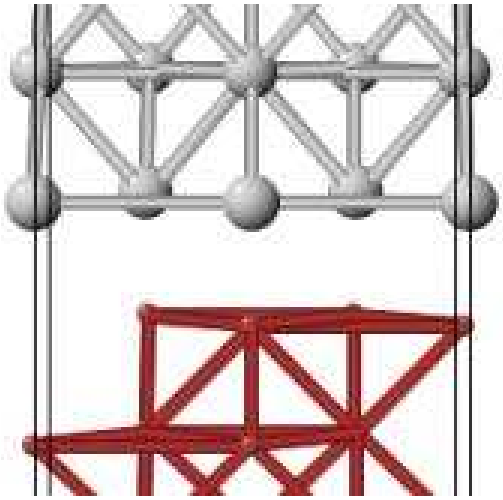

Figure 54: Molecular dynamics simulation of a Ni-Al system of 40 atoms at a temperature of 0K. The grey atoms are aluminum and the red are nickel atoms.

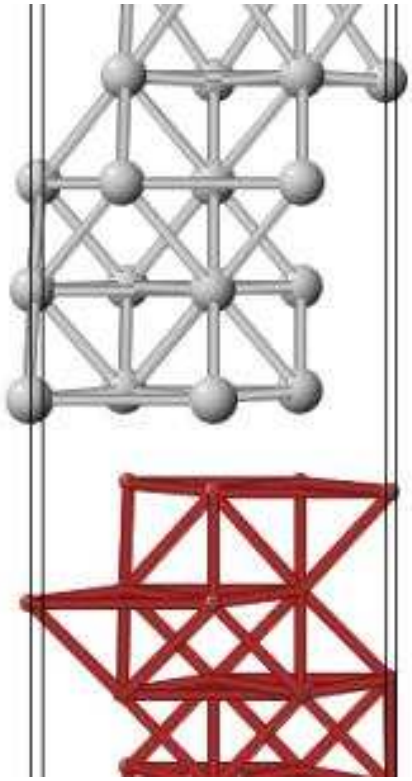

Figure 55: Molecular dynamics simulation of a Ni-Al system of 40 atoms at a temperature of 100°C. The grey atoms are aluminum and the red are nickel atoms.

in a Ni-Al mixture, initiation might sometimes occur before the melting temperature of Al depending on the extent of mixing between the reactants as well as other factors such as particle sizes and morphology [76][**?**]. This study indicates that reaction initiation temperature between Ni and Al lies in the range 100°C-400°C. The number of atoms modeled in this numerical case-study is a very small sample size. Analysis of a larger sample, which is one of the future tasks, will give a better understanding about this pre-initiation temperature.

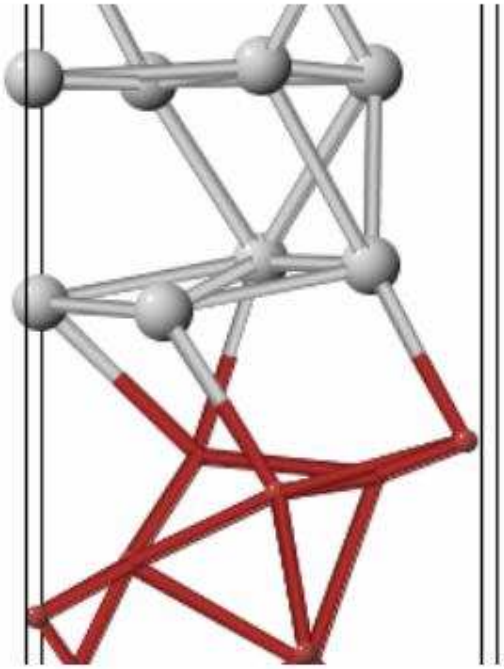

Figure 56: Molecular dynamics simulation of a Ni-Al system of 40 atoms at a temperature of 400°C. The grey atoms are aluminum and the red are nickel atoms.

A larger system of nickel and aluminum was also studied. The number of layers of nickel and aluminum were increased to 7. The gap between the layers is 6 A° and each layer consists of four atoms. The same procedure as was described above was followed. First, the wave function of this system was optimized using CPMD. The convergence criteria was set at 1e-3 in this case also. At the end

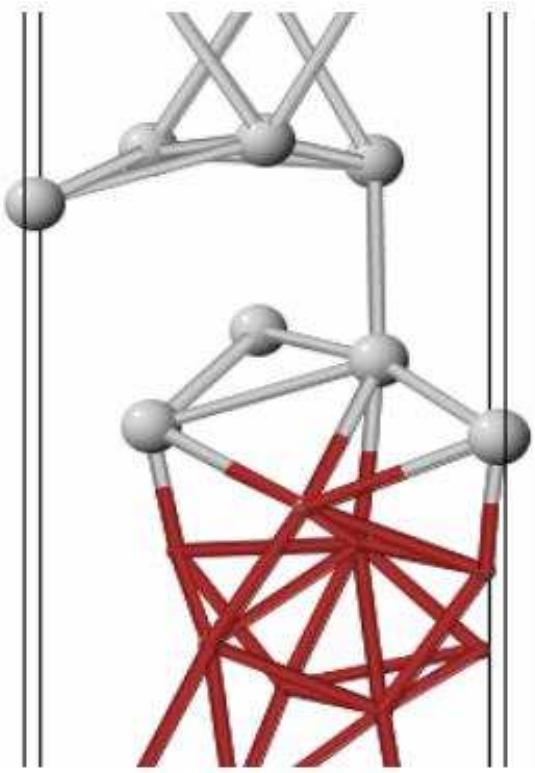

Figure 57: Molecular dynamics simulation of a Ni-Al system of 40 atoms at a temperature of 500°C. The grey atoms are aluminum and the red are nickel atoms.

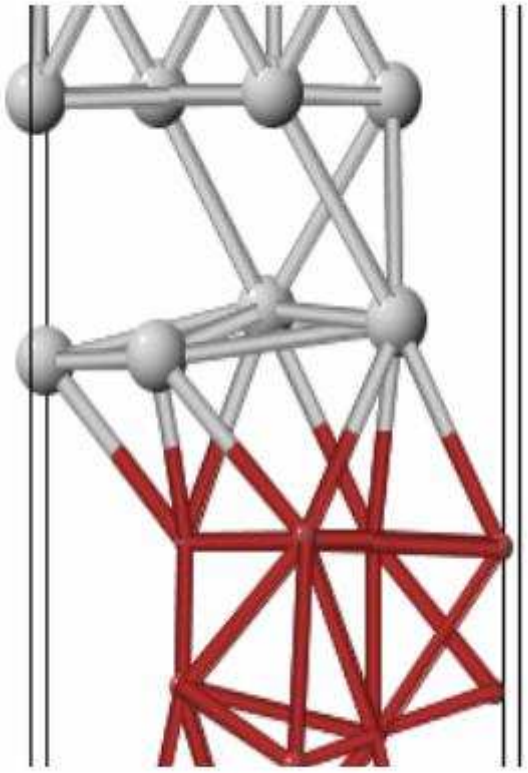

Figure 58: Molecular dynamics simulation of a Ni-Al system of 40 atoms at a temperature of 600°C. The grey atoms are aluminum and the red are nickel atoms.

of this run, the optimized wave functions are all stored in a file and this file is used in the subsequent MD run. The Car-Parrinello MD simulation was run at the melting temperature of aluminum. All the parameters were the same as in the previous case study. Fig. 59 shows that after 1769 time steps, there is an interaction between the nickel and the aluminum atoms. This indicates that a reaction between the nickel and aluminum occurs when the system is thermally initiated.

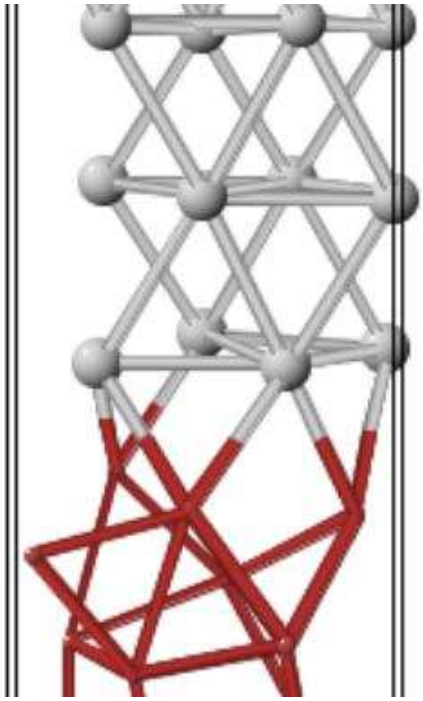

Figure 59: Molecular dynamics simulation of a Ni-Al system of 56 atoms at a temperature of 660°C. The grey atoms are aluminum and the red are nickel atoms.

In the above studies, all the nickel layers were placed together and separated from all the aluminum layers placed together. But to better model a mixture, a numerical study of alternating nickel and aluminum layers was conducted. Two layers of nickel are followed by two layers of aluminum and the molecular dynamics calculation was carried out at 660°C. The interaction between nickel

and aluminum occurs at each interface, indicating a chemical reaction. Fig. 60 depicts the result obtained.

What has been accomplished is a preliminary work on the initiation of chemical reaction by the use of ab-initio molecular dynamics that shows correct trends. For example, bonds are not formed between Ni and Al at temperatures of 0K and 100°C (373K). The bonds between nickel and aluminum are formed at the melting temperature of Al. Bonding is also observed at 400°C (673K) and 500°C (773K). These observations should be further investigated by considering -

- Air in the pores of energetic mixtures that contain Ni and Al instead of assuming vacuum in the pores. (In some cases, the pores are filled with binders and structural reinforcements). Inclusion of air in the pores have shown significant improvements in the calculation of the equation state
- Perform calculations with different pseudopotentials
- Perform and compare with pure MD calculations, with a large number of atoms. Potentials for these calculations can be calculated from ab-initio methods
- Consider steady increase of temperature or addition of heat at a varying rate
- Verify if adiabatic assumptions are violated in using CPMD

A more detailed study of this problem will provide a better understanding of the reaction mechanism in this mixture. This information could then be used at the higher modeling levels such as the mesoscopic or the continuum level.

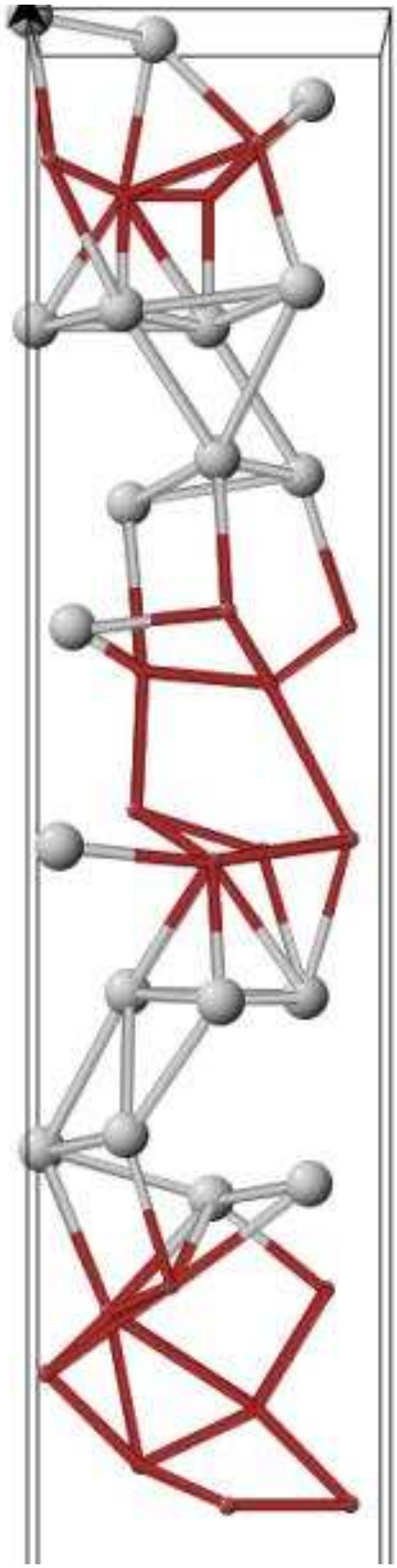

Figure 60: Molecular dynamics simulation of a Ni-Al system with alternating nickel and aluminum layers. The grey atoms are aluminum and the red are nickel atoms.

Chapter VIII

DISCUSSION

The model that has been developed for shock-induced chemical reactions in energetic materials and numerically analyzed for two specific cases - Al, Fe_2O_3 and Ni, Al will be discussed in this chapter. The numerical method that has been used to solve the partial differential equations is the MUSCL scheme [68][69][87] for the spatial dimension and the second order TVD Runge-Kutta (Total Variation Diminishing) method for the time dimension. It was observed that using schemes like the two-step Richtmyer scheme to study the shock processes due to impact of a projectile on the energetic material leads to a significant amount of computational oscillations. Adding artificial viscosity to damp these oscillations was not satisfactory. Instead the numerical scheme was changed to the non-oscillatory scheme MUSCL scheme so that these oscillations are kept to a minimum.

The mesh size that was used for all the calculations obtained in this thesis is 60μm. The effect of changing the mesh size is also studied. Figure 61 is the pressure and temperature obtained in the Al, Fe_2O_3 mixture for an impact velocity of 500m/s and a mesh size of 6μm, which is one order of magnitude lower than the usual mesh size used in this thesis work. It can be observed from the plots that the computational results contain more oscillations at this lower mesh size. And thus, the mesh size that was selected works very well in removing the computationally-induced oscillations in the plots.

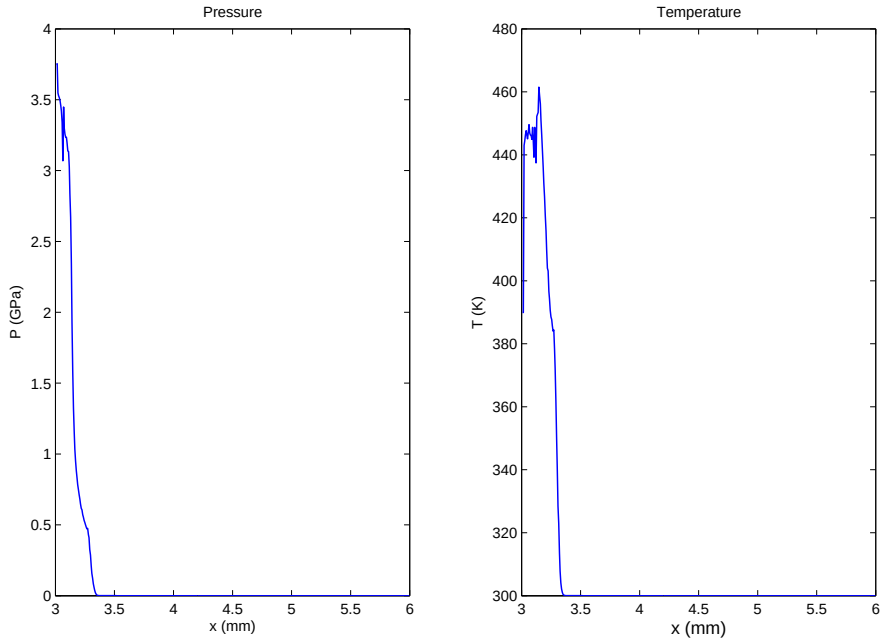

Figure 61: Effect of mesh size on the numerical analysis

The elastic precursor to the shock wave is shown in figure 62. The sudden increase in the pressure following the elastic precursor is the shock wave in the mixture. The magnitude of the elastic precursor is one or two orders less than the pressure generated in the mixture due to the shock process and this is the reason why it is not readily observable in all the other figures in this thesis.

The two mechanisms that take the reactants to the transition state are the pore collapse mechanism and the plastic work. The effect of both these mechanisms are studied for the $Al - Fe_2O_3$ composite. A porous mixture leads to a greater increase in temperature than a solid mixture. This is observed in figure 27. Thus, the reaction initiates faster in a porous mixture as compared to a non-porous mixture. As the porosity in the mixture increases, the temperature in

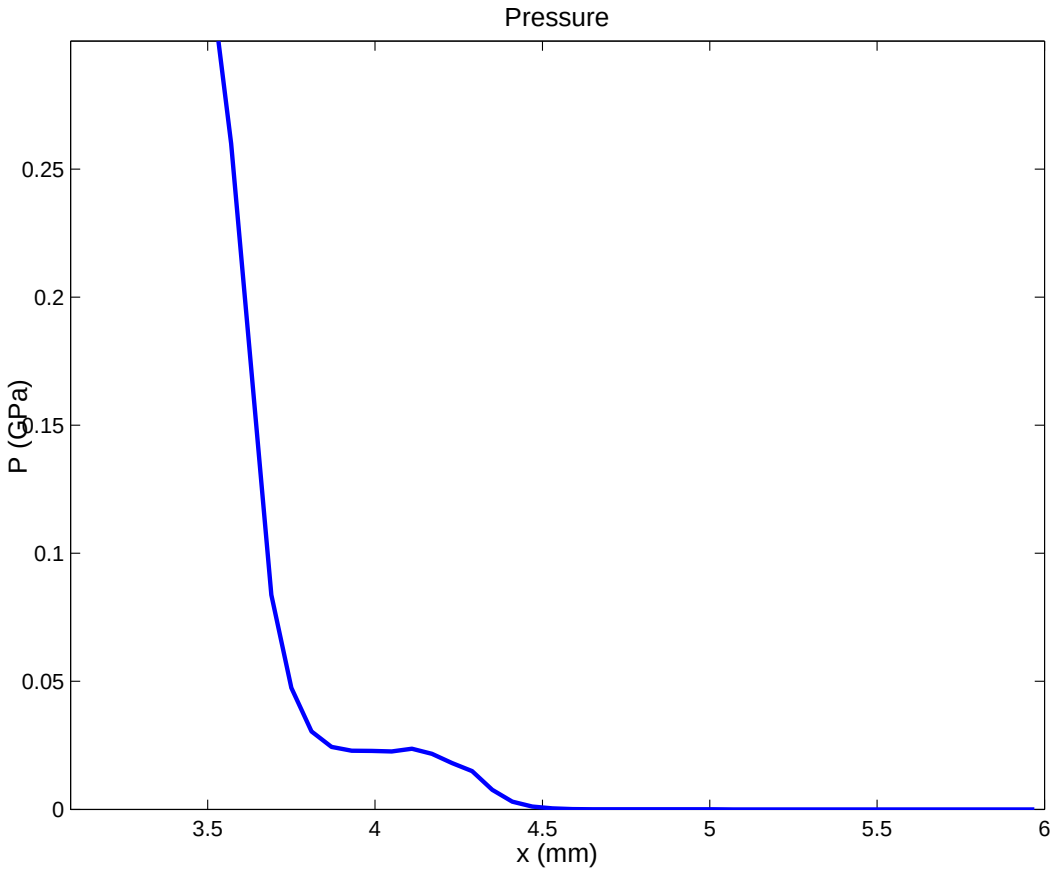

Figure 62: Elastic precursor to the shock wave

the mixture also increases and thus the reaction rate increases, which translates into a greater concentration of the reaction products. As the shock wave proceeds through the mixture, work is done in collapsing the voids and this, reduces the pressure in the system. Thus, with increasing porosity, the pressure in the composite decreases (figure 28). The reaction initiation criteria is based on the melting temperature of aluminum. The effect of pressure on the melting temperature has not been included in this model. Including this effect is one of the extensions that can be applied to this model in the future.

The initiation of chemical reaction has been experimentally observed to occur after a certain time delay behind the shock wave [12][13][130][133]. It does not occur instantaneously at the shock front. This implies that the two mechanisms of pore collapse and plastic flow that initiate the reaction do not take place instantaneously at the shock front. Thus, the void collapse relaxation time was introduced to account for the time delay in the void collapse process behind the shock front. As the void collapse relaxation time increases, it takes longer time for the void collapse process to occur. This means the temperature increase is not high in regions with lesser pore collapse. The effect of the void collapse relaxation time on the porosity in the mixture is shown in figure 31. At the end of the simulation, at approximately $0.2\mu s$, it can be observed that the pore collapse wave progresses further into the material for the 60ns relaxation time as opposed to the 120ns relaxation time. Thus, by controlling this parameter, the initiation of the void collapse process can be controlled and the subsequent initiation of chemical reaction can be controlled. The relaxation time measure associated with the pore collapse process is not a constant throughout the shock process. It depends on the state of the system. Thus, the void collapse relaxation time has been modeled as a function of the velocity because the the

mixture moves with a certain velocity into the pores, closing the pores.

The shock wave increases the yield stress in a small region behind the shock front. Many attempts to explain the heating behind the shock front without the effect of increasing yield strength have not been successful. The heating behind the shock front has been explained by researchers such as Armstrong by a mechanism known as "dislocation pile-up and sudden release" [4][5]. The heat generated by such a plastic flow mechanism has been used to explain experimental observations of temperature increase behind the shock front. This mechanism of plastic flow is theoretically modeled in this work. An evolution equation is used to describe the increase in the yield stress behind the shock front. The yield stress can increase by a factor in the range of 3-5 for mild steel [80]. As the yield stress factor increases, the plastic work can increase and consequently the heat generated by the plastic flow also increases. This is observed in figure 35 by the increase in temperature with increasing yield stress. This means that the composite reaches the reaction initiation temperature faster and thus, the reaction is initiated at an earlier time. The increase in temperature also gives rise to a faster reaction rate and thus, the formation of the product concentration at a given time interval is greater when the yield stress increases.

The chemical reaction rate relaxation time is introduced to reflect the delay in the rate of the chemical reaction. Similar to the void collapse relaxation time, the chemical reaction rate relaxation time is not a fixed parameter. It is a function of the state of the system. In many cases of the energetic mixtures (Al/Fe_2O_3 and Al/Ni) [15][48][76], the reaction initiation criteria is sometimes based on the melting temperature of aluminum. The reaction initiates once the

melting temperature of aluminum is reached [17][76][114]. Thus, a temperature-based criteria, including the temperature in the mixture as well as the melting temperature, is used to model the reaction relaxation time.

The equations formulated in this work can be used for other binary energetic materials. It is thus, also used in the analysis of shock-induced chemical reactions in an intermetallic mixture of aluminum and nickel. Two possibilities of a chemical reaction in the nickel-aluminum mixture were identified and the transition state for both the cases was obtained. For the numerical simulation, the reaction $Ni + 3Al \rightarrow NiAl_3$ was considered. The trends displayed by the intermetallic mixture are similar to those of the aluminum-iron-oxide mixture. Increasing the porosity increases the temperature in the system and leads to a greater reaction rate. The impact loading also displays a similar trend. It increases the temperature in the composite and thus, leads to a greater concentration of the product $NiAl_3$

The model developed in this research is a continuum based model. It is part of a study of energetic materials conducted at various length scales. The continuum based model can be integrated with the other models, to provide a multiscale simulation of practical applications. One such integration has already been designed [23] wherein the continuum model has been integrated with the mesoscopic model [9] to study the chemical reaction initiation and propagation in the $Al - Fe_2O_3$ mixture. The mesoscopic model provides the reaction initiation criteria based on the temperature in the hot spots in the mixture but does not provide information about the system following the generation of these reaction sites. The weighted average of the temperature in all the hot spots is used as

the reaction initiation criteria in the non-equilibrium thermodynamic continuum model to understand the state of the system following the shock waves. The continuum model comes at the end of the length scale. The analysis done at the lower length scales needs to be translated into macroscopic or bulk parameters, which is the scale of all practical applications. The continuum model can achieve this by integrating with the lower length scale models to provide a macroscopic description of the underlying processes in the system.

The thermal initiation of chemical reaction in a mixture of nickel and aluminum depends on a variety of factors such as particle sizes, morphology, rate effects etc. As a first step, the initiation of chemical reactions at a constant temperature has been studied in this thesis using ab-initio molecular dynamics. The study opens up a new area of research. The idea is to extend this work and conduct a more detailed systematic study of shock-induced chemical reactions using ab-initio molecular dynamics (ABMD). The work done to date includes the modeling of nickel and aluminum atoms in the framework of ab-initio molecular dynamics. In particular, possible reactions are studied at fixed temperatures. The preliminary work indicates reaction initiation at temperatures below the melting temperatures. This work can be further expanded by including porosity (air in the pores instead of vacuum), investigating increase in temperature at varying rates and performing calculations with different psuedopotentials. However, much work needs to be done before inputs can be provided to the continuum scale models.

Chapter IX

CONCLUSIONS AND RECOMMENDATIONS

The aim of this work has been the study of shock-induced chemical reactions in binary energetic materials, by developing the necessary framework to study the thermal, mechanical and chemical processes at the continuum level using suitable computational methods. A reactive thermite composite of aluminum, iron-oxide and epoxy has been analyzed under one-dimensional strain conditions. The following main points can be noted from this work -

- The various processes that occur in a shock problem are irreversible in nature and do not take place under equilibrium conditions (discussed in the Thermodynamics section of the Appendix). In order to accurately describe the various phenomena, a theoretical model is developed in the framework of non-equilibrium thermodynamics. The processes that occur behind the shock front do so after a time delay following the shock front. To model this behavior, the framework of extended irreversible thermodynamics is used to formulate the governing partial differential equations.
- The transition state of the reaction process has been identified at the continuum level from energy considerations. This state governs the activation energy needed by the reactants to reach the transition state and thus, governs the rate of the chemical reaction.

- Both the mechanisms of pore collapse (thermochemical model) and plastic flow (mechanochemical model) are incorporated in this model to explain the increase in temperature behind the shock front and consequently the initiation of chemical reaction in energetic mixtures of Al, Fe_2O_3 and Al, Ni. Thus, it has been shown that both these mechanisms can take the reactants to the transition state and initiate chemical reactions. By using the results of the current model on the simulation of gas-gun tests, it is possible to identify the relative importance of the two mechanisms quantitatively.

- The effect of porosity on the temperature increase behind the shock front has been studied. With increasing porosity, the temperature has been found to increase, validating the fact that pore collapse is indeed one of the mechanisms that aids in the initiation of chemical reactions. For a mixture with void fractions of 0% to 30%, the temperature has been found to increase by 450K, leading to an increase in the extent of reaction from 2.6% to 21%. Thus, the porosity content in the mixture is one way to control the extent of reaction and product concentration in the mixture.

- The second mechanism that increases the temperature behind the shock front, namely, plastic work, has also been studied. The effect of plastic work has been analyzed by increasing the factor α_Y which governs the increase in the yield stress behind the shock wave. For an increase of yield stress by factors in the range 1 to 10, the temperature in the specimen has been found to increase by 280K, leading to an increase in the extent of reaction from 8.3% to 72.8%. Even though the temperature increase due to plastic work is not as high as the increase due to pore collapse, the overall temperature in the mixture is higher in the former case as compared to the latter. This accounts for the increased extent of reaction due to plastic

work.

- Ab-initio molecular dynamics calculations of reaction initiation in energetic materials has been initiated to complement the continuum model. As a first step, the thermal initiation of reactions in the energetic mixture of Ni and Al was investigated at varying temperatures. It shows the correct trends with no bond formation between Ni and Al at temperatures of 0K and 100°C (373K) and with bonds being formed between nickel and aluminum at the melting temperature of Al.

There are some limitations to this work and they include:

- The effect of pressure on the melting temperature of aluminum has not been accounted for in the model.
- Epoxy has been modeled as an inert material and hence, does not take part in the chemical reaction.
- The energetic material has been considered to be predominantly under compression. The effects of tension-compression asymmetry has not been included in the model.
- The numerical analysis has been conducted for a problem under one-dimensional strain conditions and thus, the effects of shear strain (other than the components of the strain deviator) have not been included in the analysis.

The work that has been conducted in this research provides opportunities for the extension of the study of energetic structural materials. The following list provides some of the recommendations for future work -

- The reaction mechanism in this study was modeled as a one-step reaction process with a single transition state. This can be extended to the study of a multi-step reaction mechanism with multiple transition states.
- The governing system of partial differential equations formulated in this work is a three-dimensional system of equations. The numerical analysis has been the study of a problem in one-dimensional strain conditions. Thus, the numerical study can be extended to include the analysis of a plane stress or plane strain problem and the study of axisymmetric problems.
- The focus in this work has been the study of chemical reactions in the binary energetic materials. Interest lies in developing dual functional materials by combining the energetic characteristics with strength. Future work can include the study of structural reinforcements such as carbon fibers or carbon nanotubes and characterizing the behavior of these materials from the structural strength point of view.
- The ab-initio molecular dynamics calculation can be extended to include the effects of porosity and varying rates of adding heat to the mixture.

Coupling the continuum model with future experimental results and models at other length scales will provide a deeper understanding of the thermal, chemical and mechanical processes of multifunctional energetic structural materials and will aid in their design for practical applications.

Appendix A

DESCRIPTION OF DIFFERENT AREAS OF STUDY

The study of shock-induced chemical reactions is an interdisciplinary area. The appendix provides a more comprehensive description of the major areas of thermodynamics, ab-initio molecular dynamics and numerical methods to integrate partial differential equations is presented.

A.1 THERMODYNAMICS

Thermodynamics is a branch of physics that studies heat, work and other forms of energy. One of the primary focus of the study is the conversion of energy from heat to work and vice-versa. There are two basic axioms, principles or laws that form the foundations of thermodynamics [90].

- The first law of thermodynamics states that the energy of the universe is a constant and can neither be created nor destroyed.
- The second law of thermodynamics states that the entropy of the universe never decreases and is always greater than or equal to zero.

To discuss the subject of thermodynamics, the following terms are usually used: [117].

- Primitive variables - These variables are not defined but have mathematical properties associated with them.
- Defined variables - These are definitions given to variables in terms of the primitive variables.
- Axioms - These are mathematical relations that are satisfied by the primitive and defined variables.
- Theorems - These usually refer to the theory as a whole or some special cases and are generally statements that are proven.

A.1.1 Classical Thermodynamics

The earliest origins of thermodynamics [117] can be traced to Lambert (who in 1779 formulated the steady distribution of temperature in a semi-infinite bar heated at one end), Biot (who formulated the time-dependent partial differential equation for temperature in 1804), Fourier (in 1808, he considered three dimensional, rigid, isotropic conductors) and Duhamel (who in 1838 extended Fourier's theory to account for anisotropy). Carnot published a book in 1823 in which he discussed reversible, homogenous processes in ideal gases and maximum density. He proved a theorem, commonly known as Carnot's theorem which states that the work done in a carnot cycle is always positive and depends on the temperature of the source and sink as well as the quantity of heat absorbed by the body. His work did not consider any dissipation effects. This work was followed by the works of Clausius (1850-1862), Rankine (1850-1851) and Kelvin (1848-1851), who formed the foundations for classical thermodynamics.

Clausius (1850) made use of Carnot's axiom and further assumed that heat and work are uniformly and universally interconvertible in cycles. He worked with the ideal gas temperature for ideal gases at maximum density. He also discovered and proved the existence of internal energy. Rankine in the meantime, was formulating a more general form of thermodynamics, one in which he defined temperature as the kinetic energy of the molecules. Internal energy was implicit in his formulation but Rankine did not observe or define the internal energy. He did discover the entropy function but it was Clausius who later rediscovered it and gave it the name entropy. Kelvin, in 1851, extended Clausius' theory for ideal gases to general fluids. A few years earlier, he defined the absolute scale of temperature, one that is independent of the choice of body as a thermometer.

It was in the 1850's that the first and second 'laws' or axioms of thermodynamics were proposed. The formal statement for the first law states [3] "If the state of an otherwise isolated system is changed by the performance of work, the amount of work needed depends solely on the change effected and not on the means by which the work is performed nor on the intermediate stages through which the system passes between its initial and final states." There are two statements of the second law of thermodynamics [3]. The first is the Kelvin statement which states that "no process is possible whose sole result is the complete conversion of heat into work." The second is the Clausius statement which states that "no process is possible whose sole result is the transfer of heat from a colder to a hotter body." Over the years since its inception, these two laws have been postulated and formulated in numerous different forms.

Continuum represents a body in Euclidean space with points of Euclidean space

identified with particles. Continuum does not consider discrete atoms. It is assumed that an infinitesimal neighborhood of a point in the continuum is mapped into neighborhoods of the same point in the deformed configuration. It was Duhem (1886-1913), who first formulated the foundations for thermodynamics of a continuum in which each point of the body is assumed to obey the equations that occur in the thermodynamics of homogenous, reversible processes [117]. In the meantime, Gibbs (1873-1878) had formulated the foundations of thermodynamics, now known as the thermostatics of a system. He considered energy, entropy and absolute temperature to be primitive variables and selected volume and entropy as independent variables in his analysis. A few years later, Planck formulated the thermodynamics of systems of n variables. He considered processes that undergo changes as time proceeds, 'natural processes', that are not considered to be in equilibrium. He considered homogenous processes that are irreversible in nature and formulated the Inequality, now known as the Clausius-Planck Inequality (1887) [117]-

$$\dot{H} \geq \frac{Q}{T} \tag{259}$$

where H is the entropy, Q is the heat accumulated in the body and T is the temperature. Several years later, in 1901, Duhem formulated the Clausius-Duhem inequality which states that

$$\dot{H} \geq -\int_{bdry} \frac{\vec{q}.\vec{n}}{T}\, dA \tag{260}$$

where $\overrightarrow{q}$ is the heat flux vector and dA is an element of area on the surface of the body. Both the inequalities provide a lower limit for the increase in entropy. In 1960, Truesdell and Toupin modified the Clausius-Duhem inequality to include the body sources and published their postulate of irreversibility. This has since

been used by several researchers as the Clausius-Duhem inequality, including Coleman and Noll (in their 1963 paper). This theory is now known as the linear theory of irreversible thermodynamics or classical irreversible thermodynamics [117].

In classical irreversible thermodynamics, it is assumed that in a small or infinitesimal neighborhood, the system is in equilibrium but the global system is in non-equilibrium (near equilibrium) from point-to-point and the associated neighborhoods. In this thermodynamics formalism, the second law of thermodynamics is given by the following relation [59]

$$\eta^s = \sum_{\alpha} \mathrm{J}_\alpha \mathrm{X}_\alpha \tag{261}$$

where η^s is the rate of entropy production, X_α is the force and J_α is the associated flux. Very often, a linear relation is assumed between the fluxes and forces, in classical thermodynamics -

$$J_\alpha = \sum_{\beta} \mathrm{L}_{\alpha\beta} \mathrm{X}_\beta \tag{262}$$

where $L_{\alpha\beta}$ are phenomological coefficients. Onsager [117] introduced reciprocal relations for the phenomological coefficients and proved it in the framework of statistical mechanics.

$$\mathrm{L}_{\alpha\beta} = \mathrm{L}_{\beta\alpha} \tag{263}$$

A.1.2 Rational Thermodynamics

The concept of Rational Thermodynamics (RT) was introduced by Coleman, Noll, Toupin, Ericksen and others. Some descriptions of rational thermodynamics have been characterized, by physicists other than the originators of rational thermodynamics as follows: the subject of rational thermodynamics is bound by axioms, the absolute temperature and entropy are primitive variables and the Duhem inequality is the basic assumption [59]. In reply, Truesdell, in one of the early research works on RT [117], restated that rational thermodynamics is not a new science. While Gibbs' fundamental theories are described in terms of systems with finite degrees of freedom, the early researchers of rational thermodynamics restated the classical thermodynamics on firmer mathematical foundations and extended the concept of thermodynamics to systems of deformable bodies that can be considered as a continuum. Internal dissipation is also included. Many of the primitive variables are similar to the classical thermodynamics but were extended to consider a continuum with dissipation. One of the primitive variables of rational thermodynamics includes the spatial variable x and the associated deformable body B, which is defined as a function in initial configuration and time $x = x_k(\chi, t)$. Similarly, other variables density ρ, temperature θ, heat q, force f, internal energy e and certain parameters (γ_i) that included volume and/or measures of deformation.

In rational thermodynamics [117], the foundations for the subject of classical thermodynamics, are now considered as a branch of mathematical physics that considers the effects of heating and the change of temperature on a body. A thermokinetic process is specified by the change of a pair of functions θ and γ.

The classical thermodynamics relies on the first axiom (or first law of thermodynamics) that represents an equation representing the balance of rate of increase of the internal energy, net work and heat. The irreversibility is represented by the existence of an a-priori least upper bound B on the heat (or heating) Q (second axiom). In addition to the first and second axiom, the bodies are characterized by constitutive axioms that characterizes a body by relationships between net work (working), heat, internal energy and the least upper bound B. The constitutive axiom assumes that these four quantities are functionals that satisfy both the first and the second axiom. The second axiom or second law is further stated in the form of a Clausius-Planck inequality, in terms of entropy h.

$$\theta \dot{h} \geq Q \tag{264}$$

To extend the concepts to a deformable body and include internal dissipation, a body B is now assumed to occupy a domain of space at each time t. Each domain is known as its configuration or the motion of B including deformation. Mathematically, each configuration is related by mappings of the form

$$x = x_k(\chi, t) \tag{265}$$

where χ represents points of a continuum in the reference configuration. Similarly, the velocity field and the linear and angular momentums are defined as follows

$$\dot{x} = \dot{x}(\chi, t) \tag{266}$$

$$\vec{L} = \int_B \dot{\vec{x}}\, dm \tag{267}$$

$$\vec{H} = \int_B (\vec{x} - \vec{x}_0) \times \dot{\vec{x}}\, dm \tag{268}$$

where m is the mass, L is the linear momentum and H is the angular momentum.

Similarly, the density ρ and the Cauchy stress tensor σ are defined as functions of space and time. The governing equations consist of mass, momentum and energy.

$$\dot{\rho} + \rho\, div\, \dot{\vec{x}} = 0 \tag{269}$$

$$div\, \sigma + \rho b = \rho \ddot{\vec{x}} \tag{270}$$

$$\rho \dot{e} = \hat{W} + div\, \vec{q} + \rho \hat{s} \tag{271}$$

where e is the internal energy, $\hat{W}$ is the work done, q is the surface influx of heat and $\hat{s}$ is the heat source that depends on the volume. The principle of angular momentum results in the symmetry of the Cauchy stress tensor T, under certain assumptions.

The entropy $\bar{s}$ is defined as

$$\bar{s} = \int_B \eta \, dm \tag{272}$$

where η is the specific entropy. The irreversibility is governed by Clausius-Duhem inequality

$$\dot{s} \geq \int_{surface} \frac{\vec{q}}{\theta} ds + \int_{domain} \frac{\hat{s}}{\theta} dm \tag{273}$$

Without the source term, the rate of change of entropy reverts back to the classical thermodynamics definition (eqn. 259).

A.1.3 Extended Irreversible Thermodynamics

Another thermodynamic formulation was proposed, following the rational thermodynamics, as the Extended Irreversible Thermodynamics (EIT)[59]. This theory was proposed to analyze non-equilibrium processes such as mass diffusion, chemical reaction and plasticity. To describe a non-equilibrium process, evolution of irreversible processes is needed. In addition to the classical independent variables such as density and specific volume, non-equilibrium variables such as fluxes are also introduced as independent variables. Evolution equations are used to describe these non-equilibrium variables. These evolution equations and the associated constitutive equations are restricted by the constraints imposed by the second law of thermodynamics. These fluxes are known as fast variables that decay to their local equilibrium values after a short relaxation time. Usually researchers tend to eliminate these fast variables to get an understanding of the system in terms of slow variables. But the idea of extended

irreversible thermodynamics is just the opposite. It is to seek an understanding of the system in terms of the fast variables to describe the non-equilibrium process. These extra variables (fluxes) allow extended irreversible thermodynamics to solve a variety of complex non-equilibrium problems. It gives the freedom of introducing more variables such as fluxes of fluxes, if necessary. These new variables including fluxes are defined as extended irreversible state variables.

In extended irreversible thermodynamics, the entropy depends on the classical variables as well as on the fluxes or extended irreversible state variables. This entropy function satisfies the following equation (which is the second law of thermodynamics)[59]-

$$\rho \frac{Ds}{Dt} + \nabla . J^s \geq 0 \tag{274}$$

where s is the entropy and J^s is the flux associated with entropy. This entropy flux according to the extended irreversible thermodynamics theory is taken to be a function of all the other fluxes present in the system.

A.2 AB-INITIO METHODS OF MODELING CHEMICAL REACTIONS OF BINARY ENERGETIC MATERIALS

The characterizations of dual functional energetic-structural materials and the resulting thermally induced or shock induced (or assisted) chemical reactions need the studies of condensed matter physics and chemistry. As discussed in

previous sections, the reactants can reach transition states due to added heat and this leads to a thermally induced reaction. The shock wave effects on the binary energetic material are to heat the reactants through the energy of pore collapse or plastic work. Thus, the initial study will be to understand the thermally induced reactions. In the next step, the pore collapse dislocation creation behind the shock waves and heating can be introduced at the ab-initio level.

From the point of view of ab-initio studies of chemistry and condensed matter physics, all materials that we encounter are built from electrons and a few different kinds of nuclei. An electron at positions $\vec{r}$ is attracted to the nucleus of charge Z by forces that result from a potential energy. Similarly, a pair of electrons at $\vec{r}$ and $\vec{r'}$ repel each other by a potential energy proportional to $\frac{1}{|\vec{r}.\,\vec{r}|}$ [63]. Similarly, two nuclei at positions $\vec{R}$ and $\vec{R'}$ repel each other by a potential energy

$$\frac{Z'\,Z}{\left|\vec{R}\,.\,\vec{R'}\right|} \tag{275}$$

For a system of N electrons and M nuclei the potential energy that is described by electro static and columbic force can be described as

$$V = \sum_{i=1}^{N}\sum_{A=1}^{M}\frac{Z_A}{|\vec{r}_{iA}|} + \sum_{i=1}^{N}\sum_{j>i}^{N}\frac{1}{|\vec{r}_{ij}|} + \sum_{A=1}^{N}\sum_{B>A}^{N}\frac{Z_A Z_B}{\left|\vec{R}_{AB}\right|} \tag{276}$$

If we were working with classical mechanics, we solve the Newton equations for a system of particles (for a single particle in one dimension - x, we solve the equation $m\ddot{x} = -v_{,x}$). However the mechanics of electrons and nuclei (even though the nuclei alone can be considered as particles in classic mechanics) require quantum mechanics. In quantum mechanics, the Newton equations are

replaced by Schrodinger's equations. In one dimension - x, the Schrodinger's equation is [41]

$$i\hbar\frac{\partial\Psi}{\partial t} = \frac{h^2}{2m}\frac{\partial^2\Psi}{\partial x^2} + V\Psi \tag{277}$$

As is known, in many cases the velocities are much lesser than the speed of light and relativity efforts are neglected and h is Planck's Constant.

$$\hbar = \frac{h}{2\pi} = 1.054573 \times 10^{-34} J.s \tag{278}$$

By solving for the wave equation $\Psi(x,t)$, we can find expected values of the position x of the particle $< x >$.

$$\langle x\rangle = \int_{-\infty}^{\infty} x\left|\Psi\right|^2 dx \tag{279}$$

Similarly, the expected values of the momentum and kinetic energy can be found from $\Psi(x,t)$.

Before discussing the three dimensional problem, the one dimensional Schrodinger equation is used to explain the use of the method of Separation of Variables to simplify the problem, with

$$\Psi\left(x,t\right) = \phi\left(x\right)g\left(t\right) \tag{280}$$

$$i\hbar\frac{1}{g}\frac{dg}{dt} = -E \tag{281}$$

$$\frac{h^2}{2m}\frac{1}{\phi}\frac{d^2\phi}{dx^2} + V\phi = E\phi \tag{282}$$

where E is the constant from the separation of variables. The first equation can be readily solved. The second equation, which is known as the time independent Schrodinger's equation, is an eigen value problem that results in eigen values E_n and eigen functions ϕ_n (n= 1,2,3, :., ∞). Thus, from the expansion theorem,

$$\Psi(x,t) = \sum_{n=1}^{\infty} c_n \phi_n(x) e^{-i\frac{E_n t}{\hbar}} \tag{283}$$

Thus, in any problem the primary objective is to solve the time independent Schrodinger equation (like eqn. 282) in three dimensions and find the values of $\phi(Z_i)$ and E_n.

Time Independent Schrodinger Equations in 3D:

$$\hat{H}\phi\left(\vec{x}_1, \vec{x}_2, ..., \vec{x}_N, \vec{R}_1, \vec{R}_2, ..., \vec{R}_M\right) = E\phi\left(\vec{x}_1, \vec{x}_2, ..., \vec{x}_N, \vec{R}_1, \vec{R}_2, ..., \vec{R}_M\right) \tag{284}$$

where

$$H = -\frac{1}{2}\sum_{i=1}^{N}\nabla_i^2 - \frac{1}{2}\sum_{A=1}^{M}\frac{1}{M_A}\nabla_A^2 - V\left(Z_i, \vec{r}_{ij}, \vec{R}_{AB}, \vec{r}_{iA}\right) \tag{285}$$

$$V = -\sum_{A=1}^{M}\sum_{i=1}^{N}\frac{Z_A}{r_{iA}} + \sum_{i=1}^{N}\sum_{j>i}^{N}\frac{1}{r_{ij}} + \sum_{A=1}^{M}\sum_{B>A}^{M}\frac{Z_A Z_B}{R_{AB}} \tag{286}$$

$$\nabla_q^2 = \frac{\partial^2}{\partial x_q^2} + \frac{\partial^2}{\partial y_q^2} + \frac{\partial^2}{\partial z_q^2} \tag{287}$$

M_A is the mass of the nucleus in multiples of the mass of the electrons. Similarly, m_e is the rest mass of the electrons ($9.1094\times10^{-31}kg$), e is the elementary charge

$(1.6022 \times 10^{-19} C)$, $\hbar$ is $(1.0546 \times 10^{-34} Js)$ and $a_0 = \frac{4\pi\varepsilon_0\hbar}{m_e e^2} = 5.2918 \times 10^{-11} m$.

The objective is to solve eqn. (284) to find ϕ and E. However the differential operator contains V as a coefficient, which depends on the positions of the particles. In many problems, the objective is to determine the positions of the particles that corresponds to the lowest eigen value of the equation.

A.2.1 Born-Oppenheimer Approximation

Eqn. (284) is simplified by noting that even the mass of the lightest nucleus is about 1800 times the mass of the electron. Thus the acceleration of the nucleus is much smaller than the electron. The electron can then be assumed to be moving in a field of fixed nuclei [63]. Thus

$$\hat{H}_e = -\frac{1}{2}\sum_{i=1}^{N}\nabla_i^2 - \sum_{i=1}^{N}\sum_{A=1}^{M}\frac{Z_A}{|\vec{r}_{iA}|} + \sum_{i=1}^{N}\sum_{j>i}^{N}\frac{1}{|\vec{r}_{ij}|} \tag{288}$$

The individual terms are denoted by

$$T_e = -\frac{1}{2}\sum_{i=1}^{N}\nabla_i^2 \tag{289}$$

$$V_{ext} = \sum_{i=1}^{N}\sum_{A=1}^{M}\frac{Z_A}{|\vec{r}_{iA}|} \tag{290}$$

$$V_{ee} = \sum_{i=1}^{N}\sum_{j>i}^{N}\frac{1}{|\vec{r}_{ij}|} \tag{291}$$

Then, eqn. (284) becomes

$$\hat{H}_e \phi_e = E_e \phi_e \tag{292}$$

and

$$E_{total} = E_e + \sum_{A=1}^{M} \sum_{B>A}^{M} \frac{Z_A Z_B}{\left| \vec{R}_{AB} \right|} \tag{293}$$

A.2.1.1 Solution by variational principle

Again the solution of eqn. (292) depends on the positions $\vec{R}_A$, $\vec{Z}_A$, $\vec{r}_i$ and N. For any trial ϕ_{et}, it can be shown that

$$\int \ldots \int \phi_{et}^{*} \, \hat{H}_e \, \phi_{et} \, dx_1 \ldots dx_n \;=\; E_t \;\geq\; E_{e0} \tag{294}$$

with E_{e0} corresponding to the exact solution ϕ_{e0}. Thus, E_0 is the ground state energy.

A.2.2 Hartree-Fock Approximation

It is not realistically possible to search through all the possible N-electron wave functions to obtain the ground state wave function. Instead of an N-electron wave function, the Hartree-Fock approximation is to consider N one-electron wave functions $\chi_i(x_i)$ [63]. The product of these wave functions needs to be antisymmetrical in order to satisfy the property of the original N-electron wave

function. This approximation function is shown in eqn. (295) and is also called the Slater determinant.

$$\Phi_{er} = \Phi_{SD} = \frac{1}{\sqrt{N!}} \begin{vmatrix} \chi_1(\vec{x}_1)\,\chi_2(\vec{x}_1)\ldots\chi_N(\vec{x}_1) \\ \chi_1(\vec{x}_2)\,\chi_2(\vec{x}_2)\ldots\chi_N(\vec{x}_2) \\ \vdots\vdots\vdots \\ \chi_1(\vec{x}_N)\,\chi_2(\vec{x}_N)\ldots\chi_N(\vec{x}_N) \end{vmatrix} \tag{295}$$

The one-electron functions are a product of a spatial orbital $\phi_i(r)$ and a spin function $\sigma(s)$.

$$\chi(\vec{x}) = \phi(\vec{r})\,\sigma(s)\,;\sigma = \alpha,\beta \tag{296}$$

The spin functions are orthogonal functions.

$$\begin{aligned} \langle\alpha,\alpha\rangle &= \langle\beta,\beta\rangle = 1 \\ \langle\alpha,\beta\rangle &= \langle\alpha,\beta\rangle = 0 \end{aligned} \tag{297}$$

These one-electron functions are also called spin orbitals.

It has been shown [52] that the Hartree-Fock (HF) approximation is always larger than E_0 obtained by the Born-Oppenheimer approximations. It is to be noted the term larger implies a less negative term. Thus, a term correlation energy E_C^{HF} is defined as

$$E_C^{HF} = E_0^{BO} - E_0^{HF} < 0 \tag{298}$$

It is also shown that the HF approximation of the electrons are closer together

than the BO approximation. In general, the HF approximation is more accurate for solids. Thus, an improved method known as "Density Function Theory" is used to determine the constitutive equations and chemical reactions of condensed matter.

A.2.3 Electron Density

From the concept of a the wave function being the probability of finding the N electrons in the volume elements, the electron density is defined. What is actually defined is once again the probability density of finding, this time, any ONE electron in one particular volume element $d\overrightarrow{r}_i$. But it is commonly known as the electron density in the quantum mechanics [63].

$$\rho\left(\vec{r}\right) = N \int ... \int \left|\Psi\left(\vec{x}_1, \vec{x}_2, ..., \vec{x}_N\right)\right|^2 ds_1 d\vec{x}_2 ... d\vec{x}_N \tag{299}$$

Since it is a probability, its value is always non-negative and satisfies the following properties -

$$\rho\left(\vec{r} \to \infty\right) = 0 \tag{300}$$

$$\int \rho\left(\vec{r}\right) d\vec{r} = N \tag{301}$$

The advantage of using the electron density in the analysis at this level is that it is a quantity that can be measured experimentally by X-ray diffraction methods.

The concept of electron density can be extended to include the probability of finding two electrons simultaneously in two volume elements. This is known as the pair density $\rho_2(\vec{x}_1, \vec{x}_2)$.

$$\rho_2(\vec{x}_1, \vec{x}_2) = N(N-1) \int ... \int |\Psi(\vec{x}_1, \vec{x}_2, ..., \vec{x}_N)|^2 \, d\vec{x}_3 ... d\vec{x}_N \tag{302}$$

A.2.4 Hohenberg-Kohm theorems

First Theorem

"The external potential $V_{ext}(\vec{r})$ is (to within a constant) a unique function of $\rho(\vec{r})$. Since, in turn $V_{ext}(\vec{r})$ fixes $\hat{H}$, we see that the full many particle ground state is unique functional of $\rho(\vec{r})$."[63]

Proof: If the theorem is incorrect, there can be two $V^1_{ext}(\vec{r})$, $V^2_{ext}(\vec{r})$ that give the same $\rho(\vec{r})$ associated with the non degenerate ground state of the N particle system. Then,

$$\begin{aligned} \hat{H}_{1e} &= \hat{H}_1 = \hat{T}_e + V_{ee} + V^1_{ext} \; ; \; \phi = \phi^e_1 \; ; \; E = E^1_0 \\ \hat{H}_2 &= \hat{T}_e + V_{ee} + V^2_{ext} \; ; \; \phi = \phi^e_2 \; ; \; E = E^2_0 \end{aligned} \tag{303}$$

In general, $E^1_0 \neq E^2_0$. Both wave functions give the same $\rho(\vec{r})$. Now use ϕ^e_2 as the trial function $\hat{H}_1$,

$$\left\langle \phi^e_2 \middle| \hat{H}_1 \middle| \phi^e_2 \right\rangle = \left\langle \phi^e_2 \middle| \hat{H}_2 \middle| \phi^e_2 \right\rangle + \left\langle \phi^e_2 \middle| \hat{H}_1 - \hat{H}_2 \middle| \phi^e_2 \right\rangle \geq E^1_0 \tag{304}$$

H^e_1 and H^e_2 are different because of V^1_{ext} and V^2_{ext}.

$$E_2 + \left\langle \phi_2^e \left| V_{ext}^1 - V_{ext}^2 \right| \phi_2^e \right\rangle > E_0^1 \tag{305}$$

or

$$E_2 + \int ... \int \phi_2^e \left(V_{ext}^1 - V_{ext}^2 \right) d\vec{r} > E_0^1 \tag{306}$$

or

$$E_0^2 < E_0^1 + \int ... \int \rho\left(\vec{r}\right) \left(V_{ext}^1 - V_{ext}^2 \right) d\vec{r} \tag{307}$$

By interchanging ϕ_1 and ϕ_2, we can show that

$$E_0^1 < E_0^2 - \int ... \int \rho\left(\vec{r}\right) \left(V_{ext}^1 - V_{ext}^2 \right) d\vec{r} \tag{308}$$

By adding the equations,

$$E_0^1 + E_0^2 < E_0^1 + E_0^2 \tag{309}$$

This is contradictory and hence V_{ext}^1 and V_{ext}^2 gives the same $\rho(\vec{r})$

Second Theorem

From the first theorem, we obtain that the complete ground state energy is a functional of the ground state electron density $\rho(\vec{r}_0) = \rho_0$ [63]. Then

$$E_0\left(\rho_0\right) = T\left(\rho_0\right) + E_{ee}\left(\rho_0\right) + E_{ne}\left(\rho_0\right) + \int \rho_0\left(\vec{r}\right) V_{ext} d\vec{r} + T\left(\rho_0\right) + E_{ee}\left(\rho_0\right) \tag{310}$$

and the Hohenberg-Kohn functional is defined as

$$F_{HK}\left(\rho_0\right) = \hat{T}\left(\rho_0\right) + E_{ee}\left(\rho_0\right) = \left\langle \phi \left| \hat{T} + V_{ee} \right| \phi \right\rangle \tag{311}$$

$$E_0\left(\rho_0\right) = \int \rho_0\left(\vec{r}\right) V_{ne} d\vec{r} + F_{HK}\left(\rho_0\right) \tag{312}$$

The second Hohenberg-Kohn theorem states that $F_{HK}(\rho)$, the function that delivers the ground state energy of the system delivers the lowest energy if and only if the input density is the ground state density ρ_0.

This theorem implies that for any trial density $\rho = \rho^{tr}$ that satisfies the condition

$$\rho^{tr} \geq 0; \int \rho^{tr}\left(\vec{r}\right) d\vec{r} = N \tag{313}$$

the function $E^{tr} = T\left(\rho^{tr}\right) + E_{ee}\left(\rho^{tr}\right) + V_{ext}\left(\rho^{tr}\right)$ represents an upper bound to the true ground state energy E_0. E_0 will be the result if $\rho_{tr} = \rho_0$. For

$$\begin{aligned} \rho^{tr} &= \rho \\ H &= H_1 \\ \phi &= \phi_1 \end{aligned} \tag{314}$$

$$\begin{aligned} &\left\langle \phi_1 \left| H_1 \right| \phi_1 \right\rangle = T\left[\rho_1\right] + V_{ee}\left[\rho_1\right] + \int \rho_1 V_{ext} d\vec{r} \\ &= E\left[\rho_1\right] \geq E_0\left[\rho_0\right] = \left\langle \phi_0 \left| H_0 \right| \phi_0 \right\rangle \end{aligned} \tag{315}$$

A.2.5 Kohn-Sham Equations

If T and V are the exact kinetic and electron-electron potential energy functions [63],

$$E_{ee} \;=\; T \;+\; V \tag{316}$$

If E_{HF} is the corresponding Hartree-Fock Hermitian with T_0 being equal to the kinetic energy of non interacting electron gas, V_H being equal to the Hartree contribution and V_X being equal to the exchange contribution

$$E_{HF} \;=\; T_0 \;+\; V_H \;+\; V_X \tag{317}$$

The correlation energy contribution is

$$V_C \;=\; T \;-\; T_0 \tag{318}$$

Then

$$E_H \;=\; T_0 \;+\; V_H \tag{319}$$

and V_X is defined as

$$V_H \;=\; V \;-\; V_H \tag{320}$$

Then,

$$
\begin{aligned}
F_{HK} &= T + V + T_0 - T_0 \\
&= T_0 + V + T - T_0 \\
&= T_0 + V + V_e + V_H - V_H \\
&= T_0 + V_H + V_e + V - V_H \\
&= T_0 + V_H + V_e + V_X \\
&= T_0 + V_H + V_{XC}
\end{aligned}
\tag{321}
$$

where

$$
V_{XC} = V_e + V_X \tag{322}
$$

is the exchange correlation energy. Then

$$
H_{KS} = \hat{T}_0 + \hat{V}_H + \hat{V}_{XC} + \hat{V}_{ext} \tag{323}
$$

$$
\begin{aligned}
&\hat{V}_{XC} = \tfrac{\delta E_{XC}(\rho)}{\delta(\rho)} \qquad (a) \\
&T_0 = \tfrac{h^2}{2m}\nabla_i^2 \qquad (b) \\
&V_H = \tfrac{e^2}{4\pi\varepsilon_0}\int \tfrac{\rho\left(\vec{r}^1\right)}{\left(\vec{r}-\vec{r}^1\right)} d\vec{r} \qquad (c) \\
&\rho\left(\vec{r}\right) = \sum_{i=1}^{N} \phi^k\left(\vec{r}\right)^* \phi^k\left(\vec{r}\right) \qquad (d)
\end{aligned}
\tag{324}
$$

$\phi_i(\vec{r})$ are the single particle wave functions of the Kohn-Sham equation

$$
\hat{H}_{KS}\phi_i^k = \varepsilon_i \phi_i^k \tag{325}
$$

A.2.5.1 Method of Solution of Kohn-Sham Equations

The objective is to solve for ϕ_i^k and ε_i. It is to be noted that ϕ_i^k are not the wave functions of the electrons. The density $\rho(\vec{r})$ can be found from ϕ_i^k by using eqn. (324d). Also, ε_i are not single electron energies. However, DFT reduces the problem to the solution of Schrodinger like equations for non-interacting particles [36]. The total energy can be obtained from

$$E = \sum_i \int d^3 r \phi_i^{*k}(\vec{r}) \frac{\nabla^2}{2} \phi_i^k(\vec{r}) + \int d^3 r V_{ext}(\vec{r}) \rho(\vec{r}) + \int d^3 r \int d^3 r^1 \frac{\rho(r) \rho(r^1)}{|r - r^1|} + E_{XC} \tag{326}$$

The method of solution uses the following procedure [36]: At n=1,

(a) Guess $\rho_0(\vec{r})$

(b) Input $\rho_{n-1}(\vec{r})$

(c) Determine $\hat{V}_H$ and $\hat{V}_{XC}$

(d) Solve $\hat{H}_{KS} \phi_i^k = \varepsilon_i \phi_i^k$ to obtain ϕ_i^k and ε_i at iteration n

(e) Calculate $\rho_n(\vec{r})$. Check if it is equal to $\rho_{n-1}(\vec{r})$ If yes, the calculation is complete. Find the energy and other observable quantities. If not, return to step 2.

This still needs procedures to find $\hat{V}_{XC}$ and the final expressions for ϕ^k in steps 3 and 4.

A.2.5.2 Expressions for $\hat{V}_{XC}$

The exchange-correlation operator is written as

$$\hat{V}_{XC} = \frac{\delta E_{XC}}{\delta \rho\left(\vec{r}\right)} \tag{327}$$

There are many (more than hundred) approximate functionals for E_{XC} in the published literature. The simplest expression that is used is known as the Local Density Approximation (LDA) [36][63].

$$E_{XC} = \int \varepsilon^h\left(\rho\right) d^3r \tag{328}$$

where ε^h is the energy per unit volume of the homogenous electron gas of density $\rho(\vec{r})$. Different expressions for the LDA are given by Ceperley and Alder [19], Perdew and Zunger [88] and Perdew and Wang [89]. The next level of approximation is known as the generalized gradient approximation or GGA. GGA will have similar expression as eqn. (328) but will consider both the density and the local gradients of the homogeneous electron gas.

A.2.5.3 Trial expressions for ϕ^k

Approximate solution techniques of eqn. (325), requires trial function for ϕ^k. Similar to a Rayleigh-Ritz type of method, trial functions are assumed in the form

$$\phi_n^k = \sum_{j=1}^{p} C_j^n \phi_j^b \tag{329}$$

Once the trial functions are selected, we can use approximate methods like Galerkin method, to reduce the solution of the differential equation in step (4) to a set of algebraic equations

$$[A]^k \left\{ \begin{array}{c} C_1^n \\ \vdots \\ C_p^n \end{array} \right\} = \{0\} \tag{330}$$

and solve the eigen value problem.

In eqn. (329), ϕ_j^b are known as the basis functions. An efficient basis set needs only a few terms (p will be small). In general, convergence requirements demand a large (completeness) basis functions and result in extensive computations.

One type of the basis functions that are extensively used are known as plane wave functions. Others are known as gaussian functions. Very often, to calculate total energy of solids, plane wave expansions are used [36][52]. These waves make use of the periodicity of the crystal. For finite systems that include atoms, molecules and clusters, plane-waves are used in methods known as the supercell where the system of interest is placed in a cell of a fictitious crystal. The cell dimensions should be large to avoid interaction between neighboring cells. Usually a large number of plane waves is needed because the electron density is significant in a small portion of the supercell. In the neighborhood of the nucleus, the function ϕ^k oscillates significantly. To describe these oscillations, a large number of plane waves are needed. From the point of view of many calculations, (with the exception of transition metals), the inner electrons can be considered to be inert. This leads to the description of an atom solely based on valence electrons. This is the pseudo potential approximation. When using pseudo potentials, it is necessary to consider and determine the convergence on the basis of Brillouin sampling and the cut off energies and radii.

A.2.6 Ab-Initio Molecular Dynamics

To solve for chemical reactions at finite temperature, it is very difficult to completely solve the reaction process using ab-initio methods. Thus, ab-initio can be used to find the forces only in the nuclei at each time step. Then, the motion of the nuclei can be solved by the motion of classical mechanics. This is known as ab-initio molecular dynamics (ABMD) and is explained in this section [52].

A.2.6.1 Molecular Dynamics

The atoms or molecules form the building blocks of matter. The bulk behavior of matter is related to the behavior of its atoms and molecules. The properties of a material is governed by its atoms and molecules. Understanding the behavior of the material at this level will greatly enhance our understanding of the behavior of a system at higher modeling levels such as the mesoscopic and macroscopic levels of analysis. Molecular dynamics provides the methodology for the microscopic modeling at the molecular level. It tries to reconstruct the behavior of the molecules using appropriate models. Its underlying basis is Newton's laws of motion and the solution to the N-body problem. There are no analytical solutions to this problem and hence numerical solutions are sought after. The nuclear motions of the particles can be modeled by classical Newton's laws of motions as long as the atoms are not light atoms such as the hydrogen molecule and the frequency of vibration ν is not greater than $k_B T/h$ where k_B is the Boltzmann constant, T is the temperature and h is Planck's constant.

The equations of motion in molecular dynamics are usually formulated in the framework of Lagrangian mechanics. The Lagrange of a system of N particles with positions R, mass M and potential function or energy U can be written as-

$$L(R^N, \dot{R}^N) = \sum_{i=1}^{N} \frac{1}{2} M_i \dot{R}^{N2} - U(R^N) \tag{331}$$

Then the Euler-Lagrange equation

$$\frac{d}{dt}\left(\frac{\partial L}{\partial \dot{R}_i}\right) \;=\; \frac{\partial L}{\partial R_i} \tag{332}$$

gives the equation of motion of the system to be -

$$M_i \ddot{R}_i \;=\; F_i\left(R^N\right) \tag{333}$$

where the forces F are defined as-

$$F_i(R^N) = \; - \; \frac{\partial U(R^N)}{\partial R_i} \tag{334}$$

The same equation of motion can also be derived from the Hamilton equations.

$$\dot{R}_i = \frac{\partial H}{\partial P_i} = \frac{P_i}{M_i} \tag{335}$$

$$\dot{P}_i = -\frac{\partial H}{\partial R_i} = -\frac{\partial U}{\partial R_i} = F_i(R^N) \tag{336}$$

where the Hamiltonian H is the total energy in the system and is given as-

$$H(R^N, P^N) = \sum_{i=1}^{N} \frac{P_i^2}{2M_i} + U(R^N) \tag{337}$$

In the previous section, the potential function U was introduced in the Lagrangian L of s system of N particles. When this potential function is derived from first-principles, then the molecular dynamics formulation shifts from classical molecular dynamics to ab-initio molecular dynamics. Most ab-initio molecular dynamics calculations in the current literature are based on the Kohn-Sham approach, introduced earlier.

A.2.6.2 Born-Oppenheimer Molecular Dynamics

Earlier, the Kohn-Sham energy was introduced within the framework of the Born-Oppenheimer approximation. The potential energy U used in that case is physically the same as the potential function described in molecular dynamics. Thus, the Kohn-Sham energy from the Born-Oppenheimer approximation is used in place of the potential function in the Lagrangian expression. The Lagrangian for the Born-Oppenheimer Molecular Dynamics is then given as -

$$L_{BO}(R^N, \dot{R}^N) = \sum_{i=1}^{N} \frac{1}{2} M_i \dot{R}^{N2} - \min_{\{\phi_i\}} E^{KS}[\{\phi_i\}; R^N] \tag{338}$$

where the second term in the Lagrangian represents the minimum of the Kohn-Sham energy, i.e., the ground state energy of the system. The Kohn-Sham orbitals are orthogonal in nature, i.e. -

$$\langle \phi_i | \phi_j \rangle = \delta_{ij} \tag{339}$$

Thus, the minimization of the Kohn-Sham energy is subject to this orthogonality condition. The gradient of the potential gives the forces in the system.

$$\frac{d}{dR_i}\left[\min_{\{\phi_i\}} E^{KS}[\{\phi_i\}; R^N]\right] \tag{340}$$

The forces therefore depend linearly on the minimization of the Kohn-sham energy. Using these forces in eqn. (333, the Born-Oppenheimer (BO) Molecular Dynamics can be written as -

$$M_i\ddot{R}_i \;=\; -\,\nabla_i\;\left[\min_{\{\phi_i\}} E^{KS}[\{\phi_i\}; R^N]\right] \tag{341}$$

A.2.6.3 Car-Parrinello Molecular Dynamics

In the Car-Parrinello Molecular Dynamics, the motion of the fast electron and the slower nuclei are separated by transforming the separation of the time scales into a separation of their corresponding energies. Thus, two separate energy scales are formulated in this theory. The forces acting in a system is obtained by taking the gradient of the Lagrangian. In order to obtain the forces acting on the Kohn-Sham orbitals, Car and Parrinello formulated a Lagrangian L that is not only dependent on the nuclear positions R but also on the orbitals ϕ. This is done by introducing the concept of an extended energy functional ε^{KS} that includes the usual Kohn-Sham energy E^{KS} as well as a contribution from the orbitals.

$$\varepsilon^{KS} = E^{KS} + \sum_{ij} \Lambda_{ij}\left(\langle\phi_i|\phi_j\rangle - \delta_{ij}\right) \tag{342}$$

Using this quantity, The Lagrangian postulated by Car and Parrinello is -

$$L_{CP}[R^N,\, \dot{R}^N, \{\phi_i\}, \{\dot{\phi}_i\}] = \sum_i \frac{1}{2} M_i \dot{R}^{N2} + \sum_i \mu \left\langle \dot{\phi}_i | \dot{\phi}_i \right\rangle - \varepsilon^{KS}[\{\phi_i\}, R^N] \quad (343)$$

where μ is a fictitious mass or inertia parameter assigned to the orbital degrees of freedom. For consistency in units, its dimensions are square of time times energy. The Euler-Lagrange equation in this case can be written as -

$$\begin{array}{rcl} \frac{d}{dt}\left(\frac{\partial L_{CP}}{\partial \dot{R}_i}\right) & = & \frac{\partial L_{CP}}{\partial R_i} \\ \frac{d}{dt}\left(\frac{\delta L_{CP}}{\delta \langle \dot{\phi}_i}\right) & = & \frac{\partial L_{CP}}{\partial \langle \dot{\phi}_i} \end{array} \quad (344)$$

The equations of motion are obtained from these Euler-Lagrange equations.

$$\begin{array}{rcl} M_i \ddot{R}_i(t) & = & -\frac{\partial E^{KS}}{\partial R_i} + \sum_{ij} \Lambda_{ij} \frac{\partial}{\partial R_i} \langle \phi_i | \phi_j \rangle \\ \mu \ddot{\phi}_i(t) = -\frac{\delta E^{KS}}{\delta \langle \phi_i |} + \sum_j \Lambda_{ij} | \, \phi_j \rangle & & \end{array} \quad (345)$$

In the Car-Parrinello formulation, the temperature associated with the nuclei is proportional to kinetic energy of the nuclei $\sum_i \frac{1}{2} M_i \dot{R}_i^2$ while the electrons also have a fictitious temperature associated with it due to the fictitious mass μ through the term $\sum_i \mu \left\langle \dot{\phi}_i | \dot{\phi}_i \right\rangle$. When the minimum energy is close to the Born-Oppenheimer surface, then we say the electrons are cold electrons or that the electronic temperature is low. In this case, if the ground state wave function was optimized for the initial nuclei configuration, then it will stay close to the ground state for the full time of the simulation. The nuclei however are at a higher temperature. Thus, it is necessary for the electrons to stay at a low temperature for the duration of time while the nuclei are allowed to achieve higher temperatures. This is done by decoupling the two subsystems and adiabatic

time evolution.

Since both the nuclei position and the orbitals are considered as variables in the Car-Parrinello framework, there are two forces defined in this theory. The orbital forces are related to the Kohn-Sham Hamiltonian while the forces related to the nuclear positions are the gradient of the the Kohn-Sham energy.

$$F(\phi_i) \;=\; -H^{KS}\phi_i \tag{346}$$

$$F(R_i) \;=\; -\frac{\partial E^{KS}}{\partial R_i} \tag{347}$$

The difference between the forces in the BO Molecular Dynamics and the CP Molecular Dynamics is that there there was only one force associated with the nuclei positions. These were calculated assuming that the wave functions had already been optimized and thus their accuracy is dependent on the accuracy with which the wave functions were optimized. Whereas in CP Molecular dynamics, the optimization of the wave functions is part of the theory and thus, gives the correct forces in the system.

In this work, the chemical reaction between an intermetallic energetic mixture of Nickel (Ni) and Aluminum (Al) particles is studied using the Car-Parrinello molecular dynamics.

A.3 NUMERICAL METHODS OF INTEGRATING PARTIAL DIFFERENTIAL EQUATIONS

Analyzing problems numerically involves the use of three main fields of study - applied physics, mathematics and computers. It is impossible to separate one from the other. When studying any application or theory, it is necessary to consider the analytical or numerical solution to the problem. It is economically restrictive to study every problem experimentally. In such situations numerical simulations aid us in understanding the phenomena or problem without necessarily conducting experiments. It is possible to gain a better understanding about the fundamentals of the problem under consideration and to couple the theoretical aspects with the experimental observations. Even in many analytical problems, complexities might be introduced through the geometry, boundary conditions or by non-linearities. It is also possible that the solution itself might contain some integrals and other functions that need to be evaluated numerically in order to get numerical data. In all these cases, numerical techniques to solve the system of governing equations are required.

A.3.1 Finite Difference Methods

The most commonly used numerical techniques to solve differential equations are the finite difference methods. Partial difference equations can be classified into three main categories-

- Parabolic
- Elliptic

- Hyperbolic

In this thesis, the governing differential equations are hyperbolic equations. The consistency of a finite difference scheme is obtained from the fact that as the spatial steps ($\Delta x, \Delta y, \Delta z$) and the time step ($\Delta t$) tends to zero, the finite difference scheme approaches the differential equation being modeled. The lowest powers of the spatial and time steps also defines the order of accuracy of the scheme. For example, for a one dimensional finite difference scheme, if the lowest order of Δx is 2 and that of Δt is 1, then the finite difference method is second order accurate in space and first order accurate in time. The stability of a numerical scheme is governed by the growth in error with time. In 1928, in their classic paper, Courant, Friedrichs and Lewy discussed mathematical methods to solve hyperbolic partial difference equations using finite difference schemes [21]. They proposed the use of a constant number that defines the ratio between the spatial mesh and the temporal mesh in the finite difference schemes, in order to achieve a stable scheme. This number is called the Courant-Friedrichs-Lewy number or the CFL number. Depending on the scheme that is being used, there is a range that defines the CFL number for stability. For many schemes this range is from 0 to 1. Finite difference schemes can be implicit or explicit. Implicit schemes allow a larger time step than explicit schemes but since dynamic systems change very fast in time, this property of implicit schemes is seldom used. Explicit schemes are also more commonly used than implicit schemes because they require less computer memory storage requirements. Evaluating a parameter at a grid point in an explicit schemes requires information from a fixed number of other grid points. It is independent of the total number of grid points used in the numerical simulation. In contrast, for an implicit scheme, evaluating a parameter at a grid point requires information at all other grid points and thus, as the number of equations and the number

of meshes increases, the storage requirements becomes very large. For this very reason, for very large problems, an explicit scheme turns out to be more computationally efficient than an implicit scheme. More meshes can be employed in an explicit finite difference scheme as opposed to an implicit finite difference scheme and thus, it provides greater resolution.

The objective of this work is to model the shock-induced chemical reactions in mixtures. There are two mathematical techniques that are used by researchers in incorporating discontinuities like shocks. In the first technique, which is called the shock-fitting technique, the shock discontinuity is determined by jump relations across the shock boundary. But the drawback is that the position of the shock has to be determined from the solution and is not known a-priori. This method is thus, very complicated and is not used much. The second method, which is the shock-smearing technique, was introduced by von Neumann and Richtmyer in their classic paper [120]. Their techniques involves introducing an artificial viscosity or an added dissipation to the solution to make the solution continuous everywhere and thus, deal with discontinuities like shocks. By this method, the inherent discontinuity in the solution is replaced by a continuous region of rapidly changing variables.

To analyze shock effects in solids, Wilkins developed a program called HEMP [127], which is based on the Von Neumann scheme [125][126]. This method has been used to solve many problems that include sliding interfaces in two dimensions, magnetohydrodynamics calculations, plastic work function etc. In these methods, the dependent variables are staggered in space and time and only one of these variables, either velocity or stress, is calculated at a given grid point. Many variations of these methods have been developed over the years.

One of the very popular and widely used numerical method is the Lax-Wendroff scheme. It was introduced in 1960, by Lax and Wendroff as a means of solving a non-linear system of conservative partial differential equations. In one dimension, a conservative partial differential equation is written as -

$$\frac{\partial \{u\}}{\partial t} + \frac{\partial \{f\}}{\partial x} = 0 \tag{348}$$

where $\{u\}$ represents a vector of n dependent variables in the system, $u = u(x,t)$. The size of the vector equals the number of governing differential equations. $f = f(u(x,t))$ is a vector of the fluxes associated with each variable. By differentiating f with respect to x, we obtain the following system of equations -

$$\frac{\partial \{u\}}{\partial t} + [A]\frac{\partial \{u\}}{\partial x} = 0 \tag{349}$$

where A is a n$\times$ n matrix, defined as follows -

$$A_{ij} = \frac{\partial f_i}{\partial u_j} \tag{350}$$

Using Taylor's expansion series, $u = u(x,t)$ is expanded about the time variable t.

$$u\left(x, t+\Delta t\right) = u\left(x,t\right) + \Delta t \frac{\partial u\left(x,t\right)}{\partial t} + \frac{1}{2}\Delta t^2 \frac{\partial^2 u\left(x,t\right)}{\partial t^2} + O\left(\Delta t^3\right) \tag{351}$$

Using equations (349) and (350), we can obtain the following relation -

$$\frac{\partial u}{\partial t} = -\frac{\partial f}{\partial x} = -A\frac{\partial u}{\partial x} \tag{352}$$

and using equations (349), (350) and (352), obtain -

$$\begin{aligned}&\frac{\partial^2 u}{\partial t^2} = -\frac{\partial}{\partial t}\left(\frac{\partial f}{\partial x}\right) = -\frac{\partial}{\partial x}\left(\frac{\partial f}{\partial t}\right) = -\frac{\partial}{\partial x}\left(\frac{\partial f}{\partial u}\frac{\partial u}{\partial t}\right) = -\frac{\partial}{\partial x}\left(A\frac{\partial u}{\partial t}\right)\\&= -\frac{\partial}{\partial x}\left(A\left(-A\frac{\partial u}{\partial x}\right)\right) = \frac{\partial}{\partial x}\left(A^2\frac{\partial u}{\partial x}\right)\end{aligned} \tag{353}$$

For a constant A matrix, this becomes -

$$\frac{\partial^2 u}{\partial t^2} = A^2\frac{\partial^2 u}{\partial x^2} \tag{354}$$

Substituting eqns. (352) and (354) back into equation (351) and neglecting third order terms and higher,

$$\begin{aligned}&\frac{\partial^2 u}{\partial t^2} = -\frac{\partial}{\partial t}\left(\frac{\partial f}{\partial x}\right) = -\frac{\partial}{\partial x}\left(\frac{\partial f}{\partial t}\right) = -\frac{\partial}{\partial x}\left(\frac{\partial f}{\partial u}\frac{\partial u}{\partial t}\right) = -\frac{\partial}{\partial x}\left(A\frac{\partial u}{\partial t}\right)\\&= -\frac{\partial}{\partial x}\left(A\left(-A\frac{\partial u}{\partial x}\right)\right) = \frac{\partial}{\partial x}\left(A^2\frac{\partial u}{\partial x}\right)\end{aligned} \tag{355}$$

The approximate value of $u(x,t)$ in numerical analysis techniques are represented as

$$u(x,t) = u_j^n \tag{356}$$

where the j refers to the spatial variable or x and n refers to the temporal variable or time t.

The first and second spatial derivatives can be approximated by the following central difference schemes -

$$\frac{\partial u}{\partial x} = \frac{u_{j+1}^n - u_{j-1}^n}{2\Delta x} \tag{357}$$

$$\frac{\partial^2 u}{\partial x^2} = \frac{u_{j+1}^n - 2u_j^n + u_{j-1}^n}{\Delta x^2} \tag{358}$$

Substituting eqns. (357) and (358) in equation (355), gives us -

$$u_j^{n+1} = u_j^n - \frac{1}{2}A\frac{\Delta t}{\Delta x}\left(u_{j+1}^n - u_{j-1}^n\right) + \frac{1}{2}\left(A\frac{\Delta t}{\Delta x}\right)^2\left(u_{j+1}^n - 2u_j^n + u_{j-1}^n\right) \tag{359}$$

There are other similar schemes where forward, backward or central difference schemes are used to approximate the derivatives in space and time. By doing a forward difference in time and central difference, forward difference or backward difference in space, three such finite difference schemes were developed.

FTCS Scheme: (Forward Time Central Space)

$$u_j^{n+1} = u_j^n - \frac{1}{2}A\frac{\Delta t}{\Delta x}\left(u_{j+1}^n - u_{j-1}^n\right) \tag{360}$$

FTFS Scheme: (Forward Time Forward Space)

$$u_j^{n+1} = u_j^n - A\frac{\Delta t}{\Delta x}\left(u_{j+1}^n - u_j^n\right) \tag{361}$$

FTBS Scheme: (Forward Time Backward Space)

$$u_j^{n+1} = u_j^n - A\frac{\Delta t}{\Delta x}\left(u_j^n - u_{j-1}^n\right) \tag{362}$$

These equations are used to calculate the variables at the grid or mesh points at each time step. Variables can also be calculated at a point midway between meshes and at every half time step instead of a full time step. The midway values can then be used to obtain the solution at each mesh point at every integer time step, thus leading to greater accuracy in solution. Such schemes are two step schemes since the solution is obtained after applying finite differences twice to the governing system of equations. One such scheme is the Richtmyer scheme [67].

$$\begin{aligned} u_{j+\frac{1}{2}}^{n+\frac{1}{2}} &= \tfrac{1}{2}\left(u_{j+1}^{n} + u_{j}^{n}\right) - \tfrac{1}{2}A\tfrac{\Delta t}{\Delta x}\left(u_{j+1}^{n} - u_{j}^{n}\right) \\ u_{j}^{n+1} &= u_{j}^{n} - A\tfrac{\Delta t}{\Delta x}\left(u_{j+\frac{1}{2}}^{n+\frac{1}{2}} - u_{j-\frac{1}{2}}^{n+\frac{1}{2}}\right) \end{aligned} \tag{363}$$

Another variation of the two step scheme is to use predicter-correcter steps. In such schemes, the first step is the predicter step and the second step is the correcter step. The 'predicted' solution from the predicter step is used to 'correct' the solution in the correcter step to obtain the final values of the variables at each grid point. An example of this scheme is the McCormick scheme.

$$\begin{aligned} u_{j}^{*} &= u_{j}^{n} - A\tfrac{\Delta t}{\Delta x}\left(u_{j+1}^{n} - u_{j}^{n}\right) \\ u_{j}^{n+1} &= \tfrac{1}{2}\left(u_{j}^{n} + u_{j}^{*}\right) - \tfrac{1}{2}A\tfrac{\Delta t}{\Delta x}\left(u_{j}^{*} - u_{j-1}^{*}\right) \end{aligned} \tag{364}$$

In equation (364), in the predicter step, forward difference in space is applied and in the correcter step, this solution is averaged in time with a backward

difference applied in space to calculate the variable at (j,n+1). Alternatively, it is also possible to reverse the finite differences in space with a backward difference in space in the predicter step and a forward difference in space in the correcter step, as depicted in equation (365).

$$\begin{aligned} u_j^* &= u_j^n - A\frac{\Delta t}{\Delta x}\left(u_j^n - u_{j-1}^n\right) \\ u_j^{n+1} &= \tfrac{1}{2}\left(u_j^n + u_j^*\right) - \tfrac{1}{2}A\frac{\Delta t}{\Delta x}\left(u_{j+1}^* - u_j^*\right) \end{aligned} \tag{365}$$

In all these schemes, typically, all the variables from the system of equations are calculated at each mesh point unlike the Neumann or Wilkins scheme. One of the drawbacks in these schemes though, is the computationally-induced oscillations that arise in the numerical solution. These oscillations can at times be inhibitive in understanding the physical aspects of the problem by camouflaging the real oscillations that arise in the solution. These oscillations can be reduced by adding an artificial viscosity or dissipative terms to the solution to damp the oscillations. But such solutions are very often not optimally stable [100]. In problems that include discontinuities like shocks, the additional dissipation terms can also lead to excessively smeared shock-fronts. One of the problems that is of immense interest in the experimental studies of shock-related chemical reactions, is the impact of a projectile on a target made of the multifunctional energetic material. In such a problem, a velocity discontinuity exists from the beginning of the analysis. Studying this problem using conventional finite difference schemes gives rise to a significant amount of numerical problems. Finite difference and related finite volume schemes are based on interpolations of discrete data using polynomials or other simple functions. A stencil is chosen to represent the grid points or meshes that are used to calculate variables at a given

mesh. A stencil is the group of points (or the meshes defined by the points) that is used in the calculation of the variables in the mesh under consideration, i.e, the computation of a variable v(x) in the mesh depends on the values of v(x) at the points included in the stencil. Wider the stencil chosen, more accurate is the interpolation, provided the function being interpolated is smooth within this stencil. In conventional finite difference schemes, one chooses a global stencil that is used for all meshes irrespective of the location of the mesh at all interior points. This technique works reasonably accurately for globally smooth problems. Using Fourier transforms, the stability of numerical solutions can be easily analyzed, for linear partial difference equations and for nonlinear PDE's with the assumption of local linearity. But near discontinuities, using these global stencils gives rise to oscillations. These oscillations do not decay with mesh refinement. Adding artificial viscosity to reduce the oscillations is not necessarily a good solution to the problem because the amount of artificial viscosity that needs to be added is problem dependent. Thus, fine-tuning the parameter that controls the artificial viscosity needs to be addressed for each problem. This can get very cumbersome, not to mention impractical. Another technique is to apply limiters to reduce the order of accuracy of the interpolation near the discontinuity. But as is obvious, this technique reduces the accuracy to first order near the smooth extrema.

A.3.2 Non-Oscillatory Schemes

Alternatives to the conventional finite difference methods have been developed. The main idea in these is to replace the globally smooth functions with functions or approximations that are locally smooth, thus, avoiding the crossing

of discontinuities in the interpolation procedure [100]. This is done by having varying stencils for the numerical approximation for each grid or mesh instead of a globally fixed stencil. A fixed stencil will include the mesh with the discontinuity when performing calculations near the discontinuities. By having an adaptive stencil, this can be avoided. These schemes do not have dominant computationally-induced oscillations and are thus, referred to as non-oscillatory schemes.

A.3.2.1 Stencil Selection

The strength of the non-oscillatory schemes lies in their adaptive stencils [97][98][100]. Thus, it is very important to choose the right stencil, else, the scheme will not be as effective as it can be. In this section, the approach used in selecting the appropriate stencil is explained. For ease in understanding, a one dimensional problem is considered. The methodology can be easily extended to multiple dimensions.

A given system is divided into a network of meshes. The meshes are divided at midway points.

$a = x_{\frac{1}{2}} < x_{\frac{3}{2}} < ... < x_{N-\frac{1}{2}} < x_{N+\frac{1}{2}} = b$

where the mesh M_i and the mesh size are defined, respectively, as -

$$M_j = \left[x_{j-\frac{1}{2}}, x_{j+\frac{1}{2}}\right] \tag{366}$$

$$\Delta x_j = x_{j+\frac{1}{2}} - x_{j-\frac{1}{2}} \tag{367}$$

For simplicity, we assume a uniform grid size. Each function v(x) defined in the mesh needs to be approximated with a numerical expression. Any mathematical function like polynomials or trigonometric expressions can be used to approximate the function. Most commonly used expressions are polynomials. When using a polynomial, for a k-th order accurate scheme, a polynomial p(x) of order k-1 is required (Eqn. 368).

$$p(x) = v(x) + O\left(\Delta x^k\right) \tag{368}$$

This implies $v\left(x_{j+\frac{1}{2}}\right)$ is replaced by a kth order accurate $v_{j+\frac{1}{2}}$. In order to construct a polynomial of order (k-1), we need to select k cells or meshes. This is where the non-oscillatory schemes differ from the conventional finite difference schemes. It is necessary to choose meshes to the left and right of mesh M_j (the mesh under consideration) such that including the mesh j, they sum to k. In other words, if we have l meshes to the left of mesh M_j and r to the right, then l + r + 1 = k. The number of meshes l and r are different for each mesh M_j under consideration and thus, we have a varying stencil for the numerical approximation instead of a fixed one. The idea is to avoid including the mesh with the discontinuity, if possible. This methodology works very well, especially when the function v(x) that we wish to approximate is only piecewise smooth. A function is 'smooth' when it has as many derivatives as the scheme requires. A piecewise smooth function implies that the derivatives to this function cannot be calculated at some finitely isolated points. But at such points, the function and its derivatives are assumed to have finite left and right limits.

Care should be taken in selecting the meshes for the stencil. One of the most important non-oscillatory schemes is the Essentially Non-Oscillatory (ENO) schemes, proposed by Harten, Enquist, Osher and Chakravarthy in 1987 [20]. Their scheme uses Newton divided differences in choosing the appropriate stencil for each mesh, which is defined in eqn. (369).

$$V\left[x_{i-\frac{1}{2}},...,x_{i-\frac{1}{2}+j}\right]=\frac{V^{(j)}(\eta)}{j!} \tag{369}$$

For a function V(x), the 0-th degree divided difference is defined as -

$$V\left[x_{i-\frac{1}{2}}\right]=V\left(x_{i-\frac{1}{2}}\right) \tag{370}$$

By induction, the j-th degree divided difference is -

$$V\left[x_{i-\frac{1}{2}},...,x_{i-\frac{1}{2}+j}\right]=\frac{V\left[x_{i+\frac{1}{2}},...,x_{i-\frac{1}{2}+j}\right]-V\left[x_{i-\frac{1}{2}},...,x_{i-\frac{3}{2}+j}\right]}{x_{i-\frac{1}{2}+j}-x_{i-\frac{1}{2}}} \tag{371}$$

This is illustrated with an example. Consider the case of j = 2.

$$\begin{aligned} V\left[x_{i-\frac{1}{2}},x_{i+\frac{1}{2}},x_{i+\frac{3}{2}}\right] &= \frac{V\ x_{i+\frac{1}{2}},x_{i+\frac{3}{2}}\ -V\ x_{i-\frac{1}{2}},x_{i+\frac{1}{2}}}{x_{i+\frac{3}{2}}-x_{i-\frac{1}{2}}} \\ &= \left\{\frac{V\ x_{i+\frac{3}{2}}\ -V\ x_{i+\frac{1}{2}}}{x_{i+\frac{3}{2}}-x_{i+\frac{1}{2}}}-\frac{V\ x_{i+\frac{1}{2}}\ -V\ x_{i-\frac{1}{2}}}{x_{i+\frac{1}{2}}-x_{i-\frac{1}{2}}}\right\}\frac{1}{x_{i+\frac{3}{2}}-x_{i-\frac{1}{2}}} \end{aligned} \tag{372}$$

Using eqn. (370), the Newton divided difference for j=2 can be obtained as

$$V\left[x_{i-\frac{1}{2}}, x_{i+\frac{1}{2}}, x_{i+\frac{3}{2}}\right] = \left\{ \frac{V\ \ x_{i+\frac{3}{2}}\ \ -V\ \ x_{i+\frac{1}{2}}}{x_{i+\frac{3}{2}} - x_{i+\frac{1}{2}}} - \frac{V\ \ x_{i+\frac{1}{2}}\ \ -V\ \ x_{i-\frac{1}{2}}}{x_{i+\frac{1}{2}} - x_{i-\frac{1}{2}}} \right\} \frac{1}{x_{i+\frac{3}{2}} - x_{i-\frac{1}{2}}} \tag{373}$$

This is true only when the function V(x) is smooth inside the stencil. If it is discontinuous at any point inside the stencil, then -

$$V\left[x_{i-\frac{1}{2}}, ..., x_{i-\frac{1}{2}+j}\right] = O\left(\frac{1}{\Delta x^j}\right) \tag{374}$$

Thus, the reason Newton divided differences are used to choose the stencil is because it is a measure of the smoothness of the function V(x) inside the stencil [100].

So we start with the mesh under consideration M_j. One mesh is added to its left and right. These stencils are defined by points $\left(x_{j-\frac{3}{2}}, x_{j-\frac{1}{2}}, x_{j+\frac{1}{2}}\right)$ and $\left(x_{j-\frac{1}{2}}, x_{j+\frac{1}{2}}, x_{j+\frac{3}{2}}\right)$ respectively. The Newton divided differences are calculated for each group of points and their absolute values are compared. If -

$$\left|V\left[x_{j-\frac{3}{2}}, x_{j-\frac{1}{2}}, x_{j+\frac{1}{2}}\right]\right| < \left|V\left[x_{j-\frac{1}{2}}, x_{j+\frac{1}{2}}, x_{j+\frac{3}{2}}\right]\right| \tag{375}$$

then, the mesh to the left of M_j is selected. Otherwise, the mesh on the right is chosen. Thus, in the former case, the stencil is

$$\mathrm{S} = \left(x_{j-\frac{3}{2}}, x_{j-\frac{1}{2}}, x_{j+\frac{1}{2}}\right) \tag{376}$$

and in the latter

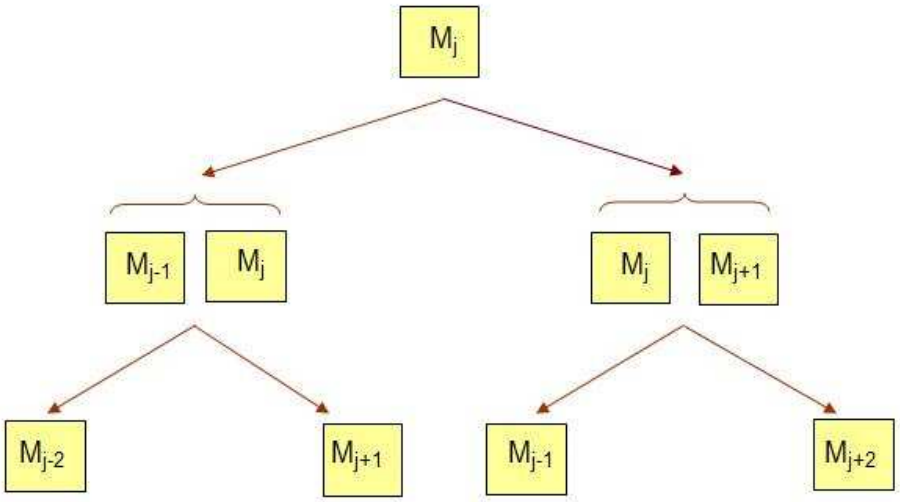

Figure 63: Selection of meshes to form the adaptive stencil in non-oscillatory schemes

$$\mathrm{S} = \left(x_{j-\frac{1}{2}}, x_{j+\frac{1}{2}}, x_{j+\frac{3}{2}} \right) \tag{377}$$

In the next step, one point or mesh is added to the left and right of the selected three points of the stencil and the above procedure is repeated to find the next mesh that needs to be included in the stencil. In this way, the required number of meshes are chosen till the required accuracy for the numerical approximation can be obtained. The number of meshes is one more than the order of the numerical integration method. This procedure is depicted in fig. 63.

A.3.2.2 Essentially Non-Oscillatory (ENO) Scheme

The next step after obtaining the adaptive stencil is to use this stencil in a

numerical scheme to solve hyperbolic equations. In this section, one of the non-oscillatory schemes is described, namely, the Essentially Non-Oscillatory scheme proposed by Harten, Enquist, Osher and Chakravarthy in 1987 [20]. Over the last couple of decades, this pioneering work has been researched further, both by its original authors and others and its formulation has been improved and extended to cover a wide area of applications. Instead of using just one stencil, the Weighted Essentially Non-Oscillatory (WENO) scheme was developed which uses all the possible stencils for each mesh. It applies a weight to each stencil and considers a convex combination of these stencils [57][71]. The stencil selection described above is based on a polynomial construction. ENO schemes that use other functions for the stencil construction have been developed [53]. Schemes to achieve significant improvements in computational cost without sacrificing on stability and accuracy have been formulated. Examples of these schemes are ENO schemes with TVD Runge-Kutta time discretizations [97][98]. Techniques such as subcell resolution to sharpen contact discontinuities have been studied [45][57][98][129]. In addition to improvements and research on the mathematical and computational concepts in the ENO schemes, a lot of work has also been done in applying these schemes to application oriented problems. For example, these schemes have been used to study gas dynamics problems [57], to simulate shock-turbulence interactions [2][98][99] etc. These schemes have been widely used in problems that include both shocks and contain smooth regions and have been found to perform very well for such problems.

The ENO scheme is explained in this section with the help of the following one-dimensional conservation equation -

$$u_t(x,t) + f_x(u(x,t)) = 0 \tag{378}$$

where u_t is the partial derivative of u with respect to t and f_x is the derivative of f with respect to x, i.e,

$$u_t = \frac{\partial u}{\partial t} \tag{379}$$

$$u_t = \frac{\partial u}{\partial x} \tag{380}$$

For a uniform grid, this scheme can then be written approximately as

$$\frac{du_j(t)}{dt} = -\frac{1}{\Delta x}\left(\tilde{f}_{j+\frac{1}{2}} - \tilde{f}_{j-\frac{1}{2}}\right) \tag{381}$$

where $u_j(t)$ is the numerical value of u(x,t) at $u(x_j, t)$. First, the finite difference scheme in the spatial direction is applied and hence the time discretization at the moment is not considered.

The numerical flux is obtained using the stencil reconstruction procedure in the ENO scheme, mentioned previously, where the function v(x) in the description is replaced by the flux function f(u(x,t)). This flux is calculated for each mesh. This means that at the end points of each mesh, there are two values of this flux, one from the calculation done for mesh M_j and the second from the calculation done for mesh M_{j-1}. There are a couple of techniques that can be used to determine which of the fluxes needs to be used to ensure stability in the numerical scheme. These are explained below -

- Upwinding using the Roe speed

  The Roe speed is defined as follows -

$$r_{j+\frac{1}{2}} = \frac{f\left(u_{j+1}\right) - f\left(u_j\right)}{u_{j+1} - u_j} \tag{382}$$

If the Roe speed $r_{j+\frac{1}{2}}$ is greater than or equal to zero, then the flux $\hat{f}^{-}_{j+\frac{1}{2}}$ from the left is used, i.e., from the mesh M_{j-1}. This is because the Roe speed indicates that wind is blowing from the left to the right. Alternatively, if the Roe speed $r_{j+\frac{1}{2}}$ is lesser than zero, then it implies the wind is blowing from right to left and we use the flux $\hat{f}^{+}_{j+\frac{1}{2}}$ from the right.

- Global Flux-splitting

  In this method, the flux f(u(x,t)) is split into two parts -

$$f(u) = f^{+}(u) + f^{-}(u) \tag{383}$$

The positive and negative fluxes have to have as many derivatives as the order of the scheme and satisfy the following conditions -

$$\frac{df^{+}(u)}{du} \geq 0 \tag{384}$$

$$\frac{df^{-}(u)}{du} \leq 0 \tag{385}$$

These criteria of the flux split narrows down the choice of possible fluxes that can be used in the scheme. There is a category of fluxes called the monotone flux. The two argument function h is a monotone flux if it satisfies the following conditions-

(a) h(a,b) is a Lipschitz continuous function in both arguments

(b) h(a,b) is a non-decreasing function in 'a' and a non-increasing function in 'b'. Symbolically $h(\uparrow, \downarrow)$.

(c) h(a,b) is consistent with the physical flux f, that is, h(a,a) = f(a)

Examples of monotone fluxes include -

(a) Godunov flux

$$h(a,b) = \begin{cases} \min_{a \le u \le b} f(u) \;\; if \;\; a \le b \\ \max_{b \le u \le a} f(u) \;\; if \;\; a > b \end{cases} \tag{386}$$

(b) Engquist-Osher flux

$$h(a,b) = \int_a^b \max(f^{'}(u), 0) du + \int_a^b \min(f^{'}(u), 0) du + f(0) \tag{387}$$

(c) Lax-Friedrichs flux

$$h(a,b) = \frac{1}{2}\left[f(a) + f(b) - \alpha(b-a)\right] \tag{388}$$

where $\alpha = \max_u \left| f^{'(u)} \right|$

Any flux that can be written in the global flux split form is also a monotone flux as shown in eqn. (389) -

$$h\left(a,b\right) = f^{+}\left(a\right) + f^{-}\left(b\right) \tag{389}$$

But the reverse is not true. Not all monotone fluxes can be written in the flux split form and thus, any monotone flux cannot be used in the ENO scheme. The Lax-Friedrichs flux, though, is a monotone flux that can be written in the flux split form and in fact, forms one of the simplest possible flux splits. And is thus, used as the global flux split.

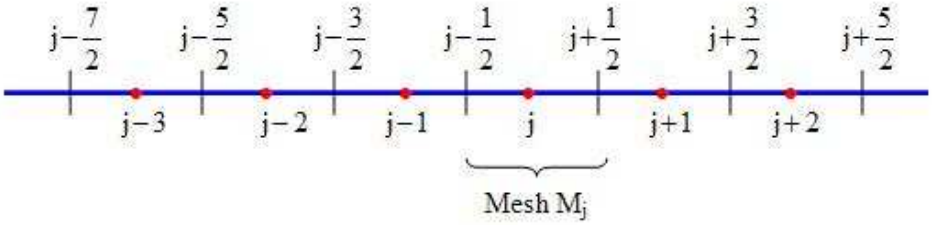

Figure 64: Mesh network in the MUSCL scheme for a one-dimensional problem

A.3.2.3 MUSCL Scheme

For the numerical analysis of very large systems of the kind that is present in shock-induced chemical reactions, it is easier to implement an alternative numerical integration method to the ENO method. This is the Monotonic Upstream-centered Scheme for Conservation Laws, abbreviated as the MUSCL scheme [68][69][87]. The adaptive stenciling procedure in this scheme is easier to implement for a large system of equations as compared to the ENO scheme. As will be shown in this section, this second order method is the similar to the second order ENO method. The procedure to implement the MUSCL scheme will be explained using the one-dimensional conservative equation as an example:

$$\frac{\partial u}{\partial t} + \frac{\partial f\left(u\right)}{\partial x} = 0 \tag{390}$$

The system is divided into a network of meshes. These meshes are divided at the midpoint location and so a mesh M_j goes from $j - \frac{1}{2}$ to $j + \frac{1}{2}$ (See fig. 64)

At the endpoints of each mesh, i.e., at points $j - \frac{1}{2}$ and $j + \frac{1}{2}$ the values of the variable u is calculated as a linear interpolation of the value in the mesh

at location u_j. Since it is a second order scheme, a linear polynomial is constructed. The idea is similar to that in the ENO scheme where a polynomial of order k-1 is constructed for a k-th order scheme. Thus, this second order spatial discretization scheme is the same as the second order ENO scheme. The difference lies in the fact that the MUSCL scheme uses the minmod function to construct the linear polynomial. The minmod function is defined as follows -

$$\min \operatorname{mod}(a,b) = \begin{cases} sign(a) \min(|a|, |b|) & a.b \rangle 0 \\ 0 & a.b \leq 0 \end{cases} \tag{391}$$

This minmod function is used to evaluate the slope S_j for the linear polynomial approximation.

$$S_j = \min \operatorname{mod} \left\{ \frac{u^n_{j+1} - u^n_j}{\Delta x}, \frac{u^n_j - u^n_{j-1}}{\Delta x} \right\} \tag{392}$$

Once the slope has been evaluated, the values of u at the end points of the mesh can be easily obtained as follows -

$$u^n_{j-\frac{1}{2}} = u^n_j - S_j \frac{\Delta x}{2} \tag{393}$$

$$u^n_{j+\frac{1}{2}} = u^n_j + S_j \frac{\Delta x}{2} \tag{394}$$

These values are calculated for each mesh and so for a given end point, there are two values, one each from the mesh on either side of the end point -

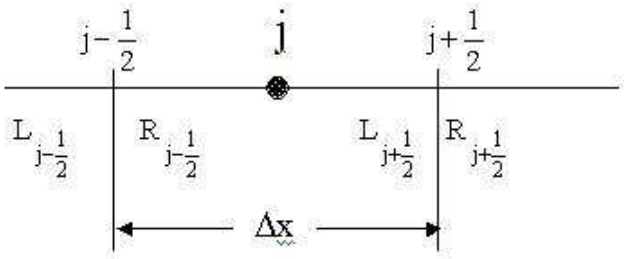

Figure 65: Depicts the double values obtained for u(x,t) at the endpoints of each mesh in the MUSCL scheme

$\left(u_{L_{j+\frac{1}{2}}}, u_{R_{j-\frac{1}{2}}}\right)$ where, $u_{L_{j+\frac{1}{2}}}$ is the value of u calculated at the right end point of mesh M_j and $u_{R_{j-\frac{1}{2}}}$ is the value of u calculated at the left end point of mesh M_{j+1}. This idea is graphically depicted in fig. 65.

The flux f(u(x,t)) is also constructed at each of these end points and will thus also have two values. Then, the Lax-Friedrichs flux is formulated as follows -

$$F^n_{j+\frac{1}{2}} = \frac{1}{2}\left[f\left(u^n_{L_{j+\frac{1}{2}}}\right) + f\left(u^n_{R_{j+\frac{1}{2}}}\right)\right] + \frac{\alpha}{2}\left(u^n_{L_{j+\frac{1}{2}}} - u^n_{R_{j+\frac{1}{2}}}\right) \tag{395}$$

$$where\ \alpha = \max_u \left|f^{'(u)}\right|$$

The Godunov scheme approximates the spatial derivative of the flux given in equation (390) as -

$$\frac{\partial f}{\partial x} = \frac{1}{\Delta x}\left(F^n_{j+\frac{1}{2}} - F^n_{j-\frac{1}{2}}\right) \tag{396}$$

and thus eqn. (390) becomes -

$$\frac{\partial u}{\partial t} = -\frac{1}{\Delta x}\left(F^n_{j+\frac{1}{2}} - F^n_{j-\frac{1}{2}}\right) \tag{397}$$

where the finite difference scheme has been applied for the spatial discretization alone.

At the boundary points, ghost cells are created. The values in the ghost cells depend on the kind of problem being solved. If it is a periodic boundary condition, then the periodicity decides the value of the variables at the boundary; for systems with support, the support constraints again governs the boundary solution. There are other options available for problems that do not fall into either of these categories. One method is where only the values inside the computational domain is used in selecting the stencil. The computational domain is the region or the mesh points whose values are required to be calculated for the current solution at another mesh point. Thus, the idea in this method is to use only meshes within the structure in constructing the stencil and avoid all ghost meshes. This can be done by having very large values at the ghost meshes and thus, making it impossible for this mesh to be chosen in the stencil. Another way to treat boundary conditions is by setting the values in the ghost meshes by extrapolation of the solution from the interior meshes.

A.3.2.4 TVD Runge-Kutta Scheme

The description in the previous section is related to the spatial discretization of the hyperbolic equation. The ENO scheme and the MUSCL scheme have been applied to approximate the spatial gradients in the governing system of equations. The method used for the time discretization is equally important and requires careful consideration. One of the most well-known and much-used numerical method is the Runge-Kutta class of schemes, proposed by Runge and

Kutta in 1895 and 1901. These can be of various orders but the two most used schemes are the Runge-Kutta second order scheme and the Runge-Kutta fourth order scheme. These are also known as RK2 and RK4, respectively. Equation (398) is the second order Runge-Kutta scheme

$$\begin{aligned} k_1 &= hf\left(x_n, y_n\right) \\ k_2 &= hf\left(x_n + \tfrac{1}{2}h, y_n + \tfrac{1}{2}k_1\right) \\ y_{n+1} &= y_n + k_2 + O\left(h^3\right) \end{aligned} \tag{398}$$

and equation (399) is the fourth order Runge-Kutta scheme.

$$\begin{aligned} k_1 &= hf\left(x_n, y_n\right) \\ k_2 &= hf\left(x_n + \tfrac{1}{2}h, y_n + \tfrac{1}{2}k_1\right) \\ k_3 &= hf\left(x_n + \tfrac{1}{2}h, y_n + \tfrac{1}{2}k_2\right) \\ k_4 &= hf\left(x_n + h, y_n + k_3\right) \\ y_{n+1} &= y_n + \tfrac{1}{6}k_1 + \tfrac{1}{3}k_2 + \tfrac{1}{3}k_3 + \tfrac{1}{6}k_4 + O\left(h^5\right) \end{aligned} \tag{399}$$

While the Runge-Kutta methods work very well and have been used extensively in the last 100 years, it has been found that if the time discretization is not done by a TVD (Total Variation Diminishing) Runge-Kutta but just by an ordinary linearly stable Runge-Kutta scheme, then even if the spatial discretization is TVD, the resulting solution is liable to have oscillations [100]. Thus, it is preferrable to use the TVD-Runge Kutta scheme as opposed to the Runge-Kutta schemes of equations (398) and (399) to solve the hyperbolic equations in this thesis. The name TVD comes from the stability criterion discussed by Shu and Osher in their 1988 paper [97], which is explained below. Since we

are now concerned with the time discretization, we shall express the spatial discretization collectively by the function $\Re(u^n)$. Thus, the equation to be solved is expressed as -

$$\frac{\partial u}{\partial t} = \Re(u^n) \tag{400}$$

then, the stability is given by the norm condition -

$$\left\|u^{n+1}\right\| \leq \|u^n\| \tag{401}$$

The norm was chosen to be the total variation norm in the paper [97] and hence, the name 'Total Variation Diminishing'. Thus, the second order TVD Runge-kutta method is -

$$\begin{aligned} \tilde{u} &= u^n + \Delta t\, \Re(u^n) \\ \tilde{\tilde{u}} &= \tilde{u} + \Delta t\, \Re(\tilde{u}) \\ u^{n+1} &= \tfrac{1}{2}\left(u^n + \tilde{\tilde{u}}\right) \end{aligned} \tag{402}$$

Thus, the governing system of hyperbolic equations, to analyze the shock-related chemical reactions of the binary energetic mixture, is solved by the MUSCL scheme for the spatial discretization and the TVD Runge-Kutta scheme for the time discretization.

REFERENCES

[1] Ackland, Graeme J., Huang, Xiangyang and Rabe, Karin M., "First-principles thermodynamics of transition metals: W, NiAl and PdTi", Phys. Rev. B **68** 214104-1:214104-7 (2003)

[2] Adams, N. and Shariff K., "A high-resolution hybrid compact-ENO scheme for shock-turbulence interaction problems", Journal of Computational Physics **127** 27-51 (1996)

[3] Adkins, C. J., Equilibrium Thermodynamics, Cambridge University Press 3^{rd} Ed.(1983)

[4] Armstrong, R. W., Cofeey, C. S. and Elban, W. L., "Adiabatic heating at a dislocation pile-up avalanche", Acta Metall. **30** 2111-2116 (1982)

[5] Armstrong, R. W., "Temperature rise at a dislocation pile-up breakthrough", Materials Science and Engineering **A122** L1-L3 (1989)

[6] Armstrong, R. W. and Zerilli, F. J., "Dislocation mechanics aspects of plastic instability and shear banding", Mechanics of Materials **17** 319-327 (1994)

[7] Armstrong, R. W., Ammon, H. L., Elban, W. L. and Tsai, D. H., "Investigation of hot spot characteristics in energetic crystals", Thermochimica Acta **6871** 1-11 (2001)

[8] Aumann, C. E., Skofronick, G. L. and Martin, J. A., "Oxidation behavior of aluminum nanopowders", J. Vac. Sc. Technol. B **13** 1178 (1995)

[9] Austin, Ryan, "Numerical simulation of the shock compression of microscale reactive particle systems", M.S Thesis Dissertation, School of Mechanical Engineering, Georgia Institute of Technology, Aug 2005

[10] Batsanov, S. S., Doronin, G. S., Klochkov, S. V. and Teut, A. I., "Synthesis reactions behind shock fronts", Combust., Explos. Shock Waves **22**(6) 765-768 (1986)

[11] Batsanov, S. S., Gogulya, M. F., Brazhinikov, M. A., Lazareva, E. V., Doronin, G. S., Klochkov, S. V., Branshchikova, M. V., Fedorov, A. V. and Simakov, G. V., "Shock compression of reacting species in the tin-chalcogen system", Sov. J. Chem. Phys. **10**(12) 2635 (1993)

[12] Batsanov, S. S., "Synthesis and modification of materials by shock waves: real time measurements and mechanisms of reaction", Materials Science and Engineering **A210** 57 (1996)

[13] Bennet, L. S., Sorrell, F. Y., Simonsen, I. K., and Horie, Y., "Ultrafast chemical reactions between nickel and aluminum powders during shock loading", Appl. Phys. Lett. **61**(5) 520-521 (1992)

[14] Bennet, L. S. and Horie, Y., "Shock-induced inorganic reactions and condensed phase detonations", Shock Waves **4** 127 (1994)

[15] Bennet, L. S., Horie, Y. and Hwang, M. M., "Constitutive model of shock-induced chemical reactions in inorganic powder mixtures",' J. Appl. Phys. **76** 3394 (1994)

[16] Benson, David J., "An implicit multi-material Eulerian formulation",' Int. J. Numer. Meth.Engng **48** 475-499 (2000)

[17] Boslough, Mark B., "A thermochemical model for shock-induced reactions (heat detonations) in solids", J. Chem. Phys. **92** 1839 (1990)

[18] Carroll, Michael and Holt, Albert C., "Suggested modification of the P-α model for porous materials", J. Appl. Phys. **43** 759 (1971)

[19] Ceperley, D. M. and Alder, B. J., "Ground State of the Electron Gas by a Stochastic Method", Phys. Rev. Lett. **45** 566569 (1980)

[20] Chakravarthy, S. R., Harten, A. and Osher, S., "Essentially non-oscillatory shock-capturing schemes of arbitrarily-high accuracy", AIAA Paper AIAA-86-0339 14p (1986)

[21] Chen, Hsin-Piao, " A new second order accurate finite difference method for dynamic response of elastic-plastic finite deformation problems", PhD Thesis Dissertation, School of Aerospace Engineering, Georgia Institute of Technology, Nov 1983

[22] Chen, Zhiying and Diang, Jiaqiang, "Molecular dynamics studies on dislocations in crystallites of nanocrystalline α-iron", NanoStructured Materials **10**(2) 205-215 (1998)

[23] Choi, Hae-Jin, "A robust design method for model and propagated uncertainty", PhD Thesis Dissertation, School of Mechanical Engineering, Georgia Institute of Technology, Dec 2005

[24] Dick, Kimberly, Dhanasekaran, T, Zhang, Zhenyuan and Meisel, Dan, "Size-dependent melting of silica-encapsulated gold nanoparticles", J. AChem. Soc. **124**(10) 2312-2317 (2002)

[25] Do, Ian P. H. and Benson, David J., "Micromechanical modeling of shock-induced chemical reactions in heterogeneous multi-material powder mixtures", Int. J. Plasticity **17** 641 (2001)

[26] Dremin, Anatoly N., *Toward Detonation Theory*, Springer (1999)

[27] Dunbar, E., Thadhani, N. N. and Graham, R. A., "High-pressure shock activation and mixing of nickel-aluminum powder mixtures", J. Mater. Sc. **8** 2903 (1993)

[28] Duvall, G. E. and Taylor, S. M. Jr., "Shock parameters in a two component mixture", J. Compos. Mater. **5** 130-139 (1971)

[29] Eck, Bernhard, Kurtulus, Yasemin, Offermans, Willy and Dronskowski, Richard, "Atomistic simulations of solid-state materials based on crystal-chemical potential concepts: applications for compounds, metals, alloys and chemical reactions", J. Alloys Compounds **338** 142 (2002)

[30] Elert, M. L., Zybin, S. V., and White, C. T., "Molecular dynamics study of shock-induced chemistry in small condensed-phase hydrocarbons", J. Chem. Phys. **118**(21) 9795-9801 (2003)

[31] Ettelaie, Rammile, Buscall, Richard, Frith William, J. and Sutton, David, "Extent of reaction in energetic particulate mixtures: Role of composition and particle size ratio", J. Chem. Phys. **110**(17) 8730-8741 (1999)

[32] Facility for the Analysis of Chemical Thermodynamics, http://www.crct.polymtl.ca/fact/, Last date accessed: Nov 15, 2005

[33] Fan, Tongxiang, Yang, Guang, Zhang, Di, Shibayanagi, Toshiya and Naka, Masaki, "Temperature dependence of melt structure in SiCp/Al composites above the liquidus", Materials Chemistry and Physics **93** 208-216 (2005)

[34] Ferranti, L., Thadhani, N. N., "Chemical reaction and mechanical behavior of multifunctional energetic structural materials", Private Communication

[35] Fickett, Wildon and Davis, William C., *Detonation*, University of California Press (1979)

[36] Fiolhais, C., Nogueira, F. and Marques, M. (Eds.), *A Primer in Density Functional Theory*, Springer (2003)

[37] Forrestal, M. J., Frew, D. J., Hanchak, S. J. and Brar, N. S., "Penetration of grout and concrete targets with ogive-nose steel projectiles", Int. J. Impact Engng. **18**(5), 465-476 (1996)

[38] Frew, D. J., Hanchak, S. J., Green, M. L. and Forrestal, M. J., "Penetration of concrete targets with ogive-nose steel rods", Int. J. Impact Engng. **21**(6), 489-497 (1998)

[39] Fried, Laurence E, Manaa M. Riad, Pagoria, Philip F. and Simpson, Randall L., "Design and synthesis of energetic materials", Annu. Rev. Mater. Res. **31** 291 (2001)

[40] Graham, R. A., Anderson, M. U., Horie, Y., You, S. K., and Holman, G. T., "Pressure measurements in chemically reacting powder mixtures with the Bauer piezoelectric polymer gage", Shock Waves **3**(2) 79-82 (1993)

[41] Griffiths, David J., *Introduction to Quantum Mechanics*, Prentice Hall (1994)

[42] Gump, Jared C. and Peiris, Suhithi, M., "Laser-initiated reactions of energetic/thermitic composites", Private Communication

[43] Hamate, Y., and Horie, Y., "A statistical approach on mechanistic modeling of high-explosive ignition", LA-UR-03-4863, Applied Physics Division, Los Alamos National Laboratory

[44] Hanagud, S. V., Principal Investigator, AFOSR MURI 2002: Multifunctional Energetic Structural Materials

[45] Harten, A., "ENO schemes with subcell resolution", Journal of Computational Physics **83** 148-184 (1989)

[46] Herrmann, W., "Constitutive equation for the dynamic compaction of ductile porous materials", J. Appl. Phys. **40** 2490 (1969)

[47] Horie, Y., Hamate, Y., Greening, D. and Dey, T., "Reactive burn modeling of solid explosives with a statistical treatment of hot spots in two spatial dimensions" LA-UR-03-4861, Applied Physics Division, Los Alamos National Laboratory

[48] Horie, Y., Graham, R. A. and Simonsen, I. K., "Synthesis of nickel aluminides under high-pressure shock loading", Materials Letters **3**(9-10) 354-359 (1985)

[49] Horie, Yukie and Kipp, Marlin E., "Modeling of shock-induced chemical reactions in powder mixtures", J. Appl. Phys. **63**(12) 5718-5727 (1988)

[50] Horie, Y. and Hamate, Y., "A New Approach to the Reactive Burn Modelig of Heterogeneous Explosives", Materials Science Forum **465-466** 1-12 (2004)

[51] Hunt, Emily M., Plantier, Keith B. and Pantoya, Michelle L.,"Nano-scale reactants in the self-propagating high-temperature synthesis of nickel aluminide", Acta Materialia **52** 3183-3191 (2004)

[52] Hutter, Jurg., "Introduction to Ab Initio Molecular Dynamics", Lecture Notes, Physical Chemistry Institute, University of Zurich (2002)

[53] Iske, A. and Soner, T., "On the structure of function spaces in optimal recovery of point functionals for ENO-schemes by radial basis functions", Numerische Mathematik **74** 177-201 (1996)

[54] Iyer, K. R., Bennet, L. S., Sorrell, F. Y. and Horie, Y., "Solid state chemical reactions at the shock front", American Institute of Physics 1337 (1994)

[55] Jeanloz, Raymond and Grover, Richard, "Birch-Murnaghan and $U_s - u_p$ equations of state", Shock waves in Condensed Matter, Edited by Schmidt, S. C. and Holmes, N. C., Elsevier Science Publishers, Amsterdam 69-72 (1987)

[56] Jesson, Ben J. and Madden, Paul A., "Ab-initio determination of the melting point of aluminum by thermodynamic integration", J. Chem. Phys. **113**(14) 5924-5934 (2000)

[57] Jiang, G. and Shu, C. W., "Efficient implementation of weighhted ENO schemes", Journal of Computational Physics **126** 202-228 (1996)

[58] Jordan, J. L., Dick, R. D., Ferranti, L., Thadhani, N. N., Austin, R. A., McDowell, D. L. and Benson, D. J., "Equation of state of aluminum-iron oxide (Fe_2O_3)-epoxy composite: Modeling and Experiment", Shock compression of condensed matter, American Physical Topical Society (2005)

[59] Jou, D., Casas-Vzquez, J. and Lebon, G., Extended Irreversible Thermodynamics, 2nd rev. and enl. ed., Springer, Berlin, New York (1996)

[60] Kittel, Charles, *Introduction to Solid State Physics*, John Wiley and Sons, Inc., third Edition (1966)

[61] Knap, J. and Ortiz, M., "An analysis of the quasicontinuum method", J. Mechanics and Physics of Solids, **49** 1899-1923 (2001)

[62] Kofman, R., Cheyssac, P., Aouaj, A., Lereah, Y., Deutscher, G., Ben-David, T., Penisson, J. M. and Bourret, A., "Surface melting enhanced by curvature effects", Surface Science, **303** 231-246 (1994)

[63] Koch, Wolfram and Holthausen, Max C. *A Chemist's Guide to Density Functional Theory*, 2nd Edition, Wiley-Vch (2001)

[64] Krueger, Barry R. and Vreeland, Thad Jr., "A Hugoniot theory for solid and powder mixtures", J. Appl. Phys., **69**(2) 710-716 (1990)

[65] Laaksonen, A. and McGraw, R., "Thermodynamics, gas-liquid nucelation, and size-dependent surface tension", Europhys. Lett., **35**(5) 367-372 (1996)

[66] Lai, S. L., Guo, J. Y., Petrova, V., Ramanath, G. and Allen L. H., "Size-dependent melting properties of small tin particles: nanocalorimetric measurements", Physical Review Letters **77**(1) 99-102 (1996)

[67] Latham, Ralph Leonard, " Interaction of Stress Waves and Cracks using a second order accurate finite difference method", PhD Thesis Dissertation, School of Aerospace Engineering, Georgia Institute of Technology, Sept 1982

[68] Leer, Bram Van., "Towards the ultimate conservative difference scheme III. Upstream-dentered finite difference schemes for ideal compressible flow", Journal of Computational Physics **23** 263-275 (1977)

[69] Leer, Bram Van., "Towards the ultimate conservative difference scheme IV. A new approach to numerical convection", Journal of Computational Physics **23** 276-299 (1977)

[70] Leer, B. V., "Towards the ultimate conservative difference scheme V. A second order sequel to Godunov's method ", Journal of Computational Physics **32** 101-136 (1979)

[71] Liu, X. D., Osher, S. and Chan, T., "Weighted essentially non-oscillatory schemes", Journal of Computational Physics **115** 200-212 (1994)

[72] Lu, Xia, " Non-equilibrium thermodynamic models for the dynamic behavior of polycrystalline solids", PhD Thesis Dissertation, School of Aerospace Engineering, Georgia Institute of Technology, Dec 2002

[73] Lu, X. and Hanagud, S., *to be published*

[74] Nanomaterials and Advanced Nanotechnnolgt, Course in Summer 2004, Georgia Instituute of Technology

[75] Marsh, Stanley P., Editor, *LASL Shock Hugoniot Data*

[76] Martin, Morgana, "Processing and characterization of energetic and structural behavior of nickel aluminum with polymer binders", M.S Thesis Dissertation, School of Materual Science Engineering, Georgia Institute of Technology, April 2005

[77] Mehl, M. J., Osburn, J. E., Papaconstantopoulos, D. A. and Klein, B. M., "Structural properties of ordered high-melting-temperature intermetallic alloys from first-principles total-energy calculations", Phys. Rev. B **41**(15) 10311-10323 (1990)

[78] Menikoff, Ralph and Kober, Edward, "Equation of state and Hugoniot locus for porous materials: P-α model revisited", Proceedings of the Conference of the American Physical Society Topical Group on Shock Compression of Condensed Matter CP#505 129 (1999)

[79] Merzhanov, A. G., "On critical conditions for thermal explosion of a hot spot", Combustion and Flame **10** 341-348 (1966)

[80] Meyers, Marc A., *Dynamic behavior of materials* (1994)

[81] Meyers, M. A., Batsanov, S. S., Gavrilkin, S. M., Chen, H. C., LaSalvia, J. C., and Marquis, F. D. S., "Effect of shock pressure and plastic strain on chemical reactions in Nb-Si and Mo-Si systems", Materials Science and Engineering **A201** 150-158 (1995)

[82] Miller, R., Ortiz, M., Phillips, R., Shenoy, V. and Tadmor, E. B., "Quasicontinuum models of fracture and plasticity", Engineering Fracture Mechanics **61** 427-444 (1998)

[83] Miller, Ronald E. and Tadmor, E. B., "The quasicontinuum method: Overview, applications and current directions", J. of Computer-Aided Materials Design **9** 203-239 (2002)

[84] Morsi, K., McShane, H. B. and McLean M., "Effect of particle size and volume fraction on hot extrusion reaction synthesis of SiC particle reinforced NiAl", Metallurgical and Materials Transactions **31A**(6) 1663-1670 (2000)

[85] Mukasyan, Alexander S., Rogachev, Alexander S. and Varma, Arvind, " Mechanisms of reaction wave propagation during combustion synthesis of advanced materials", Chemical Engineering Science **54** 3357-3367 (1999)

[86] Munir, Z. A., "Reaction Synthesis Processes: Mechanisms and Characteristics", Metallurgical Transactions A **23A** 7-13 (1992)

[87] Osher, Stanley, "Convergence of generalized MUSCL schemes", SIAM Journal Numerical Analysis **22**(5) 947-961 (1985)

[88] Perdew, J. P. and Zunger, A., "Self-interaction correction to density-functional approximations for many-electron systems", Phys. Rev. B **23**(10) 50485079 (1981)

[89] Perdew, J. P. and Wang, Y., "Accurate and simple analytic representation of the electron-gas correlation energy", Phys. Rev. B **45** 13244 (1992)

[90] Prigogine, I., Introduction to Thermodynamics of Irreverisble Processes, 3^{rd} edition, John Wiley and Sons (1968)

[91] Rajagopal, K. R. and Tao, L., Mechanics of Mixtures, World Scientific, Singapore (1995)

[92] Rice, Betsy M., Pai, Sharmila V., and Hare, Jennifer, "Predicting heats of formation of energetic materials using quantum mechanical calculations", Combustion and Flame **118** 445 (1999)

[93] Roache, P. J., *Computational Fluid Dynamics*, Hermosa (1976)

[94] Royal, T. E., Namjoshi, S., and Thadhani, N. N., "Mechanistic processes influencing shock chemistry in powder mixtures of the Ti-Si, Ti-Al and Ti-B systems", Metallurgical and Materials Transactions A **27A** 1761 (1996)

[95] Shchelkin, K. I. and Troshin, Ya. K., "Non-stationary phenomena in the gaseous detonation front", Combustion and Flame **7**(2) 143-151 (1963)

[96] Shenoy, V. B., Miller, R., Tadmor, E. B., Rodney, D., Phillips, R. and Ortiz, M., "An adaptive finite element approach to atomic-scale mechanics-the quasicontinuum method", J. Mechanics and Physics of Solids **47** 611-642 (1999)

[97] Shu, C. W., and Osher, S., "Efficient implementation of essentially non-oscillatory shock capturing schemes", Journal of Computational Physics **77** 439-471 (1988)

[98] Shu, C. W., and Osher, S., "Efficient implementation of essentially non-oscillatory shock capturing schemes II", Journal of Computational Physics **83** 32-78 (1989)

[99] Shu, C. W., Zhang, T. A., Erlebacher, G., Whitaker, D. and Osher S., "High order ENO schemes applied to two- and three- dimensional compressible flow", Applied Numerical Mathematics **92** 45-71 (1992)

[100] Shu, Chi-Wang , "Essentially non-oscillatory and weighted essentially non-oscillatory schemes for hyperbolic conservtaion laws", NASA/CR-97-206253, ICASE Report No. 97-65 (1997)

[101] Song, I. and Thadhani, N. N. , "Shock-induced chemical reactions and synthesis of nickel aluminides", Metallurgical Transactions A **23A** 41 (1992)

[102] Song, Inyoung and Thadhani, Naresh N., "Synthesis of nickel-aluminum intermetallic compounds by shock-induced chemical reactions", J Mater Synth Process **1** 347 (1993)

[103] Sugino, Osamu and Car, Roberto, "Ab initio molecular dynamics study of first-order phase transitions: melting of silicon", Phys. Rev. Lett. **74**(10) 1823-1826 (1995)

[104] Swift, D. C., Ackland, G. J., Hauer, A. and Kyrala, G. A., "First-principles equations of state for simulations of shock waves in silicon", Phys. Rev. B **64** 214107-1 (2001)

[105] Swygenhoven, H. Van and Caro, A., "Molecular dynamics computer simulation of nanophase Ni: Structure and mechanical properties", NanoStructured Materials **9** 669 (1997)

[106] Swygenhoven, H. Van, Spaczr, M. and Caro, A., "Characterization of the microstructure of nanophase Ni: A molecular dynamics simulation study", NanoStructured Materials **12** 629 (1999)

[107] Tadmor, E. B. and Phillips, Rob, "Mixed atomistic and continuum models of deformation in solids", Langmuir **12** 4529-4534 (1996)

[108] Tadmor, E. B., Smith, G. S., Bernstein, N. and Kaxiras, E., "Mixed finite element and atomistic formulation for complex crystals", Physical Review B **59**(1) 235-245 (1999)

[109] Tarver, C. M., 'What is a shock wave", Lawrence Livermore Laboratory Report '

[110] Tarver, C. M., "Chemical energy release in one-dimensional detonation waves in gaseous explosives", Combustion and Flame **43** 111-133 (1982)

[111] Tillotson, T. M., Hrubesh, L. W., Simpson, R. L., Lee, R. S., Swansiger, R. W. and Simpson, L. R., "Sol-gel processing of energetic materials", J. Non-Cryst. Solids **225** 358 (1998)

[112] Tillotson, T. M., Gash, A. E., Simpson, R. L., Hrubesh, L. W., Satcher, J. H. Jr. and Poco, J. F., "Nanostructured energetic materials using sol-gel methodologies", J. Non-Cryst. Solids **285** 338 (2001)

[113] Thadhani, N. N., Graham, R. A., Royal, T., Dunbar, E., Anderson, M. U. and Holman, G. T., "Shock-induced chemical reactions in titanium-silicon powder mixtures of different morphologies: time resolved pressure measurements and materials analysis", J. Appl. Phys. **82** 1113 (1997)

[114] Thiers, Laurent, Mukasyan, Alexander S. and Varma, Arvind, "Thermal explosion in Ni-Al system: Influence of reaction medium microstructure", Combustion and Flame **131** 198-209 (2002)

[115] Tomasi, Roberto and Munir, Zuhair A., "Effect of particle size on the reaction wave propagation in the combustion synthesis of $Al_2O_3 - ZrO_2 - Nb$ composites", Combustion and Flame **131** 198-209 (2002)

[116] Truesdell, C., "Mechanical basis of diffusion", J. Chem. Phys. **37** (10) 2336 (1962)

[117] Truesdell, C., Rational Thermodynamics, Springer (1983)

[118] Vandersall, Kevin S. and Thadhani, Naresh N., "Investigation of "Shock-induced" and "Shock-Assisted" chemical reactions in Mo+2Si powder mixtures", Metallurgical and Materials Transactions A **34A** 15 (2003)

[119] Vienna Ab-initio Simulation Package, http://cms.mpi.univie.ac.at/vasp/, Last date accessed: Nov 15, 2005

[120] Von-Neumann, J. and Richtmyer, R. D., " A Method for the Numerical Calculation of Hydrodynamic Shocks", J. Appl. Phys., **21** pp 232-257 (1950)

[121] Walker, Jeremy and Tannenbaum, Rina, "Formation of nanostructured energetic materials via modified sol-gel synthesis", Materials Research Society Symposium-Proceedings **800** 305-314 (2003)

[122] Wang, L. L., Munir, Z. A., and Maximov, Y. M., "Review- Thermite reactions: their utilization in the synthesis and processing of materials", J. Mater. Sci. **28**(14) 3693-3708 (1993)

[123] Wang, Shufeng, Yang, Yanqiang, Sun, Zhaoyong and Dlott, Dana D., "Fast spectroscopy of energy release in nanometric explosives", J. Phys. Chem. B **107** 4485-4493 (2003)

[124] Wikipedia, The Free Encyclopedia, http://en.wikipedia.org/wiki/Rankine-Hugoniot, Last date accessed: Nov 10, 2005

[125] Wilkins, M. L., "Calculation of Elastic-Plastic Flow", Methods in Computational Physics **3** 211-263, Academic Press (1964)

[126] Wilkins, M., "Finite Difference Scheme for Calculating Problems in Two Space Dimensions and Time", J. Comp. Phys. **5** 406-414 (1970)

[127] Wilkins, Mark. L., *Computer Simulation of Dynamic Phenomena*, Springer (1999)

[128] Xu, Xiao and Thadhani, Naresh. N., "Investigation of shock-induced reaction behavior of as-blended and ball-milled Ni+Ti powder mixtures using time-rsolved stress measurements", J. Appl. Phys. **96**(4) 2000-2009 (2004)

[129] Yang, H., "An artificial compression method for ENO schemes, the slope modification method", Journal of Computational Physics **89** 125-160 (1990)

[130] Yang, Y., Gould, R. D., Horie, Y. and Iyer, K. R., "Shock-induced chemical reactions in a Ni/Al powwder mixture", Appl. Phys. Lett. **70**(25) 3365-3367 (1997)

[131] Yang, Yanqiang, Sun, Zhaoyong, Wang, Shufeng and Dlott, Dana D., "Fast spectroscopy of laser-initiated nanoenergetic materials", J. Phys. Chem. B **107** 4485-4493 (2003)

[132] Yang, Yanqiang, Wang, Shufeng, Sun, Zhaoyong and Dlott, Dana D., "Propagation of shock-induced chemistry in nanoenergetic materials: The first micrometer", J. Appl. Phys. **95**(7) 3667-3676 (2004)

[133] Yano, K. and Horie, Y., "A numerical study of shock-induced particle velocity dispersion in sold mixtures", J. Appl. Phys. **84**(3) 1292-1298 (1998)

[134] Zahareiva, R. and Hanagud, S., *private communication*

[135] Zeldovich, I. B. and Kompaneets, A. S., Theory of Detonation, Academic Press (1960)

[136] Zerilli, F. J., "Dislocation mechanics-based constitutive equations", Metallurgical and Materials Transactions A **35A** 2547-2555 (2004)

[137] Zewail, Ahmed H., Chemistry Nobel Lecture "Femtochemistry: Atomic-scale dynamics of the chemical bond using ultrafast lasers" (1999)

[138] Zhang, Z., Lu, X. X. and Jiang, Q., "Finite size effect on melting enthalpy and melting entropy of nanocrystals", Physica B **270** 249-254 (1999)

[139] Zhang, M., Efremov, Yu., Schiettekatte, F., Olson, E. A., Kwan, T., Lai, S. L., Wisleder, T., Greene, J. E. and Allen L. H., "Size-dependent melting point depression of nanostructures: Nanocalorimetric measurements", Physical Review B **62**(15) 10548-10557 (2000)

[140] Zhu, Ping, Li, J. C. M. and Liu, C. T., "Reaction mechanism of combustion synthesis of NiAl", Material Science and Engineering **A329-331** 57 (2002)

VITA

Vindhya Narayanan was born in Chennai, India on 9^{th} February, 1981. She obtained her Bachelor of Technology (B. Tech) degree in Aerospace Engineering from the Indian Institute of Technology, Madras in 2002. While at IIT-Madras, she interned with the Aeronautical Development Establishment, DRDO. Her work there involved the fabrication and characterization of mechanical and vibrational properties of glass-epoxy and kevlar-epoxy composites. She joined Georgia Institute of Technology in 2002 for her Masters degree, which she received in May 2004. She continued with her graduate studies at Georgia Tech and obtained her PhD degree in Aerospace Engineering in December 2005. Her research at Georgia Tech included the investigation of thermal, chemical and mechanical processes of shock-induced chemical reactions in multifunctional energetic structural materials.